

Electrocatalytic hydrogenation of oxygenated compounds in aqueous phase – Investigation of fundamental steps at the electrode/electrolyte interface

Philipp Jürgen Fischer

Vollständiger Abdruck der von der TUM School of Natural Sciences der Technischen Universität München zur Erlangung eines

Doktors der Naturwissenschaften (Dr. rer. nat.)

genehmigten Dissertation.

Vorsitz: Prof. Dr.-Ing. Kai-Olaf M. Hinrichsen

Prüfer*innen der Dissertation:

1. Prof. Dr. Johannes A. Lercher
2. Prof. Dr. Klaus Köhler

Die Dissertation wurde am 05.09.2022 bei der Technischen Universität München eingereicht und durch die TUM School of Natural Sciences am 07.12.2022 angenommen.

Affirmation

I hereby assure that I have written the submitted thesis independently and have not used any sources and tools other than those indicated.

Place, Date, Signature

*Man merkt nie, was schon getan
wurde, man sieht immer nur, was
noch zu tun bleibt.*

Marie Skłodowska Curie

Acknowledgements

First, I would like to thank Prof. Dr. Johannes Lercher for giving me the opportunity to become a part of his group at the chair of Technical Chemistry II. It was a pleasure to work under your guidance on this interesting and challenging topic. You were always helpful with your creativity and profound knowledge and inspired me to think out of the box. I really appreciated the chance to work independently and develop my own ideas. Many thanks for training me in thinking critical about data and giving me advice before the talks and posters I presented at (inter)national conferences.

I also want to thank my supervisor, Dr. Yue Liu, and Prof. Dr. Andreas Jentys for supporting me with worthwhile feedback on my experimental work and drafts. The scientific discussions we had throughout the last years helped me to broaden my knowledge and improve my scientific rigor.

Thanks to the supervisors Hui Shi, Ricardo Bermejo de Val, Maricruz Sanchez-Sanchez, Eszter Baráth, Erika Ember and Oliver Y. Gutiérrez from PNNL who were always helpful and open to questions whenever needed.

A special thanks goes to Dr. Rachit Khare for giving me the possibility to take part in various synchrotron trips. Apart from giving me interesting insights into EXAFS spectroscopy you were always open to empirical discussions about experimental approaches and results.

Many thanks to:

My supervisor during my master thesis, Verena Höpfl, and the group of experienced old hands who helped me to integrate into the group and from whom I learned a lot about the work and the setups at the chair: Felix M. Kirchberger, Ferdinand Vogelgsang, Daniel Melzer, Andreas Ehrmeier, Martin Baumgärtl, Christoph Denk, Teresa Schachtl, the colleagues of E-Chem group Simon Krebs, Ilka Vincon, Guanhua Chen, Iris Yu, Fuli Deng, Xi Chen, Mingwu Tan, Hongwen Chen and Laura Meyer from PNNL. We always had good discussions during our meetings where we tried to find the best explanations for our results.

All the colleagues at TC II who were always open to questions and supported me during my PhD: Roland Weindl, Niklas Pfriem, Lara Milakovic, Manuel Weber, Insu Lee, Jakub Pazdera, Mirjam Wenig, Alexander Wellmann, Laura Löbbert, Florian Zahn, Christoph Gross, Martina Aigner, Lennart Wahl, Takaaki Ikuno, Lei Tao, Lingli Ni, Yong Wang and Ruixue Zhao.

The people I have been with on different EXAFS trips and who made these stays an interesting and funny time: Mirjam Wenig, Roland Weindl, Simon Krebs, Jakub Pazdera, Christoph Gross, Florian Zahn and Lennart Wahl.

The members of TCII that went to NAM in New York City: Roland Weindl, Mirjam Wenig, Jakub Pazdera and Florian Zahn and Insu Lee who joined us visiting New York. After two years of pandemic, visiting an in-person conference was highly appreciated. Many thanks to Prof. Dr. Johannes Lercher for making this possible. In combination with travelling New York City this was a perfect final of my PhD.

The administrative and technical staff at the chair: Stefanie Seibold, Kateryna Kryvko, Bettina Federmann, Verona Bekteshi Sylva, Xaver Hecht, Muhammad Iqbal, Andreas Marx and Martin Neukamm.

All the helping hands of students that I had the pleasure to work with: Christian Heiß, Angelina Cuomo, Daniel Rottmann and Fabio Fidelibus.

Mein besonderer Dank gilt meinen Eltern für ihre unablässige und bedingungslose Unterstützung während aller Höhen und Tiefen meines Lebens.

Philipp

August, 2022

Abstract

The electrocatalytic hydrogenation of aldehydes on transition metal catalysts in water was investigated. By combining electrochemical investigations with physicochemical characterization of catalysts, the adsorption of hydrogen on Pt is found to be affected by external electric potential and electrolyte composition. Thus, hydrogenation rates and selectivity of reactions can be tuned. Increasing the destabilization of hydrogen bound to the metal surface leads to higher reaction rates, but also a decreased current efficiency.

Die elektrokatalytische Hydrierung von Aldehyden an Übergangsmetallkatalysatoren in Wasser wurde untersucht. Durch Kombination elektrochemischer Messungen mit physikochemischer Charakterisierung der Katalysatoren wurde festgestellt, dass die Adsorption von Wasserstoff auf Pt durch elektrisches Potential und die Elektrolytmischung beeinflusst wird. So können Hydrierraten und Selektivitäten von Reaktionen verändert werden. Eine zunehmende Schwächung der Pt-H Bindung führt zu höheren Raten, aber auch zu einer geringeren Stromausbeute.

List of Abbreviations

AAS	Atomic Absorption Spectroscopy
AC	Activated Carbon
AIMD	Ab Initio Molecular Dynamics
BAS	Brønsted Acid Site
BzHO	Benzaldehyde
CE	Counter Electrode
CNT	Carbon NanoTubes
CV	Cyclic Voltammetry
DFT	Density Functional Theory
DSC	Differential Scanning Calorimetry
e.g.	exempli gratia
ECH	ElectroCatalytic Hydrogenation
EDL	Electrochemical Double-Layer
Eq.	Equation
FE	Faradaic Efficiency
Fig.	Figure
GC	Gas Chromatography
H _{ads}	adsorbed Hydrogen
HBE	Hydrogen Binding Energy
HER	Hydrogen Evolution Reaction
H _{opd}	overpotential deposited Hydrogen
HOR	Hydrogen Oxidation Reaction
H _{upd}	underpotential deposited Hydrogen
i.e.	id est
IS	Ionic Strength
IUPAC	International Union of Pure and Applied Chemistry
LP	Linear Polarization
ML	MonoLayer
MO	Molecular Orbital
MS	Mass Spectrometry
OCP	Open Circuit Potential
OER	Oxygen Evolution Reaction

OHL.....	O uter H elmholtz L ayer
OHP.....	O uter H elmholtz P lane
OOR	O xygen O xidation R eaction
PCET.....	P roton C oupled E lectron T ransfer
QMMD	Q uantum M echanics M olecular D ynamics
RDE.....	R otating D isk E lectrode
RE.....	R eference E lectrode
RHE.....	R eversible H ydrogen E lectrode
Rxn.	R eaction
SHE	S tandard H ydrogen E lectrode
SI.....	S upporting I nformation
TCH.....	T hermo- C hemical H ydrogenation
TEM	T ransmission E lectron M icroscopy
TGA.....	T hermo G ravimetric A nalysis
TOF	T urn O ver F requency
TPD	T emperature P rogrammed D esorption
WE.....	W orking E lectrode
XPS.....	X -ray P hotoelectron S pectroscopy

List of Figures

Introduction

Figure 1: World primary energy consumption from 1995-2020 by resources, adapted from ref. [1].	24
Figure 2: Schematic representation of future conversion and storage of (excess) renewable energy <i>via</i> heterogeneous (electro)catalysis, adapted from ref. [9].	25
Figure 3: Composition of lignocellulosic biomass feedstock with excerpts of chemical structures of lignin, cellulose and hemicellulose, reprinted from ref. [18b].	26
Figure 4: Schematic of different biomass upgrading processes after initial depolymerization of lignocellulosic raw material, adapted from ref. [19].	27
Figure 5: Overview of unsaturated, oxygen-rich molecules contained in bio-oil generated <i>via</i> pyrolysis of lignocellulosic feedstock.	28
Figure 6: Schematic representation of jR -induced potential drop between WE and RE or CE, respectively arising from uncompensated solution resistance.	30
Figure 7: a) Two-compartment batch cell used for electrocatalytic hydrogenation and water electrolysis and b) structure of <i>Nafion</i> polymer with hydrogen bonding between sulfonate side groups and water.	31
Figure 8: Volcano plots of exchange current density of transition metals as function of a) M-H bond strength, and b) <i>Gibbs</i> free energy of adsorbed H on metal surface, adapted from refs. [61a] and [61b].	35
Figure 9: a) Linear polarization (LP) curve of HER on Pt in aqueous phase, and b) resulting <i>Tafel</i> plot with different <i>Tafel</i> slopes b_c .	35
Figure 10: Development of measured current density with applied overpotential according to <i>Butler-Volmer</i> model.	38
Figure 11: Schematic representation of parallel plate model (left) and corresponding potential drop across EDL (right).	39
Figure 12: Schematic representation of diffuse double-layer model (left) and respective potential drop across EDL (right).	41
Figure 13: Schematic representation of <i>Stern</i> model (left) and respective potential drop across EDL with <i>Stern</i> potential (right).	42
Figure 14: Development of applied potential with time during linear polarization measurements.	43

Figure 15: a) Linear polarization curve of HER/HOR and b) resulting <i>Tafel</i> plot for a catalyst with an onset overpotential of $\eta = 0.01$ V and an exchange current of $ i_o = 10$ mA. ^[74]	43
Figure 16: Change of electrode potential over time during cyclic voltammetry.	44
Figure 17: Cyclic voltammetry of Pt supported on carbon nanotubes in aqueous phase.	45
Figure 18: Schematic representation of applied potential and current response during EIS. 46	
Figure 19: a), b) <i>Nyquist</i> plot for determination of real and imaginary part of impedance and its phase-shift as well as R_s , R_{CT} , C_{DL} and Z_W , and c) resulting <i>Randles</i> circuit.....	46
Figure 20: Schematic representation of variation of chemical potential of adsorbed state and thus, changing adsorption enthalpy upon variation of local electric potential.....	49
Figure 21: <i>BET</i> plot for determining monolayer adsorbed gas quantity and <i>BET</i> constant..	51
Figure 22: <i>BET</i> isotherms classified according to <i>IUPAC</i> , adapted from ref. [104].....	52
Figure 23: Schematic of a generic N ₂ physisorption setup, reprinted from <i>Naderi</i> . ^[106]	53
Figure 24: Schematic representation of H adsorption isotherms on different metal surface sites with extrapolated monolayer uptake.	53
Figure 25: Schematic overview of a H ₂ chemisorption setup, reprinted from <i>Fadoni and Lucarelli</i> . ^[113]	54
Figure 26: Schematic representation of a transmission electron microscope, reprinted from ref. [118]......	56
Figure 27: Schematic of a double beam AAS setup reprinted from <i>Beaty and Kerber</i> . ^[128] .	57

Impact of external electric potential on electrocatalytic adsorption of hydrogen on Pt nanoparticles in aqueous phase

Figure 1: a) Schematic representation of electrochemical double-layer, and b) cyclic voltammogram on Pt/ <i>CNT</i> in aqueous phase (pH 5). The M^+ and A^- in a) denote metal cations and electrolyte anions.	65
Figure 2: a) Features of H_{upd} on Pt/ <i>CNT</i> in aqueous phase and b) free energy of H adsorption on electrode surface according to Equation 4.	67
Figure 3: H_{upd} coverage of electrode surface with respect to external electric potential and electrolyte temperature.	67
Figure 4: a) Development of $\Delta G_{\text{upd}}^\circ + \mu_{\text{excess}}$ and b) change of μ_{excess} with external electric potential in the range of $T = 283\text{-}313$ K.	68
Figure 5: a) Plot of linearized <i>Gibbs-Helmholtz</i> equation, and b) development of H_{upd} adsorption heat on Pt in water with external electric potential.	70
Figure 6: a) Enthalpy and b) free energy of H_{upd} adsorption on Pt as function of electric potential and electrolyte pH.	70
Figure 7: a) Extrapolated plots of $\Delta G_{\text{upd}}^\circ + \mu_{\text{excess}}$ vs. E_{RHE} and b) HER onset overpotential $E_{\text{H}_2/\text{H}^+}^\circ$ as function of solution pH.	71
Figure 8: Linear polarization (LP) curves of HER on Pt/ <i>CNT</i> in aqueous electrolyte at different pH.	71
Figure 9: Schematic illustration of the difference between the potential energy of Pt-H antibonding state and Pt <i>Fermi</i> level. At large difference Pt-H bond is strengthened; at small difference it is weakened.	72
Figure 10: Increase of electrode work function after contact of Pt <i>Fermi</i> level with electrolyte redox couple and remaining difference with respect to electrolyte acidity.	73
Figure 11: Displacement of water molecules upon H_{upd} adsorption on Pt electrode (black), Pt <i>Fermi</i> level drop and gas phase H adsorption (yellow) on previously H_2O covered sites beyond $2/3$ ML of H_{upd}	74
Figure 12: Displacement of EDL from electrode surface upon adsorption of H on Pt (left), and distance of first water layer from electrode surface in presence and absence of adsorbed H calculated <i>via</i> DFT based AIMD simulations according to <i>Yang et al.</i> ^[27]	75
Figure S1: a) NH_3 -TPD signal of H-MFI, b) NH_3 -TPD signal of <i>CNT</i> , c-d) TGA- and pyridine MS-signal during pyridine-TPD on <i>CNT</i>	78

Figure S2: TEM image of 5 wt% Pt/ <i>CNT</i> (left) and statistical evaluation of particle size (right).....	80
Figure S3: CV peaks associated to <i>Volmer</i> reaction (left) and development of proton concentration near electrode surface over time (right).....	82
Figure S4: Cyclic voltammogram of Pt/ <i>CNT</i> in aqueous electrolyte with double-layer capacitance marked in green.	83
Scheme S1: Reaction equations for electrochemical adsorption and desorption of electrolyte species on Pt surface based on CV curve in Figure 1b.	84
Figure S5: a) Integrated areas of pseudo-capacitance in CV due to H ₂ oxidation (red) and H _{upd} formation (green) and b) temperature dependence of CV on Pt in water.	85
Figure S6: a) Shift of H _{upd} signals on Pt/ <i>CNT</i> with respect to solution pH and b) H _{upd} coverage of electrode surface as function of applied overpotential.....	88
Figure S7: a), c), e), g) Development of $\Delta G_{\text{upd}}^{\circ} + \mu_{\text{excess}}$ with external electric potential in the range of $T = 283\text{-}313$ K at pH 2.4, 3.2, 4.2 and 4.9 and b), d), f), h) course of μ_{excess} with increasing overpotential.	89
Figure S8: Plots of linearized <i>Gibbs-Helmholtz</i> equation for pH 4.9, 4.2, 3.2 and 2.4 (a-d).	90
Figure S9: <i>Tafel</i> plots with <i>Tafel</i> slopes of linear polarization curves of HER on Pt/ <i>CNT</i> in aqueous electrolytes at different pH.....	91

Electrocatalytic hydrogenation of benzaldehyde in aqueous phase – Impact of electrolyte composition on catalyst performance

Figure 1: a) Schematic representation of electrochemical double-layer and b) cyclic voltammogram on Pt/CNT in water. The M^+ and A^- in a) denote metal cations and electrolyte anions, respectively. 97

Figure 2: Cyclovoltammetry of Pt/CNT in aqueous electrolytes containing different concentrations of benzaldehyde. a)-c) refer to the different electrolyte compositions investigated, i.e., pH 4.9 and IS = 3.0 M, pH 2.4 and IS = 3.0 M, and pH 4.9 and IS = 0.6 M. 99

Figure 3: a) Peaks related to H_{upd} formation on Pt/CNT during cyclic voltammetry, and b) free energy of H_{upd} adsorption on electrode surface as function of external electric potential. 100

Figure 4: Dependence of excess potential on external electric potential at various electrolyte temperatures. 101

Figure 5: a) Plot of linearized Gibbs-Helmholtz equation $\Delta G_{\text{upd}}^{\circ} / T$ over $1/T$ with heat and entropy of H_{upd} formation on Pt at OCP, b) ΔH_{upd} as function of external electric potential, c) and d) development of turnover frequency and *Faradaic* efficiency of ECH and HER on Pt with external electric potential. 101

Figure 6: Schematic illustration of bonding and antibonding state of Pt-H bond after hybridization of metal 5 d band with H 1s orbital and filling of antibonding state with respect to Pt electrode *Fermi* level. 102

Figure 7: a) Shift of H_{upd} features on Pt/CNT in water and b) free energy of H_{upd} adsorption as function of external electric potential on SHE scale, both at different electrolyte pH. 103

Figure 8: a) Extrapolated plot of $\Delta G_{\text{upd}}^{\circ} + \mu_{\text{excess}}$ vs. E_{SHE} , b) linear polarization curves of HER on Pt/CNT at different pH and c) onset overpotential for HER, $E_{\text{H}_2/\text{H}^+}^{\circ}$, determined from a).. 103

Figure 9: a) Features of H_{upd} adsorption in CV on Pt at different electrolyte ionic strength, b) development of $\Delta G_{\text{upd}}^{\circ} + \mu_{\text{excess}}$ with external electric potential on SHE scale and c) linear polarization curves of HER measured on Pt/CNT in aqueous phase at different ionic concentration. 104

Figure 10: a) CV signals of underpotential deposited hydrogen on Pt, b) free energy of H_{upd} adsorption on metal surface as function of applied overpotential on SHE scale and c) linear

polarization curves of HER on Pt/ <i>CNT</i> , all measured in aqueous solutions containing various alkali metal cations.....	105
Figure 11: a) Correlation between $\Delta H_{\text{upd}}^{\circ}$ and $\Delta S_{\text{upd}}^{\circ}$ of H_{upd} formation on Pt for various electrolyte compositions, and b)-c) development of Faradaic efficiency with heat and entropy of H_{upd} adsorption.....	106
Figure 12: Initial turnover frequencies of electrocatalytic benzaldehyde hydrogenation and HER on Pt in aqueous electrolytes at different pH, ionic strength and alkali metal cations (a)-c)).	107
Figure 13: Displacement of EDL from electrode surface upon adsorption of H_{upd} on Pt (left), and distance of first water layer from electrode surface in presence and absence of adsorbed H calculated <i>via</i> DFT based AIMD simulations according to <i>Yang et al.</i> ^[34]	108
Figure 14: a) Open circuit potential of Pt as function of electrolyte pH measured in H_2 - and H_2 -saturated solution and b) development of turnover frequency of benzaldehyde ECH with E_{OCP} .	109
Figure 15: Transport and immobilization of hydronium ions from bulk solution to/at outer <i>Helmholtz</i> layer followed by formation of H_{upd} .	110
Figure 16: a) Composition of EDL at low (left) and high (right) ionic strength of bulk solution and b) depletion of hydronium ions close to electrode surface upon ECH and HER, respectively.	112
Figure S1: a) NH_3 -TPD signal of H-MFI, b) NH_3 -TPD signal of <i>CNT</i> , c-d) TGA- and pyridine MS-signals during pyridine-TPD performed on <i>CNT</i> .	114
Figure S2: TEM image of 5 wt% Pt/ <i>CNT</i> (left) and statistical evaluation of particle size (right).	116
Figure S3: a),c),e),g) Development of free energy of H_{upd} formation on Pt with external electric potential and b),d),f),h) excess potential as function of applied overpotential, both at pH 2.4, 3.2, 4.1, 4.9.	122
Figure S4: a)-d) Plot of linearized <i>Gibbs-Helmholtz</i> equation, $\Delta G_{\text{upd}}^{\circ} / T$ vs. $1/T$, for determining the heat and entropy of H_{upd} formation on electrode surface at OCP, i.e., $\Delta H_{\text{upd}}^{\circ}$, $\Delta S_{\text{upd}}^{\circ}$. a)-d) refer to the same solution pH as in Fig. S3.	123
Figure S5: a),c),e),g) Free energy of H_{upd} adsorption on Pt as function of external electric potential and b),d),f),h) development of μ_{excess} with applied overpotential, both at IS = 4.5, 3.5, 1.5, 0.60 M.	124

Figure S6: a)-d) Plot of linearized <i>Gibbs-Helmholtz</i> equation, $\Delta G_{\text{upd}}^{\circ} / T$ vs. $1/T$, for determining the heat and entropy of H_{upd} adsorption on electrode surface at OCP, i.e., $\Delta H_{\text{upd}}^{\circ}$, $\Delta S_{\text{upd}}^{\circ}$. a)-d) refer to the same ionic strength as in Fig. S5.....	125
Figure S7: a),c),e) Dependence of $\Delta G_{\text{upd}}^{\circ} + \mu_{\text{excess}}$ of H_{upd} formation on metal surface on applied overpotential and b),d),f) development of excess potential with external electric potential, both for aqueous electrolytes containing Li^+ , Na^+ and K^+	126
Figure S8: a)-c) Plot of linearized <i>Gibbs-Helmholtz</i> equation, $\Delta G_{\text{upd}}^{\circ} / T$ vs. $1/T$, for evaluating the $\Delta H_{\text{upd}}^{\circ}$ and $\Delta S_{\text{upd}}^{\circ}$ on Pt surface at open circuit potential for Li^+ -, Na^+ - and K^+ -containing solutions.	127
Figure S9: <i>Tafel</i> plots with <i>Tafel</i> slopes of linear polarization curves of HER on Pt/ <i>CNT</i> in aqueous electrolytes at different pH (a) and IS (b) and with different alkali metal cations (c).	128
Figure S10: Development of standard free energy of benzaldehyde adsorption on Pt ($\Delta G_{\text{BzHO}}^{\circ}$) with benzaldehyde concentration at $E_{\text{RHE}} = 0.05$ V in aqueous electrolytes of pH 4.9 and IS = 3.0 M (a), pH 2.4 and IS = 3.0 M (b) and pH 4.9 and IS = 0.6 M (c).....	130
Figure S11: a)-c) Plot of linearized <i>Gibbs-Helmholtz</i> equation, $\Delta G_{\text{BzHO}}^{\circ} / T$ vs. $1/T$, for determining the heat and entropy of benzaldehyde adsorption on electrode surface at zero concentration of BzHO and $E_{\text{RHE}} = 0.05$ V, i.e., $\Delta H_{\text{BzHO}}^{\circ}$, $\Delta S_{\text{BzHO}}^{\circ}$. a)-c) refer to the same solution composition as in Fig. S10.	130

Electrocatalytic hydrogenation of α,β unsaturated aldehydes – Influence of external electric potential, electrolyte composition and catalyst structure on carbonyl group activation

Scheme 1: Reaction network of electrocatalytic hydrogenation of <i>trans</i> -2-penten-1-al.....	137
Figure 1: Adsorption isotherms of <i>trans</i> -2-penten-1-ol and valeraldehyde on 5 wt% Ru/CNT-COOH at different temperatures (a), c) and on various catalysts supported on CNT-COOH, at 278 K (b), d)).	137
Figure 2: Cyclic voltammograms of 5 wt% Pd/CNT-COOH in pH 5 electrolyte with increasing concentration of a) <i>trans</i> -2-penten-1-ol and b) valeraldehyde.	138
Figure 3: Conversion of <i>trans</i> -2-penten-1-al and product formation during ECH at $E_{RHE} = -1.2$ V on a) 5 wt% Pd/CNT-COOH and b) 5 wt% Ru/CNT-COOH.	139
Figure 4: Arrhenius plots for determining activation energies of hydrogenation of CO and C=C group of <i>trans</i> -2-penten-1-al on a) Pd and b) Ru, at 1 bar H_2 .	140
Figure 5: Reaction orders of formation of various products in electrocatalytic <i>trans</i> -2-penten-1-al hydrogenation on a) 5 wt% Pd/CNT-COOH and b) 5 wt% Ru/CNT-COOH.	140
Figure 6: Development of product selectivity during ECH of <i>trans</i> -2-penten-1-al at $E_{RHE} = -1.2$ V on Pd- and Ru-based catalysts with increasing iron content.	141
Figure 7: Product selectivity as function of external electric potential for electrocatalytic hydrogenation of <i>trans</i> -2-penten-1-al on 5-3 wt% Ru-Fe/CNT-COOH.	142
Figure 8: Plots of linearized Langmuir equation for adsorption isotherms of a), b) valeraldehyde and c), d) <i>trans</i> -2-penten-1-ol on Pd and Ru supported on CNT-COOH, at 278 K.	143
Figure 9: van't Hoff plot for determining the adsorption heat of valeraldehyde and <i>trans</i> -2-penten-1-ol on 5 wt% Pd/CNT-COOH and 5 wt% Ru/CNT-COOH, respectively.	144
Figure 10: Development of free energy of adsorption of a) <i>trans</i> -2-penten-1-ol and b) valeraldehyde on Pd with organics concentration, at $E_{RHE} = 0.05$ V and c) corresponding plot of $\Delta G_{Org}^\circ / T$ vs. $1/T$ for determining the corresponding heats of adsorption on Pd.	145
Figure 11: Adsorption heat of valeraldehyde and <i>trans</i> -2-penten-1-ol on a) Pd and b) Ru as function of external electric potential.	145
Figure 12: Dependence of product selectivity of 5-3 wt% Ru-Fe catalyzed electrocatalytic hydrogenation of <i>trans</i> -2-penten-1-al on a) electrolyte and b) support acidity.	146

Figure 13: Selectivity of <i>trans</i> -2-penten-1-al ECH on 5-3 wt% Ru-Fe/ <i>CNT</i> -COOH at $E_{\text{RHE}} = -1.1/1.2$ V towards valeraldehyde, <i>trans</i> -2-penten-1-ol and pentan-1-ol at different metal particle sizes.	148
Figure S1: TEM images of 5-3 wt% Ru-Fe/ <i>CNT</i> -COOH reduced at 200, 350 and 500 °C (left to right).	151
Figure S2: Plots of linearized <i>Langmuir</i> equation for adsorption isotherms of a), c) valeraldehyde and b), d) <i>trans</i> -2-penten-1-ol on Ru supported on <i>CNT</i> -COOH at 295 K and different E_{RHE}	158
Figure S3: <i>van't Hoff</i> plots for determining the adsorption heat of valeraldehyde and of <i>trans</i> -2-penten-1-ol on 5 wt% Ru/ <i>CNT</i> -COOH at a) $E_{\text{RHE}} = 0.5$ V and b) $E_{\text{RHE}} = 0.1$ V.	159
Figure S4: Development of free energy of adsorption of <i>trans</i> -2-penten-1-ol (a), d), g) and valeraldehyde (b), e), h)) on Pd with organics concentration, at $E_{\text{RHE}} = 0.10, 0.15, 0.20$ V and corresponding plots of $\Delta G_{\text{Org}}^{\circ} / T$ vs. $1/T$ for deriving the organics heat of adsorption on Pd (c), f), i)).	162

List of Tables

Impact of external electric potential on electrocatalytic adsorption of hydrogen on Pt nanoparticles in aqueous phase

Table S1: Amount of $\text{Na}_2\text{HPO}_4 \cdot 2\text{H}_2\text{O}$, NaH_2PO_4 , and H_3PO_4 dissolved in 1.0 L ultrapure H_2O for preparation of buffered electrolytes.....	79
Table S2: Properties of 5 wt% Pt/CNT catalyst.	79
Table S3: Enthalpy and entropy of H_{upd} adsorption on Pt at zero overpotential and different electrolyte pH determined from slopes and y-intercepts in Fig.S8.	90
Table S4: <i>Tafel</i> slopes of HER on Pt/CNT in aqueous phase at different pH.	91

Electrocatalytic hydrogenation of benzaldehyde in aqueous phase – Impact of electrolyte composition on catalyst performance

Table S1: Amount of $\text{Na}_2\text{HPO}_4 \cdot 2\text{H}_2\text{O}$, NaH_2PO_4 , KH_2PO_4 , LiH_2PO_4 and H_3PO_4 dissolved in 1.0 L ultrapure H_2O for electrolyte preparation.	115
Table S2: Properties of 5 wt% Pt/ <i>CNT</i> catalyst.	116
Table S3: <i>Tafel</i> slopes of HER on Pt/ <i>CNT</i> in aqueous phase at different pH, IS and alkali metal cations.....	128

Electrocatalytic hydrogenation of α,β unsaturated aldehydes – Influence of external electric potential, electrolyte composition and catalyst structure on carbonyl group activation

Table 1: Turnover frequencies (TOF_{ECH}) for formation of various products in ECH of <i>trans</i> -2-penten-1-al on different catalysts.	141
Table 2: Turnover frequencies (TOF_{ECH}) for formation of various products in ECH of <i>trans</i> -2-penten-1-al on 5-3 wt% Ru-Fe/CNT-COOH at increasing cathodic overpotential... 142	142
Table 3: Adsorption heat of valeraldehyde and <i>trans</i> -2-penten-1-ol on Pd- and Ru-containing catalysts.	144
Table 4: Turnover frequencies (TOF_{ECH}) for formation of various products in ECH of <i>trans</i> -2-penten-1-al on 5-3 wt% Ru-Fe at various electrolyte and support acidity.....	147
Table 5: Turnover frequencies (TOF_{ECH}) for formation of various products in ECH of <i>trans</i> -2-penten-1-al on 5-3 wt% Ru-Fe/CNT-COOH with different metal particle size.....	148
Table S1: Amount of $\text{Na}_2\text{HPO}_4 \cdot 2\text{H}_2\text{O}$, NaH_2PO_4 and H_3PO_4 dissolved in 1.0 L ultrapure H_2O for electrolyte preparation.	150
Table S2: Amount of precursor salts for synthesis of respective metal catalysts supported on carbon nanotubes. The number in brackets determine the target metal loading in wt%.....	151
Table S3: Metal loading and external surface area of synthesized catalysts and mean particle diameter and metal dispersion of Pd-containing catalysts.	151
Table S4: Mean particle size and metal dispersion of Ru-containing catalysts after reduction at different temperatures determined from TEM images.	151
Table S5: Adsorption equilibrium constants and monolayer uptakes for adsorption of valeraldehyde and <i>trans</i> -2-penten-1-ol on 5 wt% Pd/CNT-COOH and 5 wt% Ru/CNT-COOH at OCP.	158
Table S6: Adsorption equilibrium constants and monolayer uptakes for adsorption of valeraldehyde and <i>trans</i> -2-penten-1-ol on 5 wt% Ru/CNT-COOH at different external electric potentials.	159

Table of Contents

Abstract	vi
List of Abbreviations	vii
List of Figures	ix
List of Tables	xviii
Table of Contents	xxi
1. Introduction	24
1.1 Energy consumption – current situation and future perspectives	24
1.2 Biomass as renewable feedstock	26
1.3 Electrochemical cells and electrocatalytic hydrogenation	29
1.4 Electrocatalytic activation of hydrogen and hydrogen evolution	34
1.5 Electrochemical double-layer	39
1.5.1 Parallel plate model	39
1.5.2 Diffuse double-layer model	40
1.5.3 Stern model	41
1.6 Electroanalytic techniques for probing EDL	43
1.6.1 Linear polarization	43
1.6.2 Cyclic voltammetry	44
1.6.3 Electrochemical impedance spectroscopy	45
1.7 (Electro)chemical potential	47
1.8 Catalyst characterization	50
1.8.1 Nitrogen physisorption	50
1.8.2 Hydrogen chemisorption	53
1.8.3 Transmission electron microscopy	54
1.8.4 Atomic absorption spectroscopy	56
1.9 Scope of the thesis	58
1.10 References	59

2. Impact of external electric potential on electrocatalytic adsorption of hydrogen on Pt nanoparticles in aqueous phase	63
2.1 Introduction	64
2.2 Results	67
2.3 Discussion.....	72
2.3.1 Influence of external electric potential on Pt <i>Fermi</i> level.....	72
2.3.2 Influence of electrolyte pH on ΔH_{upd} on Pt.....	75
2.4 Conclusion.....	77
2.5 Supporting information.....	78
2.5.1 Experimental	78
2.5.2 Thermodynamic quantification of CV curve	82
2.5.3 Calculation of free energy of H adsorption on Pt from H_{upd} peaks	86
2.5.4 Impact of electrolyte pH on ΔH_{upd} on Pt.....	88
2.5.5 Tafel evaluation of polarization curves	91
2.6 References	92
2.7 Associated content.....	94
3 Electrocatalytic hydrogenation of benzaldehyde in aqueous phase – Impact of electrolyte composition on catalyst performance.....	95
3.1 Introduction	96
3.2 Results	100
3.3 Discussion.....	108
3.4 Conclusion.....	113
3.5 Supporting information.....	114
3.5.1 Experimental	114
3.5.2 Calculation of free energy of H adsorption on Pt from H_{upd} peaks	120
3.5.3 Influence of electrolyte acidity on ΔH_{upd}	122
3.5.4 Influence of electrolyte ionic strength on ΔH_{upd}	124
3.5.5 Influence of electrolyte cations on ΔH_{upd}	126

3.5.6	<i>Tafel</i> analysis of polarization measurements	128
3.5.7	Calculation of thermodynamic properties of BzHO adsorption on Pt	129
3.6	References	131
3.7	Associated content	133
4	Electrocatalytic hydrogenation of α,β -unsaturated aldehydes – Influence of external electric potential, electrolyte composition and catalyst structure on carbonyl-group activation	134
4.1	Introduction	135
4.2	Results and discussion	139
4.2.1	Influence of noble metal and promoter species	139
4.2.2	Impact of external electric potential	142
4.2.3	Influence of support and electrolyte acidity and of metal particle size	146
4.3	Conclusion	149
4.4	Supporting information	150
4.4.1	Experimental	150
4.4.2	Evaluation of volumetric adsorption isotherm measurements	157
4.4.3	Evaluation of thermodynamic adsorption properties on Pd	160
4.5	References	163
4.6	Associated content	165
5	Summary and conclusion	166

1. Introduction

1.1 Energy consumption – current situation and future perspectives

In 2020, world's primary energy consumption was more than 550 EJ leading to a total carbon dioxide emission of more than 32 Gt.^[1] More than 80% of the energy that is used in the transportation sector, in industry and private households is still supplied from fossil resources, e.g., crude oil, coal, natural gas (Figure 1).^[1-2] Especially, wealthy nations as well as countries with a growing industry and population show the highest consumption of primary energy whereas in large parts of the African continent energy production and usage is still rather low and based on traditional biomass resources.^[1, 3] Therefore, it is in particular the countries of the northern hemisphere that have to fight climate changes, e.g., global warming, flooding that are caused by anthropogenic emissions of greenhouse gases.

In order to meet that goal many governments around the world like USA and EU have implemented policies and regulations that shall lead to a more efficient use of resources and an enhanced development of renewable energies.^[3-4] According to the Paris agreement from 2015 the increase in global average temperature shall be kept below 1.5 °C in order to prevent further climate changes.^[5] In order to achieve this goal, the global greenhouse gas emissions have to be reduced to net-zero by the mid of the century. The European Union aims for a 80% reduction of total greenhouse gas emissions by 2050 compared to 1990; greenhouse gas emissions arising from transportation sector shall be diminished by 60% in the same period.^[6] In terms of this, hydrogen produced *via* water electrolysis driven by renewable energies is supposed to play a key role in the transformation from a carbon-based economy towards a green society.^[7] Recent studies have shown that the electric grid of the USA could be decarbonized by up to 80% on the basis of renewable energies.^[8]

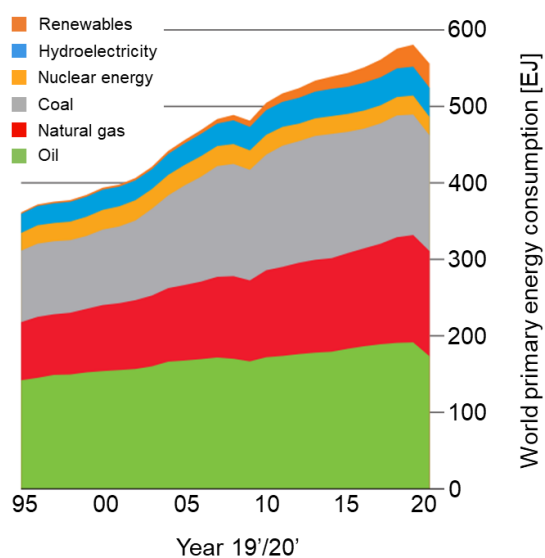


Figure 1: World primary energy consumption from 1995-2020 by resources, adapted from ref. [1].

One major drawback of non-fossil resources arises from their discontinuity. In contrast to nuclear power plants or power plants based on the combustion of fossil resources, solar and wind power demand certain climate conditions in order to be fully operational. Depending on the amount of wind and sun the energy generated from these kinds of resources varies a lot and the excess part needs to be stored, transitionally. The surplus energy can either be stored in batteries or it can be converted into potential energy *via* pumped storage hydropower. Alternatively, it can be saved in chemicals. The additional amount of energy can be used either for generating green hydrogen *via* water electrolysis or for upgrading of biomass-derived molecules towards value-added chemicals and synthetic fuels (Figure 2). When the amount of wind or sun is low these chemicals are combusted in order to reach a continuously stable energy supply. Even though, the combustion of synthetic fuels leads to the emission of carbon dioxide the process can still be considered carbon-neutral as carbon dioxide is withdrawn from the atmosphere during biomass growth.

All these processes of chemical energy conversion require the development of new heterogeneous (electro)catalysts and reactor systems that are tolerant against a fluctuating supply of energy and raw materials.^[9] Only this will allow to cope with the dynamic operating conditions coming along with the transformation towards a sustainable future that is based on renewable energy resources.

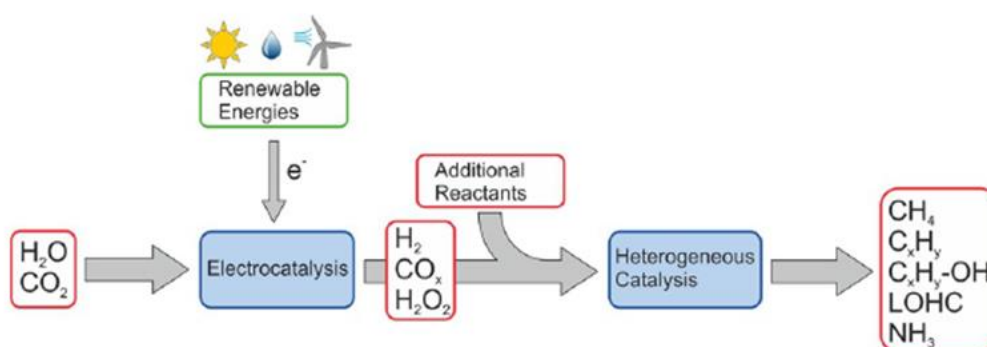


Figure 2: Schematic representation of future conversion and storage of (excess) renewable energy *via* heterogeneous (electro)catalysis, adapted from ref. [9].

1.2 Biomass as renewable feedstock

Due to climate changes and the envisaged energy transformation towards renewable and sustainable processes the use of biomass and biomass-derived feedstock in energy-related fields is of growing interest.^[10] Unlike fossil fuels like crude oil and natural gas, biomass is vastly abundant around the globe and its harvesting is less complicated and environmentally harmful.^[11] Furthermore, upgrading of biomass feedstock in biorefineries can be implemented together with renewable energy supplies, e.g., solar, wind in smaller, decentralized units with less infrastructure costs and efforts.^[12] In this context, the term biomass feedstock covers a large variety of raw materials like ocean and fresh water, forest material, annual crop production and vegetables and algae.^[11c, 13] Depending on the scenario and the used type of raw material the potential energy supply from biomass can reach up to 1200 EJ per year, which would mean more than twice the world's primary energy consumption of 2020.^[1, 14] However, the application of biomass feedstock in energy-related processes also bears the risk of burning edible portions and endangering food safety around the world, which is the basis of the food-versus-fuel debate.^[10a, 15] Furthermore, the transformation of natural ecosystems to crop plantations for power generation means the formation of monocultures.^[11c, 16] These monocultures are most often less biodiverse and suffer from land degradation due to dehydration and soil erosion.^[12c, 15b, 17] Hence, efforts are needed to combine the use of biomass feedstock as renewable energy resource with safe food supply and environmental conservation.

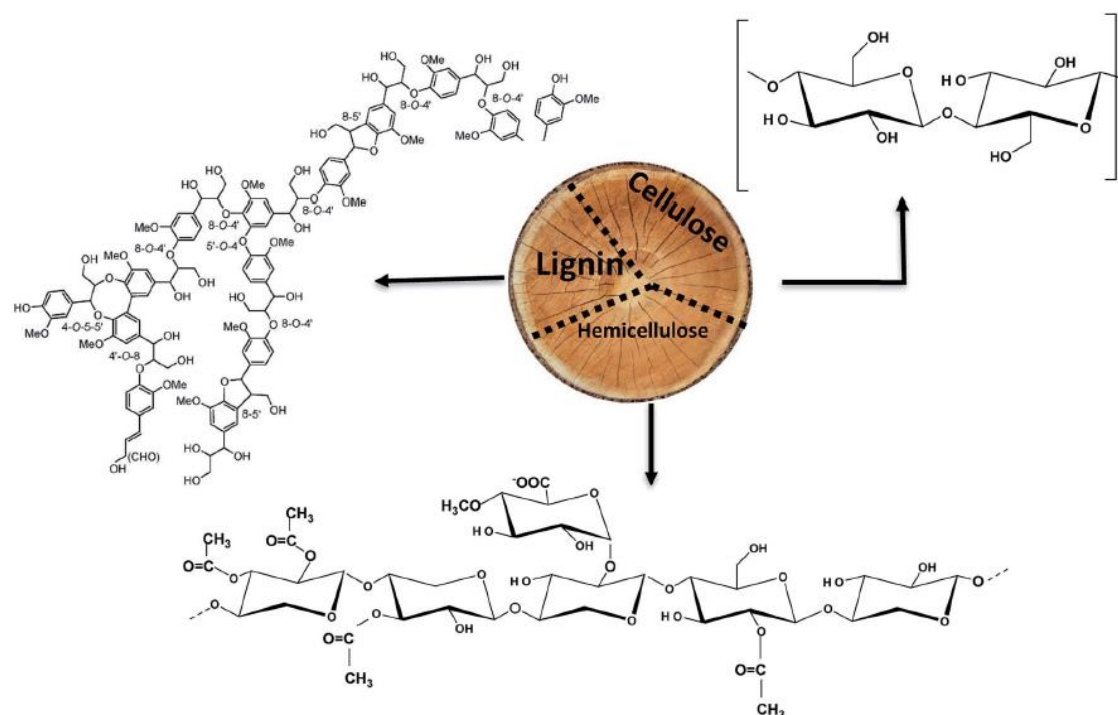


Figure 3: Composition of lignocellulosic biomass feedstock with excerpts of chemical structures of lignin, cellulose and hemicellulose, reprinted from ref. [18b].

The main component of biomass feedstock is lignocellulose, a polymer consisting of lignin, cellulose and hemicellulose (Figure 3).^[10b, 11b, 18] All three of them show polymeric structures with the major component of lignocellulosic raw materials, lignin, being made up of highly branched and substituted phenol chains. Cellulose and hemicellulose are formed by polymerization of C₅- and C₆-sugars glucose and xylose whereby cellulose only consists of glucose and hemicellulose of glucose and xylose.

Further upgrading of biomass requires pretreatment of the lignocellulosic raw material. There are several chemical and mechanical methods that all aim at the reduction of biomass in size and the decomposition of the different polymer chains into oligomers and monomers.^[10b] Most of these first upgrading steps are performed at 100-200 °C and elevated pressures in steam. Sometimes acids are added. In the following, the pretreated raw material undergoes further thermo-chemical conversion steps.^[10b, 19] Combustion of biomass at up to 1000 °C generates heat and electricity. Alternatively, the depolymerized feedstock can undergo gasification, which produces syngas (H₂ + CO) and nitrogen, a mixture that is sometimes referred to as fuel gas. This can be either used to generate electricity or in petrochemical refineries for the production of base chemicals such as methanol and ammonia. A third way of upgrading biomass feedstock is pyrolysis at 400-600 °C in the absence of air.^[20] Fast pyrolysis leads to the generation of charcoal as well as a liquid product fraction that is called pyrolysis or bi-oil. This is a mixture of unsaturated aliphatic and aromatic, oxygen-rich molecules that can be further converted to bio-fuels, base and fine chemicals. Figure 4 shows a schematic representation of various biomass upgrading steps.

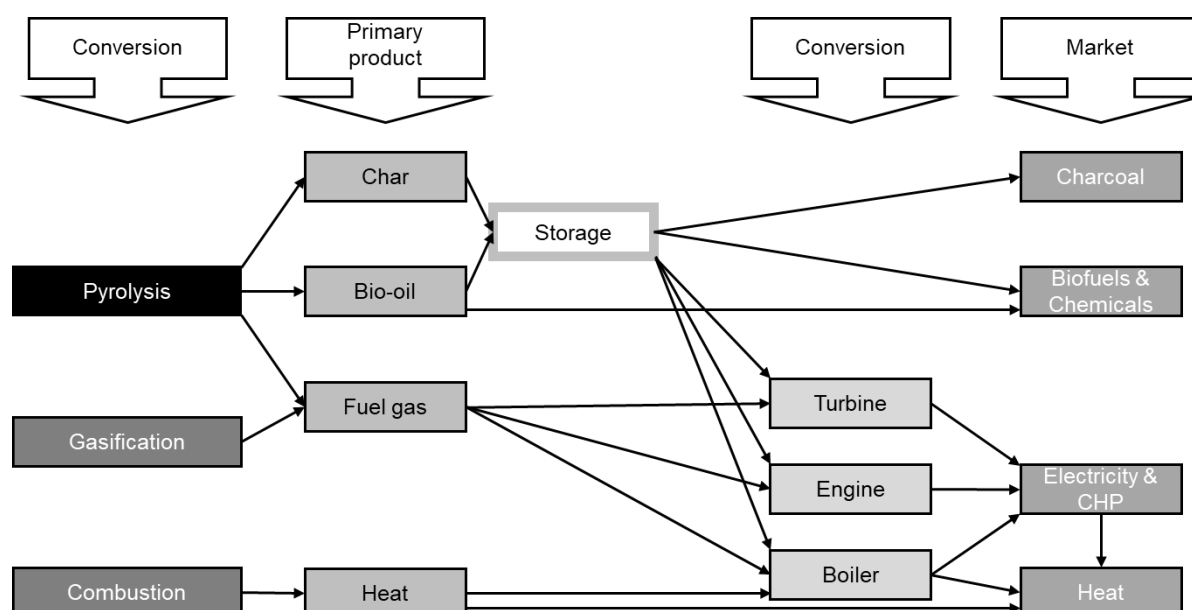


Figure 4: Schematic of different biomass upgrading processes after initial depolymerization of lignocellulosic raw material, adapted from ref. [19].

As depicted in Figure 4 it is especially the bio-oil from pyrolysis which is further upgraded to base chemicals and fuel-range products. However, as mentioned above this oil is a pool of unsaturated, aliphatic or aromatic compounds that contain large amounts of oxygen (Figure 5).^[20b] Therefore, the production of chemicals and fuels from this kind of feedstock requires further intermediate treatment steps, that is hydrodeoxygenation and hydrogenation.^[18a, 21] The degree of unsaturation as well as the oxygen-content need to be reduced in order to make these molecules potential high-value chemicals that can be used in the transportation sector or the production of pharmaceuticals and fine chemicals.^[22] Most often, this is done *via* thermal processes, e.g., thermo-chemical hydrogenation (TCH) at high pressures and several hundred degree *Celsius*, in which the reacting hydrogen is still supplied from reforming of non-sustainable fossil resources.^[21a] These drawbacks make the hydrogenation of oxygen-containing intermediates one of the most energy- and capital-intensive steps during biomass conversion.^[23]

Electrocatalytic processes like electrocatalytic hydrogenation (ECH), in contrast, are promising, sustainable alternatives for the ambient conversion of unsaturated and oxygen-rich compounds. The required hydrogen can be produced *in situ* from reduction of hydronium ions or electrolysis of water driven by renewable resources, e.g., solar, wind.^[24]

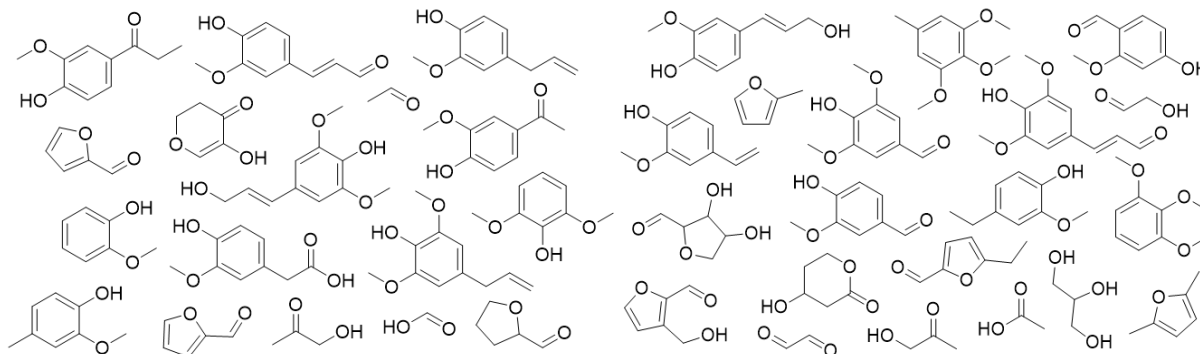


Figure 5: Overview of unsaturated, oxygen-rich molecules contained in bio-oil generated *via* pyrolysis of lignocellulosic feedstock.

1.3 Electrochemical cells and electrocatalytic hydrogenation

Electrocatalytic hydrogenation of oxygenated compounds is a promising and sustainable alternative to common and widely applied thermo-chemical processes. Due to *in-situ* formation of reduction equivalents, i.e., activated hydrogen on the catalyst surface ECH does not require the additional supply of gas-phase hydrogen that is produced from fossil resources, e.g., steam reforming.^[25] Together with reaction conditions that are close to ambient pressure and room temperature and the possibility to drive ECH *via* renewable energies electrocatalytic technologies can play a crucial role in reducing the anthropogenic carbon footprint as well as the safety-issues arising from thermo-chemical conversion steps.^[21a, 26]

Figure 7a depicts a typical two-compartment electrochemical cell that is used for running electrocatalytic hydrogenation in either batch or flow mode. The two compartments, which are referred to as cathodic and anodic half-cell, are separated by a proton-conducting polymer membrane.^[24b, 27] Most often, a *Nafion* membrane is used for this purpose. *Nafion* is a sulfonated tetrafluoroethylene-based fluoropolymer-copolymer that was first developed by *DuPont*.^[28] Its unique ion-conducting properties, which are closely related to the membrane's degree of hydration, arise from sulfonated perfluoro vinyl ether groups that are attached to a tetrafluoroethylene backbone (Figure 7b).^[29] Increasing the water content within the polymer network leads to an enhanced migration of positively charged ions, e.g., alkali metal cations, hydronium ions across the established network of hydrogen bonds.^[30] Each of the cell compartments is filled with an aqueous electrolyte containing electrolyte ions that counterbalance the movement of hydronium ions within the membrane and the liquid phase. The working and reference electrodes (WE, RE) are typically placed in the cathode compartment whereas the counter electrode (CE) is located in the anode compartment. Most typically a large surface area platinum wire or mesh serves as counter or auxiliary electrode supplying the required electrons for the reduction on the cathode side.^[31] The working electrode consists of an electrocatalyst that is immobilized on any kind of carbon material, e.g., felt, paper that is attached to a titanium or carbon rod. In terms of RE, there are two types of electrodes. The standard hydrogen electrode (SHE) is a primary reference electrode while any other RE whose potential is determined with respect to SHE, e.g., the reversible hydrogen electrode (RHE) or a Ag/AgCl electrode are secondary reference electrodes.^[32] The unique property of each reference electrode is its stability with respect to potential changes across its interface with the surrounding electrolyte.^[33] The potential difference that is applied between WE and CE causes a flow of electrons, i.e., a current flow. Hence, due to charge transfer processes the electrode/electrolyte interfaces at anode and cathode are changed upon application of an

external electric bias.^[34] This however, makes the measurement of the potential of only one of the electrodes, which is essentially the potential difference across the corresponding solid/liquid interface, with respect to the second electrode physically impossible as both interfaces change over time (Equation 1).

$$\delta E = E_{(j)} - E_{(j=0)} = \delta({}^W\Delta^S\phi) + jR_S + \delta({}^S\Delta^C\phi) \quad (1)$$

Here, $E_{(j)}$ and $E_{(j=0)}$ stand for the measured potential at a given current (density) j and at zero current (density), respectively. The jR_S represents the potential drop arising from the uncompensated solution resistance R_S and the ${}^W\Delta^S\phi$ and ${}^S\Delta^C\phi$ stand for the potential differences across the solid/liquid interfaces at WE and CE, respectively.

Hence, a third electrode with a stable electrode/electrolyte interface throughout time is needed. There is no current passed through RE, which is why the potential difference across its solid/liquid interface does not change (${}^R\Delta^S\phi = \text{const.}$) and it can be used to monitor only the potential of WE during electrocatalytic hydrogenation reactions.^[35] This bias can then be correlated to a changing interface at only the working electrode that is not superimposed by any reactions happening at the auxiliary electrode. It has to be noted that the reference electrode in the cathode compartment has to be placed in close proximity to the working electrode in order to keep the jR -drop arising from uncompensated solution resistance as low as possible (Figure 6).^[33]

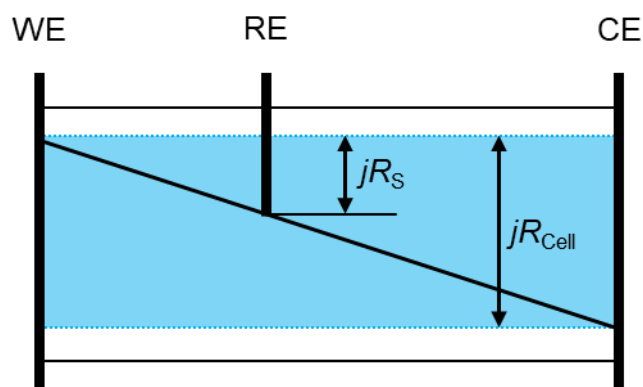


Figure 6: Schematic representation of jR -induced potential drop between WE and RE or CE, respectively arising from uncompensated solution resistance.

When an electric circuit is established between WE and CE and a potential is applied to the working electrode the external flow of electrons from anode to cathode is counterbalanced by the movement of ions within the electrolyte solution and through the membrane.^[36] While in the anodic half-cell oxygen is formed *via* water electrolysis the generated electrons are used for reduction of protons and organic molecules at the cathode that is accompanied by hydrogen formation.^[37]

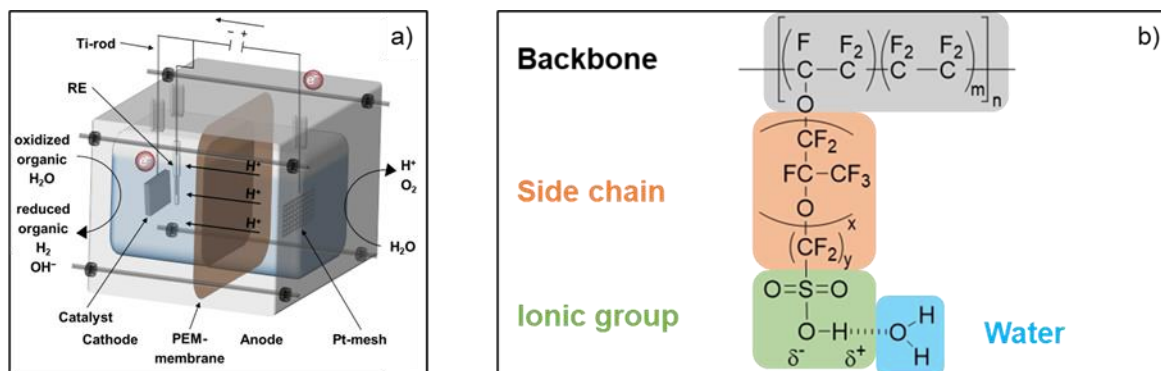
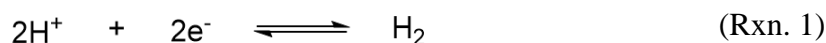


Figure 7: a) Two-compartment batch cell used for electrocatalytic hydrogenation and water electrolysis and b) structure of *Nafion* polymer with hydrogen bonding between sulfonate side groups and water.

Concerning the applied or measured potential at working electrode it can be differentiated between reversible or open circuit potential and overpotential. Consider the equilibrium between hydrogen evolution (HER) and hydrogen oxidation (HOR) reaction (Reaction 1).



Without application of an external electric bias, which is also referred to as open circuit potential (OCP), the reaction is in equilibrium resulting in a net-zero current.^[38] The reversible electrode potential of the H_2/H^+ redox couple that is measured can be correlated to the standard *Gibbs* free energy of reaction (Equation 2).^[36a] As $\Delta G_{\text{R}}^{\circ}$ of HER/HOR equilibrium is zero the reversible electrode potential ($E_{\text{H}_2/\text{H}^+}^{\circ}$) of the respective redox couple, H_2/H^+ , equals 0 V vs. SHE.^[39] This holds for a hydrogen partial pressure (p_{H_2}) of 1 bar and an activity of hydronium ions ($a_{\text{H}_3\text{O}^+}$) of 1 M.

$$E_{\text{H}_2/\text{H}^+}^{\circ} = -\frac{\Delta G_{\text{R}}^{\circ}}{nF} \quad (2)$$

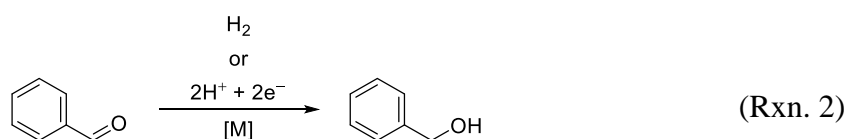
The n and F are the number of electrons transferred in the reaction and the *Faraday* constant. Depending on the activity of protons and the hydrogen pressure this reversible electrode potential can be shifted according to *Nernst* equation (Equation 3).^[40] This allows for recalculating potentials from SHE to RHE scale.

$$E_{\text{H}_2/\text{H}^+} = E_{\text{H}_2/\text{H}^+}^{\circ} + \frac{RT}{nF} \ln \left(\frac{a_{\text{H}_3\text{O}^+}}{\sqrt{p_{\text{H}_2}}} \right) = E_{\text{H}_2/\text{H}^+}^{\circ} + \frac{RT}{nF} \left[\ln(a_{\text{H}_3\text{O}^+}) - \frac{1}{2} \ln \left(\frac{p_{\text{H}_2}}{p_{\text{H}_2}^{\circ}} \right) \right] \quad (3)$$

The R refers to the universal gas constant and T to the electrolyte temperature. The $p_{\text{H}_2}^{\circ}$ stands for the H_2 partial pressure at standard conditions.

Any measured or applied potential that lies beyond this threshold value is called overpotential. Depending on whether it is more positive or more negative the cell is referred to as galvanic or electrolytic cell that either requires or supplies energy during the course of reaction.^[41]

Benzaldehyde acts as a model compound for the pool of aromatic aldehydes that is generated *via* decomposition of lignocellulosic feedstock.^[42] It can be further hydrogenated towards benzyl alcohol, which is an important chemical for the production of flavors, cosmetics and paints.^[43] This conversion can be used as a model reaction to investigate different reaction parameters and setups and their influence on performance in (electrocatalytic) hydrogenation of oxygenated compounds (Reaction 2).

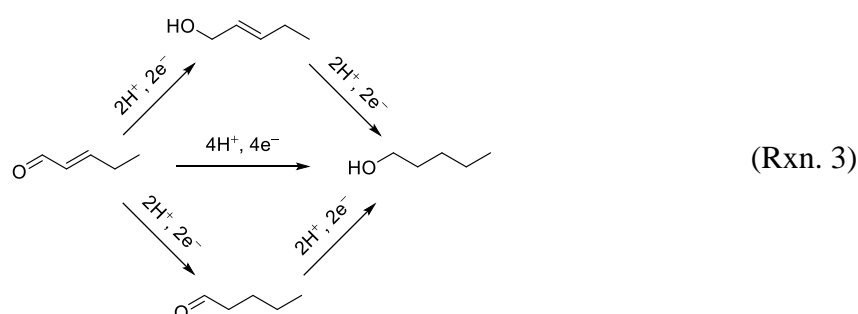


On metals with a low onset overpotential for HER, e.g., Pt group metals electrocatalytic hydrogenation of benzaldehyde proceeds *via* a proton-coupled electron transfer.^[44] The direct reduction of benzaldehyde in liquid phase requires a negative overpotential of at least -2 V vs. RHE.^[45] Hence, this is only possible on metals with an onset overpotential for HER that is more negative than this threshold value.

Depending on external electric potential, noble metal and support properties the turnover frequency (TOF) and *Faradaic* efficiency (FE) of electrocatalytic benzaldehyde hydrogenation can be tuned. *Song* et al. as well as *Sanyal* and coworker showed that amongst Pt, Pd and Rh supported on carbon Pd/C was the most active one for ECH of benzaldehyde in aqueous phase.^[23-24] The TOF of benzyl alcohol formation at a given overpotential decreased in order Pd > Rh > Pt while it increased with an increasing cathodic external electric potential on all metals. The current efficiency on the different metals followed the same trend like TOF with FE on Pd and Rh being constant throughout the investigated potential window. On Pt the *Faradaic* efficiency decreased with increasing negative overpotential. Similar results were also found by *Lopez-Ruiz* et al. who also investigated Ru.^[46] They attributed the different activities for benzaldehyde ECH on various metals to different binding energies of the organic molecule on the metal surface, which seems to be optimum on Pd. *Andrews* and coworker found that it is in general more difficult to hydrogenate aliphatic aldehydes on noble metals compared to aromatic ones.^[21b] Concerning the electrolyte composition, it was *Sanyal* who revealed that the addition of phenol during benzaldehyde ECH can help to improve the overall catalyst activity due to formation of a hydrogen-bonded complex between phenol and the carbonyl compound.^[47] *Lopez-Ruiz*, again, found that adding an organic cosolvent, e.g., ethanol,

isopropanol to the aqueous electrolyte leads to a decreased ECH activity due to competitive adsorption of the solvent molecules on the metal surface.^[48] In terms of carbon support, *Koh* and coworker showed that increasing the concentration of acid surface sites, just like rising the overall electrolyte acidity, leads to increased turnover frequencies in benzaldehyde ECH.^[49]

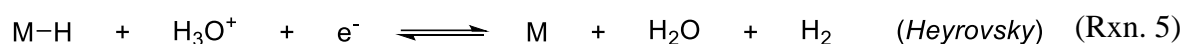
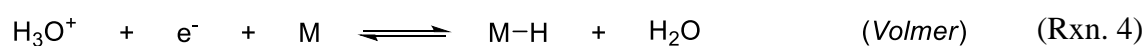
In contrast to benzaldehyde ECH, there has only been performed little research on electrocatalytic hydrogenation of α,β -unsaturated aldehydes like *trans*-2-penten-1-al (Reaction 3). So far, researchers have mainly focused on thermo-chemical hydrogenation of such compounds. In general, on noble metal catalysts hydrogenation of the double bond is thermodynamically favored over conversion of the CO group leading to low selectivity towards α,β -unsaturated alcohols.^[50] The selective hydrogenation of α,β -unsaturated aldehydes towards their corresponding allylic alcohols, however is a significant reaction in academia and in industry due to the application of α,β -unsaturated alcohols in the production of fine chemicals, fragrances and pharmaceuticals.^[51]



Therefore, during past decades researches have put lots of efforts in developing new catalyst materials for selectively activating the carbonyl group.^[52] The application of bimetallic catalysts with a second oxophilic and electropositive metal species forming *Lewis* acid sites in close proximity to noble metal particles has proven beneficial for selective CO group hydrogenation.^[53] *Dai* et al. as well as *Mahata* and coworker showed that the addition of Fe or Zn to Pt supported on carbon materials increased the selectivity of cinnamaldehyde hydrogenation towards cinnamyl alcohol by almost a factor of two.^[54] Similar results were found by *Bachiller-Baeza* who investigated the selective hydrogenation of citral over carbon-supported Ru-Fe catalysts.^[55] *Tamura* et al. found an outstandingly high selectivity for formation of allylic alcohols on Ir-ReO_x materials, in which metal oxide particles were proposed to act as anchoring sites activating the carbonyl group.^[56] Investigating cinnamaldehyde hydrogenation *Giroir-Fendler* and coworker revealed that increasing the metal particle size leads to an increased steric repulsion of C=C bond resulting in an improved selectivity for carbonyl group hydrogenation.^[57] Concerning support modifications, *Solhy* et al. showed that heat treatment of multi-walled carbon nanotubes (MWCNT) prior to catalyst synthesis leads to a decreased concentration of acid surface sites and consequently to larger metal particles.^[58]

1.4 Electrocatalytic activation of hydrogen and hydrogen evolution

Electrocatalytic activation and formation of hydrogen *via* proton reduction from aqueous phase proceeds *via* a two-step consecutive mechanism, that is either *Volmer-Heyrovsky* or *Volmer-Tafel* sequence.^[59] In the first step, hydronium ions are reductively adsorbed on the metal electrode surface according to *Volmer* equilibrium (Reaction 4). In *Heyrovsky* equilibrium, the adsorbed H atom reacts with another hydronium ion from bulk electrolyte, which is being electrocatalytically reduced, to form H₂ (Reaction 5). Alternatively, two adsorbed H atoms recombine on the metal electrode surface in a pure thermo-chemical reaction, the *Tafel* step, and desorb as H₂ (Reaction 6). Depending on ECH conditions, e.g., used metal, applied overpotential, organic compound to be reduced hydrogen evolution reaction is an inevitable side reaction that decreases the *Faradaic* efficiency of ECH.



As stated earlier, the theoretical reversible onset potential for hydrogen evolution reaction (HER) should be zero, i.e., $E_{\text{H}_2/\text{H}^+}^{\circ} = 0$ V vs. SHE.^[60] However, each metal electrode shows an additional negative onset overpotential for HER that needs to be applied to the electrode surface in order to drive the reaction.^[40] This additional energy input that is required to start H₂ formation is determined by the hydrogen binding energy, i.e., the *Gibbs* free energy of adsorbed H on the respective metal surface.^[61] As is shown in Figure 8 HER activity of different transition metals follows a volcano-type shape with respect to $E(\text{M-H})$ and ΔG_{H^*} . Platinum group metals that typically show a very low onset overpotential for hydrogen evolution reaction, that is only a few millivolts, are located at the peak of the volcano plot, which is the reason why especially these metals are most applied in hydrogen-related electrochemistry.^[62] The *Gibbs* free energy of hydrogen atoms that are adsorbed on these type of electrodes is close to zero. Metals on the left branch of the volcano in Figure 8b bind H too strongly, which leads to a blocking of active sites and an increased activation barrier for HER. Consequently, the energy input that is required to drive the reaction, i.e., the onset overpotential raises. Contrarily, metals on the right branch bind hydrogen not strong enough to stabilize the intermediate state, which gradually prevents hydrogen evolution reaction from taking place.

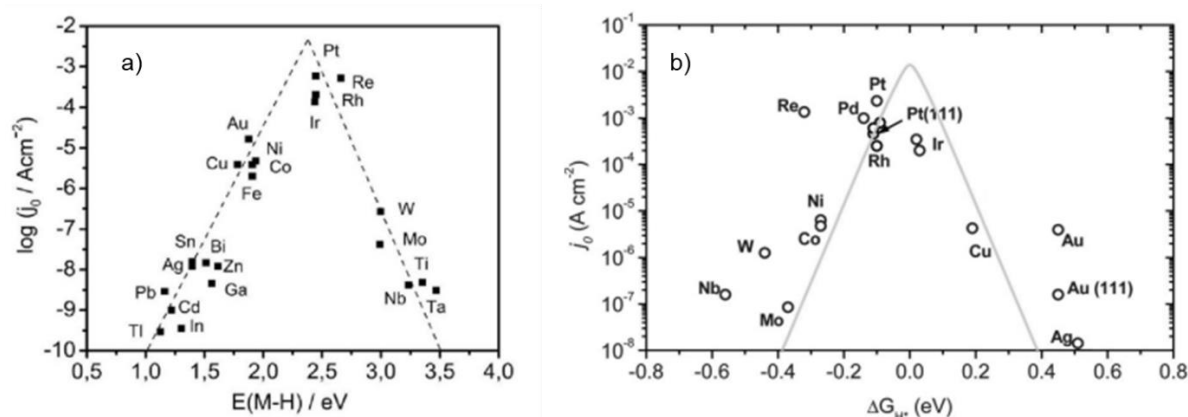


Figure 8: Volcano plots of exchange current density of transition metals as function of **a)** M-H bond strength, and **b)** Gibbs free energy of adsorbed H on metal surface, adapted from refs. [61a] and [61b].

Depending on the applied overpotential HER on Pt group metals proceeds *via* either a *Volmer-Tafel* or a *Volmer-Heyrovsky* mechanism with different rate-determining steps (r.d.s.).^[63] At low overpotentials hydrogen formation proceeds *via* a *Volmer-Tafel* mechanism with the *Tafel* step being r.d.s.. All active sites are fully covered with H from proton reduction and H_2 desorption from electrode surface limits the reaction. This results in *Tafel* slopes below 30 mV dec^{-1} (Figure 9). At medium overpotentials the HER mechanism changes to a *Volmer-Heyrovsky* sequence with the *Heyrovsky* step being rate-limiting and a *Tafel* slope of $30\text{-}120 \text{ mV dec}^{-1}$. At very high overpotentials the high electrochemical rate of HER leads to a depletion of hydronium ions close to electrode surface.^[33] Due to transport limitations the *Volmer* reaction with a *Tafel* slope larger than 120 mV dec^{-1} becomes r.d.s. of hydrogen evolution reaction. The *Tafel* slope (b_c) of each sector can be derived from *Tafel* equation with η being the applied overpotential, j standing for the measured current density and a being an empirical constant, i.e., the respective onset overpotential for HER (Equations 4-5).^[33]

$$\eta = a - b_c \log(j) \quad (4)$$

$$b_c = \left(\frac{\delta \eta}{\delta \log(j)} \right)_{T,p,c} \quad (5)$$

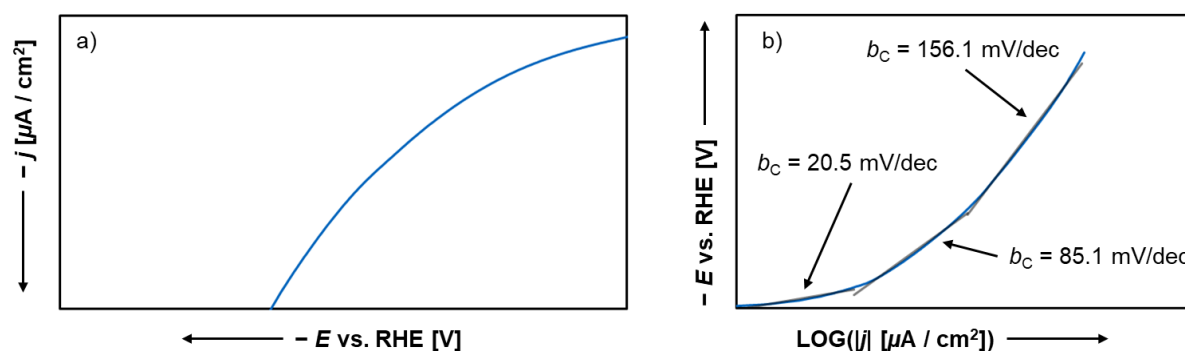


Figure 9: **a)** Linear polarization (LP) curve of HER on Pt in aqueous phase, and **b)** resulting *Tafel* plot with different *Tafel* slopes b_c .

Tafel analysis of linear polarization (LP) measurements is based on *Butler-Volmer* kinetics that describes the current-potential relation of a simple unimolecular redox reaction happening at a metal electrode.^[64] Consider a simple reaction of species A to B equivalent to proton reduction towards adsorbed H (Reaction 7).



Using transition state theory, the reaction rate (r) can be written according to Equation 6.

$$r = -k_f c_A = -\frac{kT}{h} c_{X^\ddagger} = -\frac{kT}{h} c_A \exp\left(-\frac{\Delta G^{\ddagger}}{RT}\right) \quad (6)$$

The k_f is the forward rate constant, the c_A and c_{X^\ddagger} stand for the concentration of species A and transition state X^\ddagger , respectively. The k , T and h are *Boltzmann* constant, temperature and *Planck* constant. The R is the universal gas constant and the ΔG^{\ddagger} is the standard *Gibbs* free energy of activation. Hence, the forward rate constant can be written as (Equation 7):

$$k_f = \frac{kT}{h} \exp\left(-\frac{\Delta G^{\ddagger}}{RT}\right) \quad (7)$$

In order to take into account the influence of an external electric potential on reaction rate the standard *Gibbs* free energy of activation needs to be related to the potential difference across the electrode/electrolyte interface, that is the applied overpotential η (Equation 8).

$$\Delta G^{\ddagger\eta} = \Delta G^{\ddagger} \pm \alpha F \eta \quad (8)$$

Here, $\Delta G^{\ddagger\eta}$ is the standard *Gibbs* free energy of activation influenced by an applied overpotential. The F and α denote *Faraday* constant and the charge transfer coefficient of the reaction. This factor, which usually has a value between zero and one, describes how much of the electric potential is used to lower the energetic barrier of reaction.^[65] The larger it is the more ΔG^{\ddagger} is reduced leading to a pronounced raise of reaction rate with increasing overpotential. In that sense, charge transfer coefficient is similar to symmetry factor in transition state theory that differentiates between early and late transition states.^[66] The \pm sign in Equation 8 is applicable to either cathodic or anodic reactions. Hence, for a cathodic reaction the electrochemical rate, i.e., the measured current (density) with respect to applied overpotential can be defined according to Equation 9.

$$j_c = Fr = -F \frac{kT}{h} c_A \left(\frac{\Delta G^{\ddagger}}{RT}\right) \exp\left(-\frac{\alpha F \eta}{RT}\right) = -F k_f c_A \exp\left(-\frac{\alpha F \eta}{RT}\right) \quad (9)$$

The j_c is the measured cathodic current (density).

If Reaction 7 is an equilibrium reaction as is the case for hydrogen evolution reaction, the anodic current (density), j_a , has the same expression like j_c . However, with a plus sign in the exponent, a backward rate constant (k_b) and a charge transfer coefficient of $(1-\alpha)$, that is $\alpha + (1-\alpha) = 1$. Therefore, the overall current (density), j , of an equilibrium reaction can be written as a superposition of j_c and j_a (Equation 10).

$$j = j_a - j_c = Fk_b c_A \exp\left(\frac{(1-\alpha)F\eta}{RT}\right) - Fk_f c_A \exp\left(-\frac{\alpha F\eta}{RT}\right) \quad (10)$$

If totally in equilibrium, i.e., at reversible or open circuit potential the applied overpotential as well as the net reaction rate are zero. The rate, at which the electrochemical reaction proceeds back and forth at equilibrium, is called exchange current (density), j_o , and is determined by the preexponential factors (Equation 11).

$$j_a = j_c \Leftrightarrow Fk_b c_A = Fk_f c_A = j_o \quad (11)$$

This leads to *Butler-Volmer* equation (Equation 12).

$$j = j_o \exp\left(\frac{(1-\alpha)F\eta}{RT}\right) - j_o \exp\left(-\frac{\alpha F\eta}{RT}\right) \quad (12)$$

There are two limiting cases for *Butler-Volmer* equation. Close to reversible electrode potential it is close to linear (Equation 13). This behavior can be used to determine the polarization resistance of an electrochemical reaction. At large overpotential one of the exponential terms becomes negligible. For a cathodic process like HER only the cathodic part of current (density) remains and *vice versa* (Equation 14). When written in logarithmic form Equation 14 can be used together with Equation 5 in order to determine the *Tafel* slope and the corresponding charge transfer coefficient (Equations 15-16).

$$j = j_o \frac{F\eta}{RT} \quad (13)$$

$$j = j_c = -j_o \exp\left(-\frac{\alpha F\eta}{RT}\right) \quad (14)$$

$$2.3 \log\left(\frac{j}{j_o}\right) = -\frac{\alpha F}{RT} \eta \quad (15)$$

$$b_c = \frac{\delta\eta}{\delta \log\left(\frac{j}{j_o}\right)} = -\frac{2.3RT}{\alpha F} \quad (16)$$

Figure 10 depicts the measured current density as a function of applied overpotential. The anodic and cathodic current densities are shown as j_a and j_c , respectively for $\alpha = 0.5$ and

$j_0 = 1 \text{ mA cm}^{-2}$. The z in the equations represents the number of electrons transferred during the reaction.

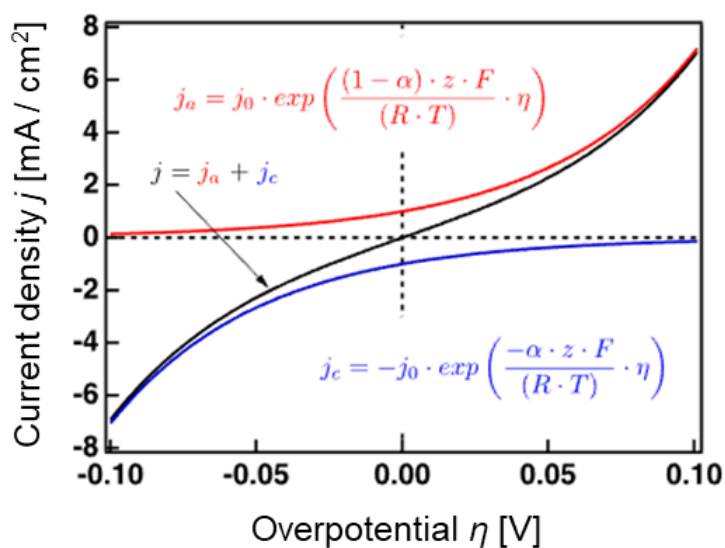


Figure 10: Development of measured current density with applied overpotential according to Butler-Volmer model.

Application of an external electric potential to a metal electrode surface not just leads to the adsorption and formation of hydrogen or ECH of an organic molecule but also to the accumulation of ionic species within the electrochemical double-layer. The structure of this interfacial layer between electrode surface and bulk electrolyte will be discussed in the next section.

1.5 Electrochemical double-layer

Immersing a charged particle, e.g., a metal electrode into an aqueous electrolyte leads to the formation of an interfacial layer between particle surface and bulk electrolyte, that is electrochemical double-layer (EDL).^[67] Within this layer, which typically has a thickness of only a few nanometer, electrolyte ions, e.g., hydronium ions and electrolyte cations and anions are accumulated and prone to adsorption on the solid surface.^[68] There are different physical models to describe the structure of this interfacial layer as well as the distribution of charge within it.^[64a]

1.5.1 Parallel plate model

The earliest model, the parallel plate or *Helmholtz* model, was developed by *Hermann von Helmholtz* in 1879.^[69] This model treats both boundaries of EDL, the particle surface as well as the bulk electrolyte, as rigid layers with fixed charges of opposite sign on either side. The electrolyte layer that points towards the solid surface is referred to as outer *Helmholtz* plane (OHP). The distance between metal surface (MS) and OHP is assumed to be constant and the potential drop across the interface is supposed to be linear. Hence, the electrochemical double-layer behaves like a parallel plate capacitor with a constant capacity C_H (Equation 17, Figure 11).

$$C_H = \frac{\varepsilon}{4\pi d} \quad (17)$$

The ε and d are the dielectric constant of the electrolyte as well as the distance between solid and liquid phase.

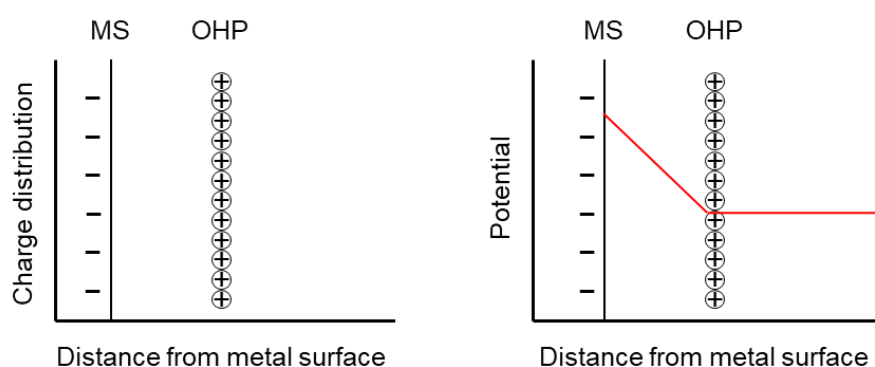


Figure 11: Schematic representation of parallel plate model (left) and corresponding potential drop across EDL (right).

However, the assumption of a constant capacity even at changing charge densities on one of the layers is disproved by experiment. The capacity of EDL changes with electrode potential. This questions the model of fixed charges on either side of the interface and leads to a second model, that is the diffuse double-layer model.

1.5.2 Diffuse double-layer model

The diffuse double-layer model, which is also referred to as *Gouy-Chapman* model, was first introduced by *Louis Georges Gouy* and *David Leonard Chapman* in 1909 and 1913, respectively.^[70] In their model, they assumed that a rigid layer of charges on the solid surface is surrounded by a cloud of oppositely charged ions in liquid phase, with the concentration of these ions decreasing with distance from the metal surface, that is the diffuse double-layer (Figure 12). The ions within this region of solution are acted upon by two forces, electrostatic interaction with the charged metal surface and thermal interaction with surrounding ions that aims to reduce their concentration gradient. Hence, the distribution and concentration of ions with respect to their distance from the solid surface can be explained by *Maxwell-Boltzmann* statistics and *Boltzmann* equation (Equation 18).^[71]

$$c_i(x) = c_{b,i} \exp\left(-\frac{z_i F (\phi_M - \phi_s)}{RT}\right) \quad (18)$$

The $c_i(x)$ and $c_{b,i}$ are the concentration of ion i at a distance x from the metal surface and in bulk solution, respectively. The z_i refers to the charge of the ion, the F is *Faraday* constant and R equals the universal gas constant. The T represents the temperature and $(\phi_M - \phi_s)$ is the potential difference between metal surface and bulk solution. So, numerator and denominator of the exponent determine the electrostatic and thermal energies that act on the ion within the diffuse double-layer. Using the *Gauss Theorem* (Equation 19) that describes the excess surface charge density of metal (q_M) as a function of the potential gradient along the interface, for a 1-1 electrolyte the excess surface charge can be calculated according to Equation 20.^[72]

$$q_M = -\varepsilon_0 \varepsilon_r \left(\frac{\delta \phi_x}{\delta x} \right) \quad (19)$$

$$q_M = \sqrt{8RT \varepsilon_0 \varepsilon_r c_b} \sinh\left(\frac{|z| F \phi_x}{2RT}\right) \quad (20)$$

The ε_0 and ε_r are the dielectric constant in vacuum and of the used electrolyte, respectively. The ϕ_x is the potential within EDL at a certain distance x from the metal surface.

Consequently, the diffuse double-layer capacitance ($C_{G,C}$) is derived by differentiating the excess surface charge with respect to potential (Equation 21). The capacitance within EDL follows a parabolic profile with a minimum at the potential of zero charge, where $q_M = 0$. There it is proportional to the square root of the ion concentration in bulk electrolyte (Equation 22).

$$C_{G.C.} = \frac{\delta q_M}{\delta \phi_x} = |z|F \sqrt{\frac{2\varepsilon_0\varepsilon_r c_b}{RT}} \cosh\left(\frac{|z|F\phi_x}{2RT}\right) \quad (21)$$

$$C_{G.C.}(\text{min}) = |z|F \sqrt{\frac{2\varepsilon_0\varepsilon_r c_b}{RT}} \quad (22)$$

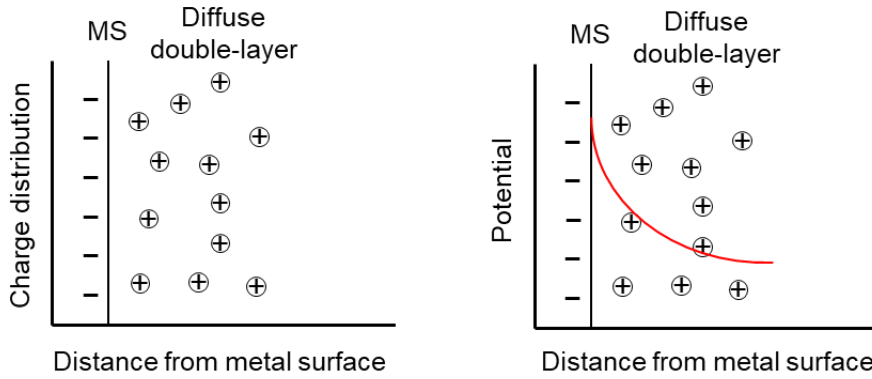


Figure 12: Schematic representation of diffuse double-layer model (left) and respective potential drop across EDL (right).

However, also this model has drawbacks, which cast doubt on its practical applicability. First of all, it is only valid in very dilute solutions and within a certain range of potential that is close to the point of zero charge. Furthermore, it completely excludes ion-ion interactions that play a role at high concentrations. Finally, the assumption of a constant dielectric constant throughout the whole diffuse double-layer might also not be true in all cases.

Therefore, a third model that combines the theories of both the *Helmholtz* and the *Gouy-Chapman* model was developed for describing the electrochemical double-layer.

1.5.3 Stern model

In 1924, *Otto Stern* developed a model for determining the potential and capacity across electrode/electrolyte interfaces that is based on the assumptions of *Helmholtz* and *Gouy-Chapman*.^[73] According to this model the interface at a charged metal surface consists of a rigid layer of counter ions, the outer *Helmholtz* plane or *Stern* layer, followed by a diffuse layer of ions that is equivalent to the diffuse double-layer (Figure 13). The charge within the interfacial layer (q_s) still has to equal the charge on the metal surface (q_M) however, it splits up into two parts arising from the *Helmholtz* layer (q_H) and the *Gouy-Chapman* layer ($q_{G.C.}$), respectively (Equation 23). In that sense, EDL behaves like two capacitors in series (Equation 24).

$$q_M = q_s = q_H + q_{G.C.} \quad (23)$$

$$\frac{1}{C_{DL}} = \frac{1}{C_H} + \frac{1}{C_{G.C.}} \quad (24)$$

At low concentrations the term arising from $\frac{1}{C_H}$ gets negligible and EDL behaves like a diffuse double-layer according to *Gouy-Chapman*. Contrarily, at high concentrations most of the charge is concentrated at the metal surface making $\frac{1}{C_{G.C.}}$ insignificant. The electrochemical double-layer can be treated as in parallel plate model.

Figure 13 also shows the potential across the interface as a function of distance from metal surface. In *Stern* model, the potential is split into a linear part within *Helmholtz* layer and a semi-exponential one in the diffuse layer. The potential at the boundary between rigid and diffuse layer, i.e., the *Stern* potential (ϕ_{Stern}) is most often set equal the potential at the electrode surface that is used for deriving the *Gouy-Chapman* part of the model.

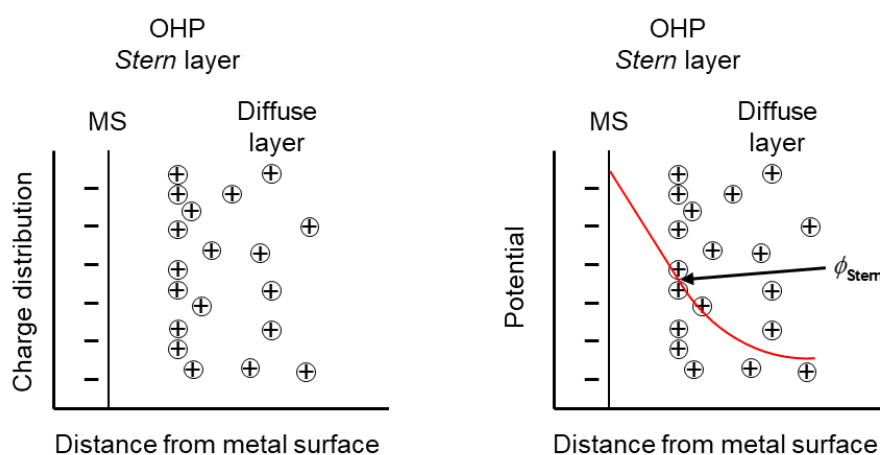


Figure 13: Schematic representation of *Stern* model (left) and respective potential drop across EDL with *Stern* potential (right).

Even this model has some deficits. For example, it doesn't take into account specific adsorption of electrolyte anions. Furthermore, it is not able to explain the influence of solvent molecules, e.g., H_2O in terms of ion solvation and its influence on EDL structure.

It has to be noted that in any of the models discussed it is assumed that a rigid layer of solvent molecules exists at the electrode surface, even below the first layer of counterions.^[33] This layer, which is sometimes referred to as inner *Helmholtz* layer, consists of oriented dipoles that are adsorbed on the solid surface *via* electrostatic interactions.

The properties of an electrochemical double-layer, e.g., its capacity, its charge transfer resistance or the accumulation and adsorption of electrolyte ions can be investigated *via* different electroanalytic techniques, that is impedance spectroscopy, cyclic voltammetry and linear polarization measurements.

1.6 Electroanalytic techniques for probing EDL

1.6.1 Linear polarization

Linear polarization (LP) measurements can be used to investigate the onset overpotential as well as the activity of an electrode for a certain electrochemical reaction, e.g., hydrogen evolution reaction.^[32] Therefore, the potential is swept with a constant scanning rate from an initial to a final value and the current response of the electrode/electrolyte interface is recorded (Figure 14).

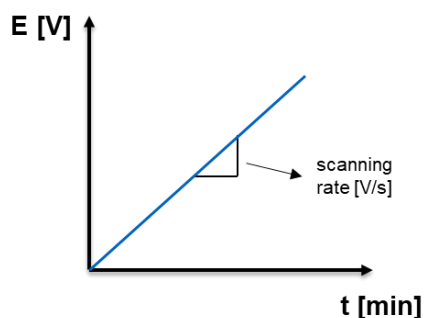


Figure 14: Development of applied potential with time during linear polarization measurements.

In *Tafel* analysis, the applied overpotential is plotted against the logarithm of the measured current density and the linear regions of the resulting graph are extrapolated into their intersection.^[33] The slopes of the linear parts give the respective *Tafel* slopes for oxidation and reduction, respectively. The onset overpotential as well as the exchange current density of the investigated catalyst/reaction system are derived from the intersection of linear regions (Figure 15).

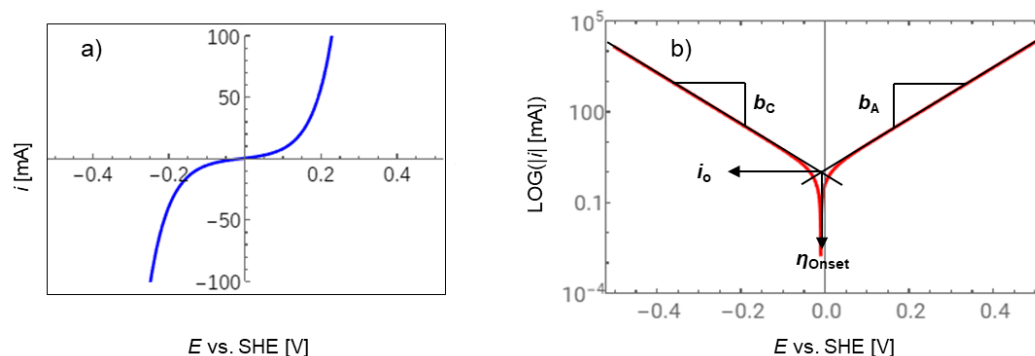


Figure 15: a) Linear polarization curve of HER/HOR and b) resulting *Tafel* plot for a catalyst with an onset overpotential of $\eta = 0.01$ V and an exchange current of $|i_0| = 10$ mA.^[74]

The lower the onset overpotential and the smaller the *Tafel* slope are the more active the used electrocatalyst is in the analyzed electrochemical redox reaction. *Tafel* analysis is based on *Butler-Volmer* model discussed above.

1.6.2 Cyclic voltammetry

In cyclovoltammetry, the applied potential is cycled with a constant scanning rate between an initial and a final potential (Figure 16).^[75]

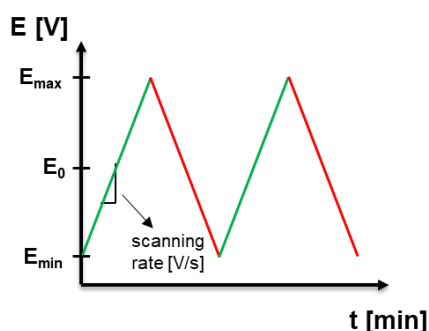


Figure 16: Change of electrode potential over time during cyclic voltammetry.

The resulting current signal can be used to investigate redox processes that are accompanied or driven by heterogeneous electron-transfer steps.^[76] As discussed above the electrochemical double-layer behaves like a capacitor with the electrode surface and the electrolyte representing the negative and positive plates, respectively. The layer of adsorbed water molecules within the inner *Helmholtz* plane acts as molecular dielectric.^[77] At a given external electric potential E , the ratio of measured current density j to scanning rate ν stands for the capacity of EDL at that point (Equation 25).

$$C_{\text{DL}} = \frac{j}{\nu} = \frac{Q_{\text{DL}}}{E} \quad (25)$$

Hence, the CV curve represents the charge Q_{DL} that is stored in between the plates of the capacitor.^[78] Usually, this charge is separated into two contributions. The inner *Helmholtz* layer mainly comprises water molecules that are adsorbed on the negatively charged electrode with their dipole moments directing towards bulk electrolyte.^[79] This accumulation of dipole moments within EDL causes a minimum charge stored in between the plates of the capacitor, that is the double-layer capacitance.^[80] In CV, this double-layer capacitance is represented by the area between the constant minima of the anodic and cathodic branch of the CV curve (Figure 17).^[81] Depending on external electric potential the curve shows additional features that lie on top of the capacitive area.^[82] This pseudo-capacitance arises from additional accumulation of charge within the double-layer, which is caused by electrochemical adsorption of electrolyte species on the electrode surface.^[32, 83] Integrating the on top area allows for quantification of the adsorbed species and calculation of the electrode surface coverage.^[81] The CV curve in Figure 17 can be divided into three sections being (I) the hydrogen region up to a potential of $E = 0.40$ V vs. RHE, (II) the potential region between 0.40 and 0.80 V vs. RHE where adsorption of electrolyte anions takes place and (III) the oxide region at potentials larger

than $E = 0.80$ V vs. RHE.^[84] Each section can be expressed *via* characteristic equations of the potential-driven adsorption and desorption of electrolyte species on Pt surface.

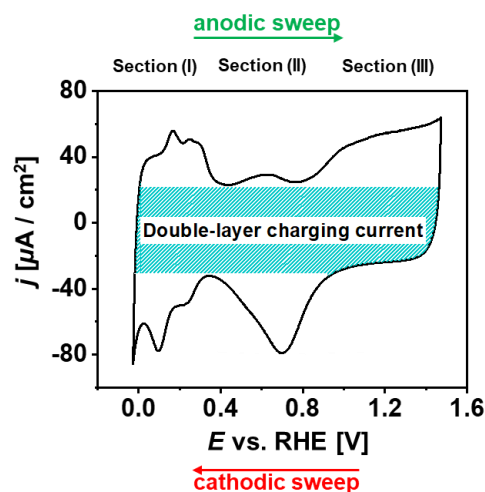


Figure 17: Cyclic voltammetry of Pt supported on carbon nanotubes in aqueous phase.

The reason for the current to peak is the fact that charge transfer across the interface is much faster than the scanning rate during CV. Therefore, the concentration of electrochemically active species at the electrode surface gradually declines with increasing reaction rate and consequently, the current starts to drop.^[85]

It has to be noted that the potential region investigated in CV is typically the window in which no water electrolysis occurs, i.e., no hydrogen or oxygen formation. As soon as HER or OER start the current drastically increases. This makes a deconvolution of features arising from electrocatalytic adsorption or desorption on the metal electrode surface impossible.

Furthermore, the peaks shown in Figure 17 are a unique property of Pt group metals.^[83]

1.6.3 Electrochemical impedance spectroscopy

The capacity as well as the charge transfer resistance of EDL can also be determined *via* electrochemical impedance spectroscopy (EIS).^[86] In EIS, a sinusoidal potential of increasing frequency is applied to the electrode/electrolyte interface and the resulting current response is recorded.^[87] Due to the resistance of the system this current signal is phase-shifted with respect to the initial potential signal (Figure 18).^[88] The overall resistance ($|Z|$) behaves like a complex number that is split into a real ($\text{Re}(Z)$) and an imaginary part ($\text{Im}(Z)$), which can be derived from Equations 26-28.^[89]

$$E(t) = E_0 \sin(\omega t) = E_0 \exp(i\omega t) \quad (26)$$

$$I(t) = I_0 \sin(\omega t + \rho) = I_0 \exp(i\omega t - \rho) \quad (27)$$

$$|Z| = \frac{E}{I} = \frac{E_0}{I_0} \frac{\sin(\omega t)}{\sin(\omega t + \rho)} = \frac{E_0}{I_0} \frac{\exp(i\omega t)}{\exp(i\omega t - \rho)} = \frac{E_0}{I_0} (\cos(\rho) + i \sin(\rho)) = \text{Re}(Z) + i \text{Im}(Z) \quad (28)$$

The $E(t)$ and E_0 are the applied potentials over time and the amplitude of the sinusoidal signal, respectively. The $I(t)$ and I_0 stand for the current over time and its amplitude, ω refers to the frequency of sinusoidal potential and ρ is the phase shift of sinusoidal current response.

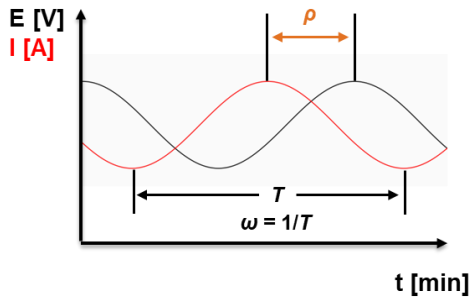


Figure 18: Schematic representation of applied potential and current response during EIS.

Plotting of imaginary against real part results in the *Nyquist* plot, from which the uncompensated solution resistance (R_s), the charge transfer resistance of EDL (R_{CT}) as well as the double-layer capacitance (C_{DL}) are extracted (Figure 19a,b).^[90] This allows for setting up the *Randles* circuit depicting how these quantities are connected in parallel or in series within EDL (Figure 19c).^[91] At very low frequencies of the initial potential signal diffusion limitation of the electroactive species through the electrochemical double-layer might occur. This gives rise to a linear region in *Nyquist* plot that is referred to as *Warburg* impedance (Z_W), which is most often connected in series to charge transfer resistance (Equation 29).^[40]

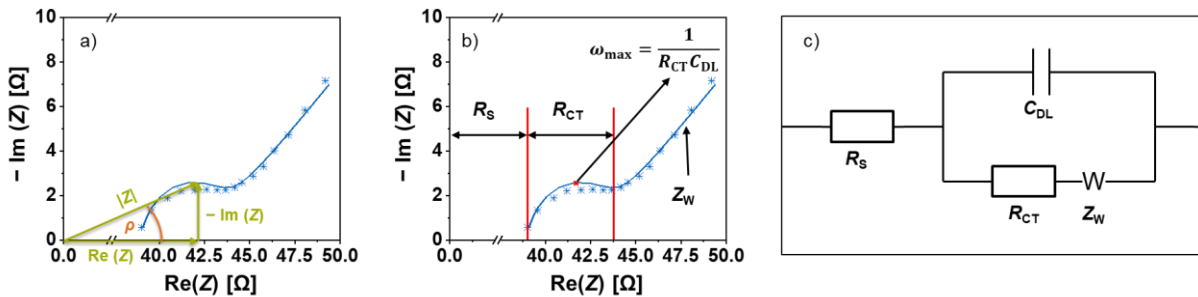


Figure 19: a), b) *Nyquist* plot for determination of real and imaginary part of impedance and its phase-shift as well as R_s , R_{CT} , C_{DL} and Z_W , and c) resulting *Randles* circuit.

$$Z_W = (1-i) \frac{\sigma}{\sqrt{\omega}} = \frac{1-i}{\sqrt{\omega}} \frac{RT\sqrt{2}}{(zF)^2 c_b \sqrt{D}} \quad (29)$$

The c_b refers to the concentration of electroactive species in bulk solution and D stands for its diffusion coefficient. The R , T , F and z are the universal gas constant, the temperature, *Faraday* constant and the number of electrons transferred. The σ denotes the *Warburg* coefficient.

1.7 (Electro)chemical potential

The chemical potential μ of a species equals its molar *Gibbs* free energy G_m and is a consequence of the second law of thermodynamics.^[36a] In equilibrium, the chemical potential of a species in a sample is constant, no matter how many phases coexist. Hence, the μ describes the probability of this species for changing its chemical or physical state in a surrounding system, i.e., the higher the chemical potential of a species is the more likely a phase transition or chemical reaction of this species gets.^[92] It is the energy that can be absorbed or released by the system upon changing the amount of a given species in a chemical reaction or phase transition.^[93] As particles always tend to move from higher to lower chemical potential spontaneous processes are accompanied by a release of energy.^[94] Assume diffusion of molecules in a closed container with areas of different concentration. At constant temperature and pressure molecules in a high-concentration area have a higher chemical potential than those in low-concentration areas. Consequently, molecules will start to diffuse from areas of higher chemical potential to regions of lower chemical potential until the concentration is equal throughout the whole container and the system is in equilibrium, i.e., at its energetic minimum. During this process molecules moving from higher to lower concentration loose part of their free energy to the environment.

The internal energy of a thermodynamic system in thermal equilibrium is influenced by the chemical potentials μ_i of its species according to Equation 30.

$$dU = TdS - pdV + \sum_{i=1}^n \mu_i dN_i \quad (30)$$

The dU , dS , dV and dN_i are the infinitesimal changes of internal energy U , entropy S , volume V and particle number N_i of species i . The T refers to the temperature of the system and p stands for its pressure. The chemical potential of a species i that is added or subtracted is defined by μ_i .

So, the chemical potential of a species i at constant entropy and volume is defined *via* Equation 31.

$$\mu_i = \left(\frac{\delta U}{\delta N_i} \right)_{S, V, N_{j \neq i}} \quad (31)$$

In practice however, it is difficult to keep the entropy and volume of a system constant, especially when particles are added or withdrawn. Therefore, *Legendre* transformation of the internal energy yields a more applicable quantity, that is the *Gibbs* free energy (G) of the system (Equation 32).^[36a] Inserting Equation 30 into the differential dG (Equation 33) leads to

Equation 34 and hence, the correlation between chemical potential and *Gibbs* free energy of a system (Equation 35).

$$G = U - \frac{dU}{dV}V - \frac{dU}{dS}S = U + pV - TS \quad (32)$$

$$dG = dU + pdV + Vdp - TdS - SdT \quad (33)$$

$$dG = Vdp - SdT + \sum_{i=1}^n \mu_i dN_i \quad (34)$$

$$\mu_i = \left(\frac{\delta G}{\delta N_i} \right)_{p,T,N_{j \neq i}} \quad (35)$$

At constant pressure and temperature, the change in *Gibbs* free energy of a system equals the change of chemical potentials of the involved species that are added or subtracted. In equilibrium, the *Gibbs* free energy of the system is at its minimum ($dG = 0$) and the increase and decrease of chemical potentials of species that are exchanged with the environment cancel each other out (Equation 36).

$$(dG)_{p,T} = \sum_{i=1}^n \mu_i dN_i = 0 \quad (36)$$

For spontaneous processes $(dG)_{p,T}$ is negative. Consider the above transport process of a species from a high-concentration area to a region of low concentration. At high concentration the chemical potential is μ_1 and at low concentration it is μ_2 , with $\mu_1 > \mu_2$. Assuming that N_1 and N_2 are equal in size but have opposite signs the change in *Gibbs* free energy at constant pressure and temperature is given by Equation 37.

$$(dG)_{p,T} = -\mu_1 dN_1 + \mu_2 dN_2 = (\mu_2 - \mu_1) dN < 0 \quad (37)$$

The chemical potential of a species i in liquid phase comprises of an ideal part and a non-ideal term (Equation 38). The ideal fraction of chemical potential consists of the chemical potential of pure species i (μ_i^o) and an activity-related term arising from, e.g., its partial pressure, concentration activity or coverage on a surface (Equation 39). As the ideal term of chemical potential excludes interactions of species i with itself and other species a non-ideal part of chemical potential, i.e., an excess potential taking into account this interplay is introduced (Equation 40).

$$\mu_i = \mu_{i,\text{ideal}} + \mu_{i,\text{excess}} = \mu_i^o + RT \ln(\chi_i) + RT \ln(\gamma_i) \quad (38)$$

$$\mu_{i,\text{ideal}} = \mu_i^o + RT \ln(\chi_i) \quad (39)$$

$$\mu_{i,\text{excess}} = RT \ln(\gamma_i) \quad (40)$$

When the system is in an electric field and the analyzed species has ionic character a third contribution to the chemical potential has to be considered.^[33] The electrochemical potential $\bar{\mu}_i$ of an ionic species i in an electric field is given in Equation 41. It consists of the species' chemical potential defined in Equation 38 and a term arising from the local electric potential, e.g., the potential across the electrode/electrolyte interface. Depending on charge and sign the electric field will cause the ionic species to move to regions where it has lower electrochemical potential and where the *Gibbs* free energy of the system is at a minimum.

$$\bar{\mu}_i = \mu_i + z_i F \phi = \mu_i^o + RT \ln(\chi_i) + RT \ln(\gamma_i) + z_i F \phi \quad (41)$$

The z_i and F are the species' charge and the *Faraday* constant. The ϕ denotes the local electric potential.

Apart from *Gibbs* free energy the (electro)chemical potential can also be related to other thermodynamic properties like the enthalpy change during a reaction (Equation 42).

$$(dH)_{p,S,N_{j \neq i}} = \sum_{i=1}^n \mu_i dN_i \quad (42)$$

Consider a unimolecular reaction, e.g., electrocatalytic H adsorption on metal electrode surface according to *Volmer* reaction (Reaction 4). Changing the electrode potential leads to a shift of the electrochemical potential of adsorbed state while the chemical potential of non-adsorbed state remains constant. Hence, *via* tuning the potential across EDL the adsorption enthalpy of H on metal electrode surface can be changed. The more the adsorbed state is destabilized, i.e., its electrochemical potential is increased the more the adsorption heat is reduced (Figure 20).

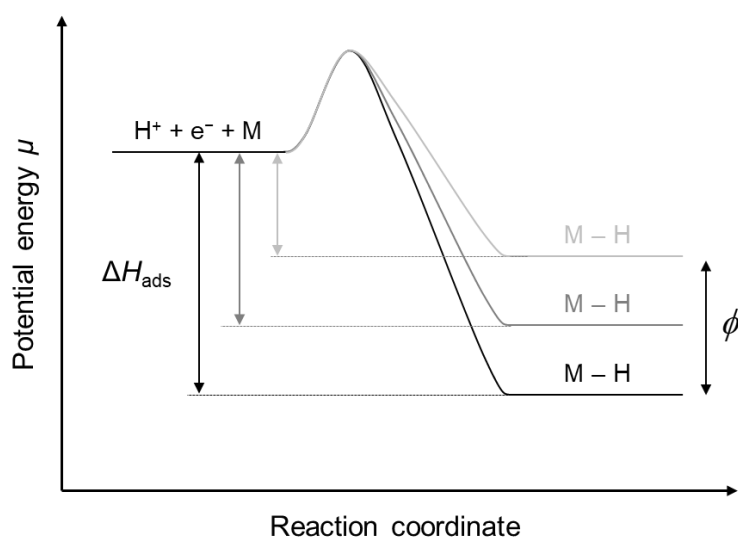


Figure 20: Schematic representation of variation of chemical potential of adsorbed state and thus, changing adsorption enthalpy upon variation of local electric potential.

1.8 Catalyst characterization

Carbon-supported transition metal catalysts are most often characterized concerning their metal loading, external surface area and metal dispersion. Therefore, catalysts are examined *via* different physicochemical methods of analysis, e.g., N₂ physisorption, H₂ chemisorption, transmission electron microscopy (TEM) and atomic absorption spectroscopy (AAS). These are discussed in the following sections.

1.8.1 Nitrogen physisorption

Adsorption is the interaction of an adsorbate with a solid surface. Depending on the bonding between adsorbate and adsorptive there are two types of adsorption, i.e., chemisorption and physisorption.^[95] In chemisorption, adsorbate molecules are bound to the solid surface *via* chemical interactions whereas in physisorption they only weakly interact *via van-der-Waals* forces. Both sorption processes need to be exothermic, which results from *Gibbs-Helmholtz* equation (Equation 43):

$$\Delta G = \Delta H - T\Delta S \quad (43)$$

The ΔG is the *Gibbs* free energy of adsorption and the ΔH and ΔS stand for the respective adsorption enthalpy and entropy. The T refers to the temperature.

For a spontaneous process ΔG is negative. As the entropy change during adsorption is also negative the corresponding value of ΔH has to be negative.^[36a]

Nitrogen physisorption is the most commonly used method to gather information on the surface area, pore size, and pore size distribution of catalyst materials.^[96] The principle of N₂ physisorption is based on the physical adsorption of a gas on the surface of a material. Therefore, it is assumed that all surface sites are initially populated equally and that there is no interaction between adsorbed species. Since polar adsorbates tend to chemisorb strongly on specific adsorption sites, a nonpolar gas is needed to fulfill these assumptions.^[97] In N₂ physisorption adsorption and desorption isotherms of a sample are measured at 77 K with nitrogen as adsorbate.^[98] Heavier gases such as krypton would improve the sensitivity however, these methods suffer from limitations concerning measurement scale and conditions. Before the measurement, the sample is outgassed to remove any contaminations.^[99] By plotting the adsorbed amount as a function of partial pressure of adsorbate gas at a certain temperature an adsorption isotherm is recorded. The part of isotherm until completion of a first monolayer follows *Langmuir* equation (Equation 44).^[100]

$$n_{\text{Upt.}} = n_{\text{Upt.}}^{\text{ML}} \frac{Kp}{1 + Kp} \quad (44)$$

The $n_{\text{Upt.}}$ and $n_{\text{Upt.}}^{\text{ML}}$ refer to the uptake of adsorbate on the solid surface and the uptake required for one monolayer of adsorbate, respectively. The K is the adsorption equilibrium constant and p stands for the partial pressure of adsorbate gas.

However, in physisorption the first layer of adsorbate can serve as sites for further adsorption. Therefore, another isotherm for describing multiple layer adsorption on a solid surface is needed. One of the most well-known isotherms for describing multilayer adsorption, the *BET* isotherm, was introduced by *Brunauer, Emmet and Teller* in 1938 (Equation 45).^[101]

$$n_{\text{Upt.}} = n_{\text{Upt.}}^{\text{ML}} \frac{cp}{\left(1 - \frac{p}{p^\circ}\right)(p^\circ + p(c-1))} \quad (45)$$

The c refers to the *BET* constant and p° is the vapor pressure of adsorptive in bulk phase. The *BET* constant depends on the adsorption heats of first, second and higher adsorption layers.

Linearization of Equation 45 allows for determining the monolayer adsorbed gas quantity v_{ML} and the *BET* constant from the slope and y-intercept of the resulting plot of $\frac{1}{v\left(1 - \frac{p^\circ}{p}\right)}$ vs. $\frac{p}{p^\circ}$

(Figure 21, Equations 46-48).

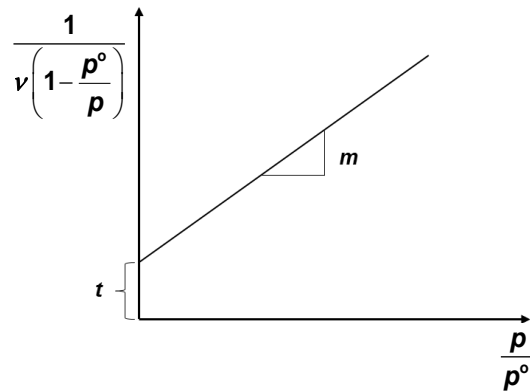


Figure 21: *BET* plot for determining monolayer adsorbed gas quantity and *BET* constant.

$$\frac{1}{v\left(1 - \frac{p^\circ}{p}\right)} = \frac{c-1}{v_{\text{ML}}c} \frac{p}{p^\circ} + \frac{1}{v_{\text{ML}}c} \quad (46)$$

$$v_{\text{ML}} = \frac{1}{m+t} \quad (47)$$

$$c = 1 + \frac{m}{t} \quad (48)$$

The v stands for the adsorbed gas quantity.

The *BET* method is used in material science and catalysis to calculate the total surface area (S_{total}) as well as the *BET* or specific surface area (S_{BET}) of a sample (Equations 49-50).^[102]

$$S_{\text{total}} = \frac{V_{\text{ML}} N_A s}{V_m} \quad (49)$$

$$S_{\text{BET}} = \frac{S_{\text{total}}}{m_{\text{Sample}}} \quad (50)$$

The N_A , V_m and s represent the *Avogadro* number, the molar volume of adsorbate gas as well as the adsorbate cross section, respectively. The m_{Sample} is the adsorbent or sample mass.

Depending on the pore diameters of a sample hysteresis phenomena have to be considered. A hysteresis during adsorption/desorption process means a difference in the adsorption and desorption branches of an isotherm. This phenomenon can be explained by the fact that mesoporous materials allow capillary condensation.^[103] The condensate is showing a different partial pressure than the adsorbate leading to different behavior during desorption. The hysteresis is depending on multiple parameters and can be interpreted by the different types of isotherms defined by *IUPAC* (Figure 22).^[104]

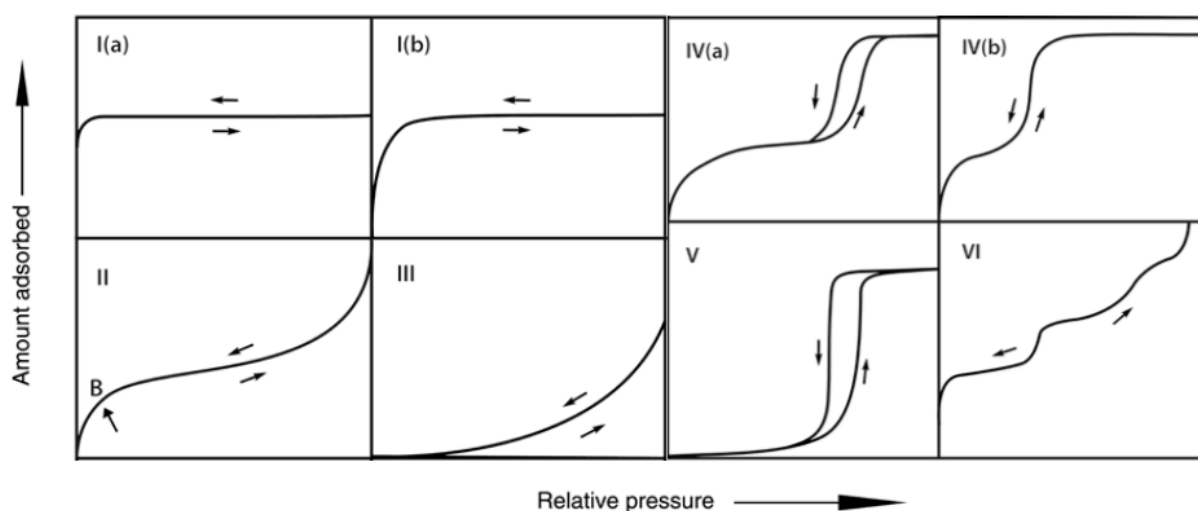


Figure 22: *BET* isotherms classified according to *IUPAC*, adapted from ref. [104].

It has to be noted that the part of the isotherm used for calculating the total and specific surface area is the region of monolayer adsorption, which usually doesn't show hysteresis phenomena.^[105] Figure 23 shows a schematic representation of an instrument for *BET* analysis.

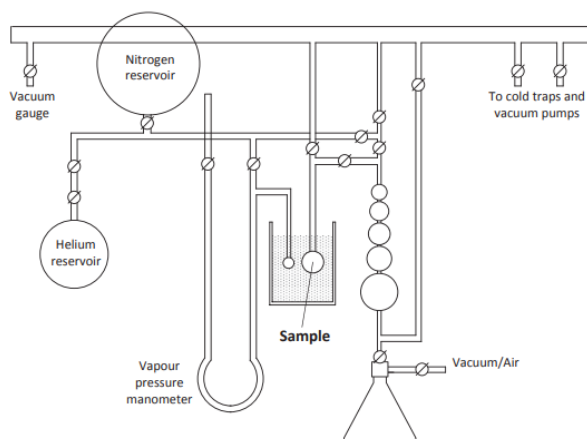


Figure 23: Schematic of a generic N_2 physisorption setup, reprinted from *Naderi*.^[106]

1.8.2 Hydrogen chemisorption

Hydrogen chemisorption is used to determine the number of exposed active metal sites on the surface of the examined sample.^[107] After sample activation in vacuum known amounts of probing gas, i.e., H_2 are dosed into the sample cell and the equilibrium pressure established between sample and gas phase is measured for each dose.^[108] By plotting the adsorbed volume against equilibrium pressure, this results in an adsorption isotherm for monolayer uptake of hydrogen on all metal surface sites (isotherm A). However, in catalysis it can be distinguished between weakly binding surface sites and strongly binding sites.^[109] It is the latter ones that are interesting in terms of reaction kinetics and thermodynamics. Hence, *via* back-sorption method the fully covered sample is evacuated again at room temperature. This allows for removal of only the weakly bound hydrogen from the catalyst surface. In a second adsorption measurement, only these sites are covered again with hydrogen, which results in a second isotherm for H adsorption on weakly binding metal surface sites (isotherm B).^[110] Subtracting isotherm B from isotherm A gives the hydrogen adsorption isotherm on strongly binding metal surface sites, that is the active surface sites of the sample (isotherm C). Figure 24 shows different isotherms of hydrogen adsorption on a metal surface determined *via* H_2 chemisorption.

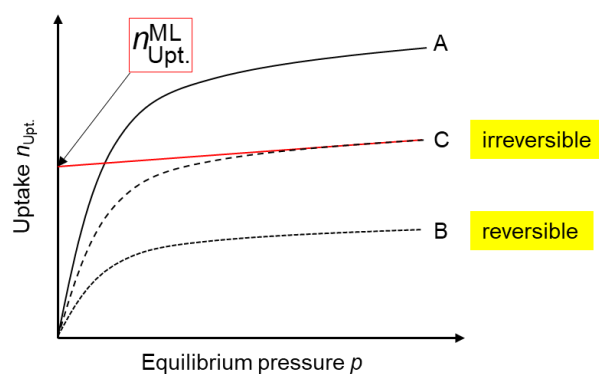


Figure 24: Schematic representation of H adsorption isotherms on different metal surface sites with extrapolated monolayer uptake.

By extrapolating the linear part of isotherm C to zero pressure the monolayer uptake of H on active surface sites $V_{\text{Upt.}}^{\text{ML}}$ can be determined.^[111] Using this value, the active metal surface area (S_M) and the metal dispersion (D) of the catalyst can be calculated according to Equations 51-52. The average particle diameter (d_p) is derived from Equation 53.

$$S_M = \frac{V_{\text{Upt.}}^{\text{ML}}}{V_{\text{mol}}} N_A \nu s \quad (51)$$

$$D = \frac{S_M M_W}{N_A s} \quad (52)$$

$$d_p = \frac{g}{S_M \rho} \quad (53)$$

The ν is the adsorption stoichiometric coefficient, e.g., for H on Pt $\nu = 1$. The N_A and V_{mol} refer to *Avogadro* constant and molar volume; the s stands for the adsorbate cross-sectional area. The M_W and ρ are the metal's molecular weight and density, respectively. The g is a geometric factor depending on the metal particle shape, e.g., $g = 6$ for spherical particles.^[112] Figure 25 gives a diagram of a typical apparatus for H_2 chemisorption measurements.

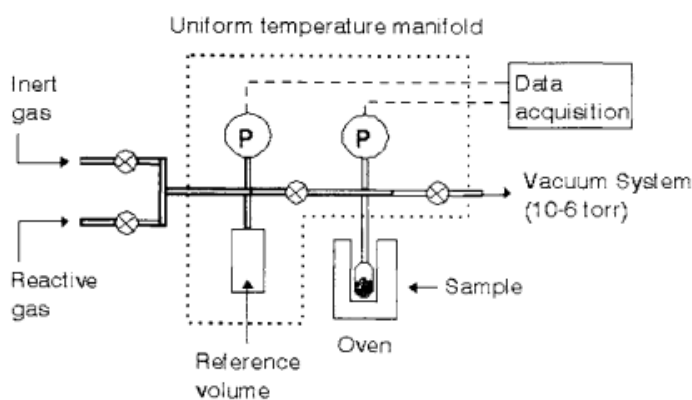


Figure 25: Schematic overview of a H_2 chemisorption setup, reprinted from *Fadoni and Lucarelli*.^[113]

1.8.3 Transmission electron microscopy

Transmission electron microscopy (TEM) is a widely applied technique in material science for imaging nanoscale structures that are below 100 nm in size.^[114] In a common transmission electron microscope, a beam of electrons is generated *via* application of high voltage to an emission source or cathode made of either tungsten or lanthanum hexaboride.^[115] Given a sufficient current, electrons are emitted into vacuum *via* thermionic or field electron emission. According to *Louis de Broglie* electrons generated with a high acceleration voltage have a very small wavelength (λ) leading to a significantly higher resolution of TEM compared to light microscopy (Equation 54).^[36a, 116]

$$\lambda = \frac{h}{p} = \frac{h}{m_e v} = \frac{h}{\sqrt{2m_e e \phi}} \quad (54)$$

The h and p refer to *Planck* constant and the electron's momentum, respectively. The m_e and v are its mass and speed. The e and ϕ stand for the elemental charge and the acceleration voltage that is applied to the cathode.

Objective lenses and slits in the column only allow for transmission of electrons within a very small energy range leading to a well-defined electron beam.^[117] The focused beam is applied to the specimen prepared on a sample holder or grid, the thickness of which has to be less than 100 nm for electrons to pass through.^[118] The transmitted electrons are refocused and magnified onto an imaging device, e.g., a fluorescent screen that allows for converting the electronic information into a visible form.^[119] Depending on the density of the sample the incoming electrons are scattered at different angles, which leads to variation of the transmitted intensity.^[120] High-density areas scatter electrons more strongly leading to a decreased intensity of electrons passing through the sample. Consequently, metal particles on a low-density support, e.g., carbon, alumina or silica appear as dark spots in bright-field TEM images. Therefore, TEM images can be used to determine the mean particle size (d_p) and dispersion (D) of supported transition metal catalysts (Equations 55-56).

$$d_p = \frac{\sum_i d_i^3}{\sum_i d_i^2} \quad (55)$$

$$D = \frac{gV_M}{d_p S} \quad (56)$$

The d_i refers to the particle diameters measured from TEM images. The g is a geometric factor depending on the metal particle shape, e.g., $g = 6$ for spherical particles. The V_M and S are the volume of metal atom and its cross-sectional area, respectively.

Figure 26 shows a model of a common transmission electron microscope.

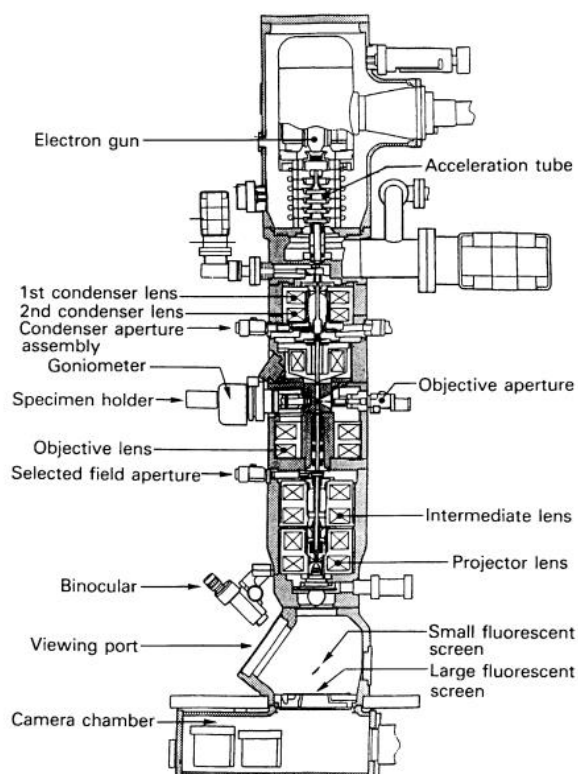


Figure 26: Schematic representation of a transmission electron microscope, reprinted from ref. [118].

1.8.4 Atomic absorption spectroscopy

Atomic absorption spectroscopy (AAS) is a powerful technique for quantitative analysis of chemical elements in an unknown sample that is based on the absorption of light by atoms in gaseous state.^[121] Based on the atomic absorption spectrum of a sample the concentration of specific analytes, e.g., chemical elements can be determined.^[122] Therefore, the calibration with standard solutions of known analyte concentration is required in order to establish the relation between measured absorbance (A) and analyte concentration (c) according to *Beer-Lambert* law (Equation 57).^[123]

$$A = \log\left(\frac{I_0}{I}\right) = \log(T^{-1}) = \varepsilon cd \quad (57)$$

The I and I_0 represent the intensity of light after having passed through the sample and its initial intensity, respectively. The T stands for the ratio between I and I_0 , which is the transmittance of the sample. The ε and d are the absorption coefficient of the sample and the light's pass length through the sample.

In common AAS setups a flame atomizer is used to bring the sample in the gaseous state and to nebulize it into the atomization chamber.^[124] Afterwards, the analyte is radiated with light of element-specific wavelength, which is emitted by a hollow cathode lamp.^[125] Hollow cathode lamps are line sources as they emit only the characteristic wavelength spectrum of the element

that is to be analyzed.^[126] This is possible because these types of line sources contain the element of interest as cathode. Once, a high voltage is applied between anode and cathode of the lamp the inert filling gas is ionized and accelerated towards the cathode. There, the impacting ions cause excitation of the element atoms that emit their characteristic spectrum upon relaxation.^[36a] In double beam instruments, the emitted light is split into a sample beam that passes through the atomization chamber and a reference beam that bypasses the sample.^[127] After the sample chamber the beams are unified and their ratio of intensities is formed using photomultiplier tubes as detector. This way, fluctuations in the spectral source and the detector are canceled out, which results in a more stable signal than for single beam spectrometers. Figure 27 depicts a schematic representation of a double beam AAS instrument.

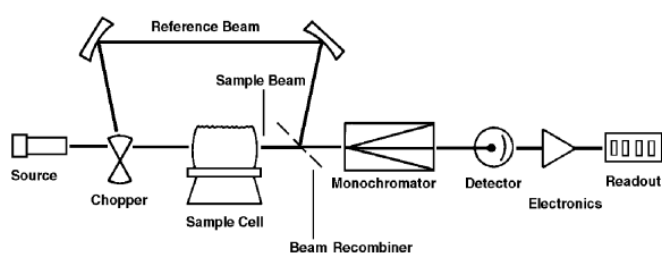


Figure 27: Schematic of a double beam AAS setup reprinted from *Beaty and Kerber*.^[128]

1.9 Scope of the thesis

In scope of this work, the electrocatalytic hydrogenation of oxygenated compounds on *CNT*-supported transition metal catalysts in water is investigated. A special focus is put on the elucidation of fundamental steps occurring at the electrode/electrolyte interface, i.e., the electrochemical double-layer.

The electrocatalytic activation of hydrogen on the metal electrode surface is the first elementary step in ECH of organic molecules. The first part of this work analyses how the variation of external electric potential on Pt electrode surface alters the thermodynamic stability of H adsorbed on the metal surface. The *Fermi* level of Pt is found to shift upon modification of applied overpotential. Therefore, the role of *Fermi* level adjustment on Pt-H bond strength and catalyst activity in hydrogen evolution reaction is analyzed.

In the second section the impact of electrolyte composition on Pt-H bond strength in aqueous phase is investigated. Depending on solution pH, ionic strength and containing alkali metal cations the adsorption heat and entropy of H on electrode surface are evaluated. The results are correlated to catalyst activity in electrocatalytic hydrogenation of benzaldehyde. The pH of electrolyte is found to have the largest influence on H adsorption on Pt and reaction kinetics of ECH.

In contrast to aromatic aldehydes, the (electrocatalytic) hydrogenation of unsaturated aliphatic aldehydes towards (un)saturated alcohols is more challenging. The last section examines the electrocatalytic hydrogenation of *trans*-2-penten-1-al on Pd- and Ru-containing catalysts. The effect of external electric potential and catalyst composition, e.g., noble metal, support acidity, particle size on reaction kinetics and selectivity is investigated. Furthermore, the addition of promotor species as well as changing the electrolyte pH are analyzed. The outcome is correlated to adsorption properties of different functional groups on the metal electrode surface. The application of a large cathodic overpotential to a bimetallic Ru-Fe catalyst in less acidic solution turned out to be most beneficial for selective hydrogenation of the carbonyl group.

1.10 References

- [1] BP (2021), *Statistical Review of World Energy 2021*, BP London, <https://www.bp.com/content/dam/bp/business-sites/en/global/corporate/pdfs/energy-economics/statistical-review/bp-stats-review-2021-full-report.pdf> (07.07.2022).
- [2] A. Majewski (2019), *Energy Alternatives*, DieselNet Technology Guide https://dieselnet.com/tech/energy_alternatives.php (07.07.2022).
- [3] R. Hannah, R. Max, R. Pablo (2020), *Energy Production and Consumption*, <https://ourworldindata.org/energy> (07.07.2022).
- [4] a) P. S. REN21, *Secretariat Renewable Energy Policy Network for the 2017*, 21; b) B. Johansson, *Energy* **2013**, 61, 598-605; c) C. C. IPCC, *Contribution of working group III to the fifth assessment report of the intergovernmental panel on climate change 2014*, 1454.
- [5] United Nations (2015), *Paris Agreement*, Paris, https://unfccc.int/sites/default/files/english_paris_agreement.pdf (08.07.2022).
- [6] a) European Commission, *WHITE PAPER Roadmap to a Single European Transport Area – Towards a competitive and resource efficient transport system*, **2011**; b) European Commission, *Communication from the Commission to the European Parliament, the Council, the European Economic and Social Committee and the Committee of the Regions Youth Opportunities Initiative*, **2011**.
- [7] a) IRENA, *Global hydrogen trade to meet the 1.5°C climate goal*, International Renewable Energy Agency, Abu Dhabi; b) European Commission, E. Directorate-General for, B. Breitschopf, L. Zheng, M. Plaisir, J. Bard, R. Schröer, D. Kawale, J. Koornneef, Y. Melese, M. Schaaphok, J. Gorenstein Dedecca, C. Bene, O. Cerny, F. Gérard, *The role of renewable H₂ import & storage to scale up the EU deployment of renewable H₂ : report*, Publications Office of the European Union, **2022**; c) European Commission, *Implementing the repower EU action plan: investment needs, hydrogen accelerator and achieving the bio-methane targets*, **2022**.
- [8] a) M. M. Hand, S. Baldwin, E. DeMeo, J. M. Reilly, D. Arent, G. Porro, M. Meshek, D. Sandor (2012), *Renewable Electricity Futures Study*, Golden, CO, <https://www.nrel.gov/docs/fy13osti/52409-ES.pdf> (08.07.2022); b) A. E. MacDonald, C. T. M. Clack, A. Alexander, A. D. Dunbar, J. M. Wilczak, Y. Xie, *Nature Climate Change* **2016**, 6, 526-531.
- [9] K. F. Kalz, R. Kraehnert, M. Dvoyashkin, R. Dittmeyer, R. Gläser, U. Krewer, K. Reuter, J.-D. Grunwaldt, *ChemCatChem* **2017**, 9, 17-29.
- [10] a) F. Bilgili, E. Koçak, Ü. Bulut, S. Kuşkaya, *Renewable and Sustainable Energy Reviews* **2017**, 71, 830-845; b) A. Tursi, *Biofuel Research Journal* **2019**, 6, 962-979; c) N. S. Bentsen, C. Felby, *Biotechnology for Biofuels* **2012**, 5, 25; d) W. G. Hohenstein, L. L. Wright, *Biomass and Bioenergy* **1994**, 6, 161-173.
- [11] a) A. Corma, S. Iborra, A. Velty, *Chemical Reviews* **2007**, 107, 2411-2502; b) G. W. Huber, A. Corma, *Angewandte Chemie International Edition* **2007**, 46, 7184-7201; c) C. B. Field, J. E. Campbell, D. B. Lobell, *Trends in Ecology & Evolution* **2008**, 23, 65-72.
- [12] a) C. Vezzoli, F. Ceschin, L. Osanjo, M. K. M'Rithaa, R. Moalosi, V. Nakazibwe, J. C. Diehl, in *Designing Sustainable Energy for All: Sustainable Product-Service System Design Applied to Distributed Renewable Energy* (Eds.: C. Vezzoli, F. Ceschin, L. Osanjo, M. K. M'Rithaa, R. Moalosi, V. Nakazibwe, J. C. Diehl), Springer International Publishing, Cham, **2018**, pp. 23-39; b) E. J. Hengeveld, W. J. T. van Gemert, J. Bekkering, A. A. Broekhuis, *Biomass and Bioenergy* **2014**, 67, 363-371; c) J. Bekkering, T. A. Broekhuis, W. J. T. van Gemert, *Engineering in Life Sciences* **2010**, 10, 585-594.
- [13] L. J. R. Nunes, T. P. Causer, D. Ciolkosz, *Renewable and Sustainable Energy Reviews* **2020**, 120, 109658.
- [14] a) F. Rosillo-Calle, *Journal of Chemical Technology & Biotechnology* **2016**, 91, 1933-1945; b) R. Slade, A. Bauen, R. Gross, *Nature Climate Change* **2014**, 4, 99-105.
- [15] a) E. de Jong, R. J. A. Gosselink, in *Bioenergy Research: Advances and Applications* (Eds.: V. K. Gupta, M. G. Tuohy, C. P. Kubicek, J. Saddler, F. Xu), Elsevier, Amsterdam, **2014**, pp. 277-313; b) S. Prasad, A. P. Ingle, in *Sustainable Bioenergy* (Eds.: M. Rai, A. P. Ingle), Elsevier, **2019**, pp. 327-346.
- [16] T. Abbasi, S. A. Abbasi, *Renewable and Sustainable Energy Reviews* **2010**, 14, 919-937.
- [17] E. M. W. Smeets, A. P. C. Faaij, *Climatic Change* **2007**, 81, 353-390.
- [18] a) G. W. Huber, S. Iborra, A. Corma, *Chemical Reviews* **2006**, 106, 4044-4098; b) K. Alper, K. Tekin, S. Karagöz, A. J. Ragauskas, *Sustainable Energy & Fuels* **2020**, 4, 4390-4414; c) T. Ghislain, X. Duret, P. N. Diouf, J.-M. Lavoie, in *Handbook on Characterization of Biomass, Biowaste and Related By-products* (Ed.: A. Nzihou), Springer International Publishing, Cham, **2020**, pp. 499-535.
- [19] A. V. Bridgwater, *Biomass and Bioenergy* **2012**, 38, 68-94.
- [20] a) M. Sharifzadeh, M. Sadeqzadeh, M. Guo, T. N. Borhani, N. V. S. N. Murthy Konda, M. C. Garcia, L. Wang, J. Hallett, N. Shah, *Progress in Energy and Combustion Science* **2019**, 71, 1-80; b) P. K. Kanaujia,

- Y. K. Sharma, M. O. Garg, D. Tripathi, R. Singh, *Journal of Analytical and Applied Pyrolysis* **2014**, *105*, 55-74.
- [21] a) U. Sanyal, J. Lopez-Ruiz, A. B. Padmaperuma, J. Holladay, O. Y. Gutiérrez, *Organic Process Research & Development* **2018**, *22*, 1590-1598; b) E. Andrews, J. A. Lopez-Ruiz, J. D. Egbert, K. Koh, U. Sanyal, M. Song, D. Li, A. J. Karkamkar, M. A. Derewinski, J. Holladay, O. Y. Gutiérrez, J. D. Holladay, *ACS Sustainable Chemistry & Engineering* **2020**, *8*, 4407-4418.
- [22] C. H. Lam, S. Das, N. C. Erickson, C. D. Hyzer, M. Garedew, J. E. Anderson, T. J. Wallington, M. A. Tamor, J. E. Jackson, C. M. Saffron, *Sustainable Energy & Fuels* **2017**, *1*, 258-266.
- [23] Y. Song, U. Sanyal, D. Pangotra, J. D. Holladay, D. M. Camaioni, O. Y. Gutiérrez, J. A. Lercher, *Journal of Catalysis* **2018**, *359*, 68-75.
- [24] a) U. Sanyal, J. Lopez-Ruiz, A. B. Padmaperuma, J. D. Holladay, O. Y. Gutiérrez, *Organic Process Research & Development* **2018**, *22*, 1590-1598; b) C. H. Lam, W. Deng, L. Lang, X. Jin, X. Hu, Y. Wang, *Energy & Fuels* **2020**, *34*, 7915-7928; c) K. Li, Y. Sun, *Chemistry – A European Journal* **2018**, *24*, 18258-18270.
- [25] Y. Song, O. Y. Gutiérrez, J. Herranz, J. A. Lercher, *Applied Catalysis B: Environmental* **2016**, *182*, 236-246.
- [26] a) S. A. Akhade, N. Singh, O. Y. Gutiérrez, J. Lopez-Ruiz, H. Wang, J. D. Holladay, Y. Liu, A. Karkamkar, R. S. Weber, A. B. Padmaperuma, M.-S. Lee, G. A. Whyatt, M. Elliott, J. E. Holladay, J. L. Male, J. A. Lercher, R. Rousseau, V.-A. Glezakou, *Chemical Reviews* **2020**, *120*, 11370-11419; b) E. J. Biddinger, O. Y. Gutierrez, J. Holladay, *Journal of Applied Electrochemistry* **2021**, *51*, 1-3.
- [27] a) J. C.-H. Lam, C. Lowe, Z. Li, K. Longe, J. Rayburn, M. Caldwell, C. Houdek, J. Maguire, D. Miller, C. Saffron, J. Jackson, *Green Chem.* **2014**, *17*; b) A. Kadier, M. S. Kalil, W. Logroño, A. Mohamed, H. A. Hasan, in *Encyclopedia of Sustainability Science and Technology* (Ed.: R. A. Meyers), Springer New York, New York, NY, **2017**, pp. 1-20.
- [28] K. A. Mauritz, R. B. Moore, *Chemical Reviews* **2004**, *104*, 4535-4586.
- [29] a) C. Heitner-Wirguin, *Journal of Membrane Science* **1996**, *120*, 1-33; b) A. Kusoglu, A. Z. Weber, *Chemical Reviews* **2017**, *117*, 987-1104.
- [30] Y. Sone, P. Ekdunge, D. Simonsson, *Journal of The Electrochemical Society* **1996**, *143*, 1254-1259.
- [31] V. Hacker, C. Sumeder, *Electrical Engineering: Fundamentals*, De Gruyter, **2020**.
- [32] C. H. Hamann, A. Hamnett, W. Vielstich, *Electrochemistry*, Wiley, **1998**.
- [33] N. Eliaz, E. Gileadi, *Physical Electrochemistry - Fundamentals, Techniques and Applications*, 2 ed., Wiley-VCH, Weinheim, Germany, **2019**.
- [34] S. V. Bagotsky, in *Fundamentals of Electrochemistry*, **2005**, pp. 19-31.
- [35] R. Holze, *Experimental Electrochemistry: A Laboratory Textbook*, Wiley, **2009**.
- [36] a) P. W. Atkins, J. de Paula, *Physikalische Chemie, Vol. 5*, WILEY-VCH GmbH & Co. KGaA, Weinheim, **2013**; b) in *Solar-Hydrogen Energy Systems* (Ed.: T. Ohta), Pergamon, **1979**, pp. 35-58.
- [37] a) M. Carmo, D. L. Fritz, J. Mergel, D. Stolten, *International Journal of Hydrogen Energy* **2013**, *38*, 4901-4934; b) S. Shiva Kumar, V. Himabindu, *Materials Science for Energy Technologies* **2019**, *2*, 442-454.
- [38] P. Sharma, O. P. Pandey, in *PEM Fuel Cells* (Ed.: G. Kaur), Elsevier, **2022**, pp. 1-24.
- [39] N. A. Lange, J. Speight, *Lange's Handbook of Chemistry, 70th Anniversary Edition*, McGraw-Hill Education, **2005**.
- [40] A. J. Bard, L. R. Faulkner, *Electrochemical Methods: Fundamentals and Applications*, Wiley, **2000**.
- [41] R. V. Kumar, T. Sarakonsri, in *High Energy Density Lithium Batteries*, **2010**, pp. 1-25.
- [42] a) G. Ren, G. Li, Y. Zhang, A. Wang, X. Wang, Y. Cong, T. Zhang, N. Li, *Sustainable Energy & Fuels* **2022**, *6*, 1156-1163; b) R. Wang, G. Li, J. Xu, A. Wang, Y. Cong, X. Wang, T. Zhang, N. Li, *Green Chemistry* **2021**, *23*, 5474-5480.
- [43] a) L. Wilson, S. Martin, *Annals of emergency medicine* **1999**, *33*, 495-499; b) M. Ash, I. Ash, *Handbook of Preservatives*, Synapse Information Resources, **2004**.
- [44] D. C. Cantu, A. B. Padmaperuma, M.-T. Nguyen, S. A. Akhade, Y. Yoon, Y.-G. Wang, M.-S. Lee, V.-A. Glezakou, R. Rousseau, M. A. Lilga, *ACS Catalysis* **2018**, *8*, 7645-7658.
- [45] A. P. Doherty, C. A. Brooks, *Electrochimica Acta* **2004**, *49*, 3821-3826.
- [46] J. A. Lopez-Ruiz, E. Andrews, S. A. Akhade, M.-S. Lee, K. Koh, U. Sanyal, S. F. Yuk, A. J. Karkamkar, M. A. Derewinski, J. Holladay, V.-A. Glezakou, R. Rousseau, O. Y. Gutiérrez, J. D. Holladay, *ACS Catalysis* **2019**, *9*, 9964-9972.
- [47] U. Sanyal, K. Koh, L. C. Meyer, A. Karkamkar, O. Y. Gutiérrez, *Journal of Applied Electrochemistry* **2021**, *51*, 27-36.
- [48] J. A. Lopez-Ruiz, U. Sanyal, J. D. Egbert, O. Y. Gutiérrez, J. D. Holladay, *ACS Sustainable Chemistry & Engineering* **2018**, *6*, 16073-16085.

- [49] K. Koh, U. Sanyal, M. S. Lee, G. Cheng, M. Song, V. A. Glezakou, Y. Liu, D. Li, R. Rousseau, O. Y. Gutiérrez, A. Karkamkar, M. Derewinski, J. A. Lercher, *Angewandte Chemie International Edition* **2019**, *59*, 1501-1505.
- [50] a) K. Tomishige, Y. Nakagawa, M. Tamura, *Green Chemistry* **2017**, *19*, 2876-2924; b) X. Lan, T. Wang, *ACS Catalysis* **2020**, *10*, 2764-2790; c) P. Gallezot, D. Richard, *Catalysis Reviews* **1998**, *40*, 81-126.
- [51] P. Mäki-Arvela, J. Hájek, T. Salmi, D. Y. Murzin, *Applied Catalysis A: General* **2005**, *292*, 1-49.
- [52] P. Claus, *Topics in Catalysis* **1998**, *5*, 51-62.
- [53] V. Ponec, *Applied Catalysis A: General* **1997**, *149*, 27-48.
- [54] a) Y. Dai, X. Gao, X. Chu, C. Jiang, Y. Yao, Z. Guo, C. Zhou, C. Wang, H. Wang, Y. Yang, *Journal of Catalysis* **2018**, *364*, 192-203; b) N. Mahata, F. Gonçalves, M. F. R. Pereira, J. L. Figueiredo, *Applied Catalysis A: General* **2008**, *339*, 159-168.
- [55] B. Bachiller-Baeza, A. Guerrero-Ruiz, P. Wang, I. Rodríguez-Ramos, *Journal of Catalysis* **2001**, *204*, 450-459.
- [56] M. Tamura, K. Tokonami, Y. Nakagawa, K. Tomishige, *Chemical Communications* **2013**, *49*, 7034-7036.
- [57] A. Giroir-Fendler, D. Richard, P. Gallezot, *Catalysis Letters* **1990**, *5*, 175-181.
- [58] A. Solhy, B. F. Machado, J. Beausoleil, Y. Kihn, F. Gonçalves, M. F. R. Pereira, J. J. M. Órfão, J. L. Figueiredo, J. L. Faria, P. Serp, *Carbon* **2008**, *46*, 1194-1207.
- [59] a) N. Dubouis, A. Grimaud, *Chemical Science* **2019**, *10*, 9165-9181; b) B. E. Conway, B. V. Tilak, *Electrochimica Acta* **2002**, *47*, 3571-3594.
- [60] G. Prentice, in *Encyclopedia of Physical Science and Technology (Third Edition)* (Ed.: R. A. Meyers), Academic Press, New York, **2003**, pp. 143-159.
- [61] a) A. R. Zeradjanin, J.-P. Grote, G. Polymeros, K. J. J. Mayrhofer, *Electroanalysis* **2016**, *28*, 2256-2269; b) C. G. Morales-Guio, L.-A. Stern, X. Hu, *Chemical Society Reviews* **2014**, *43*, 6555-6569.
- [62] D. M. Heard, A. J. J. Lennox, *Angewandte Chemie International Edition* **2020**, *59*, 18866-18884.
- [63] T. Shinagawa, A. T. Garcia-Esparza, K. Takanebe, *Scientific Reports* **2015**, *5*, 13801.
- [64] a) J. O. M. Bockris, A. K. N. Reddy, M. E. Gamboa-Aldeco, *Modern Electrochemistry 2nd Edition*, Springer US, **1998**; b) J. Newman, K. E. Thomas-Alyea, *Electrochemical Systems*, Wiley, **2004**.
- [65] K. E. Heusler, *Berichte der Bunsengesellschaft für physikalische Chemie* **1994**, *98*, 644-645.
- [66] a) D. G. Truhlar, B. C. Garrett, S. J. Klippenstein, *The Journal of Physical Chemistry* **1996**, *100*, 12771-12800; b) G. S. Hammond, *Journal of the American Chemical Society* **1955**, *77*, 334-338.
- [67] D. C. Grahame, *Chemical Reviews* **2002**, *41*, 441-501.
- [68] S. Srinivasan, in *Fuel Cells: From Fundamentals to Applications* (Ed.: S. Srinivasan), Springer US, Boston, MA, **2006**, pp. 27-92.
- [69] H. Helmholtz, *Annalen der Physik* **1853**, *165*, 211-233.
- [70] a) M. Gouy, *Journal de Physique Théorique et Appliquée* **1910**, *9*, 457-468; b) D. L. Chapman, *The London, Edinburgh, and Dublin Philosophical Magazine and Journal of Science* **1913**, *25*, 475-481.
- [71] a) A. H. Carter, *Classical and Statistical Thermodynamics*, Prentice Hall, **2001**; b) C. Cercignani, C. i. m. estivo, *Kinetic Theories and the Boltzmann Equation: Lectures Given at the 1st 1981 Session of the Centro Internazionale Matematico Estivo (C.I.M.E.) Held at Montecatini, Italy, June 10-18, 1981*, Springer, **1984**.
- [72] C. F. Gauss, *Carl Friedrich Gauss Werke: 5*, Koniglichen Gesellschaft der wissenschaften, **1867**.
- [73] O. Stern, *Zeitschrift für Elektrochemie und angewandte physikalische Chemie* **1924**, *30*, 508-516.
- [74] Q.-D. Trinh, Wolfram Demonstrations Project, **2011**.
- [75] N. Elgrishi, K. J. Rountree, B. D. McCarthy, E. S. Rountree, T. T. Eisenhart, J. L. Dempsey, *Journal of Chemical Education* **2018**, *95*, 197-206.
- [76] R. S. Nicholson, I. Shain, *Analytical Chemistry* **1964**, *36*, 706-723.
- [77] Z. Stojek, in *Electroanalytical Methods* (Ed.: F. Scholz), Springer, **2010**.
- [78] J. Heinze, *Angewandte Chemie International Edition in English* **1984**, *23*, 831-847.
- [79] J. O. M. Bockris, B. E. Conway, E. B. Yeager, *The Double Layer*, Plenum Press, **1980**.
- [80] N. Eliaz, E. Gileadi, *Physical Electrochemistry: Fundamentals, Techniques, and Applications*, Wiley, **2019**.
- [81] R. S. Nicholson, *Analytical Chemistry* **1965**, *37*, 1351-1355.
- [82] P. T. Kissinger, W. R. Heineman, *Journal of Chemical Education* **1983**, *60*, 702.
- [83] G. Jerkiewicz, *Electrocatalysis* **2010**, *1*, 179-199.
- [84] F. G. Will, C. A. Knorr, *Zeitschrift für Elektrochemie, Berichte der Bunsengesellschaft für physikalische Chemie* **1960**, *64*, 258-269.
- [85] J. Wang, *Analytical Electrochemistry*, Wiley, **2006**.
- [86] D. C. Loveday, P. Peterson, B. Rodgers—Gamry, **2004**.
- [87] E. Barsoukov, J. R. Macdonald, *Impedance Spectroscopy: Theory, Experiment, and Applications*, Wiley, **2005**.

- [88] G. Láng, *Materials and Corrosion* **1994**, *45*, 582-582.
- [89] G. W. Walter, *Corrosion Science* **1986**, *26*, 681-703.
- [90] M. Kendig, J. Scully, *Corrosion* **1990**, *46*, 22-29.
- [91] F. Mansfeld, *Electrochimica Acta* **1990**, *35*, 1533-1544.
- [92] F. Mandl, *Statistical Physics*, Wiley, **2013**.
- [93] G. Job, F. Herrmann, *European Journal of Physics* **2006**, *27*, 353-371.
- [94] C. Kittel, H. K. Charles Kittel, K. Charles, H. Kroemer, K. Herbert, *Thermal Physics*, W. H. Freeman, **1980**.
- [95] A. W. Adamson, A. P. Gast, *Physical Chemistry of Surfaces*, Wiley-Interscience, New York, **1997**.
- [96] P. Bertier, K. Schweinar, H. Stanjek, A. Ghanizadeh, C. Clarkson, A. Busch, N. Kampman, D. Prinz, A. Amann, B. Krooss, V. Pipich, *CMS Workshop Lectures* **2016**, *21*, 151-161.
- [97] M. Naderi, in *Progress in Filtration and Separation* (Ed.: S. Tarleton), Elsevier, **2015**, pp. 585-608.
- [98] D. A. H. Hanaor, M. Ghadiri, W. Chrzanowski, Y. Gan, *Langmuir* **2014**, *30*, 15143-15152.
- [99] V. Gómez-Serrano, C. M. González-García, M. L. González-Martín, *Powder Technology* **2001**, *116*, 103-108.
- [100] J. B. Condon, *Surface Area and Porosity Determinations by Physisorption: Measurement, Classical Theories and Quantum Theory*, Elsevier Science, **2006**.
- [101] S. Brunauer, P. H. Emmett, E. Teller, *Journal of the American Chemical Society* **1938**, *60*, 309-319.
- [102] A. Galarneau, D. Mehlhorn, F. Guenneau, B. Coasne, F. Villemot, D. Minoux, C. Aquino, J.-P. Dath, *Langmuir* **2018**, *34*, 14134-14142.
- [103] F. Sotomayor, K. Cychosz, M. Thommes, **2018**.
- [104] M. Thommes, K. Kaneko, A. V. Neimark, J. P. Olivier, F. Rodriguez-Reinoso, J. Rouquerol, K. S. W. Sing, *Pure and Applied Chemistry* **2015**, *87*, 1051-1069.
- [105] G. Fagerlund, *Matériaux et Constructions* **1973**, *6*, 239-245.
- [106] M. Naderi, in *Progress in Filtration and Separation* (Ed.: S. Tarleton), Academic Press, Oxford, **2015**, pp. 585-608.
- [107] K. Oura, V. G. Lifshits, A. Saranin, A. V. Zotov, M. Katayama, *Surface Science: An Introduction*, Springer Berlin Heidelberg, **2003**.
- [108] R. P. H. Gasser, *An Introduction to Chemisorption and Catalysis by Metals*, Clarendon Press, **1985**.
- [109] J. K. Norsko, *Reports on Progress in Physics* **1990**, *53*, 1253-1295.
- [110] A. Clark, *The Chemisorptive Bond: Basic Concepts*, Academic Press, **1974**.
- [111] A. Dąbrowski, *Studies in Surface Science and Catalysis, Vol. 120*, Elsevier, **1999**.
- [112] M. A. Aramendía, V. Borau, C. Jiménez, J. M. Marinas, A. Moreno, *Colloids and Surfaces A: Physicochemical and Engineering Aspects* **1996**, *106*, 161-165.
- [113] M. Fadoni, L. Lucarelli, in *Studies in Surface Science and Catalysis, Vol. 120* (Ed.: A. Dąbrowski), Elsevier, **1999**, pp. 177-225.
- [114] E. Ruska, *Microscopica acta. Supplement* **1980**, 1-140.
- [115] R. Egerton, *Physical Principles of Electron Microscopy: An Introduction to TEM, SEM, and AEM*, Springer US, **2011**.
- [116] L. de Broglie, *Nature* **1929**, *124*, 369-369.
- [117] D. B. Murphy, *Fundamentals of Light Microscopy and Electronic Imaging*, Wiley, **2002**.
- [118] B. Fultz, J. M. Howe, *Transmission Electron Microscopy and Diffractometry of Materials*, Springer Berlin Heidelberg, **2012**.
- [119] L. Reimer, H. Kohl, *Transmission Electron Microscopy: Physics of Image Formation*, Springer New York, **2008**.
- [120] J. Hren, J. Goldstein, D. Joy, *Introduction to Analytical Electron Microscopy*, **1979**.
- [121] a) A. Walsh, *Spectrochimica Acta* **1955**, *7*, 108-117; b) B. Welz, M. Sperling, M. R. Sperling, *Atomic Absorption Spectrometry*, Wiley, **1999**.
- [122] J.-M. Mermet, *Analytical and Bioanalytical Chemistry* **2006**, *385*, 14-15.
- [123] a) Beer, *Annalen der Physik* **1852**, *162*, 78-88; b) J. H. Lambert, *Photometria sive de mensura et gradibus luminis, colorum et umbrae*, sumptibus viduae E. Klett, typis C.P. Detleffsen, **1760**.
- [124] D. D. Miller, M. A. Rutzke, in *Food Analysis*, **2010**, pp. 421-442.
- [125] T. H. Risby, in *Comprehensive Analytical Chemistry, Vol. 47* (Eds.: S. Ahuja, N. Jespersen), Elsevier, **2006**, pp. 227-246.
- [126] G. Schwedt, T. C. Schmidt, O. J. Schmitz, *Analytische Chemie: Grundlagen, Methoden und Praxis*, Wiley, **2016**.
- [127] R. Garca, A. P., in *Atomic Absorption Spectroscopy*, **2012**.
- [128] R. D. Beaty, J. D. Kerber, **1997**.

2. Impact of external electric potential on electrocatalytic adsorption of hydrogen on Pt nanoparticles in aqueous phase

Abstract

Water as solvent tremendously affects hydrogen adsorption on noble metal catalysts like Pt that are used in hydrogen evolution reaction (HER) and electrocatalytic hydrogenation (ECH) of oxygenated compounds, e.g., aldehydes, ketones, carboxylic acids.

In water, H adsorbed on Pt that formed *via* reduction of hydronium ions from bulk solution is less stabilized than hydrogen adsorbing under vacuum. Depending on externally applied electric potential (E_{RHE}) and electrolyte pH the adsorption enthalpy in liquid phase (ΔH_{upd}) is reduced to -10 kJ mol^{-1} . The effect of applied overpotential is attributed to a shifting of electrode *Fermi* level and a different filling of Pt-H antibonding state (E^*). The influence of solution acidity can be rationalized *via* an additional energetic contribution that arises when the electrochemical double-layer (EDL) is moved away from the metal surface. Its strength is mainly determined by the number of H_3O^+ accumulated within EDL.

2.1 Introduction

As the first elementary step, dissociative adsorption of H_2 plays a significant role in catalytic hydrogenation reactions. The strength of hydrogen binding on metal is usually evaluated by the heat of adsorption of H_2 or hydrogen binding energy (HBE),^[1] which depends on adsorption geometry,^[2] reaction phase,^[3] etc.. The surface electronic structure of an electrode is considered as a key point that could establish a correlation between physical properties of a surface and its chemical reactivity like chemisorption of H_2 .^[4] The reactivity of a metal surface could be determined by the position of d-bands relative to *Fermi* level.^[5] The more degree the antibonding state being filled by electrons, the weaker the metal-H bond. Thus, the targeting reactivity of catalyst could be achieved by modulating its surface electronic structure. It is proved that the d-band center of Pt surface could be lowered by introducing 3d metals like Ni, Co on subsurface of Pt experimentally and theoretically.^[6] For gas phase adsorption of H_2 , the dissociative adsorption energy on Pt becomes weak with alloyed Cu.^[4] In aqueous phase, different metal electrodes were evaluated for hydrogen chemisorption and it was found that the metal with lower d-band center gives a less activation energy of hydrogen adsorption.^[7]

Inspired by the mentioned work, the impact of electronic structure at Pt surface on H adsorption is evaluated in this work by tuning external potential on Pt electrode in water. Additionally, the impact of electrolyte pH on Pt-H bond strength is investigated. The filling of Pt-H antibonding state could be modulated by external potential, resulting in a decreased stabilization of Pt-H at increasing cathodic overpotential. The energy input required for displacing the electrochemical double-layer from electrode surface alters with solution acidity. At low pH, a high energetic contribution compensates H adsorption heat more strongly than at high pH.

Immersing a metal electrode into an aqueous electrolyte leads to formation of an electrochemical double-layer (EDL). Consisting of inner and outer *Helmholtz* plane this interfacial region between electrode surface and bulk electrolyte has a thickness of only a few nanometer.^[8] Electrolyte ions, e.g., hydronium ions and electrolyte cations and anions are accumulated within this layer and prone to adsorption on electrode surface (Figure 1a).^[9] Adsorption and desorption of different electrolyte species can be driven by application of an external electric potential and for Pt-group metal electrodes it can be monitored by cyclic voltammetry (CV).^[10] Figure 1b shows the cyclic voltammogram of Pt/*CNT* in water in the potential range of -0.05 to 1.45 V vs. RHE. Beyond this potential window electrochemical water splitting, e.g., hydrogen and oxygen evolution become the predominant reactions leading to a rapid current increase that superimposes features arising from adsorption and desorption of

electrolyte ions. Anodic features in CV arise from oxidation processes whereas the cathodic part is caused by reduction reactions.

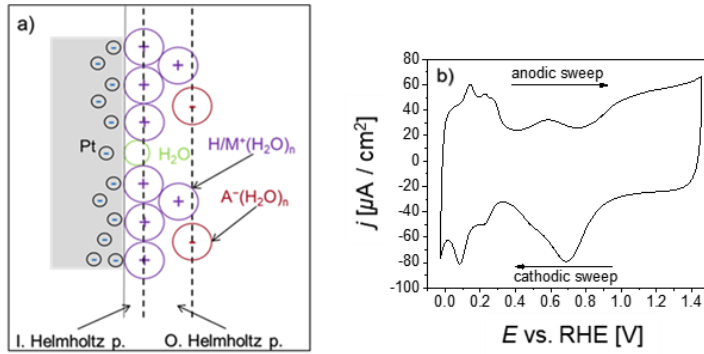


Figure 1: a) Schematic representation of electrochemical double-layer, and b) cyclic voltammogram on Pt/CNT in aqueous phase (pH 5). The M⁺ and A⁻ in a) denote metal cations and electrolyte anions.

At $E = 0.05\text{-}0.40$ V vs. RHE, underpotential deposited hydrogen on Pt is formed *via* reductive adsorption of hydronium ions from bulk electrolyte according to reversible *Volmer* reaction (Reaction 1).



Assuming the above reaction in quasi-equilibrium the free energy of H adsorption on Pt surface is calculated based on the (electro)chemical potentials of reactants and products (Equation 1-4).

$$\mu_{\text{el}} = -F\phi_{\text{Pt}} \quad (1)$$

$$\mu_{\text{H}^+} = \mu_{\text{H}^+}^\circ + RT \ln \frac{a_{\text{H}^+}}{a_{\text{H}^+}^\circ} + F\phi_{\text{aq}} \quad (2)$$

$$\mu_{\text{H}} = \mu_{\text{H}}^\circ + RT \ln \frac{\theta_{\text{H}}}{1 - \theta_{\text{H}}} + \mu_{\text{excess}} \quad (3)$$

$$\Delta G_{\text{upd}}^\circ + \mu_{\text{excess}} = -RT \ln \frac{\theta_{\text{H}}}{1 - \theta_{\text{H}}} - F\eta \quad (4)$$

The μ_{H^+} is the hydronium ion's chemical potential and μ_{H} is the chemical potential of adsorbed H on Pt surface. It should be noted that the electron is also treated as a reactant that has the chemical potential (μ_{el}) as its *Fermi* level according to *IUPAC* definition. The μ_{el} is determined by the electric potential on Pt, ϕ_{Pt} (Eq. 1). The μ_{H^+} consists of its standard chemical potential $\mu_{\text{H}^+}^\circ$, a thermodynamic activity (a_{H^+}) dependent term and an electrostatic potential energy term ($F\phi_{\text{aq}}$) that arises from the potential (ϕ_{aq}) in bulk electrolyte (Eq. 2). Here, F is *Faraday* constant. The μ_{H} comprises the standard chemical potential of H_{ads} (μ_{H}°), a term that

is determined by the H_{upd} coverage (θ_{H}) and an excess chemical potential term μ_{excess} accounting for the effect from non-ideality (Eq. 3). The variable η is the applied overpotential on RHE scale. The free energy of H_{upd} adsorption on metal surface comprises the standard *Gibbs* free energy change ($\Delta G_{\text{upd}}^{\circ}$) defined by θ_{H} and the excess potential (μ_{excess}) arising from the electric overpotential (Eq. 4). A detailed derivation of Equation 4 is given in Section 3 of supporting information.

2.2 Results

The free energy of H_{upd} adsorption on Pt is derived from CV and is plotted as function of external electric potential in Figure 2.

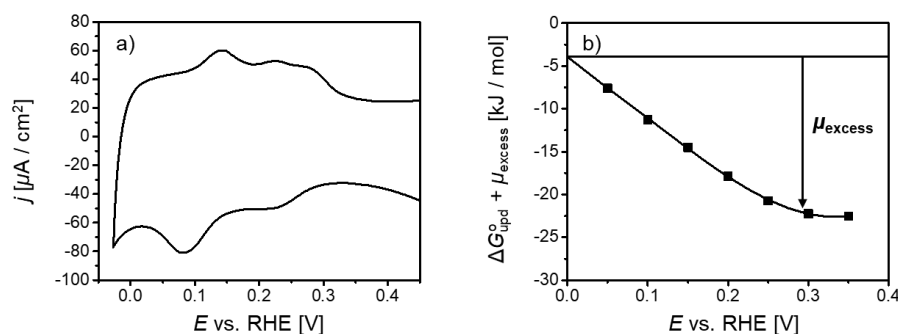


Figure 2: a) Features of H_{upd} on Pt/CNT in aqueous phase and b) free energy of H adsorption on electrode surface according to Equation 4.

The charge stored within *Helmholtz* layers due to H_{upd} formation is calculated *via* integrating the area below the anodic branch of H_{upd} region. Based on a monolayer charge of $210 \mu\text{C cm}^{-2}$ the coverage of Pt in water with underpotential deposited hydrogen can be determined (Figure 3).^[11] More detailed information are given in Section 2 of SI.

Figure S5b shows the temperature dependence of CV on Pt in the range of $T = 283\text{-}313 \text{ K}$. Increasing the temperature reduces the intensity of CV features and hence, θ_{H} of electrode surface.

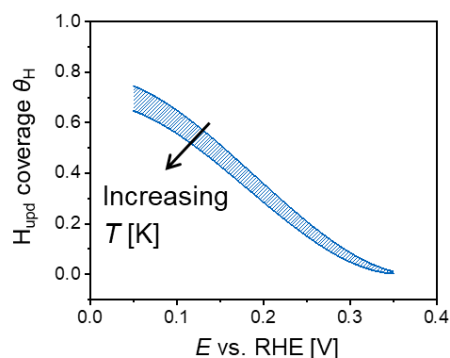


Figure 3: H_{upd} coverage of electrode surface with respect to external electric potential and electrolyte temperature.

At $E_{\text{RHE}} = 0.05\text{-}0.35 \text{ V}$, the H_{upd} coverage on Pt electrode decreases from 0.70 to 0.0 ML. The adsorption isotherm also indicates that θ_{H} does not exceed $2/3$ of a monolayer (ML). This phenomenon of a sub-monolayer coverage with underpotential deposited hydrogen has been observed by many researchers in the past.^[12] As will be discussed later this is because of a sudden breakdown of electrode potential due to displacement of water molecules upon adsorption of H_{upd} beyond $2/3$ ML. The remaining 33% of active surface sites can be covered *via* dissociative adsorption of H_2 from gas phase. If formed electrocatalytically at potentials

more negative than the onset potential of HER, this type of adsorbed H is sometimes referred to as overpotential deposited hydrogen (H_{Opd}).^[13]

If H_{Opd} on Pt behaves ideally, i.e., $\mu_{\text{excess}} = 0$ the value of Equation 4 would be $\Delta G_{\text{upd}}^{\circ}$ thus, being invariant with overpotential η . However, this is excluded by Figure 4 which plots the variation of $\Delta G_{\text{upd}}^{\circ} + \mu_{\text{excess}}$ with increasing external electric potential. The $\Delta G_{\text{upd}}^{\circ} + \mu_{\text{excess}}$ increases from -7 to -22 kJ mol^{-1} in the range of 0.05 to -0.35 V vs. RHE. The standard *Gibbs* free energy change ($\Delta G_{\text{upd}}^{\eta=0} = \Delta G_{\text{upd}}^{\circ}$) is obtained as the y-intercept in Fig. 4a *via* extrapolating the $\Delta G_{\text{upd}}^{\circ} + \mu_{\text{excess}}$ to $\eta = 0$ V and is used to determine the adsorption enthalpy and entropy at zero overpotential. Assuming the excess potential μ_{excess} to be a function of applied electric potential it has to be zero at zero overpotential. Figure 4b plots the μ_{excess} , that is the difference between the free energy of H adsorption at a given external electric potential and its value at $\eta = 0$ V ($\Delta G_{\text{upd}}^{\eta=0}$) with respect to applied overpotential. All plots of μ_{excess} overlap and raise from -5 to -20 kJ mol^{-1} with increasing anodic overpotential, demonstrating that μ_{excess} hardly changes with temperature ($\partial\mu/\partial T = 0$). Therefore, the entropic contribution to μ_{excess} is zero ($\Delta S_{\text{excess}} = 0$), that μ_{excess} has only an enthalpic term (Equations 5&6). This rules out the option of μ_{excess} being a function of H_{Opd} coverage, as we explain next.

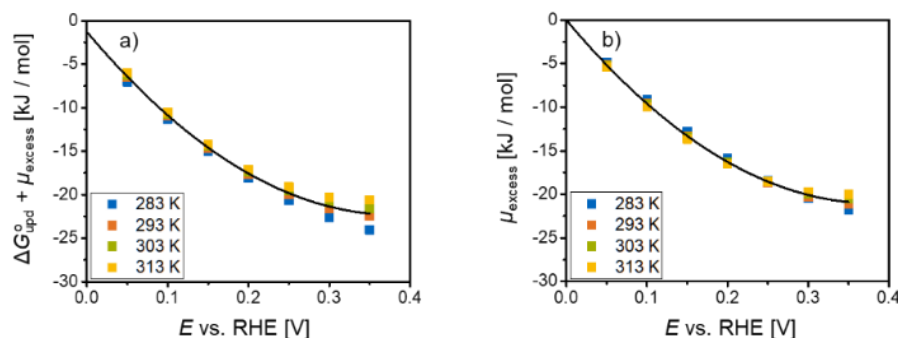


Figure 4: a) Development of $\Delta G_{\text{upd}}^{\circ} + \mu_{\text{excess}}$ and b) change of μ_{excess} with external electric potential in the range of $T = 283\text{-}313$ K.

$$\frac{\partial\mu_{\text{excess}}}{\partial T} = 0 = \frac{\partial}{\partial T}(\Delta H_{\text{excess}} - T\Delta S_{\text{excess}}) = -\Delta S_{\text{excess}} \quad (5)$$

$$\mu_{\text{excess}} = \Delta H_{\text{excess}} \quad (6)$$

If μ_{excess} would be a function of H_{Opd} coverage it should have an entropic term changing ΔG_{upd} and ΔS_{upd} with increasing overpotential. *Iglesia* and coworker found an increase in entropy loss upon liquid phase H adsorption on Pt from -20 to -60 $\text{J mol}^{-1} \text{K}^{-1}$ in the coverage range of

20-80%.^[14] In contrast, *Gómez* et al. calculated adsorption entropies of H on different Pt single crystals immersed in water to be constant over the whole H_{upd} range.^[15] Furthermore, if μ_{excess} would be a function of H_{upd} coverage the result in Figure 4 would be interpreted to change $\Delta G_{\text{upd}}^{\circ} + \mu_{\text{excess}}$ by about 25 kJ mol^{-1} in the range of $\theta_{\text{H}} = 0-0.7 \text{ ML}$. As the excess potential only comprises an enthalpic term, the adsorption enthalpy of H_{upd} on Pt would change by roughly 25 kJ mol^{-1} , as well. However, this would contradict to reported H adsorption enthalpies on Pt, e.g., by *Ertl*, *Norton* or *Iglesia* that only change by $5-10 \text{ kJ mol}^{-1}$ in the investigated coverage range.^[14, 16]

The adsorption enthalpy and entropy at OCP, i.e., zero overpotential $\Delta H_{\text{upd}}^{\eta=0}$ and $\Delta S_{\text{upd}}^{\eta=0}$ are calculated *via* linearizing *Gibbs-Helmholtz* equation and plotting $\Delta G_{\text{upd}}^{\circ} / T$ over $1/T$ (Equation 7, Figure 5a). The $\Delta H_{\text{upd}}^{\eta=0}$ and $\Delta S_{\text{upd}}^{\eta=0}$ were $-16.8 \text{ kJ mol}^{-1}$ and $-52 \text{ J mol}^{-1} \text{ K}^{-1}$, respectively. When applying an overpotential, the adsorption entropy should in principle have $\Delta S_{\text{upd}}^{\eta=0}$ and ΔS_{excess} terms (Equation 8a). However, because the ΔS_{excess} is zero the adsorption entropy for H_{upd} on Pt in water stays invariant of $-52 \text{ J mol}^{-1} \text{ K}^{-1}$. This is in good agreement with data that have been published by *Gómez* et al. who determined the entropy of hydrogen adsorption on different Pt facets in aqueous phase:^[15] $-48 \text{ J mol}^{-1} \text{ K}^{-1}$ on Pt(111), $-56 \text{ J mol}^{-1} \text{ K}^{-1}$ on Pt(100) and in the range of -55 to $-70 \text{ J mol}^{-1} \text{ K}^{-1}$ on Pt(110). *Iglesia* and coworker found an entropy of liquid phase hydrogen adsorption on Pt of $-45 \text{ J mol}^{-1} \text{ K}^{-1}$.^[14]

$$\frac{\Delta G_{\text{upd}}^{\eta=0}}{T} = \frac{1}{T} \left(\Delta H_{\text{upd}}^{\eta=0} - T \Delta S_{\text{upd}}^{\eta=0} \right) = \frac{\Delta H_{\text{upd}}^{\eta=0}}{T} - \Delta S_{\text{upd}}^{\eta=0} \quad (7)$$

$$\Delta S_{\text{upd}}(\eta) = \Delta S_{\text{upd}}^{\eta=0} + \Delta S_{\text{excess}} = \Delta S_{\text{upd}}^{\eta=0} \quad (8a)$$

$$\Delta H_{\text{upd}}(\eta) = \Delta H_{\text{upd}}^{\eta=0} + \Delta H_{\text{excess}}(\eta) \quad (8b)$$

The enthalpy of H adsorption on Pt in aqueous phase is a function of the applied overpotential η that consists of $\Delta H_{\text{upd}}^{\eta=0}$ and ΔH_{excess} terms (Equation 8b). Note that we have shown ΔH_{excess} equals μ_{excess} . With the obtained values of $\Delta H_{\text{upd}}^{\eta=0}$ and ΔH_{excess} the adsorption enthalpy (ΔH_{upd}) is plotted with respect to η in Figure 5b. At $\eta = 0.35-0.05 \text{ V}$, the ΔH_{upd} decreases from -38 to -22 kJ mol^{-1} . *Marković* et al. calculated a change of H adsorption heat on Pt(111) in aqueous phase from -42 to -23 kJ mol^{-1} at an overpotential of $0.33-0.07 \text{ V}$.^[17] In reports of *Gómez* and coworker, the ΔH_{upd} decreases from -40 to -25 kJ mol^{-1} in the same potential range.^[15]

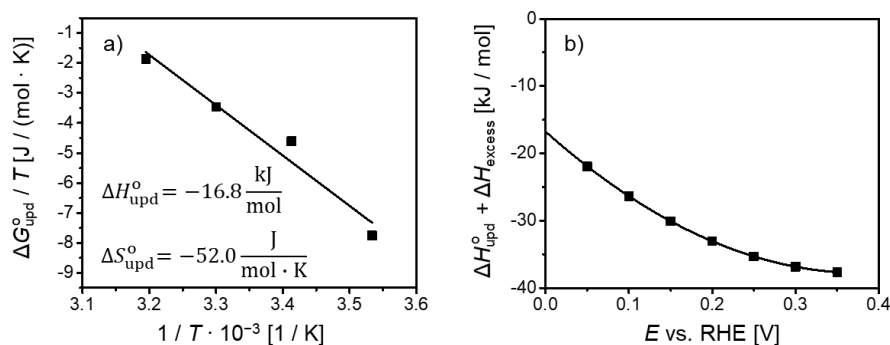


Figure 5: a) Plot of linearized *Gibbs-Helmholtz* equation, and b) development of H_{upd} adsorption heat on Pt in water with external electric potential.

After showing the H_{upd} adsorption on Pt changes with external electric potential, we next investigate how it is influenced by solution pH. Using the same CV method, the coverage of underpotential deposited hydrogen on Pt at different pH were measured (Figure S6). Following the same data treatment as previously developed, the adsorption enthalpy ΔH_{upd} and free energy $\Delta G_{\text{upd}}^{\circ} + \mu_{\text{excess}}$ are shown as a function of overpotential in Figure 6. The detailed data treatment is given in Section 4 of supporting information. The ΔH_{upd} and $\Delta G_{\text{upd}}^{\circ} + \mu_{\text{excess}}$ raise with increasing positive overpotential. In addition, decreasing the hydronium ion concentration in bulk electrolyte, i.e., increasing pH shifts values more negative, indicating a strengthened Pt-H bond (Figure 6). These findings are in line with results from *Sheng* and *Nash* who found H_{upd} peaks on polycrystalline Pt to be shifted towards more anodic overpotential at high pH, correlating this to an increased hydrogen binding energy.^[1, 18] Quantum Mechanics Molecular Dynamics (QMMD) performed by *Goddard* et al. also revealed a higher binding strength of H towards electrode surface in less acidic electrolytes.^[19]

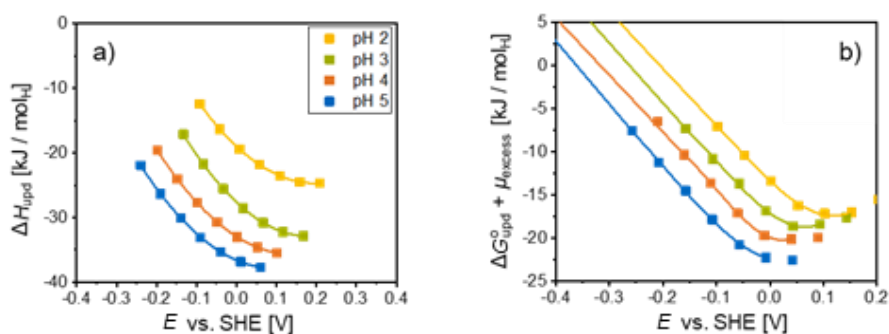


Figure 6: a) Enthalpy and b) free energy of H_{upd} adsorption on Pt as function of electric potential and electrolyte pH.

Hydrogen evolution reaction (HER) is facilitated in acidic electrolytes compared to alkaline solutions. Extrapolating the free energy of H_{upd} adsorption in Figure 6b to zero allows for determining the onset overpotential ($E_{\text{H}_2/\text{H}^+}^{\circ}$) of HER. The increase of ΔH_{upd} with increasing

electrolyte pH results in a more negative $E_{\text{H}_2/\text{H}^+}^{\circ}$, shifting from -0.008 to -0.015 V vs. RHE at pH 2-5 (Figure 7).

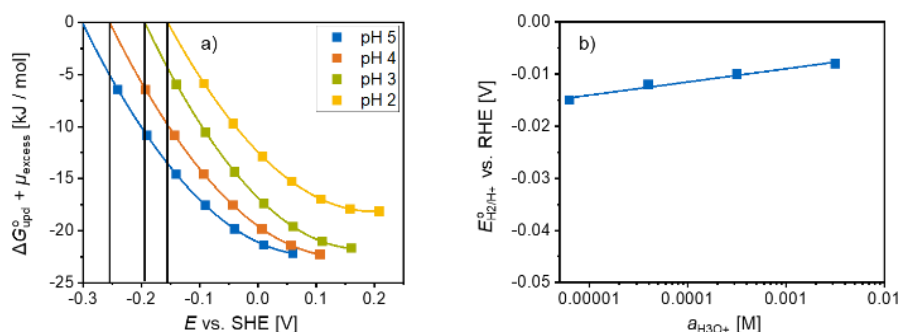


Figure 7: a) Extrapolated plots of $\Delta G_{\text{upd}}^{\circ} + \mu_{\text{excess}}$ vs. E_{RHE} and b) HER onset overpotential $E_{\text{H}_2/\text{H}^+}^{\circ}$ as function of solution pH.

The effect of pH on hydrogen binding and HER is corroborated by *Tafel* evaluation of linear polarization measurements (SI Section 5). With lowering electrolyte acidity, the $E_{\text{H}_2/\text{H}^+}^{\circ}$ is shifted to more negative values on RHE scale, revealing almost the same trend as determined by extrapolating the free energy of H_{upd} adsorption on Pt surface (Figure 8). This trend is in accordance with literature results from *Koper et al.* who found the onset overpotential for HER to be gradually shifted to more negative values when changing the electrolyte pH from 1 to 13.^[20] *Chan* and coworker provided a similar trend based on DFT calculations and the assumption of a change from acidic *Volmer/Heyrovsky* to alkaline *Volmer/Heyrovsky* steps at an increasing solution pH.^[21] According to their interpretation the proton donor for HER changes from hydronium ions to water molecules in alkaline media making kinetics of HER less favorable.

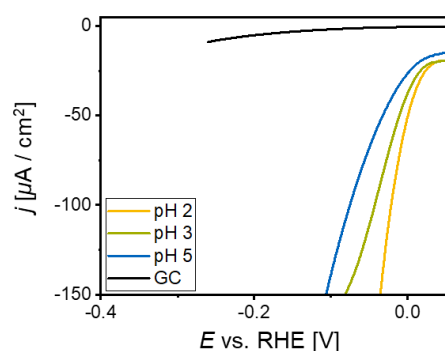


Figure 8: Linear polarization (LP) curves of HER on Pt/CNT in aqueous electrolyte at different pH.

2.3 Discussion

2.3.1 Influence of external electric potential on Pt *Fermi* level

When H is adsorbed on electrode surface a Pt-H bond is formed. For a single Pt atom, the bond of Pt-H is formed by combination of bonding and antibonding states, which result from hybridization of its 5d orbital with 1s orbital of H atom.^[22] For Pt metal, the 5d atomic orbitals of all Pt atoms overlap and form the 5d band.^[5] This 5d band hybridizes with 1s orbital of H atom to form bonding (valence band) and antibonding states (conduction band), in which a band gap exists between antibonding and bonding states. In molecular orbital theory, a chemical bond has bonding and antibonding states. The more filling of antibonding state by electrons, the weaker the strength of a chemical bond. For the case of H_{upd} on electrode surface, the more probabilities of antibonding state being occupied by electrons, the weaker the strength of Pt-H bond. The electron energy level can be described by the *Fermi* level of Pt-H bond. The electron densities in metal or semiconductor bands are related to the corresponding *Fermi* levels that could be determined by the corresponding work function.

As shown in Figure 9, the filling of antibonding state of Pt-H depends on the difference of the potential energy of antibonding state (E^*) and the *Fermi* level of Pt/CNT (E_F), the two of which are sometimes assumed to level up at the same energy.^[23] The smaller the difference between these two the higher the probability of antibonding state being occupied by electrons, which leads to a weakening of Pt-H bond. On the contrary, a large gap between E^* and E_F strengthens Pt-H bond.

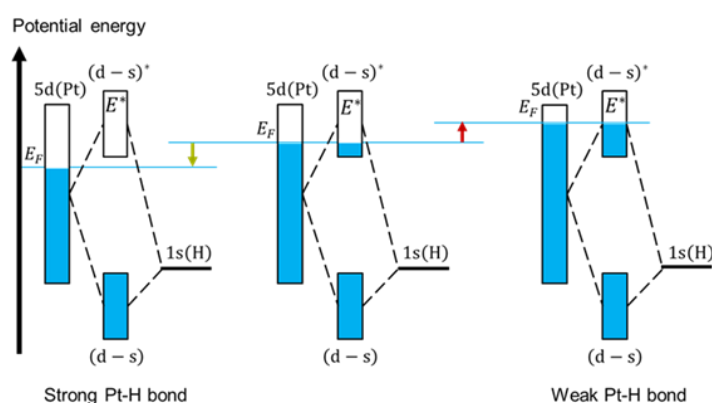


Figure 9. Schematic illustration of the difference between the potential energy of Pt-H antibonding state and Pt *Fermi* level. At large difference Pt-H bond is strengthened; at small difference it is weakened.

The system of reaction in this work involves Pt electrode, water solution, hydronium ions and hydrogen formed from HER with external electric potential. The discussion would follow three steps, (1) immersion of Pt electrode into electrolyte containing H_2/H^+ redox couple, (2) formation of adsorbed H according to *Volmer* equilibrium and (3) modulating *Fermi* level of Pt with external electric potential.

In the first step, Pt electrode is immersed into water in the presence of hydronium ion and hydrogen. Several studies have found that the work function of Pt would be lowered in the presence of condensed water. When Pt is immersed in water its work function is reduced to 2.12 eV according to *Musumeci et al.*^[24] *Yoon* reported that in bulk liquid water, the work function of Pt is reduced by 1.2 eV.^[25] But all this research only focused on the influence of water in the absence of redox couple such as hydronium ion and hydrogen. According to *Girault* and coworker the *Fermi* level of a virtual electron in solution ($E_{F,\text{electrolyte}}$) can be defined as superposition between an ideal term and a non-ideal part. The ideal part being the difference between the chemical potentials of reduced and oxidized species of that redox couple (E_{redox}) and the non-ideality being an outer potential arising from plane solvent (ϕ_{bulk}) (Equation 9).^[26]

$$E_{F,\text{electrolyte}} = E_{\text{redox}} + \phi_{\text{bulk}} \quad (9)$$

Depending on the activity of protons in solution, the chemical potential of the oxidized species is altered, giving rise to a change of the work to bring an electron at rest in vacuum to the solution to take part in the redox reaction. The work function and hence, the *Fermi* level of that virtual electron in solution is shifted. In our case, reduced and oxidized species of the electrolyte are Pt-H and ($\text{Pt}^* + \text{H}^+ + \text{e}^-$) in analogy to bonding and antibonding state of Pt-H bond. The redox potential of H_2/H^+ at pH 5 is 4.16 eV, lower than that (5.60 eV) of Pt electrode leading to electrons flowing from the electrolyte redox couple towards Pt electrode. Depending on electrolyte pH, Pt work function decreases to up to 4.91 eV, which is in good agreement with the value of 5.00 eV that was found by *Neugebauer et al.* from density functional theory molecular dynamics simulations.^[23] At the same time, OCP on Pt electrode decreases from 0.695 V_{RHE} at pH 2 to 0.615 V_{RHE} at pH 5 indicating that the remaining gap between Pt *Fermi* level and electrolyte redox couple increases with lowering electrolyte acidity (Figure 10).

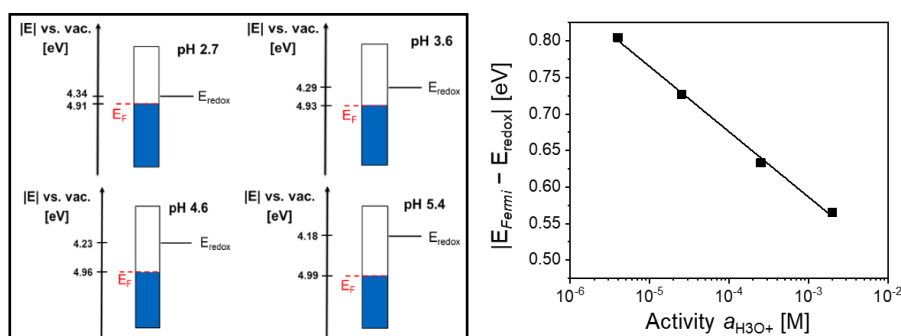


Figure 10: Increase of electrode work function after contact of Pt *Fermi* level with electrolyte redox couple and remaining difference with respect to electrolyte acidity.

In the second step, Pt-H bond is generated by reductive adsorption of H^+ from the electrolyte solution onto Pt surface. At 0 V vs. SHE only the reduced state of electrolyte redox couple is filled with electrons and the *Volmer* equilibrium lies almost completely on the side of Pt-H,

giving rise to a large adsorption heat of H_{upd} on Pt. *Nørskov* and coworker have reported that Pt-H bond has bonding and antibonding states, with *Fermi* level of Pt-H lying close to antibonding state.^[4] As shown in Fig. 10, the *Fermi* level of Pt should be around 4.90 eV.

When adding an external electric potential to Pt electrode, the equilibrium junction formed in the first two steps between Pt-H and electrolyte would be broken with the work function of Pt-H being altered and of electrolyte remaining constant in the reaction time. When a more negative (compared to $E_{\text{SHE}} = 0$ V) potential is added to Pt electrode, the work function of Pt would decrease further, meaning an increase of *Fermi* level in Pt electrode. As a result, the electron density within the oxidized state of H_2/H^+ gradually increases and the reverse reaction of *Volmer* equilibrium, the oxidative desorption of Pt-H, gets more pronounced until the reaction is in complete equilibrium at $E = 0$ V vs. RHE. Consequently, at a more negative external electric potential the heat release upon Pt-H formation is gradually compensated by its oxidative decomposition. In analogy, with increasing Pt *Fermi* level the filling of antibonding state of Pt-H bond is rising, leading to a weak binding of H_{upd} on Pt.

Considering the maximum H_{upd} coverage of $2/3$ ML, *Neugebauer* and coworker showed that this is caused by the replacement of water molecules from Pt electrode surface.^[23] As soon as the coverage exceeds $2/3$ ML the metal surface can essentially be considered water free, again. This resembles the situation under vacuum where the work function of Pt is 5.60 eV. Hence, an electrocatalytic formation of underpotential deposited hydrogen beyond 66% coverage of Pt surface sites would immediately increase the electrode potential by 0.6 eV. So, $2/3$ ML of H_{upd} mark the threshold coverage for onset of hydrogen evolution reaction and formation of up to $1/3$ ML of overpotential deposited hydrogen on sites that had previously been covered by H_2O (Figure 11).

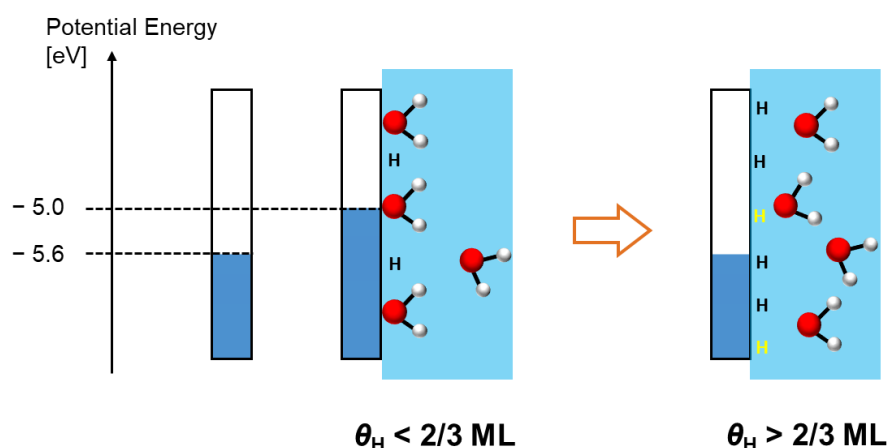


Figure 11: Displacement of water molecules upon H_{upd} adsorption on Pt electrode (black), Pt *Fermi* level drop and gas phase H adsorption (yellow) on previously H_2O covered sites beyond $2/3$ ML of H_{upd} .

2.3.2 Influence of electrolyte pH on ΔH_{upd} on Pt

We hypothesize that the impact of pH on adsorption enthalpy can be explained by the work that has to be paid for removing the electrochemical double-layer from electrode surface and that is determined by the electrostatic energy E_e stored within EDL (Equation 10, Figure 12). In a previous work, we have shown that water molecules are shifted away by 0.5 Å from Pt(111) surface upon adsorption of H.^[27]

$$W = E_e \cdot \Delta d \cdot n_{\text{H}^+(\text{H}_2\text{O})_n}^2 \quad (10a)$$

$$E_e = \frac{q_e^2}{2\epsilon S} \quad (10b)$$

The Δd is the distance that EDL has to be moved away from Pt surface. The $n_{\text{H}^+(\text{H}_2\text{O})_n}$ stands for the number of hydrated hydronium ions at the electrode surface. The ϵ is the electrolyte permittivity and S is the Pt surface area. The q_e is the charge stored within EDL.

With lowering pH, the number of hydrated hydronium ions that are accumulated close to electrode surface increases. Hence, the E_e of EDL and the work that is necessary for removing EDL from Pt surface and that partly compensates ΔH_{upd} increase with increasing electrolyte acidity.

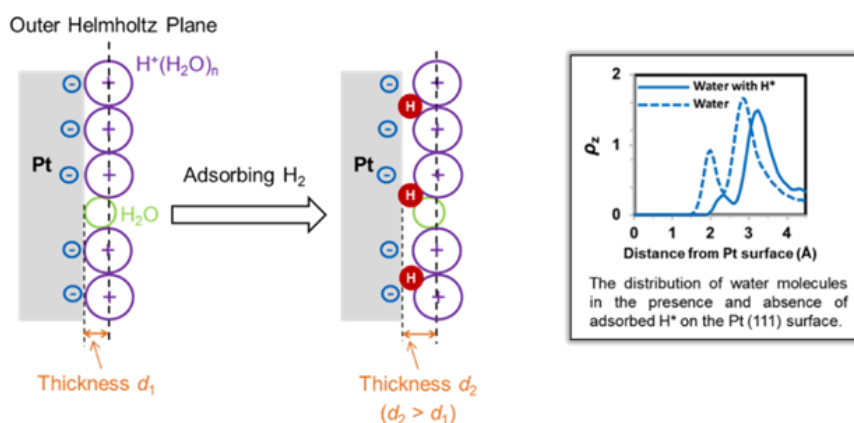


Figure 12: Displacement of EDL from electrode surface upon adsorption of H on Pt (left), and distance of first water layer from electrode surface in presence and absence of adsorbed H calculated via DFT based AIMD simulations according to Yang et al.^[27]

Sheng as well as Nash correlated the effect of electrolyte pH on CV curves recorded on Pt to an increased hydrogen binding energy (HBE) on Pt in less acidic electrolytes (Fig. S6a).^[1, 18] However, Janik et al. attributed this pH induced shift of H_{upd} features to co-adsorption of hydroxide ions and alkali metal cations.^[28] In their view, co-adsorption of OH^- in the H_{upd} region is more favored at low pH, disfavoring H adsorption in highly acidic electrolytes. With increasing pH however, they hypothesize that adsorption of cations gets more dominant repelling OH^- from electrode surface and making binding of underpotential deposited hydrogen

more feasible. According to QMMD from *Goddard* and coworker the increased binding strength of H_{upd} at high pH is due to weakened water adsorption in alkaline media.^[19] As they showed Pt electrode surface got charged more negative by 0.75 V when changing the pH from 0.2 to 12.8, increasing its hydrophobic character and hindering water adsorption.

The generally lower hydrogen adsorption entropy in liquid phase compared to gas phase, which is around $-125 \text{ J mol}^{-1} \text{ K}^{-1}$, might be explained by water molecules gaining entropy upon being displaced from electrode surface upon H_{upd} formation.^[27]

2.4 Conclusion

Cyclic voltammetry is a facile technic for investigating energetic properties of Pt electrodes immersed in aqueous electrolytes and how these are influenced by application of an external electric potential. A typical CV curve acts like a fingerprint of the electrochemical double-layer. On the scale of applied potential, it reveals the electrolyte species that are accumulated within the interfacial layer between electrode and electrolyte and that are electrochemically adsorbed on the metal surface.

The potential region between 0.05 and 0.40 V vs. RHE, that is the H_{upd} region reflects the coverage of electrode surface with underpotential deposited hydrogen. The temperature dependence of H_{upd} peaks allows for calculating the adsorption heat of H_{upd} on Pt in aqueous phase that can be altered by variation of external electric potential and electrolyte pH. The ΔH_{upd} increases from -22 to -38 kJ mol^{-1} in the potential range of 0.05 to 0.35 V vs. RHE. The entropy of H_{upd} adsorption stays constant at around -55 $\text{J mol}^{-1} \text{K}^{-1}$. Increasing the electrolyte acidity from pH 5 to 2 reduces the adsorption heat at OCP from -17 to -9 kJ mol^{-1} . The adsorption entropy is changed from -52 to -22 $\text{J mol}^{-1} \text{K}^{-1}$.

The observed trend for $\Delta H_{\text{upd}}^{\circ}$ is explained by the influence of external electric potential on electrode *Fermi* level and the semiconductor or metallic behavior of Pt-H bond. An equilibrium junction between Pt-H and electrolyte is formed when H adsorbs on Pt electrode immersed into water. This equilibrium junction would be broken when Pt electrode is added with more negative or positive external potential relative to OCP. At rising anodic potential, the *Fermi* level of Pt electrode is decreased leading to less filling of Pt-H antibonding state and a strong Pt-H bond. In contrast, a rising cathodic potential increases Pt *Fermi* level, giving more filling of Pt-H antibonding state by electrons. The Pt-H bond is weakened.

The change of $\Delta H_{\text{upd}}^{\circ}$ with electrolyte pH is explained *via* the work that has to be paid for partly displacing EDL from electrode surface. Decreasing the solution pH leads to a pronounced accumulation of H_3O^+ within EDL and thus, the work that partly compensates $\Delta H_{\text{upd}}^{\circ}$ increases.

These investigations on underpotential deposited hydrogen adsorption on Pt in aqueous phase can help to understand the effect of electrode potential and electrolyte composition on catalyst performance in HER and electrocatalytic hydrogenation of organic molecules.

2.5 Supporting information

2.5.1 Experimental

Materials

Graphitized Multiwalled Carbon Nanotubes (GMWCNT, ≥ 99.9 wt%) with an outer diameter of 20-30 nm, an inner diameter of 5-10 nm and a length of 10-30 μm , in the following referred to as *CNT*, were purchased from *Cheap Tubes Inc.* Temperature programmed desorption (TPD) of ammonia and pyridine revealed a low amount of acid surface sites on *CNT* of only 75.6 and 72.2 $\mu\text{mol} / \text{g}_{\text{CNT}}$, respectively (Figure S1). MS-signals during NH_3 -TPD (500 $^\circ\text{C}$, 10 K min^{-1} , 60 min) were recorded with a *PrismaTM* mass spectrometer from *Pfeiffer Vacuum* and were normalized to H-MFI with a concentration of acid surface sites of 400 $\mu\text{mol} / \text{g}_{\text{H-MFI}}$. Pyridine-TPD (600 $^\circ\text{C}$, 5 K min^{-1} , 30 min, 50 mL min^{-1} N_2) was performed on a TGA-MS setup with a *SENSYS evo TG-DSC* from *SETARAM Instrumentation* and an *OmniStarTM* mass spectrometer from *Pfeiffer Vacuum*.

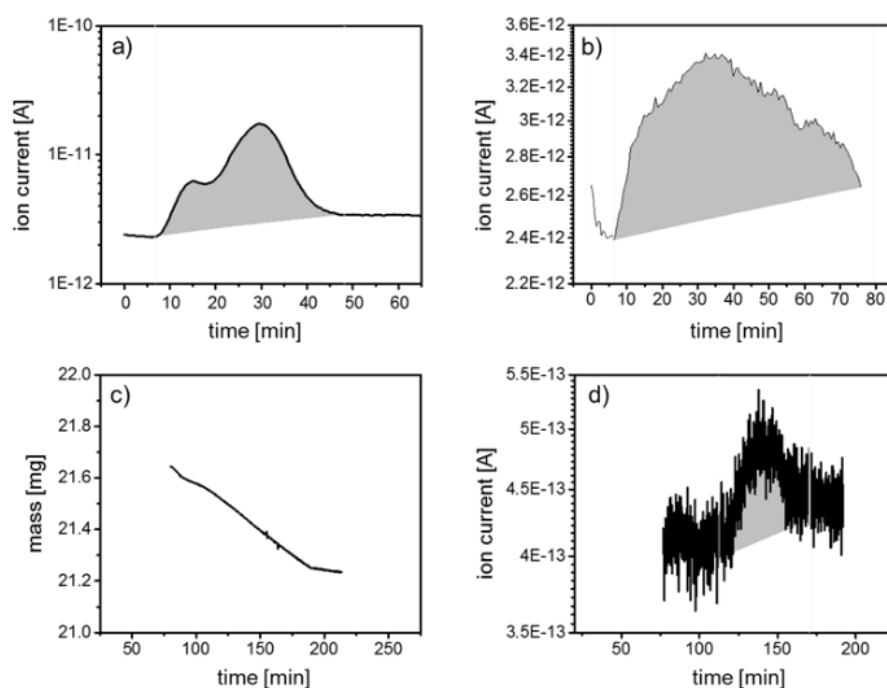


Figure S1: **a)** NH_3 -TPD signal of H-MFI, **b)** NH_3 -TPD signal of *CNT*, **c-d)** TGA- and pyridine MS-signal during pyridine-TPD on *CNT*.

Chloroplatinic acid hexahydrate ($\text{H}_2\text{PtCl}_6 \cdot 6\text{H}_2\text{O}$, $\geq 37.5\%$ Pt basis) as well as ethanol ($\geq 99.8\%$) were bought from *Sigma-Aldrich*. Sodium phosphate monobasic (NaH_2PO_4 , $\geq 99.0\%$), sodium phosphate dibasic dihydrate ($\text{Na}_2\text{HPO}_4 \cdot 2\text{H}_2\text{O}$ $\geq 98.0\%$) and phosphoric acid (H_3PO_4 , $\geq 99.0\%$) were also purchased from *Sigma-Aldrich*. Aqueous buffer solutions (0.5 M) were prepared by dissolving the required amounts of salts and phosphoric acid in 1 L ultrapure water with a resistivity of 18.2 $\text{M}\Omega$ from a *Purist* system supplied by *Rephile* (Table S1). All chemicals were used without further purification. Helium gas (He, 99.996 Vol%) for purging

the electrolyte solution and hydrogen gas (H_2 , 99.999 Vol%) for electrode calibration were both from *Westfalen*.

Table S1: Amount of $\text{Na}_2\text{HPO}_4 \cdot 2\text{H}_2\text{O}$, NaH_2PO_4 , and H_3PO_4 dissolved in 1.0 L ultrapure H_2O for preparation of buffered electrolytes.

pH	$m(\text{Na}_2\text{HPO}_4 \cdot 2\text{H}_2\text{O})$ [g]	$m(\text{NaH}_2\text{PO}_4)$ [g]	$m(\text{H}_3\text{PO}_4)$ [g]
2.4	---	30.0	24.5
3.1	---	54.0	4.90
4.2	---	59.4	0.49
4.9	1.34	59.1	---

Catalyst synthesis

The *CNT* supported Pt nanoparticle catalyst (*Pt/CNT*) was prepared by a standard impregnation method followed by reduction in H_2 . In specific, the desired amount of $\text{H}_2\text{PtCl}_6 \cdot 6\text{H}_2\text{O}$ for a 5 wt% *Pt/CNT* catalyst (0.14 g) was dissolved in 200 mL ethanol. After addition of 1.00 g *CNT* the suspension was stirred and sonicated for 15 minutes. The alternative treatment of stirring and sonication was repeated three times. The solvent was removed by evaporation and the solid was dried at 60 °C, overnight. The final catalyst was received after reduction at 250 °C (0.5 K min^{-1}) for 3 hours in H_2 flow (100 mL min^{-1}). Metal particle size, metal dispersion and external surface area of the final catalyst were determined *via* H_2 chemisorption and N_2 physisorption measurements using a *Surfer* station from *Thermo Fischer Scientific* and by transmission electron microscopy (TEM) (Figure S2). The exact metal loading of the catalyst was determined by atomic absorption spectroscopy (AAS) using an *iCE 3000 SERIES AA Spectrometer* from *Thermo Fisher Scientific*. The results are summarized in Table S2.

Table S2: Properties of 5 wt% *Pt/CNT* catalyst.

Metal concentration c_{Pt} [wt%]	4.6
Particle size d_{P} (TEM) [nm]	4.3
Particle size d_{P} (H_2 chemisorption) [nm]	4.3
Metal dispersion (TEM) [%]	23
Metal dispersion (H_2 chemisorption) [%]	25.6
External surface area [$\text{m}^2 / \text{g}_{\text{CNT}}$]	120

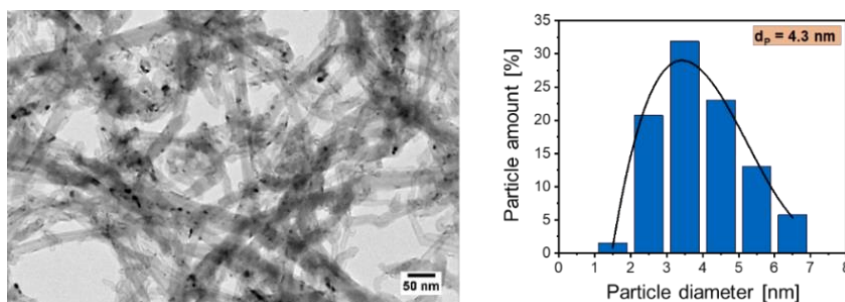


Figure S2: TEM image of 5 wt% Pt/CNT (left) and statistical evaluation of particle size (right).

The catalyst dispersion according to TEM was calculated based on the determined mean particle diameter d_p using Equations S1-S2.^[29]

$$d_p = \frac{\sum_{i=1}^n d_i^3}{\sum_{i=1}^n d_i^2} \quad (\text{S1})$$

$$D = \frac{g \cdot V_{\text{Pt}}}{d_p \cdot S} \cdot 100 \quad (\text{S2})$$

The d_i are the particle diameters measured from TEM images. The g refers to the particle shape correction factor that is 6 for spherical particles. The V_{Pt} refers to the volume per Pt atom calculated with a mean atomic radius of 1.5 Å. The S is the Pt average transversal section, which has a value of 8.9 Å².

Cyclic voltammetry and linear polarization

Cyclic voltammetry (CV) and linear polarization (LP) measurements were performed in a three-electrode setup using a *Modulated Speed Rotator* (MSR) rotating disk electrode (RDE) and an RDE glass cell with water jacket both from *PINE research*. The electric potential was controlled with an *SP-300* potentiostat from *BioLogic*. A glassy carbon RDE tip (5.0 mm OD) coated with catalyst (0.3 mg) was used as working electrode (WE). For catalyst coating 2.0 mg of Pt/CNT was suspended in 200 μL ethanol and sonicated for 30 min. 30 μL of suspension were transferred onto glassy carbon disk and dried before immersion into electrolyte. A platinum wire served as counter electrode (CE) and an Ag/AgCl electrode was used as reference electrode (RE). The RDE tip, CE and RE, were purchased from *PINE research*. Before each experiment, the Ag/AgCl RE was immersed in H₂ saturated ($p(\text{H}_2) = 1$ bar) 0.5 M phosphate buffer and calibrated against a platinum wire to adjust the measured external potentials from the Ag/AgCl scale to the reversible hydrogen electrode (RHE) scale. The RDE glass cell was immersed into a potassium permanganate solution prior to use in CV/LP to remove any organic contaminations. Before filling with electrolyte, it was flushed with a 3% H₂O₂ / 1 M H₂SO₄

solution followed by rinsing with ultrapure water. The WE, CE and RE were immersed in 100 mL 0.5 M phosphate buffer and the temperature (283-313 K) was adjusted with a *FC 600s* chiller from *Julabo*. During CV and LP, the RDE tip was rotated at 400 rpm and the electric potential was cycled/scanned between -0.05 and 1.45 V vs. RHE and -0.15 and 0.40 V vs. RHE, respectively with a scanning rate of 50 mV s^{-1} . Stable CV curves were reached after the tenth cycle. A He-stream of 10 mL min^{-1} through the electrolyte was maintained throughout all experiments to assure for complete removal of excess H_2 and O_2 from the electrolyte.

The current density measured during CV/LP was calculated by normalizing the measured current to the Pt surface area using the metal dispersion according to Equations S3-S4.

$$n_{\text{Pt-Surf.}} = \frac{m_{\text{Cat}} \cdot c_{\text{Pt}} \cdot D}{M_{\text{Pt}}} \quad (\text{S3})$$

$$A_{\text{Pt-Surf.}} = \frac{n_{\text{Pt-Surf.}}}{2 \cdot 10^{-9}} \quad (\text{S4})$$

The m_{Cat} refers to the mass of catalyst, c_{Pt} refers to the metal concentration of the catalyst, D is its metal dispersion and M_{Pt} is the molecular weight of Pt.

2.5.2 Thermodynamic quantification of CV curve

Cyclic voltammetry is a powerful technique for investigating redox processes that are accompanied or driven by heterogeneous electron-transfer steps.

Taking the *Volmer* reaction ($\text{Pt}^* + \text{H}^+ + \text{e}^- \longrightarrow \text{Pt-H}$) as an example, at $E_{\text{RHE}} = 0.40 \text{ V}$, there is only the double-layer charging current flowing and the protons near the electrode surface are uniformly distributed. When the potential is swept to more negative values the current increases due to *Volmer* reaction and the establishment of a new equilibrium near the electrode surface. After reaching its peak value the current starts to drop. This behavior can be explained by the electron-transfer being much faster than the potential sweep rate. Hence, the concentration of protons near the electrode surface will gradually decline and thus, the current will start to drop (Figure S3).^[30]

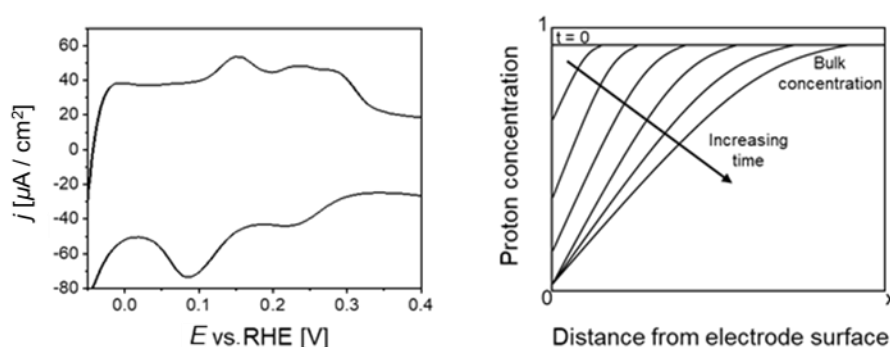


Figure S3: CV peaks associated to *Volmer* reaction (left) and development of proton concentration near electrode surface over time (right).

As Figure 1a implies the electrochemical double-layer (EDL) behaves like a capacitor with the electrode surface and electrolyte representing its negative and positive plates and the layer of adsorbed water molecules within inner *Helmholtz* plane acting as molecular dielectric.^[31] At a given external electric potential E_{RHE} , the ratio of measured current density j to scanning rate ν equals the capacity of EDL (Equation S5).

$$C_{\text{DL}} = \frac{j}{\nu} = \frac{Q_{\text{DL}}}{E_{\text{RHE}}} \quad (\text{S5})$$

The measured CV curve represents the charge Q_{DL} that is stored in between the plates of the capacitor. Usually, this charge is separated into two contributions. The inner *Helmholtz* layer mainly comprises water molecules that are adsorbed on the negatively charged electrode with their dipole moments directing towards bulk electrolyte.^[32] This accumulation of dipole moments within EDL causes a minimum charge stored in between the plates of the capacitor, that is the double-layer capacitance and that is $350 \mu\text{F cm}^{-2}$ in our case.^[33] In CV, this double-layer capacitance is represented by the area between the constant minima of anodic and cathodic branches of CV curve (Figure S4). Depending on external electric potential the CV

curve shows additional features that lie on top of the capacitive area.^[34] This pseudo-capacitance arises from additional accumulation of charge within the double-layer, which is caused by electrochemical adsorption of electrolyte species on the electrode surface.^[35] The amount of adsorbed species and hence, the electrode surface coverage are calculated *via* integrating the on-top area.

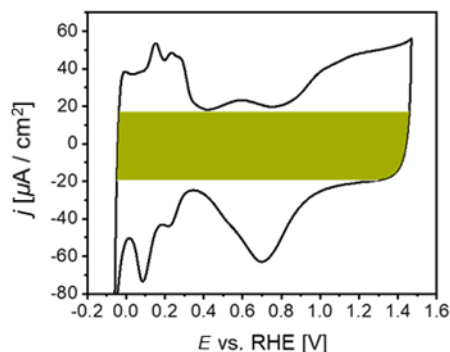
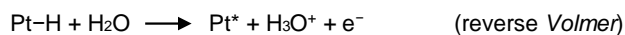


Figure S4: Cyclic voltammogram of Pt/CNT in aqueous electrolyte with double-layer capacitance marked in green.

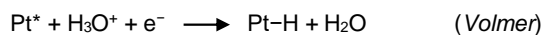
The CV curve in Figure 1b can be divided into three sections being (I) the hydrogen region up to a potential of $E = 0.40$ V vs. RHE, (II) the potential region between 0.40 and 0.80 V vs. RHE where adsorption of electrolyte anions takes place and (III) the oxide region at potentials larger than $E = 0.80$ V vs. RHE. Each section can be expressed *via* characteristic equations of potential-driven adsorption and desorption of electrolyte species on Pt surface (Scheme S1).

Section (I)

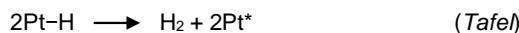
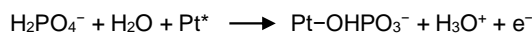
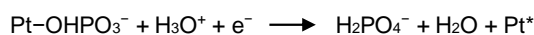
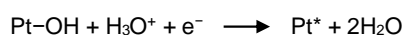
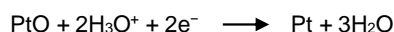
(1) Hydrogen desorption



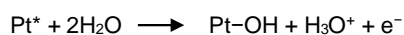
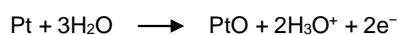
(6) Hydrogen adsorption



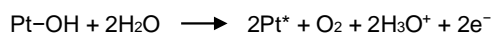
(7) Hydrogen evolution

**Section (II)**(2) Adsorption of H_2PO_4^- (6) Pt-oxide reduction & H_2PO_4^- desorption**Section (III)**

(3) Pt-oxide formation



(4) Oxygen evolution



Scheme S1: Reaction equations for electrochemical adsorption and desorption of electrolyte species on Pt surface based on CV curve in Figure 1b.

The integration of the on-top area below the anodic branch of CV curve in the potential range of 0.05-0.40 V vs. RHE gives the additional amount of charge stored within *Helmholtz* layers due to electrochemical adsorption of underpotential deposited hydrogen. With a monolayer charge of $210 \mu\text{C cm}^{-2}$ the measured charge can be related to H_{upd} coverage on Pt in aqueous phase (Equations S6-S8).^[36] The add-area between 0.00 and 0.05 V vs. RHE is omitted for calculations for two reasons. First, the onset potential for formation of underpotential deposited hydrogen on Pt group metals is regarded to be 0.05 V vs. RHE.^[37] Second, the formation of molecular hydrogen during cathodic sweep cannot be fully excluded. This hydrogen is oxidized at $E = 0.00-0.05$ V vs. RHE, giving rise to an additional signal in CV that cannot be deconvolved from the peaks arising from electrochemical H adsorption (Figure S5a).

$$A_{H_{\text{upd}}} = \int j \cdot dE \quad (\text{S6})$$

$$Q_{\text{H}} = \frac{1}{\nu} \cdot \int j \cdot dE \quad (\text{S7})$$

$$\theta_{\text{H}} = \frac{Q_{\text{H}}}{Q_{\text{H,ML}}} \quad (\text{S8})$$

The j denotes the measured current density, and the E stands for the potential on RHE scale. The ν represents the scanning rate, and the $Q_{\text{H,ML}}$ is the amount of charge that is associated with the adsorption of H_{upd} monolayer on Pt.

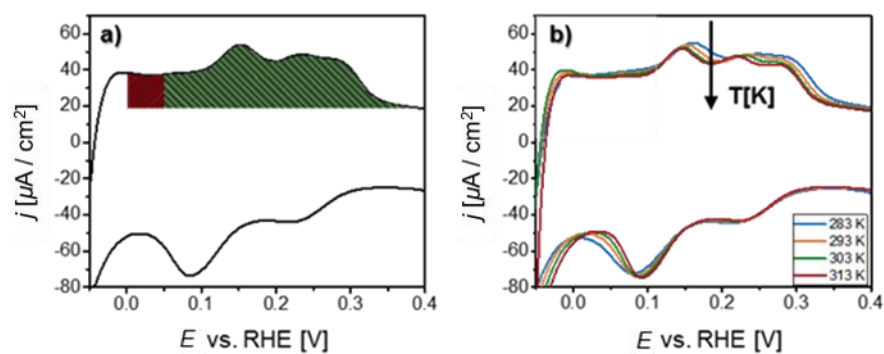


Figure S5: a) Integrated areas of pseudo-capacitance in CV due to H_2 oxidation (red) and H_{upd} formation (green) and b) temperature dependence of CV on Pt in water.

2.5.3 Calculation of free energy of H adsorption on Pt from H_{upd} peaks

The calculations for deriving the free energy of H_{upd} adsorption on Pt ($\Delta G_{\text{upd}}^{\circ} + \mu_{\text{excess}}$) are based on the assumption of *Volmer* reaction (Rxn. 1) being in quasi-equilibrium. Therefore, the change of the *Gibbs* free energy of the reaction has to be zero ($\Delta G = 0$) and the chemical potentials of reactants and products have to be equal (Equation S9).

$$\mu_{\text{H}^+} + \mu_{\text{el}} = \mu_{\text{H}} \quad (\text{S9})$$

With the expression μ_{H^+} , μ_{H} and μ_{el} in Equations S10-S12, Equation S9 is reformulated to Equation S13.

$$\mu_{\text{el}} = -F\phi_{\text{Pt}} \quad (\text{S10})$$

$$\mu_{\text{H}^+} = \mu_{\text{H}^+}^{\circ} + RT \ln \frac{a_{\text{H}^+}}{a_{\text{H}^+}^{\circ}} + F\phi_{\text{aq}} \quad (\text{S11})$$

$$\mu_{\text{H}} = \mu_{\text{H}}^{\circ} + RT \ln \frac{\theta_{\text{H}}}{1 - \theta_{\text{H}}} + \mu_{\text{excess}} \quad (\text{S12})$$

$$\mu_{\text{H}}^{\circ} - \mu_{\text{H}^+}^{\circ} + \mu_{\text{excess}} + F(\phi_{\text{Pt}} - \phi_{\text{aq}}) = RT \ln \frac{a_{\text{H}^+}}{a_{\text{H}^+}^{\circ}} - RT \ln \frac{\theta_{\text{H}}}{1 - \theta_{\text{H}}} \quad (\text{S13})$$

The μ_{H^+} is the hydronium ion's chemical potential, and μ_{H} is the chemical potential of adsorbed H on Pt surface. It should be noted here that the electron is also treated as a reactant, which has the chemical potential (μ_{el}) as its *Fermi* level according to *IUPAC* definition. The μ_{el} is determined by the electric potential on Pt, ϕ_{Pt} (Eq. S10). The μ_{H^+} consists of its standard chemical potential $\mu_{\text{H}^+}^{\circ}$, a thermodynamic activity (a_{H^+}) dependent term and an electrostatic potential energy term ($F\phi_{\text{aq}}$) that arises from the potential (ϕ_{aq}) in bulk electrolyte (Eq. S11). Here, F is *Faraday* constant. The μ_{H} comprises the standard chemical potential of H_{ads} (μ_{H}°), a term that is determined by the H_{upd} coverage (θ_{H}) and an excess chemical potential term μ_{excess} accounting for the effect from non-ideality (Eq. S12).

Under open circuit, the system is essentially the reversible hydrogen electrode, that the electric potential on Pt and in bulk aqueous phase are $\phi_{\text{Pt,RHE}}$ and $\phi_{\text{aq,RHE}}$. When applying an overpotential (η), the electrode potential has the following relations (Equation S14):

$$\phi_{\text{Pt}} - \phi_{\text{aq}} = \eta + (\phi_{\text{Pt,RHE}} - \phi_{\text{aq,RHE}}) \quad (\text{S14a})$$

$$\phi_{\text{Pt,RHE}} - \phi_{\text{aq,RHE}} = \phi_{\text{Pt,SHE}} - \phi_{\text{aq,SHE}} + RT \ln \frac{a_{\text{H}^+}}{a_{\text{H}^+}^\circ} \quad (\text{S14b})$$

Equation S14b is the relation between RHE and SHE (Standard Hydrogen Electrode) based on *Nernst* equation. Therefore, substituting the $(\phi_{\text{Pt}} - \phi_{\text{aq}})$ term in Equation S13 by Equation S14, we get

$$\mu_{\text{H}}^\circ - (\mu_{\text{H}^+}^\circ + F\phi_{\text{aq,SHE}}) - (-F\phi_{\text{Pt,SHE}}) + \mu_{\text{excess}} = -RT \ln \frac{\theta_{\text{H}}}{1 - \theta_{\text{H}}} - F\eta \quad (\text{S15})$$

Note that the first three terms on the left side of Equation 15 are the standard *Gibbs* free energy change ($\Delta G_{\text{upd}}^\circ$) of H_{upd} adsorption on Pt in water (Rxn 1), defined in Equation S16. Hence, using this relation Equation S15 can be rearranged to Equation S17 (free energy of H adsorption).

$$\Delta G_{\text{upd}}^\circ = \mu_{\text{H}}^\circ - (\mu_{\text{H}^+}^\circ + F\phi_{\text{aq,SHE}}) - (-F\phi_{\text{Pt,SHE}}) \quad (\text{S16})$$

$$\Delta G_{\text{upd}}^\circ + \mu_{\text{excess}} = -RT \ln \frac{\theta_{\text{H}}}{1 - \theta_{\text{H}}} - F\eta \quad (\text{S17})$$

2.5.4 Impact of electrolyte pH on ΔH_{upd} on Pt

The impact of electrolyte pH on $\Delta H_{\text{upd}}^{\circ}$ on Pt electrode was evaluated based on the deviations shown in Sections 2-3 of SI.

Figure S6 shows CV curves and H_{upd} coverage on Pt at different electrolyte pH, respectively. With increasing pH the H_{upd} peaks of CV curve are gradually shifted to more positive potentials on RHE scale indicating a stronger binding of H_{upd} on electrode surface, which is in line with findings from *Sheng* and coworker.^[38] The coverage of Pt with hydrogen is less influenced by electrolyte pH.

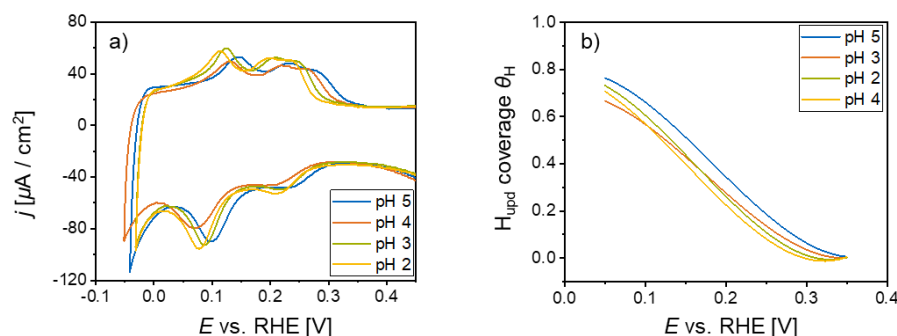


Figure S6: **a)** Shift of H_{upd} signals on Pt/CNT with respect to solution pH and **b)** H_{upd} coverage of electrode surface as function of applied overpotential.

The free energy of H_{upd} adsorption on electrode surface at different pH was calculated from the temperature dependence of θ_{H} , which was determined from CV curves recorded at $T = 283\text{--}313\text{ K}$. Applying Equation S17, the $\Delta G_{\text{upd}}^{\circ} + \mu_{\text{excess}}$ is shown as function of applied overpotential on RHE scale in Figure S7a,c,e for different electrolyte pH. Figure S7b,d,f plots the μ_{excess} at different pH as function of applied overpotential. The standard *Gibbs* free energy change $\Delta G_{\text{upd}}^{\eta=0} = \Delta G_{\text{upd}}^{\circ}$ is obtained as the y-intercept in Fig. S7a,c,e *via* extrapolating $\Delta G_{\text{upd}}^{\circ} + \mu_{\text{excess}}$ to $\eta = 0\text{ V}$ and is used to calculate the adsorption enthalpy and entropy at zero overpotential.

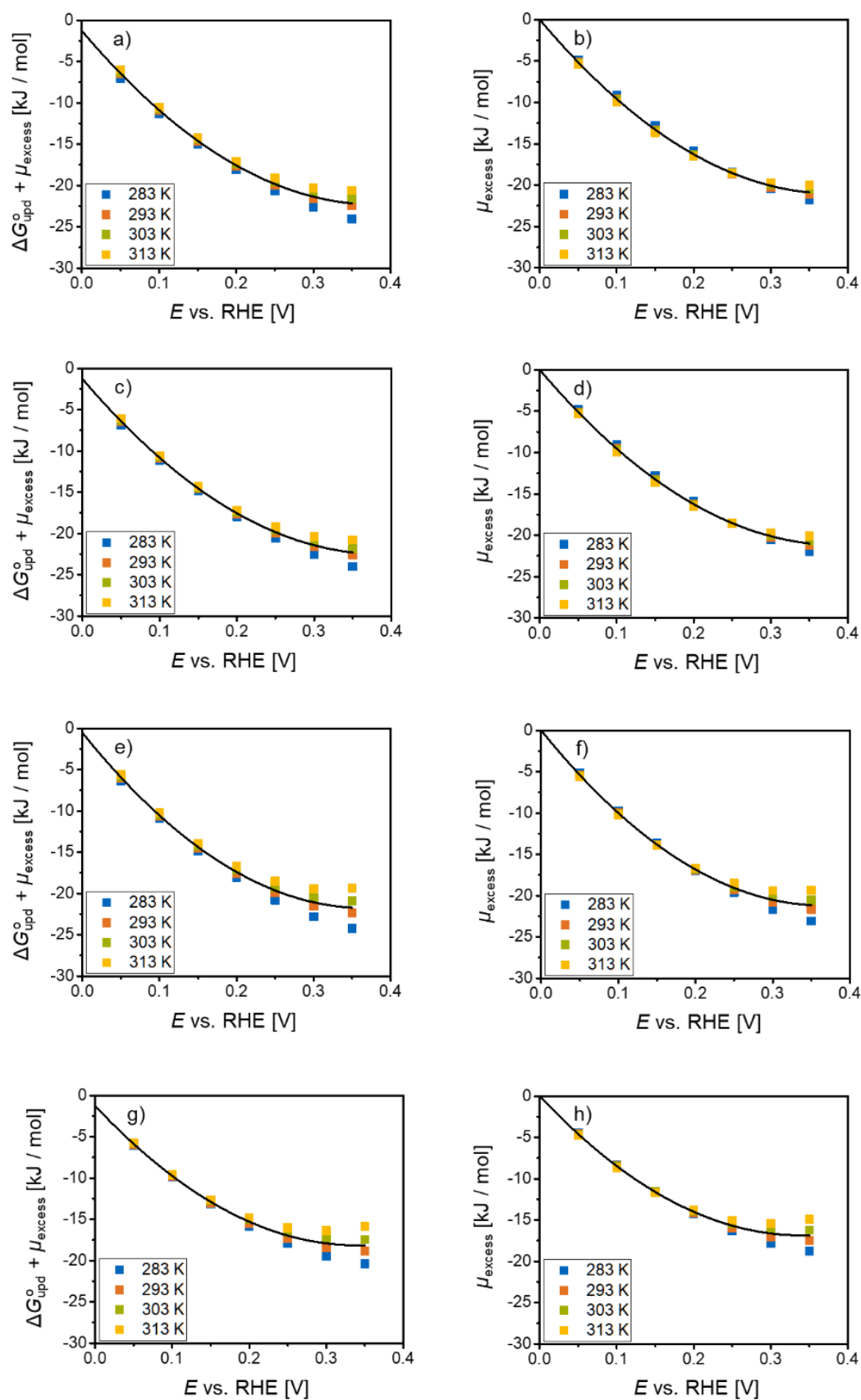


Figure S7: a), c), e), g) Development of $\Delta G_{\text{upd}}^{\circ} + \mu_{\text{excess}}$ with external electric potential in the range of $T = 283\text{--}313\text{ K}$ at pH 2.4, 3.2, 4.2 and 4.9 and b), d), f), h) course of μ_{excess} with increasing overpotential.

The adsorption enthalpy and entropy at OCP, i.e., zero overpotential ($\Delta H_{\text{upd}}^{\eta=0}$, $\Delta S_{\text{upd}}^{\eta=0}$) were calculated *via* linearizing *Gibbs-Helmholtz* equation and plotting $\Delta G_{\text{upd}}^{\circ}/T$ over $1/T$ (Equation 16, Figure S8). Table S3 summarizes the values of $\Delta H_{\text{upd}}^{\eta=0}$ and $\Delta S_{\text{upd}}^{\eta=0}$ at different pH.

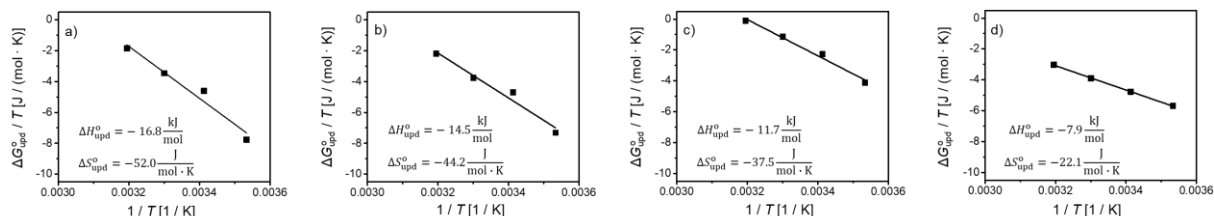


Figure S8: Plots of linearized *Gibbs-Helmholtz* equation for pH 4.9, 4.2, 3.2 and 2.4 (a-d).

Table S3: Enthalpy and entropy of H_{upd} adsorption on Pt at zero overpotential and different electrolyte pH determined from slopes and y-intercepts in Fig.S8.

pH	$\Delta H_{\text{upd}}^{\eta=0}$ [kJ/mol]	$\Delta S_{\text{upd}}^{\eta=0}$ [J/(mol K)]
2.4	- 7.9	- 22
3.2	- 11.7	- 38
4.2	- 14.5	- 44
4.9	- 16.8	- 52

2.5.5 Tafel evaluation of polarization curves

Polarization curves of Pt/CNT in aqueous electrolytes of different pH were evaluated according to *Tafel* analysis via plotting E_{RHE} vs. $\text{LOG}(|j| [\mu\text{A cm}^{-2}])$. *Tafel* slopes of hydrogen evolution reaction were determined from linear regions of *Tafel* plots (Figure S9, Table S4).

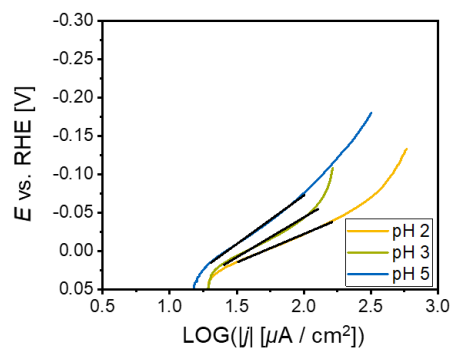


Figure S9: *Tafel* plots with *Tafel* slopes of linear polarization curves of HER on Pt/CNT in aqueous electrolytes at different pH.

Table S4: *Tafel* slopes of HER on Pt/CNT in aqueous phase at different pH.

pH	<i>Tafel</i> slope b_c [mV/dec]
2	- 74.0
3	- 103.8
5	- 126.5

2.6 References

- [1] W. Sheng, Z. Zhuang, M. Gao, J. Zheng, J. G. Chen, Y. Yan, *Nature Communications* **2015**, *6*, 5848.
- [2] a) W. Moritz, R. Imbihl, R. J. Behm, G. Ertl, T. Matsushima, *The Journal of chemical physics* **1985**, *83*, 1959-1968; b) P. Ferrin, S. Kandoi, A. U. Nilekar, M. Mavrikakis, *Surface science* **2012**, *606*, 679-689.
- [3] M. Takenouchi, S. Kudoh, K. Miyajima, F. Mafune, *The Journal of Physical Chemistry A* **2015**, *119*, 6766-6772.
- [4] B. Hammer, J. Nørskov, *Surface Science* **1995**, *343*, 211-220.
- [5] B. Hammer, J. K. Nørskov, *Nature* **1995**, *376*, 238-240.
- [6] a) B. S. Mun, M. Watanabe, M. Rossi, V. Stamenkovic, N. M. Markovic, P. N. Ross Jr, *The Journal of chemical physics* **2005**, *123*, 204717; b) J. Rossmeisl, G. S. Karlberg, T. Jaramillo, J. K. Nørskov, *Faraday discussions* **2009**, *140*, 337-346.
- [7] a) P. Quaino, E. Santos, G. Soldano, W. Schmickler, *Advances in Physical Chemistry* **2011**; b) E. Santos, W. Schmickler, *Electrochimica acta* **2008**, *53*, 6149-6156; c) J. K. Nørskov, T. Bligaard, A. Logadottir, J. Kitchin, J. G. Chen, S. Pandelov, U. Stimming, *Journal of The Electrochemical Society* **2005**, *152*, J23; d) E. Santos, W. Schmickler, *Angewandte Chemie International Edition* **2007**, *46*, 8262-8265.
- [8] a) C. H. Hamann, A. Hamnett, W. Vielstich, *Electrochemistry. Weinheim: Wiley-VCH* **1998**, 12-65; b) N. Eliaz, E. Gileadi, *Physical Electrochemistry: Fundamentals, Techniques, and Applications*, John Wiley & Sons, **2019**.
- [9] J. O. M. Bockris, B. E. Conway, E. B. Yeager, *The Double Layer*, Plenum Press, **1980**.
- [10] P. T. Kissinger, W. R. Heineman, *Journal of Chemical Education* **1983**, *60*, 702.
- [11] S.-A. Sheppard, S. A. Campbell, J. R. Smith, G. W. Lloyd, F. C. Walsh, T. R. Ralph, *Analyst* **1998**, *123*, 1923-1929.
- [12] a) B. E. Conway, G. Jerkiewicz, *Electrochimica Acta* **2000**, *45*, 4075-4083; b) G. Jerkiewicz, *Electrocatalysis* **2010**, *1*, 179-199.
- [13] G. Olivieri, A. Goel, A. Kleibert, D. Cvetko, M. A. Brown, *Phys. Chem. Chem. Phys.* **2016**, *18*, 29506-29515.
- [14] M. Garcia-Dieguez, D. D. Hibbitts, E. Iglesia, *J. Phys. Chem. C* **2019**, *123*, 8447-8462.
- [15] R. Gómez, J. M. Orts, B. Álvarez-Ruiz, J. M. Feliu, *The Journal of Physical Chemistry B* **2004**, *108*, 228-238.
- [16] a) K. Christmann, G. Ertl, T. Pignet, *Surface Science* **1976**, *54*, 365-392; b) P. R. Norton, P. J. Richards, *Surface Science* **1974**, *44*, 129-140.
- [17] N. M. Marković, T. J. Schmidt, B. N. Grgur, H. A. Gasteiger, R. J. Behm, P. N. Ross, *The Journal of Physical Chemistry B* **1999**, *103*, 8568-8577.
- [18] X. Yang, J. Nash, N. Oliveira, Y. Yan, B. Xu, *Angew. Chem., Int. Ed.* **2019**, *58*, 17718-17723.
- [19] T. Cheng, L. Wang, B. V. Merinov, W. A. Goddard, *Journal of the American Chemical Society* **2018**, *140*, 7787-7790.
- [20] I. Ledezma-Yanez, W. D. Z. Wallace, P. Sebastián-Pascual, V. Climent, J. M. Feliu, M. T. M. Koper, *Nature Energy* **2017**, *2*, 17031.
- [21] P. S. Lamoureux, A. R. Singh, K. Chan, *ACS Catal.* **2019**, *9*, 6194-6201.
- [22] a) G. L. Miessler, P. J. Fischer, D. A. Tarr, *Inorganic Chemistry*, Pearson, **2014**; b) M.-S. Liao, Q.-E. Zhang, W. H. E. Schwarz, *Z. Anorg. Allg. Chem.* **1998**, *624*, 1419-1428.
- [23] S. Surendralal, M. Todorova, J. Neugebauer, *Physical review letters* **2021**, *126* 16, 166802.
- [24] F. Musumeci, G. H. Pollack, *Chem Phys Lett* **2012**, *536*, 65-67.
- [25] Y. Yoon, R. Rousseau, R. S. Weber, D. Mei, J. A. Lercher, *Journal of the American Chemical Society* **2014**, *136*, 10287-10298.
- [26] M. D. Scanlon, P. Peljo, M. A. Méndez, E. Smirnov, H. H. Girault, *Chemical Science* **2015**, *6*, 2705-2720.
- [27] G. Yang, S. A. Akhade, X. Chen, Y. Liu, M.-S. Lee, V.-A. Glezakou, R. Rousseau, J. A. Lercher, *Angew. Chem., Int. Ed.* **2019**, *58*, 3527-3532.
- [28] I. T. McCrum, M. J. Janik, *J. Phys. Chem. C* **2016**, *120*, 457-471.
- [29] A. Borodziński, M. Bonarowska, *Langmuir* **1997**, *13*, 5613-5620.
- [30] a) J. Wang, *Analytical Electrochemistry*, Wiley, **2006**; b) R. S. Nicholson, I. Shain, *Analytical Chemistry* **1964**, *36*, 706-723.
- [31] Z. Stojek, in *Electroanalytical Methods* (Ed.: F. Scholz), Springer, **2010**.
- [32] J. O. M. Bockris, B. E. Conway, E. B. Yeager, *The Double Layer*, Plenum Press, **1980**.
- [33] N. Eliaz, E. Gileadi, *Physical Electrochemistry: Fundamentals, Techniques, and Applications*, Wiley, **2019**.
- [34] P. T. Kissinger, W. R. Heineman, *Journal of Chemical Education* **1983**, *60*, 702.

-
- [35] a) C. H. Hamann, A. Hamnett, W. Vielstich, *Electrochemistry*, Wiley, **1998**; b) G. Jerkiewicz, *Electrocatalysis* **2010**, *1*, 179-199.
- [36] S.-A. Sheppard, S. A. Campbell, J. R. Smith, G. W. Lloyd, F. C. Walsh, T. R. Ralph, *Analyst* **1998**, *123*, 1923-1929.
- [37] O. Diaz-Morales, T. J. P. Hersbach, C. Badan, A. C. Garcia, M. T. M. Koper, *Faraday Discussions* **2018**, *210*, 301-315.
- [38] W. Sheng, Z. Zhuang, M. Gao, J. Zheng, J. G. Chen, Y. Yan, *Nature Communications* **2015**, *6*, 5848.

2.7 Associated content

Publication

This chapter is based on a manuscript planned for submission (Philipp Fischer[†], Xi Chen[†], Yue Liu, Johannes A. Lercher)

Contributions

P.F. did main contributions in catalyst preparation, CV and LP measurements and data analysis. X.C. contributed to data analysis. P.F. and X.C. contributed equally to manuscript preparation. Y.L. contributed to data analysis and manuscript preparation. Y.L. and J.A.L. conceived the research. The manuscript was written through contributions of all authors.

Acknowledgements

The authors would like to thank German Research Foundation DFG, the Federal Ministry of Education and Research of Germany as well as the Bavarian Ministry of Science and Art and the cluster of e-conversion for their support. Xaver Hecht, Muhammad Iqbal and Andreas Marx are thanked for their technical support and measuring H₂ chemisorption as well as N₂ physisorption, Martin Neukamm for doing elemental analysis and Roland Weindl for measuring TEM.

3 Electrocatalytic hydrogenation of benzaldehyde in aqueous phase – Impact of electrolyte composition on catalyst performance

Abstract

The composition of aqueous phase, e.g., acidity, ionic strength, cations as well as external electric potential influence thermodynamic properties of H adsorbed on Pt electrode surface. Depending on stabilization of Pt-H bond the catalyst performance in electrocatalytic hydrogenation (ECH) of biomass-derived compounds varies.

Application of an increasing negative overpotential to Pt surface destabilizes electrocatalytically adsorbed H on Pt surface leading to a rate increase in hydrogen evolution reaction (HER) and ECH of benzaldehyde (BzHO). This effect is attributed to a shifting of electrode *Fermi* level and a different filling of Pt-H antibonding state (E^*) by electrons.

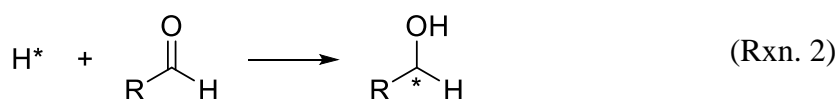
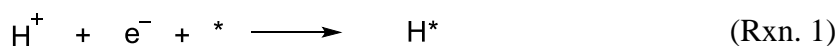
Considering various electrolyte compositions, changing the electrolyte pH has the largest impact on Pt-H bond strength and entropic changes upon H_{upd} adsorption. Lowering electrolyte pH causes a reduction of hydrogen binding strength on metal surface. Additionally, the entropic loss upon immobilization of hydrogen is decreased. These effects are attributed to an enhanced amount of H_3O^+ within EDL in highly acidic solutions. The energetic contribution for moving away EDL from Pt surface increases and hence, compensates hydrogen adsorption heat. At low pH, hydronium ions in bulk phase have a low configurational entropy already before adsorption, decreasing only slightly more upon immobilization. Lowering solution pH accelerates rates of HER and benzaldehyde ECH.

In terms of ionic strength and electrolyte cations the observed changes are rather subtle. Nevertheless, they follow similar trends like for solution acidity. Destabilization of H on Pt increases in order $4.5 < 3.0 < 1.5 < 0.6 \text{ M}$ and $Li^+ < Na^+ < K^+$. However, concerning rates of HER and ECH an opposite trend is received. This might be caused by a different stabilization of benzaldehyde on electrode surface.

3.1 Introduction

Due to ongoing climate changes and global warming caused by a continuous pollution and emission of greenhouse gases, e.g., CO₂ a departure from non-renewable energy and carbon sources is getting a political objective around the world.^[1] Biomass is a green and sustainable alternative to fossil resources like crude oil for the production of a broad variety of base chemicals and fuel-range compounds.^[2] In fast pyrolysis, the non-edible lignocellulosic feedstock is first converted towards bio-oil, which is a blend of different oxygen-rich molecules and aromatics.^[3] The large amount of oxygen-containing functional groups within these molecules together with a large degree of unsaturation renders bio-oil a low energy material that is susceptible to polymerization.^[4] Hence, further treatment, e.g., hydrogenation, hydrodeoxygenation is required in order to remove oxygen and increase the hydrogen content of the mixture.

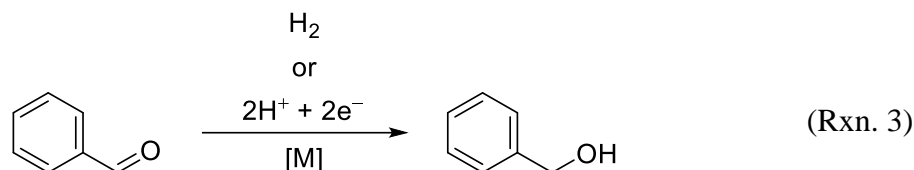
Electrocatalytic hydrogenation (ECH) of organic compounds, e.g., aldehydes, ketones, aromatics is a sustainable alternative to common hydrogenation reactions that are typically run at elevated temperatures and pressures.^[5] In ECH of oxygenated compounds, the required hydrogen is supplied *via in situ* reduction of protons from the electrolyte solution, i.e., water electrolysis.^[4, 6] In a proton coupled electron transfer (PCET), H-atoms adsorbed on the metal electrode surface are formed according to *Volmer* reaction and consecutively transferred to an organic substrate (Reactions 1-2).^[7]



In contrast to common hydrogenation reactions ECH can be performed under near ambient conditions, i.e., low temperature and atmospheric pressure.^[8] Furthermore, the required energy for generating reduction equivalents (H^{*}) can be supplied by renewable resources, e.g., solar, wind making ECH independent of fossil materials and supplies.^[9] Hence, electrocatalytic hydrogenation can help to reduce the anthropogenic carbon footprint as well as parts of the capital cost associated with thermo-chemical hydrogenation, making it a promising economically and environmentally friendly technology for biomass-upgrading.^[5a, 6, 10]

The decomposition of lignocellulose yields a pool of unsaturated aldehydes, ketones, carboxylic acids and aromatics.^[11] Benzaldehyde acts as a model compound for these type of unsaturated and oxygen-rich molecules.^[12] Its hydrogenation towards benzyl alcohol, which is an important chemical for the production of flavors, cosmetics and paints, can be used as a

model reaction to investigate different reaction parameters and setups and their influence on performance in (electrocatalytic) hydrogenation of oxygenated compounds (Reaction 3).^[13]



Aqueous phase ECH of benzaldehyde on Pt, however, suffers from a rather poor *Faradaic* efficiency (FE) and rate, which can be altered by variation of electrolyte composition and external electric potential.^[7, 10a, 14] The dependence of FE and rate on electrolyte composition and applied potential is related to the heat (ΔH_{upd}) and free energy ($\Delta G_{\text{upd}}^{\circ} + \mu_{\text{excess}}$) of underpotential deposited hydrogen (H_{upd}) adsorption on Pt. The ΔH_{upd} and $\Delta G_{\text{upd}}^{\circ} + \mu_{\text{excess}}$ are determined from H_{upd} signals in cyclic voltammetry (CV) of Pt in water.

When a metal electrode is immersed into an aqueous electrolyte an electrochemical double-layer (EDL) consisting of inner and outer *Helmholtz* plane is formed.^[15] Within this interfacial region between bulk electrolyte and electrode surface electrolyte ions, e.g., hydronium ions and electrolyte cations and anions are accumulated and prone to adsorption on the metal surface.^[16] This process can be driven by an external electric potential and in case of Pt-group metal electrodes it can be investigated by CV.^[17] Figure 1 shows the cyclic voltammogram of Pt/CNT in aqueous solution in the potential range of -0.05 to 1.45 V vs. RHE. Beyond this potential window electrochemical water splitting, e.g., hydrogen and oxygen evolution become the prevailing reactions leading to a rapid current increase that superimposes features arising from adsorption and desorption of electrolyte ions. Anodic features of the curve arise due to oxidation processes whereas the cathodic part is caused by reduction reactions.

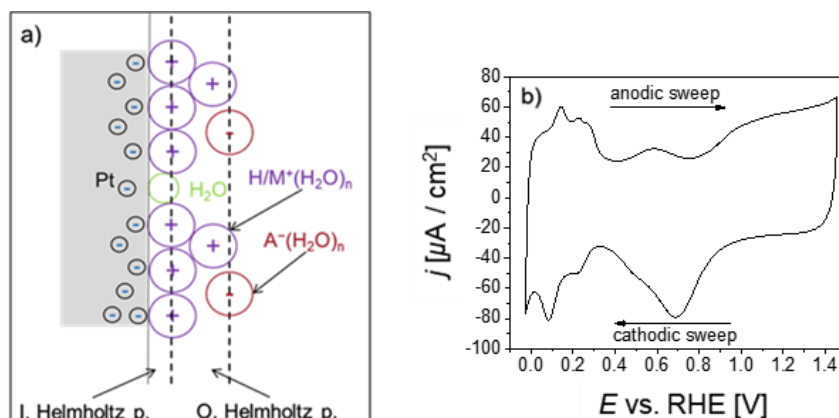


Figure 1: a) Schematic representation of electrochemical double-layer and b) cyclic voltammogram on Pt/CNT in water. The M^+ and A^- in a) denote metal cations and electrolyte anions, respectively.

At $E_{\text{RHE}} = 0.05\text{-}0.45$ V, the CV curve relates to formation of H_{upd} on Pt according to reversible *Volmer* equilibrium (Reaction 4), which is assumed to be quasi-equilibrated.



The free energy of H_{upd} formation on electrode surface is determined using the (electro)chemical potentials of reactants and products of *Volmer* equilibrium (Equations 1-4).

$$\mu_{\text{el}} = -F\phi_{\text{Pt}} \quad (1)$$

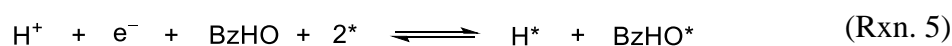
$$\mu_{\text{H}^+} = \mu_{\text{H}^+}^{\circ} + RT \ln \frac{a_{\text{H}^+}}{a_{\text{H}^+}^{\circ}} + F\phi_{\text{aq}} \quad (2)$$

$$\mu_{\text{H}} = \mu_{\text{H}}^{\circ} + RT \ln \frac{\theta_{\text{H}}}{1 - \theta_{\text{H}}} + \mu_{\text{excess}} \quad (3)$$

$$\Delta G_{\text{upd}}^{\circ} + \mu_{\text{excess}} = -RT \ln \frac{\theta_{\text{H}}}{1 - \theta_{\text{H}}} - F\eta \quad (4)$$

The μ_{H^+} is the hydronium ion's chemical potential, and μ_{H} is the chemical potential of adsorbed H on Pt surface. The electron is also treated as a reactant that has the chemical potential (μ_{el}) as its *Fermi* level according to *IUPAC* definition. The μ_{el} is determined by the electric potential on Pt, ϕ_{Pt} (Eq. 1). The μ_{H^+} comprises its standard chemical potential $\mu_{\text{H}^+}^{\circ}$, a thermodynamic activity (a_{H^+}) dependent term and an electrostatic potential energy term ($F\phi_{\text{aq}}$), which arises from the potential (ϕ_{aq}) in bulk electrolyte (Eq. 2). Here, F is *Faraday* constant. The μ_{H} consists of the standard chemical potential of H_{upd} (μ_{H}°), a term that is determined by the H_{upd} coverage (θ_{H}) and an excess chemical potential term μ_{excess} accounting for the effect from non-ideality (Eq. 3). The variable η is the applied overpotential on RHE scale, i.e., E_{RHE} . The free energy of H_{upd} formation on metal surface includes the standard *Gibbs* free energy change ($\Delta G_{\text{upd}}^{\circ}$) defined by θ_{H} and the excess potential (μ_{excess}) arising from the electric overpotential (Eq. 4). A detailed derivation of Equation 4 is given in Section 2 of supporting information.

The standard free energy of benzaldehyde adsorption on Pt is calculated from the repression of H_{upd} signals in CV at increasing benzaldehyde concentration (Figure 2). Parallel adsorption of benzaldehyde and H_{upd} is assumed to be quasi-equilibrated (Reaction 5).



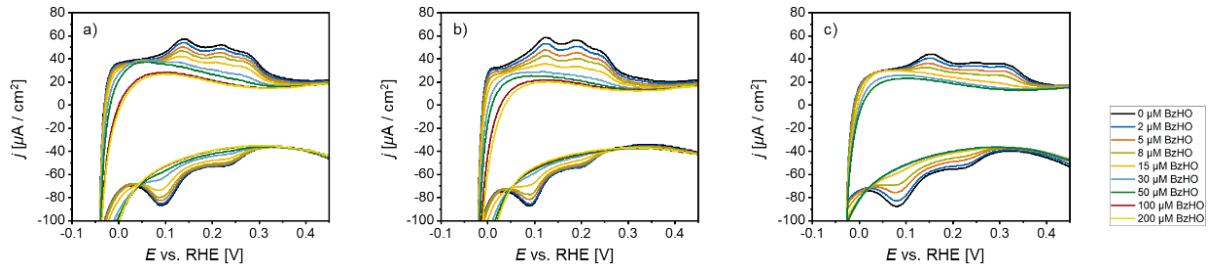


Figure 2: Cyclovoltammometry of Pt/CNT in aqueous electrolytes containing different concentrations of benzaldehyde. **a)-c)** refer to the different electrolyte compositions investigated, i.e., pH 4.9 and IS = 3.0 M, pH 2.4 and IS = 3.0 M, and pH 4.9 and IS = 0.6 M.

Using the electrochemical potential of e^- and μ_{H^+} defined above (Equations 1-2) and the chemical potentials of H_{upd} of benzaldehyde in solution and adsorbed on Pt the standard *Gibbs* free energy of benzaldehyde adsorption at $E_{\text{RHE}} = 0.05$ V is calculated *via* Equations 5-8.

$$\mu_{\text{BzHO}} = \mu_{\text{BzHO}}^{\circ} + RT \ln c_{\text{BzHO}} \quad (5)$$

$$\mu_{\text{H}} = \mu_{\text{H}}^{\circ} + RT \ln \frac{\theta_{\text{H}}}{1 - \theta_{\text{H}} - \theta_{\text{BzHO}}} + \mu_{\text{excess}} \quad (6)$$

$$\mu_{\text{BzHO}^*} = \mu_{\text{BzHO}^*}^{\circ} + RT \ln \frac{\theta_{\text{BzHO}}}{1 - \theta_{\text{H}} - \theta_{\text{BzHO}}} \quad (7)$$

$$\Delta G_{\text{BzHO}}^{\circ} = RT \ln c_{\text{BzHO}} - RT \left(\ln \frac{\theta_{\text{H}}}{1 - \theta_{\text{H}} - \theta_{\text{BzHO}}} + \frac{\theta_{\text{BzHO}}}{1 - \theta_{\text{H}} - \theta_{\text{BzHO}}} \right) - F\eta - (\Delta G_{\text{upd}}^{\circ} + \mu_{\text{excess}}) \quad (8)$$

The μ_{BzHO} is the chemical potential of benzaldehyde in aqueous phase that is determined by its standard chemical potential ($\mu_{\text{BzHO}}^{\circ}$) and its concentration in water (c_{BzHO}). The μ_{BzHO^*} is the chemical potential of benzaldehyde adsorbed on Pt surface comprising the standard chemical potential of adsorbed BzHO ($\mu_{\text{BzHO}^*}^{\circ}$) and a term depending on the electrode coverage with H_{upd} (θ_{H}) and benzaldehyde (θ_{BzHO}). Benzaldehyde coverage was calculated from the amount of θ_{H} that is suppressed at a given concentration of BzHO.

A detailed derivation of Equation 8 is given in Section 7 of supporting information.

3.2 Results

The free energy of H_{upd} adsorption on Pt surface is calculated from H_{upd} features of CV curve in the potential range of 0.05-0.40 V vs. RHE (Equation 4, Figure 3). Figure S3a-b in SI shows the $\Delta G_{\text{upd}}^{\circ} + \mu_{\text{excess}}$ and μ_{excess} as function of external electric potential at pH 5 and different temperatures. Formation of underpotential deposited hydrogen on electrode surface leads to pseudo-capacitance in cyclic voltammetry that relates to the additional charge stored within EDL due to reductive proton adsorption.^[15b, 17] Assuming a monolayer charge of $210 \mu\text{C}/\text{cm}^2$ the integration of these features gives θ_{H} under external electric potential.^[18]

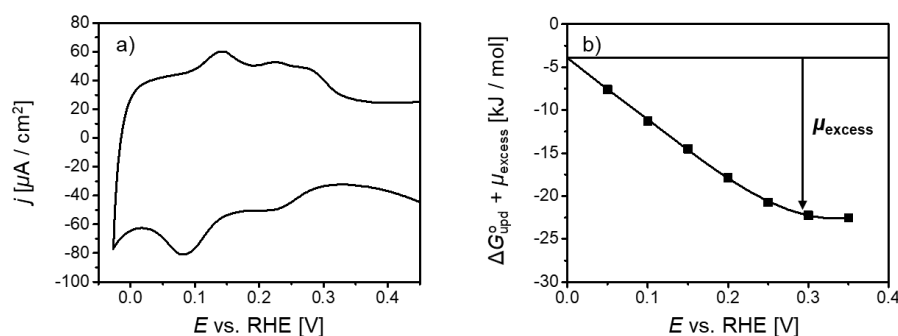


Figure 3: **a)** Peaks related to H_{upd} formation on Pt/CNT during cyclic voltammetry, and **b)** free energy of H_{upd} adsorption on electrode surface as function of external electric potential.

Increasing the temperature during cyclic voltammetry reduces the intensity of H_{upd} features and hence, Pt surface coverage with underpotential deposited hydrogen. At 283-313 K, θ_{H} at $E_{\text{RHE}} = 0.05 \text{ V}$ decreases from 75 to 65%. This temperature dependence of CV signals allows for calculating thermodynamic properties of H_{upd} on electrode surface, e.g., $\Delta H_{\text{upd}}^{\circ}$, $\Delta S_{\text{upd}}^{\circ}$. Since the excess potential is a function of external electric potential instead of H_{upd} coverage it has to be zero at open circuit potential (OCP), i.e., zero overpotential. If μ_{excess} would be a function of θ_{H} the free energy of H_{upd} formation on metal surface would be invariant. However, as can be seen from Figure 3b, $\Delta G_{\text{upd}}^{\circ} + \mu_{\text{excess}}$ raises with increasing anodic overpotential. The standard free energy of adsorption of underpotential deposited hydrogen on Pt at OCP ($\Delta G_{\text{upd}}^{\eta=0} = \Delta G_{\text{upd}}^{\circ}$) is determined from the y-intercept in Figure 3b and is used to calculate $\Delta H_{\text{upd}}^{\circ}$ and $\Delta S_{\text{upd}}^{\circ}$ on Pt electrode. Figure 4 shows that μ_{excess} hardly changes with temperature. Hence, its derivative by T equals zero ($\partial\mu/\partial T = 0$), that it has no entropic term ($\Delta S_{\text{excess}} = 0$) but only an enthalpic contribution. The $\Delta S_{\text{upd}}^{\circ}$ is constant throughout the whole potential window investigated whereas $\Delta H_{\text{upd}}^{\circ}$ changes with external electric potential (Equation 9-11, Figure 5b).

$$\frac{\partial \mu_{\text{excess}}}{\partial T} = 0 = \frac{\partial}{\partial T} (\Delta H_{\text{excess}} - T \Delta S_{\text{excess}}) = -\Delta S_{\text{excess}} \quad (9)$$

$$\mu_{\text{excess}} = \Delta H_{\text{excess}} \quad (10)$$

$$\Delta H_{\text{upd}}(\eta) = \Delta H_{\text{upd}}^{\eta=0} + \Delta H_{\text{excess}}(\eta) \quad (11)$$

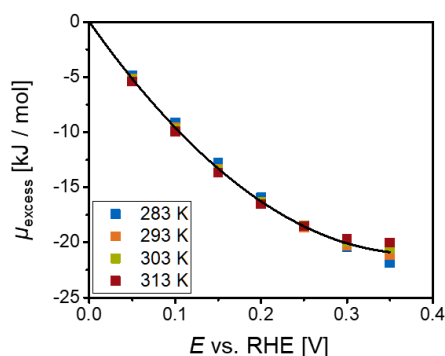


Figure 4: Dependence of excess potential on external electric potential at various electrolyte temperatures.

Linearizing Gibbs-Helmholtz equation and plotting $\Delta G_{\text{upd}}^{\circ} / T$ over $1/T$ gives a straight line, the slope of which is the heat of underpotential deposited hydrogen adsorption on electrode surface under OCP ($\Delta H_{\text{upd}}^{\circ}$) (Figure 5a). The entropy of H_{upd} formation on Pt at zero overpotential is read from the y-intercept ($\Delta S_{\text{upd}}^{\circ}$). The $\Delta H_{\text{upd}}^{\circ}$ increases with increasing anodic overpotential due to shifting of the electrode *Fermi* level. A decreased stabilization of Pt-H bond at increasing cathodic overpotential accelerates rates of benzaldehyde ECH and HER but decreases the Faradaic efficiency (Figures 5c-d).

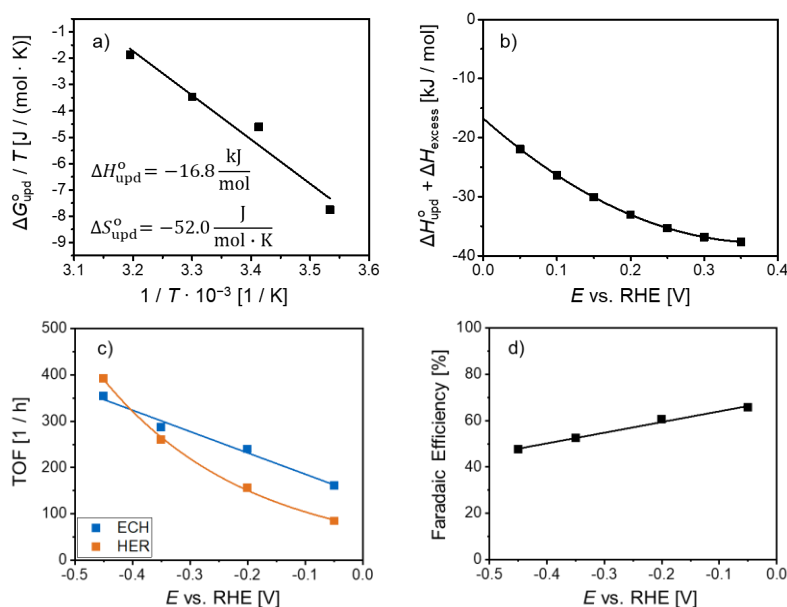


Figure 5: a) Plot of linearized Gibbs-Helmholtz equation $\Delta G_{\text{upd}}^{\circ} / T$ over $1/T$ with heat and entropy of H_{upd} formation on Pt at OCP, b) ΔH_{upd} as function of external electric potential, c) and d) development of turnover frequency and *Faradaic* efficiency of ECH and HER on Pt with external electric potential.

The change of ΔH_{upd} with respect to external electric potential is explained by a shifting of electrode *Fermi* level upon variation of applied overpotential. According to *Nørskov* et al. Pt *Fermi* level is lying close to Pt-H antibonding state. *Neugebauer* and coworker assume both to level up.^[19] In MO-theory, Pt-H bond is formed via hybridization of metal 5d band with H 1s orbital resulting in bonding and antibonding state.^[20] An increasing cathodic potential raises the *Fermi* level in Pt electrode and hence, the filling of Pt-H antibonding state by electrons, destabilizing Pt-H bond (Figure 6).

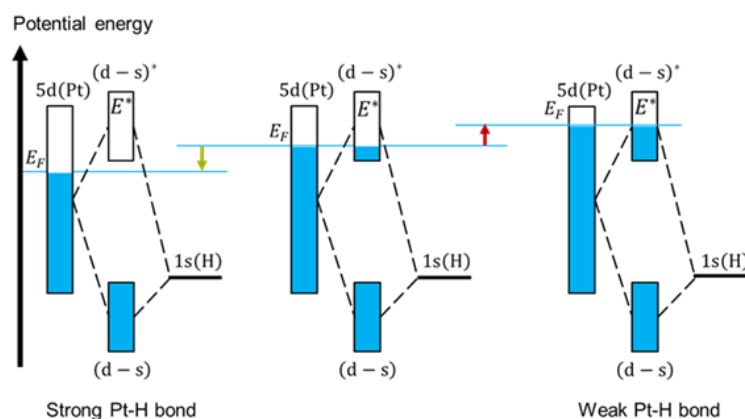


Figure 6: Schematic illustration of bonding and antibonding state of Pt-H bond after hybridization of metal 5 d band with H 1s orbital and filling of antibonding state with respect to Pt electrode *Fermi* level.

At increasing electrolyte acidity, H_{upd} peaks in cyclic voltammetry are shifted to more negative potentials on RHE scale (Figure 7a). Consequently, Pt H bond is weakened at low pH. This is in line with results from *Sheng* and *Nash* and coworker who found a decrease of hydrogen binding energy (HBE) on Pt(100) from -0.35 to -0.25 eV at pH 10.0.^[21] The shifting of H_{upd} signals correlates with a decrease in free energy of H_{upd} formation on Pt surface on SHE scale (Figure 7b). Increasing hydronium ion concentration in electrolyte solution leads to a more positive value of $\Delta G_{\text{upd}}^{\circ} + \mu_{\text{excess}}$ and hence, a reduced stabilization of underpotential deposited hydrogen on metal surface. Figure S3 in SI shows the free energy of H_{upd} adsorption on Pt electrode surface and the respective excess potential as function of external electric potential for pH 2-5. Lowering electrolyte pH leads to a reduced temperature dependence of H_{upd} coverage on Pt. At open circuit potential, the heat of underpotential deposited hydrogen adsorption on metal surface is reduced from -16.8 to -7.9 kJ/mol at pH 5-2 (Figure S4). The $\Delta S_{\text{upd}}^{\circ}$ decreases from -52 to -22.1 J/(mol·K). This is in accordance to *Goddard* et al. who showed from quantum mechanics molecular dynamics (QMMD) that the binding strength of H on electrode surface is reduced in highly acidic solution.^[22] *Singh* and coworker found a decrease of hydrogen binding energy (HBE) on Pt(110) from -20 to -12 kJ/mol at pH 9-1.^[23]

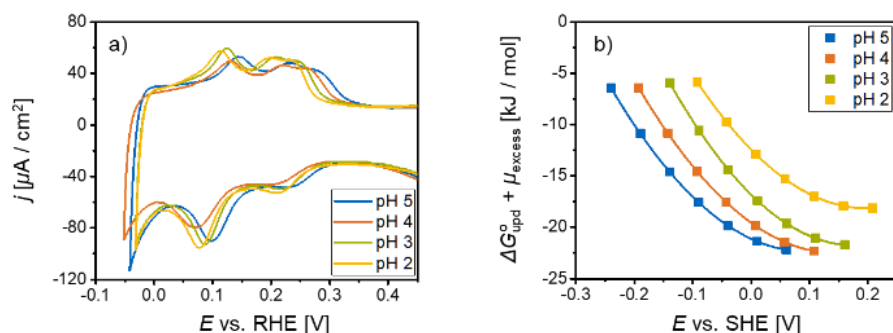


Figure 7: a) Shift of H_{upd} features on Pt/CNT in water and b) free energy of H_{upd} adsorption as function of external electric potential on SHE scale, both at different electrolyte pH.

Extrapolating the free energy of H_{upd} formation on Pt electrode surface to zero results in the onset overpotential for hydrogen evolution reaction (HER), $E_{\text{H}_2/\text{H}^+}^{\circ}$ (Figure 8a). With decreasing electrolyte acidity, i.e., increasing electrolyte pH $E_{\text{H}_2/\text{H}^+}^{\circ}$ is shifted towards more cathodic potentials. Due to increased binding strength of H_{upd} on metal surface the energy required to drive HER on Pt in alkaline solutions is increased and hence, $E_{\text{H}_2/\text{H}^+}^{\circ}$ is shifted from -0.008 to -0.015 V_{RHE} at pH 2-5 (Figure 8c). This behavior is also observed in linear polarization measurements and *Tafel* analysis (SI Section 6) where $E_{\text{H}_2/\text{H}^+}^{\circ}$ on Pt shifts gradually more negative in the same pH range (Figure 8b). *Koper* and coworker showed that the onset overpotential for HER gradually moved to more cathodic potentials when increasing the electrolyte pH from 1 to 13.^[24] *Chan* et al. proposed a change from acidic Volmer/Heyrovsky to alkaline Volmer/Heyrovsky sequence for HER when decreasing the electrolyte acidity.^[25] In their view, the proton donor for hydrogen evolution reaction changes from hydronium ions in acidic solutions to water molecules in alkaline electrolytes making HER on Pt less favorable, i.e., leading to a more negative $E_{\text{H}_2/\text{H}^+}^{\circ}$.

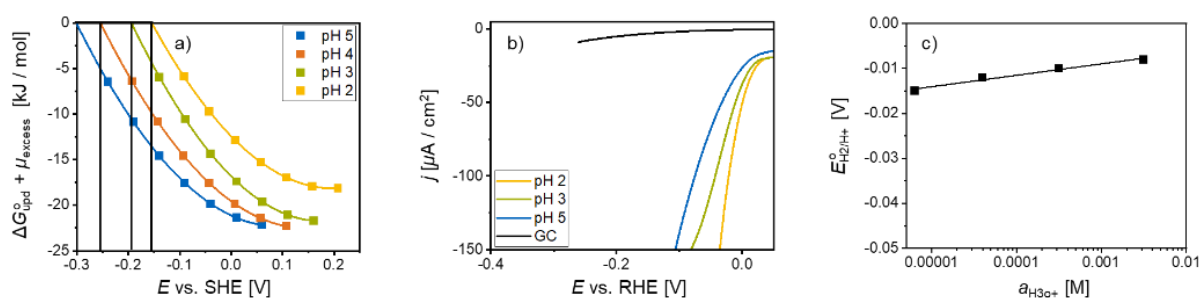


Figure 8: a) Extrapolated plot of $\Delta G_{\text{upd}}^{\circ} + \mu_{\text{excess}}$ vs. E_{SHE} , b) linear polarization curves of HER on Pt/CNT at different pH and c) onset overpotential for HER, $E_{\text{H}_2/\text{H}^+}^{\circ}$, determined from a).

Figure 9a shows the effect of changing electrolyte ionic strength on H_{upd} features in cyclic voltammetry on Pt/CNT. In contrast to changing pH, the peaks arising from underpotential deposited hydrogen formation on metal electrode surface, especially during anodic sweep, are

only slightly shifted towards more positive potentials when ionic strength is increased. The free energy of H_{upd} adsorption shows only very subtle deviations with altering electrolyte ionic strength (Figure 9b). Hence, the onset overpotential for hydrogen evolution on Pt, i.e., $E_{\text{H}_2/\text{H}^+}^{\circ}$ remains almost constant when varying the ion concentration of electrolyte. This is also observed in linear polarization measurements and *Tafel* analysis (Figure 9c). Nevertheless, the coverage of electrode surface with underpotential deposited hydrogen increases with lowering electrolyte ionic strength (SI Section 4, Figure S5). Consequently, adsorption enthalpy and entropy of H_{upd} formation on Pt surface at open circuit potential, i.e., $\Delta H_{\text{upd}}^{\circ}$, $\Delta S_{\text{upd}}^{\circ}$ are shifting with ionic concentration of aqueous phase (Figure S6). The $\Delta H_{\text{upd}}^{\circ}$ increases from -14.3 to -17.7 kJ/mol at IS = 0.60-4.50 M. The entropy is changing from -42.9 to -55.2 J/(mol·K) in the same range. Ryu and coworker found a change in selectivity of *cis*-2-butene-1,4-diol hydrogenation on Pt in aqueous phase that was attributed to a different migration of hydronium ions from bulk solution to metal surface depending on ionic strength.^[26] In their view, a low ion concentration leads to a pronounced accumulation of hydronium ions at Pt surface and hence, an increased interfacial acidity within electrochemical double-layer. As stated above, lowering the electrolyte pH weakens the binding of underpotential deposited hydrogen on Pt electrode surface.

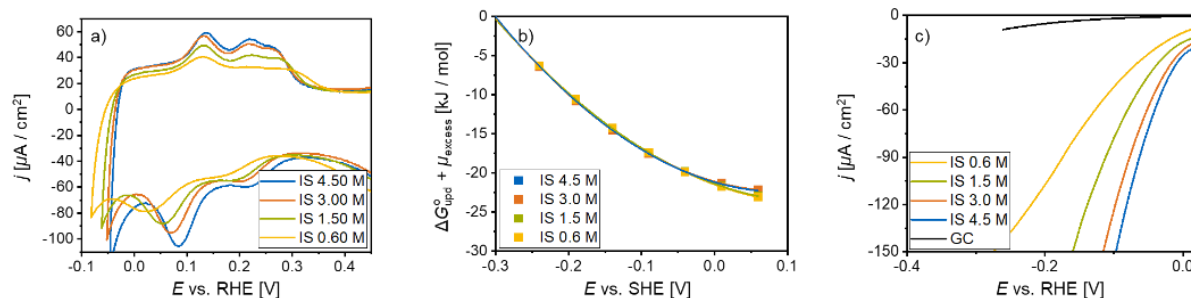


Figure 9: **a)** Features of H_{upd} adsorption in CV on Pt at different electrolyte ionic strength, **b)** development of $\Delta G_{\text{upd}}^{\circ} + \mu_{\text{excess}}$ with external electric potential on SHE scale and **c)** linear polarization curves of HER measured on Pt/CNT in aqueous phase at different ionic concentration.

Altering the electrolyte alkali metal cation (Li^+ , Na^+ , K^+) influences H_{upd} features on Pt in water (Figure 10a). In row of Li^+ , Na^+ and K^+ the binding strength of underpotential deposited hydrogen on Pt metal surface is gradually reduced. The $\Delta G_{\text{upd}}^{\circ} + \mu_{\text{excess}}$ is decreased when changing the electrolyte cation from lithium to sodium and further to potassium (Figure S7). Yet, this deviation of free energy of H_{upd} formation on Pt is rather subtle. Therefore, the onset potential for hydrogen evolution changes hardly, which is also observed in linear polarization measurements and *Tafel* analysis (Figure 10b-c). However, the temperature dependence of H_{upd} peaks allows for calculating a changing adsorption enthalpy of H_{upd} on Pt with respect to different cations (Figure S8). When potassium ions are present in the electrolyte the $\Delta H_{\text{upd}}^{\circ}$ is at

– 15.3 kJ/mol whereas it is around – 17.9 kJ/mol for lithium ion containing solutions. The entropy loss upon H_{upd} adsorption on electrode surface is increasing from – 44.7 J/(mol·K) for K^+ to – 53.7 J/(mol·K) in case of Li^+ . When comparing these results with literature values the picture gets quite ambiguous. *Bandarenka* et al. showed that the concentration of alkali metal cations, e.g., Li^+ , Na^+ , K^+ close to Pt electrode surface is up to 80 times higher than the respective concentration in bulk solution.^[27] They also showed that the activity for HER on Pt and Ir electrodes immersed in alkali metal cation containing electrolytes is increasing in the order of $Li^+ < Na^+ < K^+ Rb^+ < Cs^+$, which would mean an opposite trend to our results.^[28] However, it was again *Bandarenka* who found the former trend for HER/HOR and OER/OOR on Pt being changed in electrolytes containing sulfate ions.^[29] At this point, it cannot be excluded that the presence of phosphate ions in aqueous electrolytes used for these investigations influences the effect of alkali metal cations on H_{upd} formation on Pt in a similar way. Contrarily, *Marković* and coworker revealed that due to formation of $OH_{\text{ad}}-M^+(H_2O)_n$ clusters near the electrode surface, the size of which is depending on the cation radius, the electrocatalytic activity of Pt in water increases in the order of $Li^+ < Na^+ < K^+ < Cs^+$.^[30] This would be in line with findings of a decreasing binding strength of underpotential deposited hydrogen on Pt surface in row of $Li^+ > Na^+ > K^+$.

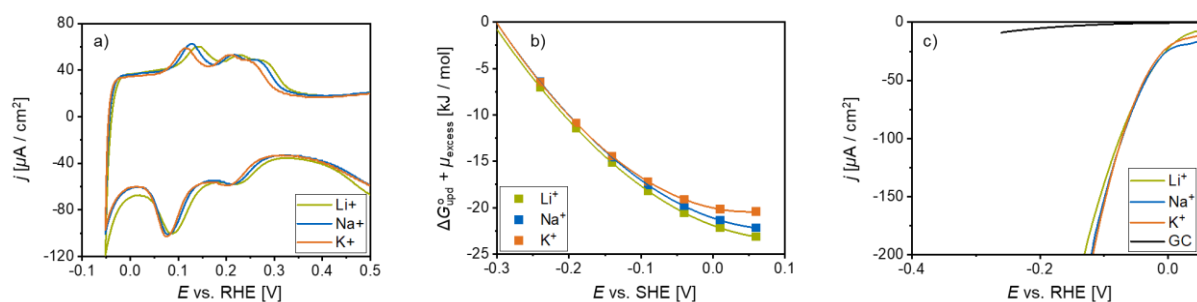


Figure 10: **a)** CV signals of underpotential deposited hydrogen on Pt, **b)** free energy of H_{upd} adsorption on metal surface as function of applied overpotential on SHE scale and **c)** linear polarization curves of HER on Pt/CNT, all measured in aqueous solutions containing various alkali metal cations.

Figure 11a plots the correlation between heat and entropy of H_{upd} adsorption on Pt electrode surface at open circuit potential for different electrolyte compositions. Due to the imposed equilibrium of $\Delta G_{\text{Volmer}} = 0$ the ΔH_{upd}^0 and ΔS_{upd}^0 change simultaneously. A rising adsorption enthalpy causes an increase in the adsorption entropy and *vice versa*. In general, the more the hydrogen atom is stabilized on metal electrode surface the less favoured hydrogen evolution reaction is, leading to a pronounced probability of H-atom being transferred to an organic molecule, e.g., benzaldehyde. Hence, an increasing binding strength of H on Pt surface favors electrocatalytic hydrogenation of benzaldehyde resulting in an improved *Faradaic* efficiency (FE) (Figure 11b-c). The largest FE of around 72% is reached in an aqueous electrolyte at pH 6.5. An electrolyte pH of 2 gives the lowest FE, which is around 35%. *Song* et al. showed

that FE of phenol ECH on Pt and Rh increases from 29 to 40% when going from pH 3 to 5 and from 44 to 95% in the pH range of 3-10, respectively.^[8]

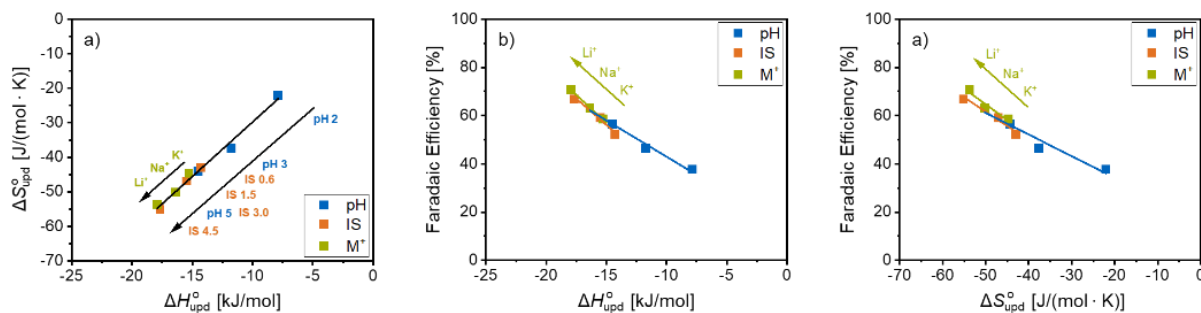


Figure 11: a) Correlation between $\Delta H_{\text{upd}}^{\circ}$ and $\Delta S_{\text{upd}}^{\circ}$ of H_{upd} formation on Pt for various electrolyte compositions, and b)-c) development of Faradaic efficiency with heat and entropy of H_{upd} adsorption.

A weak binding of H on Pt surface at low pH leads to improved activity for HER, i.e., *Tafel* slopes are increasing from -74.0 to -126.5 mV/dec at pH 2-5 (Figure S9, Table S3). This also enhances initial rates of benzaldehyde ECH (Figure 12a). The initial turnover frequency (TOF) increases from 150 to 500 1/h at pH 6-2. The rate of HER increases from 200-1300 1/h. This trend in TOF of ECH is in line with *Singh* and *Song* and coworker who revealed an enhancement of TOF of aqueous phase (electrocatalytic) phenol hydrogenation on Pt from 5 to 35 1/s and from 15 to 29 1/s, in the pH range of 10-1.^[8, 23] According to *Yang* et al. the TOF of aqueous phase phenol hydrogenation on zeolite supported Pt increases from 0.5 to 4.5 1/s when the *Brønsted* acid site (BAS) concentration of zeolite support is increased from 50 to 650 $\mu\text{mol/g}_{\text{zeolite}}$.^[31] *Chen* and coworker found a rate enhancement of aqueous phase phenol hydrogenation on Pt when going from pH 5 to pH 2, e.g., the turnover frequency increased by almost a factor of six, from 0.035 to 0.2 1/s.^[32]

The effect of ionic strength on stabilization of Pt-H and catalyst activity for HER and benzaldehyde ECH is rather small compared to changing electrolyte acidity. The *Tafel* slope of hydrogen evolution reaction decreases only from -172.4 to -124.8 mV/dec at IS = 0.60-4.50 M (Figure S9, Table S3). In the same IS range, the initial turnover frequency of electrocatalytic benzaldehyde hydrogenation increases from 200 to 300 1/h; the HER rate remains almost constant at around 400 1/h (Figure 12b). *Pfriem* et al. found a rate enhancement of phenol dehydration in aqueous phase from 0.01 to 0.08 1/s at IS = 0-5 M.^[33] Unlike the situation at varying electrolyte acidity where FE drops with increasing catalyst activity and decreasing hydrogen binding strength it increases with increasing ionic strength – from 52 to 67% at IS = 0.60-4.50 M. Therefore, it has to be assumed that changing the ionic environment in aqueous phase not only influences hydrogen binding on electrode surface but also the interaction between organic molecule and catalyst surface.

For altering alkali metal cations, no clear trend of catalyst activity in electrocatalytic hydrogenation and hydrogen evolution could be observed. As can be seen in linear polarization and *Tafel* analysis HER on Pt/*CNT* seems to be unaffected by changing the metal cations in aqueous phase (Figure S9, Table S3). The *Tafel* slope is around -120 to -125 mV/dec for all alkali metal cations investigated. Hence, the initial TOF of benzaldehyde ECH on Pt/*CNT* in lithium containing electrolyte, which is roughly 350 1/h, seems to be an outlier, especially as there is almost no change in TOF (250 1/h) for sodium and potassium containing solutions (Figure 12c).

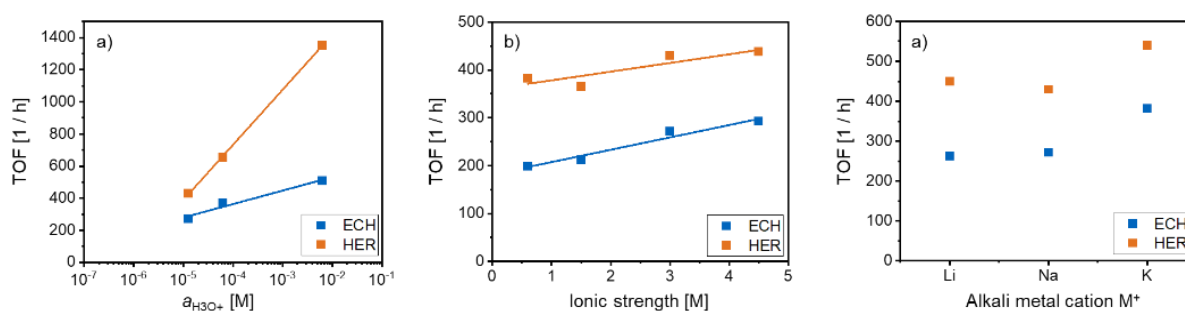


Figure 12: Initial turnover frequencies of electrocatalytic benzaldehyde hydrogenation and HER on Pt in aqueous electrolytes at different pH, ionic strength and alkali metal cations (a-c).

3.3 Discussion

The electrostatic energy that is stored within the electrochemical double-layer (EDL), E_e , is determined by the amount of charged species, e.g., hydronium ions, electrolyte cations, anions, which are accumulated within EDL (Equation 12a). This energy gives rise to a work that has to be paid for moving away EDL from metal electrode surface upon formation of underpotential deposited hydrogen (Equation 12b). *Yang et al.* showed from Density Functional Theory (DFT) based *ab initio* molecular dynamics (AIMD) simulations that the first water layer on Pt(111) is moved away by roughly 0.5 Å upon H adsorption (Figure 13).^[34]

$$E_e = \frac{q_e^2}{2\epsilon S} \quad (12a)$$

$$W = E_e \cdot \Delta d \cdot n_{\text{H}^+(\text{H}_2\text{O})_n}^2 \quad (12b)$$

The q_e is the charge stored within EDL, the ϵ is the electrolyte permittivity and the S is the Pt surface area. The Δd is the distance that EDL has to be displaced from electrode surface for H_{upd} formation and the $n_{\text{H}^+(\text{H}_2\text{O})_n}$ stands for the number of hydronium ions accumulated within *Helmholtz* layers.

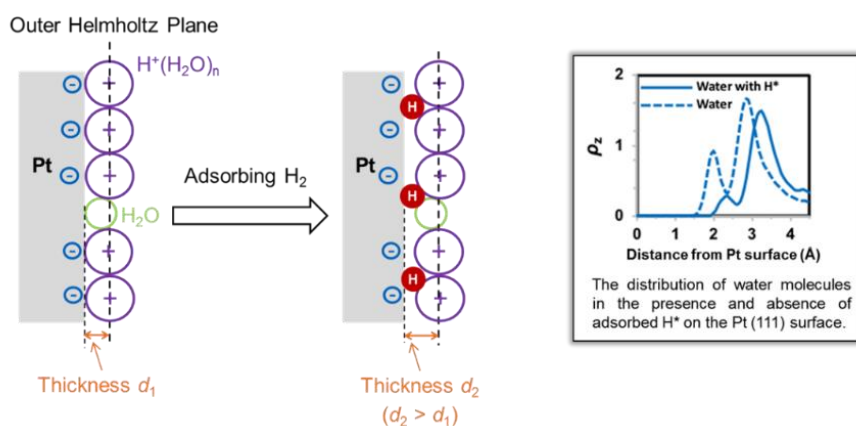


Figure 13: Displacement of EDL from electrode surface in presence and absence of adsorbed H upon Pt (left), and distance of first water layer from electrode surface in presence and absence of adsorbed H calculated *via* DFT based AIMD simulations according to *Yang et al.*^[34]

An increasing electrolyte acidity leads to an increased accumulation of charge within the electrochemical double-layer and hence, to a larger work that is necessary to shift away EDL from Pt surface. This energetic contribution gradually compensates the heat release upon adsorption of H_{upd} on metal surface. Therefore, binding strength of Pt-H is reduced and catalyst activity for HER and benzaldehyde ECH is increased. However, the *Faradaic* efficiency decreases with increasing acidity, which we currently hypothesize to be due to a non-optimum interaction between benzaldehyde molecules and Pt electrode surface, especially at low pH.

Janik et al. attributed a pH induced shift of H_{upd} binding strength to co-adsorption of hydroxide ions and alkali metal cations.^[35] They hypothesized that co-adsorption of OH^- in the H_{upd} region is more favored at low pH, disfavoring adsorption of H in highly acidic electrolytes. At increasing pH however, cation adsorption that repels OH^- gets more pronounced, making formation of H_{upd} more feasible. According to QMMD from *Goddard* and co-worker the large binding strength of underpotential deposited hydrogen at low concentration of H_3O^+ is caused by weakened water adsorption in alkaline media.^[22] Changing electrolyte pH from 0 to 13 charges Pt electrode surface more negatively by 0.75 V increasing its hydrophobic character and hindering water adsorption. *Surendranath* and coworker introduced the formation of a proton and/or electron-transfer induced electric field within EDL that influences the chemical potential of hydronium ions close to electrode surface and therefore, the rate of (electrocatalytic) hydrogenation.^[36] At low electrolyte pH the electric field is strong, becoming evident in a more positive open circuit potential and an increased hydrogenation rate (Figure 14). The development of E_{OCP} on Pt with electrolyte acidity follows *Nernst* equation with a slope of 55 and 61 mV/pH, respectively.

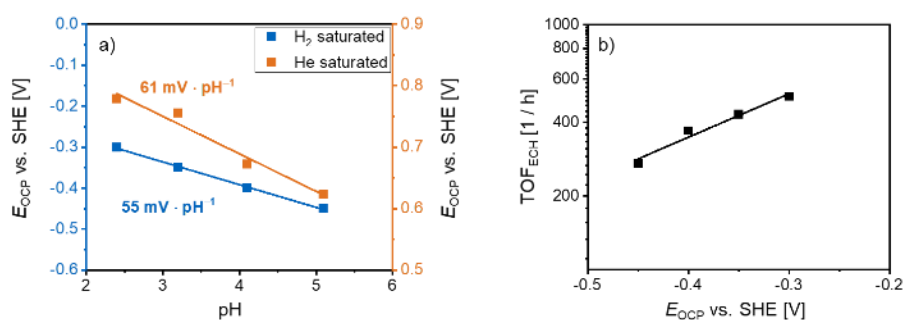


Figure 14: a) Open circuit potential of Pt as function of electrolyte pH measured in H_2 - and He-saturated solution and b) development of turnover frequency of benzaldehyde ECH with E_{OCP} .

Additionally, entropic changes during H_{upd} adsorption on Pt need to be considered when explaining pH-dependent stabilization of Pt-H. *Rossmesl* and coworker developed a model tackling different activities of HER in alkaline and acidic media based on entropic losses of hydronium ions during reductive adsorption on metal electrode surface.^[37] In their view, H_3O^+ ions from bulk solution are first transported towards the outer *Helmholtz* layer (OHL) followed by migration through EDL and H_{upd} formation (Figure 15). The authors propose that most of entropic changes happen already in the first transport step towards the outer boundary of EDL. There hydronium ions get immobilized in an intermediate state and lose part or all of their configurational entropy. The configurational entropy throughout the electrochemical double-layer is assumed to be constant. Thus, in alkaline electrolytes where there is low concentration of bulk H_3O^+ the entropic loss upon reaching the intermediate state at OHL is large, causing a large $\Delta H_{\text{upd}}^{\circ}$ ($\Delta G_{\text{Volmer}} = 0$) and slowing down HER kinetics. Contrarily, in acidic

electrolytes with a high hydronium ion concentration in bulk $\Delta S_{\text{upd}}^{\circ}$ and consequently, $\Delta H_{\text{upd}}^{\circ}$ are low, favoring hydrogen evolution reaction.

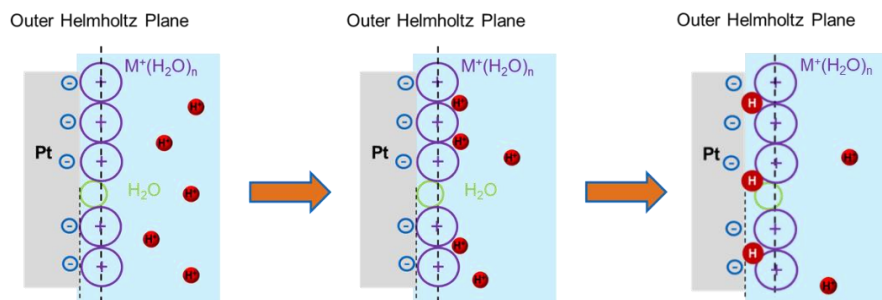


Figure 15: Transport and immobilization of hydronium ions from bulk solution to/at outer *Helmholtz* layer followed by formation of H_{upd} .

Currently, it can not be determined whether there is also an entropic effect arising from reorganization of water molecules that are displaced from electrode surface upon H_{upd} adsorption. This would explain the generally more positive adsorption entropy in liquid phase compared to gas phase, which is around $-125 \text{ J}/(\text{mol}\cdot\text{K})$, as molecules gain configurational entropy once they are released from the rigid structure within EDL.^[34] So, the entropic effects determined in this work might be a superposition of entropic changes arising from immobilization of hydronium ions and release of water molecules.

An increasing ionic strength is hypothesized to influence the concentration of hydronium ions close to electrode surface as well as the thickness of electrochemical double-layer (Figure 16a). Using a multi-ion surface charge-regulation model, *Barisik* et al. showed that for silica nanoparticles in aqueous phase the hydronium ion concentration close to particle surface is decreasing with increasing potassium concentration in bulk solution.^[38] According to the model introduced for different electrolyte pH this would mean a reduced work to move away EDL during H_{upd} formation and hence, a strong Pt-H bond. Additionally, *Brown* and coworker investigated the surface potential of silica nanoparticles in aqueous phase of different NaCl concentration *via* X-ray photoelectron spectroscopy (XPS) and revealed that the thickness of EDL decreases with increasing sodium concentration.^[39] Consequently, at high ionic strength the electrochemical double-layer is more rigid leading to a pronounced entropy loss upon immobilization of H_3O^+ at OHL. At current state, it can not be excluded whether there is an influence of electrolyte ionic strength on thermodynamic properties and binding strength of benzaldehyde on metal electrode surface. When increasing the electrolyte acidity from pH 5 to 2 the adsorption heat is decreased from -6.1 to $0 \text{ kJ}/\text{mol}$. The $\Delta S_{\text{BzHO}}^{\circ}$ is changing from 71.2 to $93.9 \text{ J}/(\text{mol}\cdot\text{K})$ in the same pH range. Decreasing the electrolyte ionic strength from 3.0 to 0.6 M alters the adsorption properties from -6.1 to $-12.4 \text{ kJ}/\text{mol}$ and from 71.2 to $50.2 \text{ J}/(\text{mol}\cdot\text{K})$, respectively (Figure S11). These numbers are in line with results from

Singh and coworker who found liquid phase phenol adsorption heat and entropy on Pt and Rh to be about -10 to -12 kJ/mol and in the range of 50 to 60 J/(mol·K), respectively.^[40] *Campbell* et al. determined a somewhat higher liquid phase adsorption enthalpy of benzaldehyde and phenol on Pt of around -40 kJ/mol.^[41] A decreased stabilization of organic molecules on electrode surface at high ionic strength could explain the slightly increased rate of benzaldehyde ECH at high IS. This explanation might also hold for increasing electrolyte acidity, however, with changing thermodynamic properties of H_{upd} adsorption overwhelming this aspect. *Eckstein* and coworker, for example, found an increasing adsorption heat of cyclohexanol in zeolite pores when the concentration of *Brønsted* acid sites and hence, the ionic strength within the pores of H-MFI is decreased.^[42]

It has to be noted that the values of $\Delta H_{\text{BzHO}}^{\circ}$ and $\Delta S_{\text{BzHO}}^{\circ}$ determined in this work are below the corresponding enthalpy and entropy for gas phase adsorption of organic molecules on noble metals. *Hammer* and coworker found an adsorption heat for gas phase benzaldehyde adsorption on Pt(111) of -100 kJ/mol.^[43] According to *Campbell* et al. phenol on Pt(111) has a gas phase adsorption heat of -200 kJ/mol.^[44] *Martin* and coworker calculated a standard gas phase entropy of benzaldehyde of 336 J/(mol·K).^[45] Using Equation 13 from *Sellers* et al. gives a gas phase adsorption entropy of benzaldehyde of -128 J/(mol·K), which is comparable to the value of $\Delta S_{\text{Phenol,gas}}^{\circ}$ from *Singh* et al., that is -122 J/(mol·K).^[40, 46] This difference between gas and liquid phase adsorption properties of organic molecules, e.g., benzaldehyde or phenol on noble metal catalysts is explained by displacement of water molecules from metal surface.^[40] This leads to an energetic contribution that compensates the heat release upon adsorption of organic molecules. Furthermore, the configurational entropy of water molecules increases upon being rejected from metal surface.

$$\Delta S_{\text{BzHO,gas}}^{\circ} = (0.70S_{\text{BzHO,gas}}^{\circ} - 3.3R) - S_{\text{BzHO,gas}}^{\circ} \quad (13)$$

Depending on the type of alkali metal cation in aqueous phase it can be assumed that the electrolyte pH in close proximity to Pt surface is different. Electrocatalytic hydrogenation and hydrogen evolution reaction lead to formation of a depletion region with respect to H_3O^+ close to electrode surface and hence, to an increase in local pH (Figure 16b).^[15b, 47] According to *Bell* et al. this increase in acidity can (partly) be compensated by the presence of hydrated alkali metal cations.^[48] The larger the cation radius the smaller the pK_a of $M^+(H_2O)_n$ and therefore, the more easy the hydrated cation is hydrolysed (Reaction 6). As the cation radius increases in order of $Li^+ < Na^+ < K^+$ the amount of H_3O^+ from hydrolysis increases in the same direction. The buffering effect is largest for K^+ and smallest for Li^+ , decreasing the local pH within EDL

in order of $\text{Li}^+ > \text{Na}^+ > \text{K}^+$. Hence, the work to displace the electrochemical double-layer from Pt surface increases in the same order as cation radius, gradually destabilizing Pt-H bond in water.

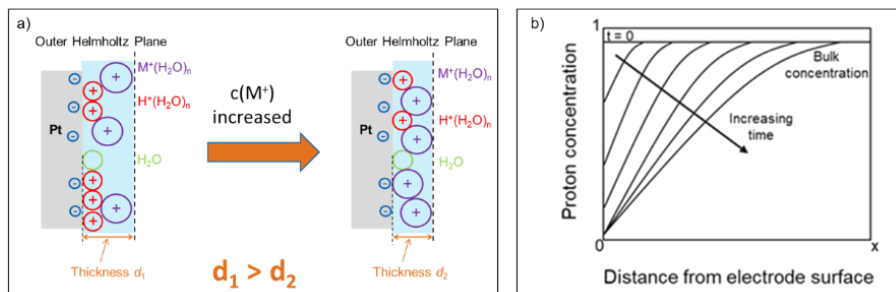
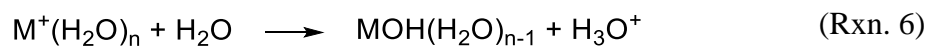


Figure 16: a) Composition of EDL at low (left) and high (right) ionic strength of bulk solution and b) depletion of hydronium ions close to electrode surface upon ECH and HER, respectively.

3.4 Conclusion

The composition of aqueous electrolytes influences the performance and activity of Pt/CNT in hydrogen evolution reaction and electrocatalytic benzaldehyde hydrogenation. Currently, it is assumed that these changes are mainly caused by the effect of electrolyte composition on electrocatalytic activation of H_3O^+ from bulk solution and stabilization of Pt-H. However, an influence on thermodynamic properties of adsorbed organic molecules, e.g., chemical potential, adsorption heat and entropy, can not be fully excluded. In general, a decreasing stabilization of Pt-H bond increases the initial rates of benzaldehyde ECH and HER while at the same time decreasing the reaction's *Faradaic* efficiency. Lowering the electrolyte pH and/or increasing its ionic strength leads to a reduced binding strength of benzaldehyde on Pt electrode surface. However, the effect on initial rates and FE is rather subtle and most likely overwhelmed by the impact of changing H_{upd} adsorption strength.

The strongest impact on $\Delta H_{\text{upd}}^\circ$ and $\Delta S_{\text{upd}}^\circ$ as well as on initial rates were observed for altering electrolyte acidity. This is explained by the work that has to be paid for moving away EDL from Pt electrode surface upon H_{upd} adsorption and the entropy loss of H_3O^+ upon being immobilized in an intermediate state at OHL. The effect of changing ion concentration and type of alkali metal cation is comparable and similar to that of varying pH though, it is less pronounced in both cases. For different ionic strength, the entropy loss of hydronium ions that depends on compactness of EDL at outer *Helmholtz* layer is hypothesized to mostly determine catalyst performance in HER and ECH. For different metal cations, the concentration of hydronium ions close to electrode surface is proposed to shift depending on the degree of cation hydrolysis. Hence, the work to displace EDL that partly compensates H_{upd} adsorption heat changes with respect to the type of alkali metal cation.

3.5 Supporting information

3.5.1 Experimental

Materials

Graphitized Multiwalled Carbon Nanotubes (GMWCNT, ≥ 99.9 wt%) with an outer diameter of 20-30 nm, an inner diameter of 5-10 nm and a length of 10-30 μm , in the following referred to as *CNT*, were purchased from *Cheap Tubes Inc.* In temperature programmed desorption (TPD) of ammonia and pyridine, *CNT* revealed a low amount of acid surface sites of only 75.6 and 72.2 $\mu\text{mol} / \text{g}_{\text{CNT}}$, respectively (Figure S1). A *PrismaTM* mass spectrometer from *Pfeiffer Vacuum* was used for recording MS-signals during NH_3 -TPD (500 $^\circ\text{C}$, 10 K min^{-1} , 60 min) that were normalized to H-MFI with a concentration of acid surface sites of 400 $\mu\text{mol} / \text{g}_{\text{H-MFI}}$. Pyridine-TPD (600 $^\circ\text{C}$, 5 K min^{-1} , 30 min, 50 mL min^{-1} N_2) was done on a TGA-MS setup with a *SENSYS evo* TG-DSC from *SETARAM Instrumentation* and an *OmniStarTM* mass spectrometer from *Pfeiffer Vacuum*.

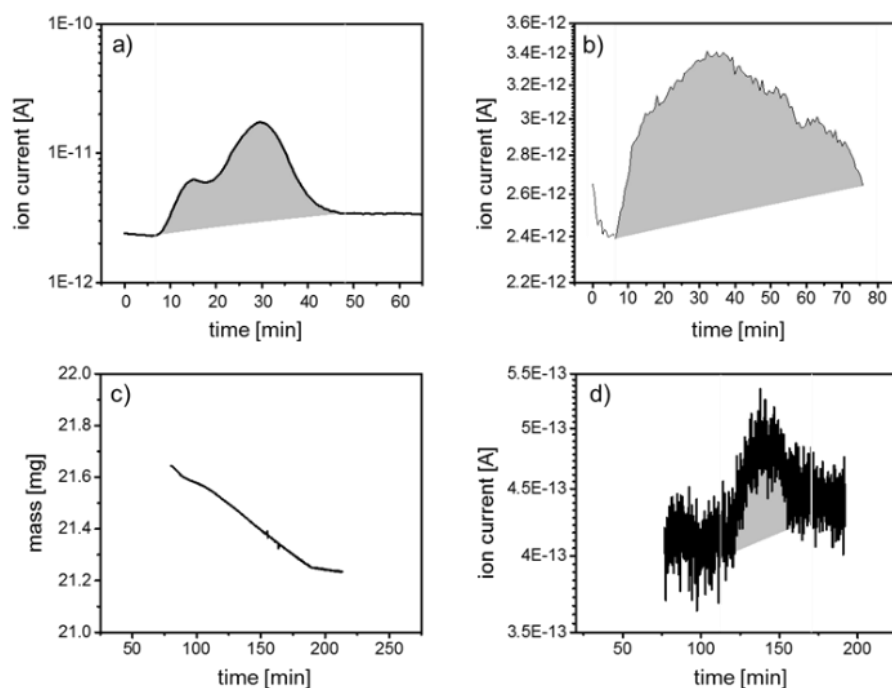


Figure S1: a) NH_3 -TPD signal of H-MFI, b) NH_3 -TPD signal of *CNT*, c-d) TGA- and pyridine MS-signals during pyridine-TPD performed on *CNT*.

Chloroplatinic acid hexahydrate ($\text{H}_2\text{PtCl}_6 \cdot 6\text{H}_2\text{O}$, $\geq 37.5\%$ Pt basis) as well as ethanol ($\geq 99.8\%$) were supplied by *Sigma-Aldrich*. Benzaldehyde ($\geq 99.5\%$) for electrocatalytic hydrogenation (ECH) experiments and *m*-cresol (for synthesis) for GC analysis were bought from *Sigma-Aldrich*. Sodium phosphate monobasic (NaH_2PO_4 , $\geq 99.0\%$), potassium phosphate monobasic (KH_2PO_4 , 99.5-100.5%), lithium phosphate monobasic (LiH_2PO_4 , 99%), sodium phosphate dibasic dihydrate ($\text{Na}_2\text{HPO}_4 \cdot 2\text{H}_2\text{O}$ $\geq 98.0\%$) and phosphoric acid (H_3PO_4 , $\geq 99.0\%$) were purchased from *Sigma-Aldrich*. Aqueous buffer solutions with different

pH, ionic strength and alkali metal cations were prepared by dissolving the required amounts of salts and phosphoric acid in 1 L ultrapure water with a resistivity of 18.2 M Ω from a *Purist* system supplied by *Rephile* (Table S1). All chemicals were used without further purification. Helium gas (He, 99.996 Vol%) for purging the electrolyte solution and hydrogen gas (H₂, 99.999 Vol%) for electrode calibration were both supplied by *Westfalen*.

Table S1: Amount of Na₂HPO₄ · 2H₂O, NaH₂PO₄, KH₂PO₄, LiH₂PO₄ and H₃PO₄ dissolved in 1.0 L ultrapure H₂O for electrolyte preparation.

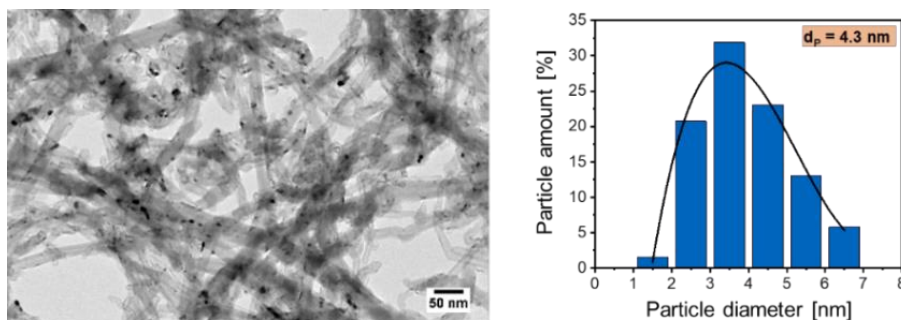
pH	IS [M]	M ⁺	m(Na ₂ HPO ₄ · 2H ₂ O) [g]	m(NaH ₂ PO ₄) [g]	m(H ₃ PO ₄) [g]	m(KH ₂ PO ₄) [g]	m(LiH ₂ PO ₄) [g]
2.4			---	30.0	24.5	---	---
3.1	3	Na	---	54.0	4.9	---	---
4.2			---	59.4	0.49	---	---
4.9			1.34	59.1	---	---	---
			2.00	88.6	---	---	---
4.9	3	Na	1.34	59.1	---	---	---
	1.5		0.67	29.5	---	---	---
	0.6		0.27	11.8	---	---	---
4.9	3	Li	1.34	---	---	---	51.2
		Na	1.34	59.1	---	---	---
		K	1.34	---	---	67.0	---

Catalyst synthesis

Platinum nanoparticles supported on *CNT* (Pt/*CNT*) were prepared *via* impregnation followed by reduction in H₂. Therefore, the desired amount of H₂PtCl₆ · 6H₂O to reach a 5 wt% metal loading (0.14 g) was dissolved in 200 mL ethanol. After addition of 1.00 g of *CNT* support the suspension was stirred and sonicated for 15 minutes, each. The suspension was alternatively stirred and sonicated three times. Afterwards, the solvent was evaporated, and the solid was dried at 60 °C overnight. The final catalyst was received after reducing the precipitate at 250 °C (0.5 K min⁻¹) for 3 hours under flowing H₂ (100 mL min⁻¹). In order to determine the metal particle size, the metal dispersion and the external surface area the final catalyst was analyzed *via* H₂ chemisorption and N₂ physisorption measurements using a *Surfer* station from *Thermo Fischer Scientific* and by transmission electron microscopy (TEM) (Figure S2). The exact metal loading of the catalyst was determined by atomic absorption spectroscopy (AAS) using an *iCE 3000 SERIES AA Spectrometer* from *Thermo Fisher Scientific*. The results are summarized in Table S2.

Table S2: Properties of 5 wt% Pt/CNT catalyst.

Metal concentration c_{Pt} [wt%]	4.6
Particle size d_p (TEM) [nm]	4.3
Particle size d_p (H₂ chemisorption) [nm]	4.3
Metal dispersion (TEM) [%]	23
Metal dispersion (H₂ chemisorption) [%]	25.6
External surface area [m² / g_{CNT}]	120

**Figure S2:** TEM image of 5 wt% Pt/CNT (left) and statistical evaluation of particle size (right).

The catalyst dispersion according to TEM was calculated based on the determined mean particle diameter d_p using Equations S1-S2.^[48]

$$d_p = \frac{\sum_{i=1}^n d_i^3}{\sum_{i=1}^n d_i^2} \quad (S1)$$

$$D = \frac{g \cdot V_{Pt}}{d_p \cdot S} \cdot 100 \quad (S2)$$

The d_i are the particle diameters measured from TEM images. The g refers to the particle shape correction factor that is 6 for spherical particles. The V_{Pt} refers to the volume per Pt atom calculated with a mean atomic radius of 1.5 Å. The S is the Pt average transversal section, which has a value of 8.9 Å².

Cyclic voltammetry and linear polarization

Cyclovoltammetry (CV) and linear polarization (LP) measurements were performed in a rotating disk electrode (RDE) setup using a *Modulated Speed Rotator* (MSR) and an RDE glass cell with water jacket both from *PINE research*. The electric potential was controlled with an *SP-300* potentiostat from *BioLogic*. In a three-electrode configuration, a glassy carbon RDE tip (5.0 mm OD) with catalyst coating (0.3 mg) was used as working electrode (WE). For catalyst coating, 2.0 mg of Pt/CNT was suspended in 200 μL ethanol and sonicated for 30 min. 30 μL of suspension were transferred onto glassy carbon disk and dried before immersion into electrolyte. A platinum wire served as counter electrode (CE) and an Ag/AgCl electrode was

used as reference electrode (RE). The RDE tip as well as CE and RE were purchased from *PINE research*. Before each experiment, the Ag/AgCl electrode was calibrated against a reversible hydrogen electrode (RHE). Therefore, its potential was measured against a platinum wire in a H₂ saturated electrolyte that was intended to be used in CV and LP measurements, respectively. The RDE glass cell was stored in a potassium permanganate solution prior to use to remove any organic contaminations. Before filling with electrolyte, it was flushed with a 3% H₂O₂ / 1 M H₂SO₄ solution followed by rinsing with ultrapure water. The WE, CE and RE were immersed in 100 mL phosphate buffer and the temperature (283-313 K) was adjusted with a *FC 600s* chiller from *Julabo*. The rotation speed of RDE tip was set to 400 rpm and the external electric potential was cycled and scanned between – 0.05 and 1.45 V vs. RHE and – 0.10 and 0.40 V vs. RHE during CV and LP, respectively. The scanning rate was 50 mV s⁻¹. Stable CV curves were reached after the tenth cycle. Excess H₂ and O₂ were removed from the electrolyte solution *via* purging with He (20 mL min⁻¹) throughout the experiments.

For determination of benzaldehyde adsorption heat and entropy on Pt, different concentrations of benzaldehyde (0-200 μM) were added to the electrolyte during CV.

The current density measured during CV was calculated by normalizing the measured current to the Pt surface area using the metal dispersion (Equations S3-S4).

$$n_{\text{Pt-Surf.}} = \frac{m_{\text{Cat}} \cdot c_{\text{Pt}} \cdot D}{M_{\text{Pt}}} \quad (\text{S3})$$

$$A_{\text{Pt-Surf.}} = \frac{n_{\text{Pt-Surf.}}}{2 \cdot 10^{-9}} \quad (\text{S4})$$

The m_{Cat} refers to the mass of catalyst, c_{Pt} refers to the metal concentration of the catalyst, D is its metal dispersion and M_{Pt} is the molecular weight of Pt.

Electrocatalytic hydrogenation of benzaldehyde

Electrocatalytic hydrogenation (ECH) experiments were performed in a two-compartment batch cell. In a three-electrode setup, the working and reference electrode (WE, RE) were placed in the cathode compartment. The counter electrode (CE) was located in the anode half-cell and both compartments were separated by a *Nafion*TM N117 membrane from *Ion Power*. The membrane was activated by a treatment in 3% H₂O₂ (1 h), deionized water (2 h) and 1 M H₂SO₄ (1 h) at 90 °C before storage in deionized water. The working electrode consisted of a carbon felt (30 × 15 × 6.35 mm) that was coated with Pt/CNT catalyst and attached to a titanium rod (Gr. 2). For catalyst coating, 20 mg of catalyst were suspended in 2 mL of an isopropyl alcohol/water (25/75 v/v) mixture. After sonication for 30 min the

suspension was drop casted onto the felt and allowed to dry at room temperature. The reference electrode was a leakless miniature Ag/AgCl reference electrode from *eDAQ* that was calibrated against RHE prior to each experiment. A Pt-wire ($\varnothing 1.0$ mm, 99.997%) from *Alfa Aesar* served as counter electrode. The potential during ECH was controlled *via* a *SP-300* potentiostat from *BioLogic*.

Before each experiment, the anode and cathode half-cells were filled with 60 mL aqueous electrolyte, of which the catholyte was stirred at 650 rpm throughout the whole experiment. Furthermore, the electrolyte was continuously purged with He (20 mL min^{-1}) to avoid accumulation of H_2 and O_2 from HER and OER at cathode and anode, respectively. After an initial polarization step of WE (-40 mA , 30 min) to assure for complete reduction of the Pt nanoparticles supported on *CNT*, the required amount of benzaldehyde to reach a 20 mM solution ($122 \mu\text{L}$) was added to the catholyte. Electrocatalytic hydrogenation was performed at an *jR*-corrected potential of $E = -0.05 \text{ V vs. RHE}$ at WE. All experiments were performed at room temperature.

During ECH runs, 0.5 mL aliquots were regularly withdrawn from the catholyte and extracted in 1.0 mL EtOAc. *m*-Cresol (5 mM) was added as external standard and the organic phase was analyzed by gas chromatography (GC). A *GC-2010 Plus* gas chromatograph with an *AOC 20i* autosampler from *Shimadzu* and a *DB-WAX* column (30 m, 0.32 mm, $0.25 \mu\text{m}$) from *Agilent Technologies* was used for investigating reaction kinetics of benzaldehyde ECH.

Turnover Frequencies (TOF) and initial rates (r_{init}) of product formation were calculated according to Equations S5-S6.

$$r_{\text{init}} = \frac{\partial n}{\partial t} \cdot \frac{1}{m_{\text{Pt-Surf.}}} \quad (\text{S5})$$

$$\text{TOF} = \frac{\partial n}{\partial t} \cdot \frac{1}{n_{\text{Pt-Surf.}}} \quad (\text{S6})$$

The $m_{\text{Pt-Surf.}}$ and $n_{\text{Pt-Surf.}}$ refer to the mass and mol of surface Pt that were determined from metal dispersion of the catalyst (Equations S7, S3).

$$m_{\text{Pt-Surf.}} = m_{\text{Cat}} \cdot c_{\text{Pt}} \cdot D \quad (\text{S7})$$

The m_{cat} refers to the mass of catalyst, c_{Pt} refers to the metal concentration of the catalyst and D is the metal dispersion of Pt/*CNT*.

The current efficiency, i.e., *Faradaic* efficiency (FE) of benzaldehyde ECH was calculated as the ratio between the amount of electric charge used for hydrogenation (Q_{ECH}), that equals the amount of product formed and the total charge passed through the cell (Q_{HER}), that is the amount

of hydrogen, which is activated *via* reduction of protons from electrolyte solution (Equations S8- S10).

$$Q_{\text{ECH}} = n_{\text{BzHO}} \cdot z \cdot N_{\text{A}} \cdot e \quad (\text{S8})$$

$$Q_{\text{HER}} = \int_0^t I \cdot dt \quad (\text{S9})$$

$$FE = \frac{Q_{\text{ECH}}}{Q_{\text{HER}}} \quad (\text{S10})$$

The n_{BzHO} refers to the amount of benzyl alcohol formed, the z is the number of electrons required for electrocatalytic benzaldehyde hydrogenation, which is two. The N_{A} is *Avogadro* constant, e refers to the elemental charge and I is the current passed through the cell. The t stands for the reaction time.

3.5.2 Calculation of free energy of H adsorption on Pt from H_{upd} peaks

The derivation of free energy of H adsorption on Pt ($\Delta G_{\text{upd}}^{\circ} + \mu_{\text{excess}}$) is based on the assumption of *Volmer* reaction (Rxn. 4) being quasi-equilibrated, i.e., the change in *Gibbs* free energy of the reaction being zero ($\Delta G = 0$) and the chemical potentials of reactants and products being equal (Equation S11).

$$\mu_{\text{H}^+} + \mu_{\text{el}} = \mu_{\text{H}} \quad (\text{S11})$$

With the expression of μ_{H^+} , μ_{H} and μ_{el} in Equations S12-S14, Equation S11 is reformulated to Equation S15.

$$\mu_{\text{el}} = -F\phi_{\text{Pt}} \quad (\text{S12})$$

$$\mu_{\text{H}^+} = \mu_{\text{H}^+}^{\circ} + RT \ln \frac{a_{\text{H}^+}}{a_{\text{H}^+}^{\circ}} + F\phi_{\text{aq}} \quad (\text{S13})$$

$$\mu_{\text{H}} = \mu_{\text{H}}^{\circ} + RT \ln \frac{\theta_{\text{H}}}{1 - \theta_{\text{H}}} + \mu_{\text{excess}} \quad (\text{S14})$$

$$\mu_{\text{H}}^{\circ} - \mu_{\text{H}^+}^{\circ} + \mu_{\text{excess}} + F(\phi_{\text{Pt}} - \phi_{\text{aq}}) = RT \ln \frac{a_{\text{H}^+}}{a_{\text{H}^+}^{\circ}} - RT \ln \frac{\theta_{\text{H}}}{1 - \theta_{\text{H}}} \quad (\text{S15})$$

The μ_{H^+} is the hydronium ion's chemical potential, and μ_{H} is the chemical potential of adsorbed H on Pt surface. The electron is treated as a reactant with a chemical potential (μ_{el}) that is its *Fermi* level according to *IUPAC* definition, which is determined by the electric potential on Pt, ϕ_{Pt} (Eq. S12). The μ_{H^+} consists of its standard chemical potential $\mu_{\text{H}^+}^{\circ}$, a thermodynamic activity (a_{H^+}) dependent term and an electrostatic potential energy term ($F\phi_{\text{aq}}$) that arises from the potential (ϕ_{aq}) in bulk electrolyte (Eq. S13). Here, F is *Faraday* constant. The μ_{H} comprises the standard chemical potential of H_{ads} (μ_{H}°), a term that is determined by the H_{upd} coverage (θ_{H}) and an excess chemical potential term μ_{excess} accounting for the effect from non-ideality (Eq. S14).

At open circuit potential, the system is essentially the reversible hydrogen electrode, i.e., the electric potential on Pt and in bulk aqueous phase are $\phi_{\text{Pt,RHE}}$ and $\phi_{\text{aq,RHE}}$. When applying an overpotential (η), the electrode potential has the following relations:

$$\phi_{\text{Pt}} - \phi_{\text{aq}} = \eta + (\phi_{\text{Pt,RHE}} - \phi_{\text{aq,RHE}}) \quad (\text{S16a})$$

$$\phi_{\text{Pt,RHE}} - \phi_{\text{aq,RHE}} = \phi_{\text{Pt,SHE}} - \phi_{\text{aq,SHE}} + RT \ln \frac{a_{\text{H}^+}}{a_{\text{H}^+}^\circ} \quad (\text{S16b})$$

Equation S16b is the relation between RHE and SHE (Standard Hydrogen Electrode) based on *Nernst* equation. Therefore, substituting the $(\phi_{\text{Pt}} - \phi_{\text{aq}})$ term in Equation S15 by Equation S16, gives:

$$\mu_{\text{H}}^\circ - (\mu_{\text{H}^+}^\circ + F\phi_{\text{aq,SHE}}) - (-F\phi_{\text{Pt,SHE}}) + \mu_{\text{excess}} = -RT \ln \frac{\theta_{\text{H}}}{1 - \theta_{\text{H}}} - F\eta \quad (\text{S17})$$

The first three terms on the left side of Equation 17 are the standard *Gibbs* free energy change ($\Delta G_{\text{upd}}^\circ$) of H_{upd} adsorption on Pt in aqueous electrolytes (Rxn 1), defined in Equation S18. Hence, using this relation Equation S17 can be rearranged to Equation S19 (free energy of H adsorption).

$$\Delta G_{\text{upd}}^\circ = \mu_{\text{H}}^\circ - (\mu_{\text{H}^+}^\circ + F\phi_{\text{aq,SHE}}) - (-F\phi_{\text{Pt,SHE}}) \quad (\text{S18})$$

$$\Delta G_{\text{upd}}^\circ + \mu_{\text{excess}} = -RT \ln \frac{\theta_{\text{H}}}{1 - \theta_{\text{H}}} - F\eta \quad (\text{S19})$$

3.5.3 Influence of electrolyte acidity on ΔH_{upd}

The free energy of H_{upd} adsorption on metal electrode surface was calculated for different pH using the temperature dependence of H_{upd} coverage on Pt from CV. Applying Equation S19, $\Delta G_{\text{upd}}^{\circ} + \mu_{\text{excess}}$ is shown as function of applied overpotential in Figure S3a,c,e,g for investigated electrolyte pH. Figure S3b,d,f,h plots the μ_{excess} with respect to external electric potential. The standard *Gibbs* free energy change $\Delta G_{\text{upd}}^{\eta=0} = \Delta G_{\text{upd}}^{\circ}$ is obtained from the y-intercept in Fig. S3a,c,e,g *via* extrapolation of $\Delta G_{\text{upd}}^{\circ} + \mu_{\text{excess}}$ to $\eta = 0$ V and is used to calculate the adsorption enthalpy and entropy at zero overpotential.

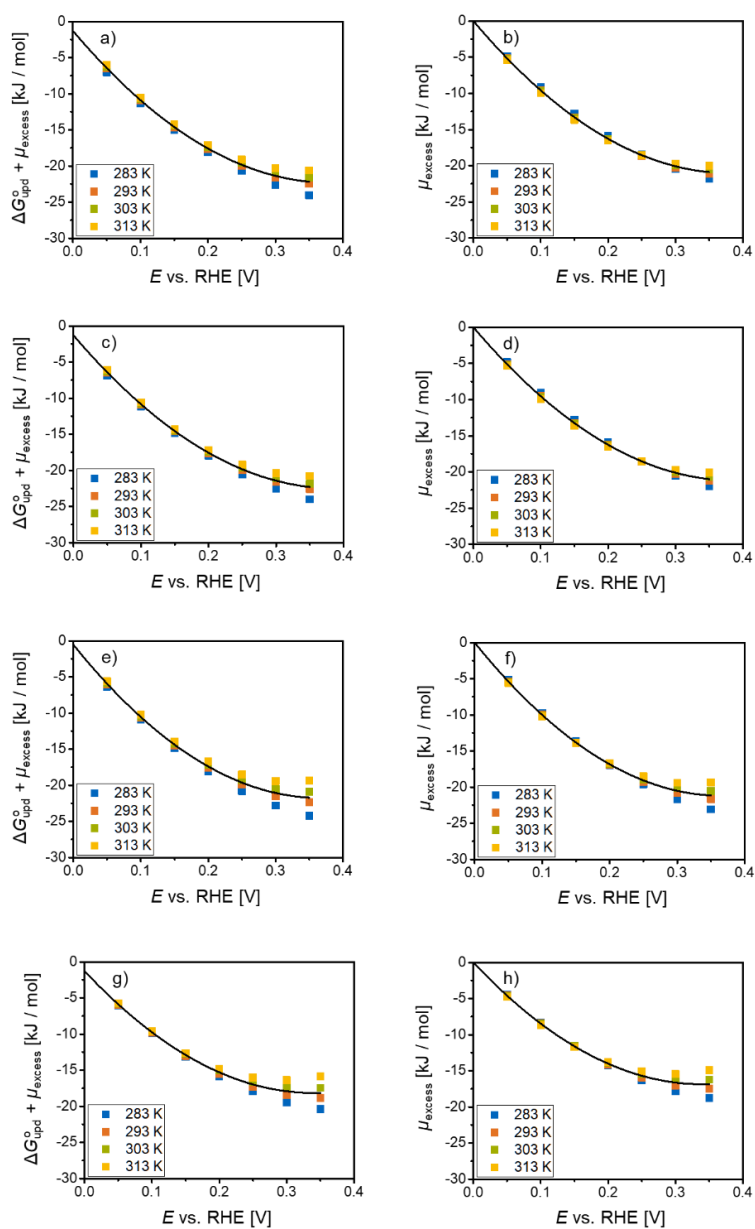


Figure S3: a),c),e),g) Development of free energy of H_{upd} formation on Pt with external electric potential and b),d),f),h) excess potential as function of applied overpotential, both at pH 2.4, 3.2, 4.1, 4.9.

Plotting $\Delta G_{\text{upd}}^{\circ} / T$ against $1/T$ allows for determining the adsorption heat and entropy of H_{upd} on Pt electrode surface from the slope and y-intercept of the resulting line plot (Figure S4).

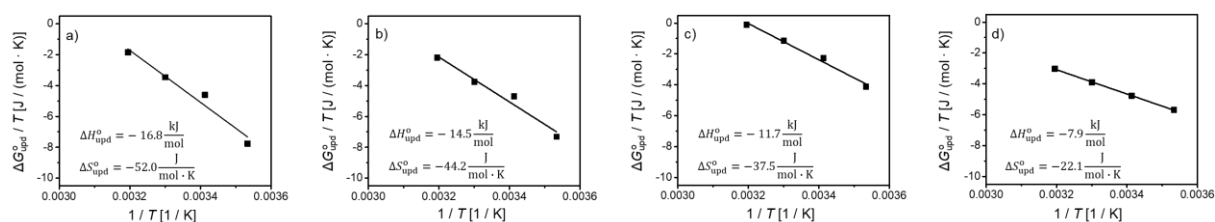


Figure S4: a)-d) Plot of linearized *Gibbs-Helmholtz* equation, $\Delta G_{\text{upd}}^{\circ} / T$ vs. $1/T$, for determining the heat and entropy of H_{upd} formation on electrode surface at OCP, i.e., $\Delta H_{\text{upd}}^{\circ}$, $\Delta S_{\text{upd}}^{\circ}$. a)-d) refer to the same solution pH as in Fig. S3.

3.5.4 Influence of electrolyte ionic strength on ΔH_{upd}

The free energy of underpotential deposited hydrogen formation on Pt surface was calculated for ionic strengths in the range of 0.60-4.50 M. Applying Equation S19, $\Delta G_{\text{upd}}^{\circ} + \mu_{\text{excess}}$ is shown as function of applied overpotential in Figure S5a,c,e,g for investigated electrolyte IS. Figure S5b,d,f,h plots the excess potential with respect to external electric potential. The standard *Gibbs* free energy change $\Delta G_{\text{upd}}^{\eta=0} = \Delta G_{\text{upd}}^{\circ}$ is obtained from the y-intercept in Fig. S5a,c,e,g *via* extrapolating $\Delta G_{\text{upd}}^{\circ} + \mu_{\text{excess}}$ to $\eta = 0$ V and is used to calculate the adsorption enthalpy and entropy at zero overpotential.

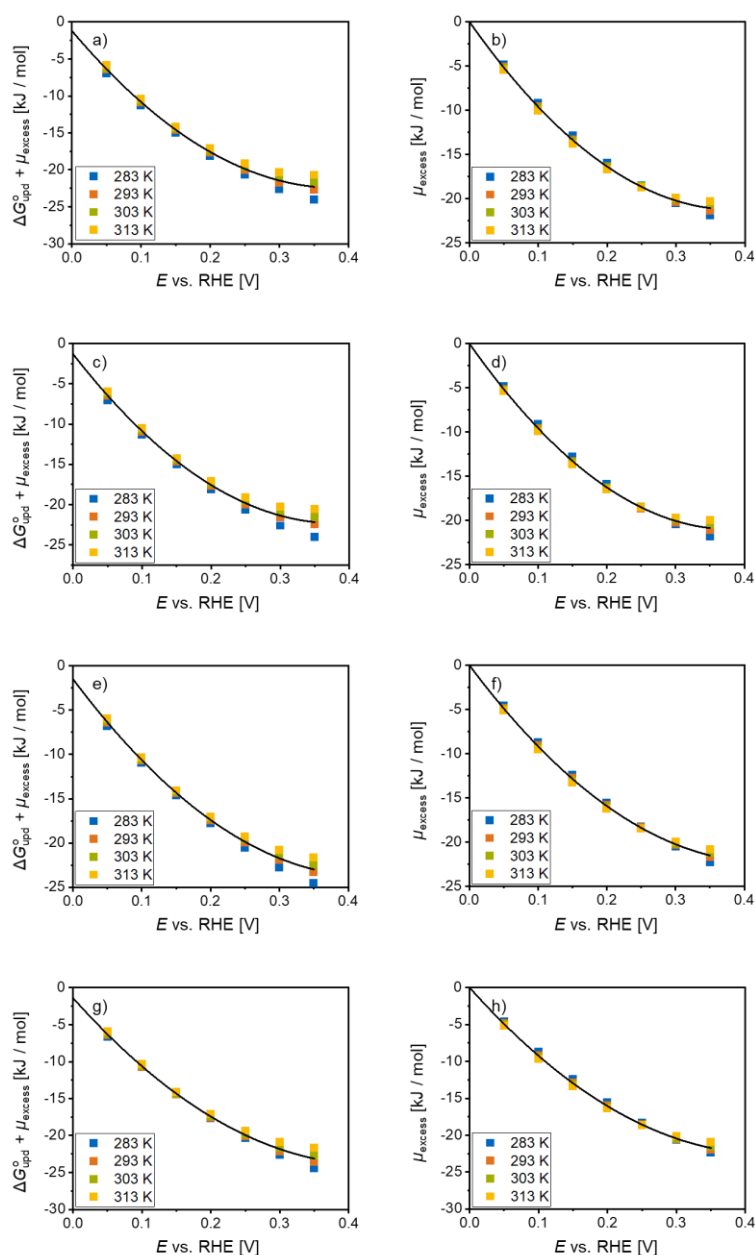


Figure S5: a),c),e),g) Free energy of H_{upd} adsorption on Pt as function of external electric potential and b),d),f),h) development of μ_{excess} with applied overpotential, both at IS = 4.5, 3.5, 1.5, 0.60 M.

Plotting $\Delta G_{\text{upd}}^{\circ} / T$ against $1/T$ allows for evaluating the $\Delta H_{\text{upd}}^{\circ}$ and $\Delta S_{\text{upd}}^{\circ}$ on Pt electrode surface from the slope and y-intercept of the resulting straight line (Figure S6).

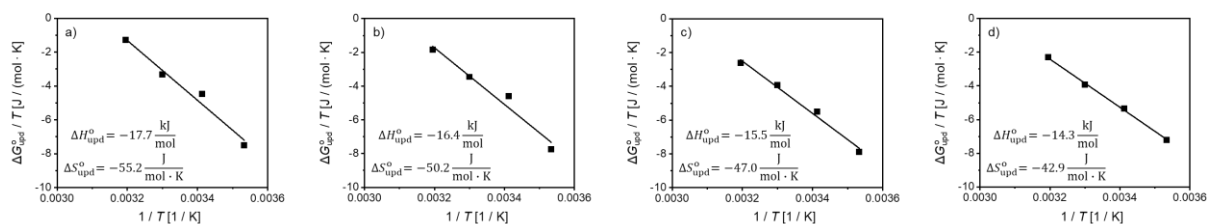


Figure S6: a)-d) Plot of linearized *Gibbs-Helmholtz* equation, $\Delta G_{\text{upd}}^{\circ} / T$ vs. $1/T$, for determining the heat and entropy of H_{upd} adsorption on electrode surface at OCP, i.e., $\Delta H_{\text{upd}}^{\circ}$, $\Delta S_{\text{upd}}^{\circ}$. a)-d) refer to the same ionic strength as in Fig. S5.

3.5.5 Influence of electrolyte cations on ΔH_{upd}

The $\Delta G_{\text{upd}}^{\circ} + \mu_{\text{excess}}$ of H_{upd} adsorption on Pt electrode was calculated for aqueous electrolytes containing different alkali metal cations, i.e., Li^+ , Na^+ , K^+ . Therefore, the temperature dependence of H_{upd} signals was evaluated and the free energy of H_{upd} formation is shown as function of external electric potential in Figure S7a,c,e. Figure S7b,d,f plots the μ_{excess} with respect to applied overpotential. The standard *Gibbs* free energy change $\Delta G_{\text{upd}}^{\eta=0} = \Delta G_{\text{upd}}^{\circ}$ is obtained from the y-intercept in Fig. S7a,c,e *via* extrapolation of $\Delta G_{\text{upd}}^{\circ} + \mu_{\text{excess}}$ to $\eta = 0$ V and is used to calculate the heat and entropy of H_{upd} adsorption at zero overpotential.

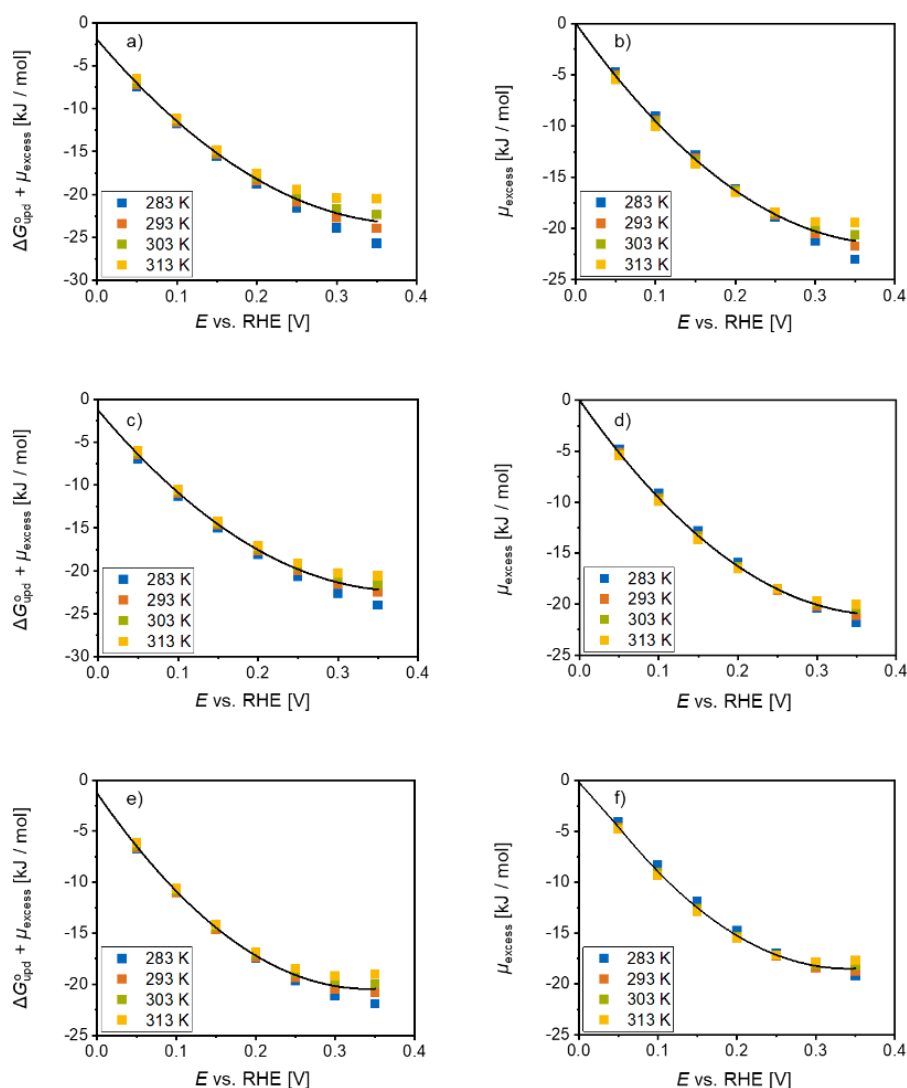


Figure S7: a),c),e) Dependence of $\Delta G_{\text{upd}}^{\circ} + \mu_{\text{excess}}$ of H_{upd} formation on metal surface on applied overpotential and b),d),f) development of excess potential with external electric potential, both for aqueous electrolytes containing Li^+ , Na^+ and K^+ .

Plotting $\Delta G_{\text{upd}}^{\circ} / T$ against $1/T$ allows for calculating the heat and entropy of H_{upd} adsorption on metal electrode surface, i.e., $\Delta H_{\text{upd}}^{\circ}$ and $\Delta S_{\text{upd}}^{\circ}$ from the slope and y-intercept of the graph (Figure S8).

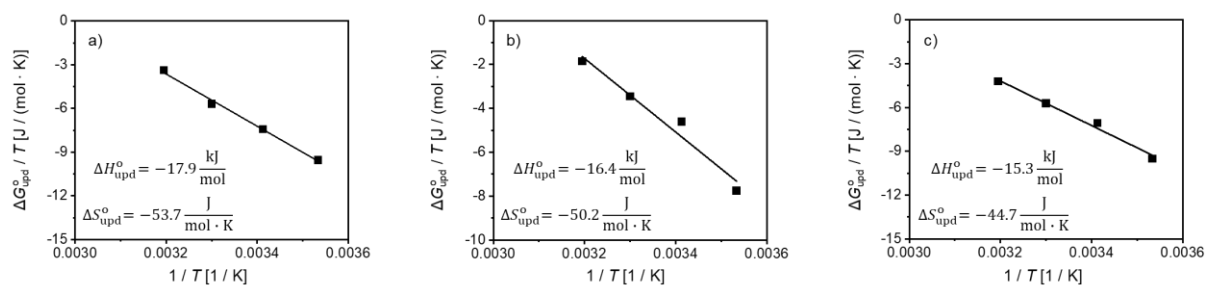


Figure S8: a)-c) Plot of linearized *Gibbs-Helmholtz* equation, $\Delta G_{\text{upd}}^0 / T$ vs. $1/T$, for evaluating the ΔH_{upd}^0 and ΔS_{upd}^0 on Pt surface at open circuit potential for Li⁺-, Na⁺- and K⁺-containing solutions.

3.5.6 Tafel analysis of polarization measurements

Polarization curves measured on Pt/CNT in aqueous electrolytes of different composition were evaluated according to *Tafel* analysis via plotting E_{RHE} vs. $\text{LOG}(|j| [\mu\text{A cm}^{-2}])$. *Tafel* slopes of hydrogen evolution reaction were determined from linear regions of *Tafel* plots (Figure S9, Table S3).

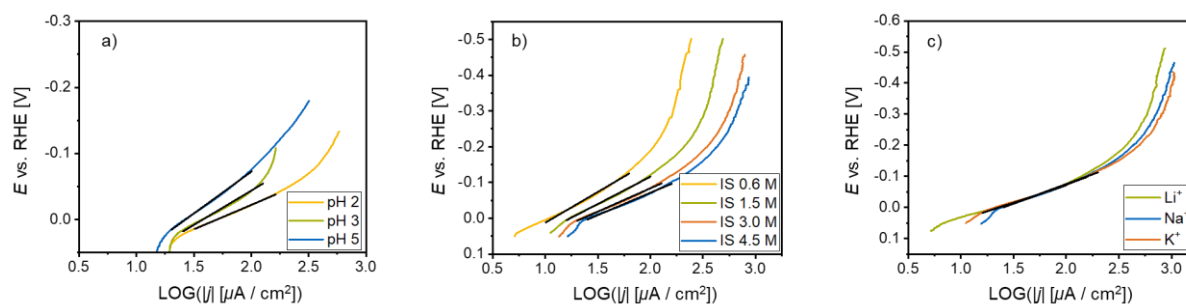


Figure S9: *Tafel* plots with *Tafel* slopes of linear polarization curves of HER on Pt/CNT in aqueous electrolytes at different pH (a) and IS (b) and with different alkali metal cations (c).

Table S3: *Tafel* slopes of HER on Pt/CNT in aqueous phase at different pH, IS and alkali metal cations.

pH	<i>Tafel</i> slope b_c [mV/dec]	IS [M]	<i>Tafel</i> slope b_c [mV/dec]	Cation M^+	<i>Tafel</i> slope b_c [mV/dec]
2	- 74.0	0.60	- 172.4	Li	- 122.5
3	- 103.8	1.50	- 152.4	Na	- 123.3
5	- 126.5	3.00	- 130.5	K	- 124.6
		4.50	- 124.8		

3.5.7 Calculation of thermodynamic properties of BzHO adsorption on Pt

The standard free energy of benzaldehyde adsorption on Pt in water ($\Delta G_{\text{BzHO}}^{\circ} = \Delta G_{\text{BzHO}}^{c=0}$) is calculated based on the assumption of Reaction 5 being quasi-equilibrated, i.e., the change in *Gibbs* free energy of the reaction being zero ($\Delta G = 0$) and the chemical potentials of reactants and products being equal (Equation S20).

$$\mu_{\text{H}^+} + \mu_{\text{el}} + \mu_{\text{BzHO}} = \mu_{\text{H}} + \mu_{\text{BzHO}^*} \quad (\text{S20})$$

With the expression of μ_{H^+} , and μ_{el} defined in Equations S12-S13 and the expressions of μ_{H} , μ_{BzHO} and μ_{BzHO^*} in Equations S21-S23, Equation S20 can be reformulated to Equation S24.

$$\mu_{\text{H}} = \mu_{\text{H}}^{\circ} + RT \ln \frac{\theta_{\text{H}}}{1 - \theta_{\text{H}} - \theta_{\text{BzHO}}} + \mu_{\text{excess}} \quad (\text{S21})$$

$$\mu_{\text{BzHO}} = \mu_{\text{BzHO}}^{\circ} + RT \ln c_{\text{BzHO}} \quad (\text{S22})$$

$$\mu_{\text{BzHO}^*} = \mu_{\text{BzHO}^*}^{\circ} + RT \ln \frac{\theta_{\text{BzHO}}}{1 - \theta_{\text{H}} - \theta_{\text{BzHO}}} \quad (\text{S23})$$

$$\begin{aligned} & \mu_{\text{H}}^{\circ} - \left(\mu_{\text{H}^+}^{\circ} + F\phi_{\text{aq,SHE}} \right) - \left(-F\phi_{\text{Pt,SHE}} \right) + \mu_{\text{excess}} + \mu_{\text{BzHO}^*}^{\circ} - \mu_{\text{BzHO}}^{\circ} = \\ & = RT \ln c_{\text{BzHO}} - RT \left(\ln \frac{\theta_{\text{H}}}{1 - \theta_{\text{H}} - \theta_{\text{BzHO}}} + \frac{\theta_{\text{BzHO}}}{1 - \theta_{\text{H}} - \theta_{\text{BzHO}}} \right) - F\eta \end{aligned} \quad (\text{S24})$$

The μ_{BzHO} is the chemical potential of benzaldehyde in aqueous phase that is determined by its standard chemical potential ($\mu_{\text{BzHO}}^{\circ}$) and its concentration in water (c_{BzHO}). The μ_{BzHO^*} is the chemical potential of benzaldehyde adsorbed on Pt surface consisting of the standard chemical potential of adsorbed BzHO ($\mu_{\text{BzHO}^*}^{\circ}$) and a term depending on electrode coverage with H_{upd} and benzaldehyde (θ_{H} , θ_{BzHO}). In Eq. S24, the derivation for H_{upd} formation on Pt from Section 2 of SI is extended by the influence of parallel adsorption of benzaldehyde. The recalculation of electric potentials ϕ_{Pt} and ϕ_{aq} from absolute to RHE scale is shown in Equation S16.

Hence, the left side of Equation S24 comprises the standard free energy of H_{upd} adsorption on Pt on RHE scale (Equation S18), an excess chemical potential, i.e., an excess free energy of H_{upd} adsorption and the standard free energy of benzaldehyde adsorption on Pt in aqueous phase (Equations S25-S26).

$$\Delta G_{\text{BzHO}}^{\circ} = \mu_{\text{BzHO}^*}^{\circ} - \mu_{\text{BzHO}}^{\circ} \quad (\text{S25})$$

$$\Delta G_{\text{BzHO}}^{\circ} = RT \ln c_{\text{BzHO}} - RT \left(\ln \frac{\theta_{\text{H}}}{1 - \theta_{\text{H}} - \theta_{\text{BzHO}}} + \frac{\theta_{\text{BzHO}}}{1 - \theta_{\text{H}} - \theta_{\text{BzHO}}} \right) - F\eta - \left(\Delta G_{\text{upd}}^{\circ} + \mu_{\text{excess}} \right) \quad (\text{S24})$$

Figure S10 shows $\Delta G_{\text{BzHO}}^{\circ}$ on Pt as a function of benzaldehyde concentration at $E_{\text{RHE}} = 0.05$ V for three different electrolytes, i.e., pH 2 (IS = 3.0 M), pH 5 (IS = 3.0 M), IS = 0.6 M (pH 5).

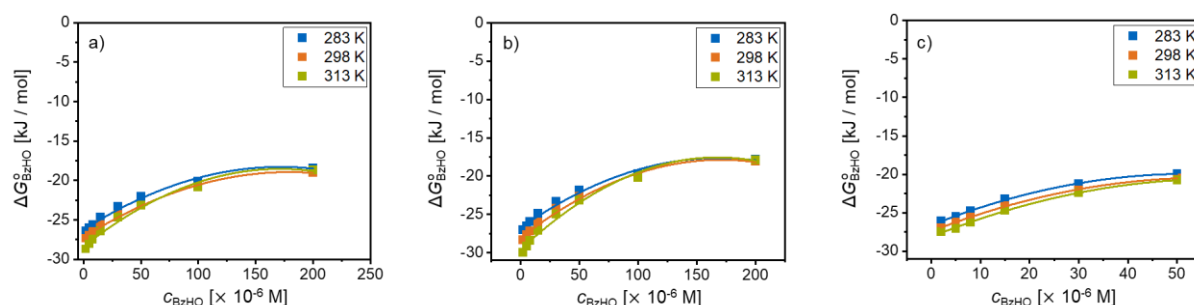


Figure S10: Development of standard free energy of benzaldehyde adsorption on Pt ($\Delta G_{\text{BzHO}}^{\circ}$) with benzaldehyde concentration at $E_{\text{RHE}} = 0.05$ V in aqueous electrolytes of pH 4.9 and IS = 3.0 M (a), pH 2.4 and IS = 3.0 M (b) and pH 4.9 and IS = 0.6 M (c).

Extrapolating the plots of $\Delta G_{\text{BzHO}}^{\circ}$ vs. c_{BzHO} to zero concentration and inserting the resulting standard free energies of benzaldehyde adsorption into linearized *Gibbs-Helmholtz* equation gives the standard heat and entropy of benzaldehyde adsorption on Pt, that is the slope and y-intercept of $\Delta G_{\text{BzHO}}^{\circ} / T$ vs. $1/T$ plot (Figure S11).

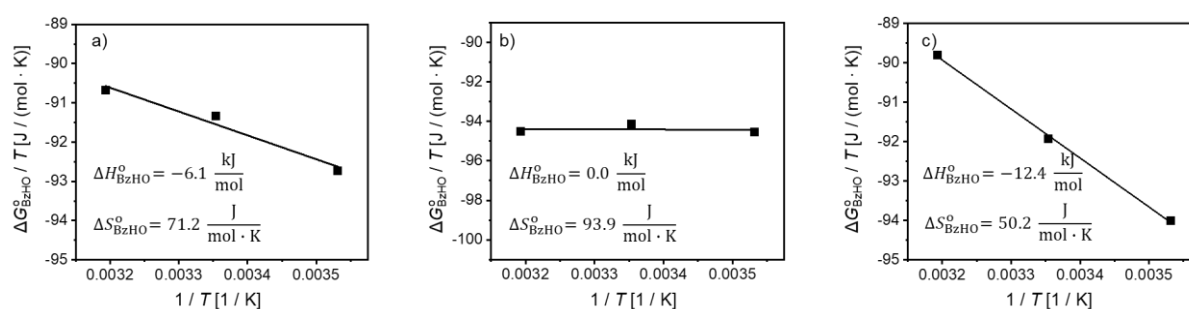


Figure S11: a)-c) Plot of linearized *Gibbs-Helmholtz* equation, $\Delta G_{\text{BzHO}}^{\circ} / T$ vs. $1/T$, for determining the heat and entropy of benzaldehyde adsorption on electrode surface at zero concentration of BzHO and $E_{\text{RHE}} = 0.05$ V, i.e., $\Delta H_{\text{BzHO}}^{\circ}$, $\Delta S_{\text{BzHO}}^{\circ}$. a)-c) refer to the same solution composition as in Fig. S10.

3.6 References

- [1] a) A. F. Ghoniem, *Progress in Energy and Combustion Science* **2011**, *37*, 15-51; b) F. Johnsson, J. Kjærstad, J. Rootzén, *Climate Policy* **2019**, *19*, 258-274; c) N. Bauer, I. Mouratiadou, G. Luderer, L. Baumstark, R. J. Brecha, O. Edenhofer, E. Kriegler, *Climatic Change* **2016**, *136*, 69-82.
- [2] a) B. M. Upton, A. M. Kasko, *Chemical Reviews* **2016**, *116*, 2275-2306; b) G. W. Huber, S. Iborra, A. Corma, *Chemical Reviews* **2006**, *106*, 4044-4098.
- [3] A. V. Bridgwater, *Biomass and Bioenergy* **2012**, *38*, 68-94.
- [4] C. H. Lam, S. Das, N. C. Erickson, C. D. Hyzer, M. Garedew, J. E. Anderson, T. J. Wallington, M. A. Tamor, J. E. Jackson, C. M. Saffron, *Sustainable Energy & Fuels* **2017**, *1*, 258-266.
- [5] a) S. A. Akhade, N. Singh, O. Y. Gutiérrez, J. Lopez-Ruiz, H. Wang, J. D. Holladay, Y. Liu, A. Karkamkar, R. S. Weber, A. B. Padmaperuma, M.-S. Lee, G. A. Whyatt, M. Elliott, J. E. Holladay, J. L. Male, J. A. Lercher, R. Rousseau, V.-A. Glezakou, *Chemical Reviews* **2020**, *120*, 11370-11419; b) E. J. Biddinger, O. Y. Gutierrez, J. Holladay, *Journal of Applied Electrochemistry* **2021**, *51*, 1-3; c) L. Zhang, T. U. Rao, J. Wang, D. Ren, S. Sirisomboonchai, C. Choi, H. Machida, Z. Huo, K. Norinaga, *Fuel Processing Technology* **2022**, *226*, 107097.
- [6] K. Li, Y. Sun, *Chemistry – A European Journal* **2018**, *24*, 18258-18270.
- [7] Y. Song, U. Sanyal, D. Pangotra, J. D. Holladay, D. M. Camaioni, O. Y. Gutiérrez, J. A. Lercher, *Journal of Catalysis* **2018**, *359*, 68-75.
- [8] Y. Song, O. Y. Gutiérrez, J. Herranz, J. A. Lercher, *Applied Catalysis B: Environmental* **2016**, *182*, 236-246.
- [9] J. A. Lopez-Ruiz, U. Sanyal, J. D. Egbert, O. Y. Gutiérrez, J. D. Holladay, *ACS Sustainable Chemistry & Engineering* **2018**, *6*, 16073-16085.
- [10] a) N. Singh, U. Sanyal, G. Ruehl, K. A. Stoerzinger, O. Y. Gutiérrez, D. M. Camaioni, J. L. Fulton, J. A. Lercher, C. T. Campbell, *Journal of Catalysis* **2020**, *382*, 372-384; b) C. H. Lam, W. Deng, L. Lang, X. Jin, X. Hu, Y. Wang, *Energy & Fuels* **2020**, *34*, 7915-7928.
- [11] a) T. Kan, V. Strezov, T. J. Evans, *Renewable and Sustainable Energy Reviews* **2016**, *57*, 1126-1140; b) D. K. Ratnasari, A. Bijl, W. Yang, P. G. Jönsson, *Catalysts* **2020**, *10*.
- [12] G. Liang, A. Wang, L. Li, G. Xu, N. Yan, T. Zhang, *Angewandte Chemie International Edition* **2017**, *56*, 3050-3054.
- [13] J. T. Bhanushali, I. Kainthla, R. S. Keri, B. M. Nagaraja, *ChemistrySelect* **2016**, *1*, 3839-3853.
- [14] U. Sanyal, J. Lopez-Ruiz, A. B. Padmaperuma, J. D. Holladay, O. Y. Gutiérrez, *Organic Process Research & Development* **2018**, *22*, 1590-1598.
- [15] a) C. H. Hamann, A. Hamnett, W. Vielstich, *Electrochemistry. Weinheim: Wiley-VCH* **1998**, 12-65; b) N. Eliaz, E. Gileadi, *Physical Electrochemistry: Fundamentals, Techniques, and Applications*, John Wiley & Sons, **2019**.
- [16] J. O. M. Bockris, B. E. Conway, E. B. Yeager, *The Double Layer*, Plenum Press, **1980**.
- [17] P. T. Kissinger, W. R. Heineman, *Journal of Chemical Education* **1983**, *60*, 702.
- [18] N. M. Marković, T. J. Schmidt, B. N. Grgur, H. A. Gasteiger, R. J. Behm, P. N. Ross, *The Journal of Physical Chemistry B* **1999**, *103*, 8568-8577.
- [19] S. Surendralal, M. Todorova, J. Neugebauer, *Physical review letters* **2021**, *126* 16, 166802.
- [20] a) B. Hammer, J. K. Nørskov, *Surface Science* **1995**, *343*, 211-220; b) G. L. Miessler, P. J. Fischer, D. A. Tarr, *Inorganic Chemistry*, Pearson, **2014**.
- [21] a) W. Sheng, Z. Zhuang, M. Gao, J. Zheng, J. G. Chen, Y. Yan, *Nature Communications* **2015**, *6*, 5848; b) X. Yang, J. Nash, N. Oliveira, Y. Yan, B. Xu, *Angew. Chem., Int. Ed.* **2019**, *58*, 17718-17723.
- [22] T. Cheng, L. Wang, B. V. Merinov, W. A. Goddard, *Journal of the American Chemical Society* **2018**, *140*, 7787-7790.
- [23] N. Singh, M.-S. Lee, S. A. Akhade, G. Cheng, D. M. Camaioni, O. Y. Gutiérrez, V.-A. Glezakou, R. Rousseau, J. A. Lercher, C. T. Campbell, *ACS Catalysis* **2019**, *9*, 1120-1128.
- [24] I. Ledezma-Yanez, W. D. Z. Wallace, P. Sebastián-Pascual, V. Climent, J. M. Feliu, M. T. M. Koper, *Nature Energy* **2017**, *2*, 17031.
- [25] P. S. Lamoureux, A. R. Singh, K. Chan, *ACS Catal.* **2019**, *9*, 6194-6201.
- [26] J. Ryu, Y. Surendranath, *Journal of the American Chemical Society* **2019**, *141*, 15524-15531.
- [27] B. Garlyyev, S. Xue, S. Watzele, D. Scieszka, A. S. Bandarenka, *The Journal of Physical Chemistry Letters* **2018**, *9*, 1927-1930.
- [28] S. Xue, B. Garlyyev, S. Watzele, Y. Liang, J. Fichtner, M. D. Pohl, A. S. Bandarenka, *ChemElectroChem* **2018**, *5*, 2326-2329.
- [29] J. Tymoczko, V. Colic, A. Ganassin, W. Schuhmann, A. S. Bandarenka, *Catal. Today* **2015**, *244*, 96-102.
- [30] D. Strmcnik, K. Kodama, D. van der Vliet, J. Greeley, V. R. Stamenkovic, N. M. Marković, *Nature Chemistry* **2009**, *1*, 466-472.

- [31] G. Yang, V. Maliekkal, X. Chen, S. Eckstein, H. Shi, D. M. Camaioni, E. Baráth, G. L. Haller, Y. Liu, M. Neurock, J. A. Lercher, *Journal of Catalysis* **2021**, *404*, 579-593.
- [32] X. Chen, Y. Liu, J. A. Lercher, *ECS Meeting Abstracts* **2021**, *MA2021-02*, 792-792.
- [33] N. Pfried, H. Hintermeier Peter, S. Eckstein, S. Kim, Q. Liu, H. Shi, L. Milakovic, Y. Liu, L. Haller Gary, E. Baráth, Y. Liu, A. Lercher Johannes, *Science* **2021**, *372*, 952-957.
- [34] G. Yang, S. A. Akhade, X. Chen, Y. Liu, M.-S. Lee, V.-A. Glezakou, R. Rousseau, J. A. Lercher, *Angew. Chem., Int. Ed.* **2019**, *58*, 3527-3532.
- [35] I. T. McCrum, M. J. Janik, *J. Phys. Chem. C* **2016**, *120*, 457-471.
- [36] T. S. Wesley, Y. Román-Leshkov, Y. Surendranath, *ACS Central Science* **2021**, *7*, 1045-1055.
- [37] J. Rossmeisl, K. Chan, E. Skúlason, M. E. Björketun, V. Tripkovic, *Catalysis Today* **2016**, *262*, 36-40.
- [38] M. Barisik, S. Atalay, A. Beskok, S. Qian, *The Journal of Physical Chemistry C* **2014**, *118*, 1836-1842.
- [39] M. A. Brown, A. Goel, Z. Abbas, *Angewandte Chemie International Edition* **2016**, *55*, 3790-3794.
- [40] J. Akinola, N. Singh, *Journal of Applied Electrochemistry* **2021**, *51*, 37-50.
- [41] N. Singh, U. Sanyal, J. L. Fulton, O. Y. Gutiérrez, J. A. Lercher, C. T. Campbell, *ACS Catalysis* **2019**.
- [42] S. Eckstein, P. H. Hintermeier, R. Zhao, E. Baráth, H. Shi, Y. Liu, J. A. Lercher, *Angewandte Chemie International Edition* **2019**, *58*, 3450-3455.
- [43] A. M. H. Rasmussen, B. Hammer, *The Journal of Chemical Physics* **2012**, *136*, 174706.
- [44] S. J. Carey, W. Zhao, Z. Mao, C. T. Campbell, *The Journal of Physical Chemistry C* **2019**, *123*, 7627-7632.
- [45] D. Ambrose, J. E. Connett, J. H. S. Green, J. L. Hales, A. J. Head, J. F. Martin, *The Journal of Chemical Thermodynamics* **1975**, *7*, 1143-1157.
- [46] C. T. Campbell, J. R. V. Sellers, *Journal of the American Chemical Society* **2012**, *134*, 18109-18115.
- [47] Z. Stojek, in *Electroanalytical Methods* (Ed.: F. Scholz), Springer, **2010**.
- [48] M. R. Singh, Y. Kwon, Y. Lum, J. W. Ager, A. T. Bell, *Journal of the American Chemical Society* **2016**, *138*, 13006-13012.
- [48] A. Borodziński, M. Bonarowska, *Langmuir* **1997**, *13*, 5613-5620.

3.7 Associated content

Publication

This chapter is based on a manuscript planned for submission (Philipp Fischer, Yue Liu, Johannes A. Lercher)

Contributions

P.F. did main contributions in catalyst preparation, CV, LP and kinetic measurements, data analysis and manuscript preparation. Y.L. contributed to data analysis and manuscript preparation. Y.L. and J.A.L. conceived the research. The manuscript was written through contributions of all authors.

Acknowledgements

The authors would like to thank German Research Foundation DFG, the Federal Ministry of Education and Research of Germany as well as the Bavarian Ministry of Science and Art and the cluster of e-conversion for their support. Xaver Hecht, Muhammad Iqbal and Andreas Marx are thanked for their technical support and measuring H₂ chemisorption as well as N₂ physisorption, Martin Neukamm for doing elemental analysis and Roland Weindl as well as Simon Krebs for measuring TEM. Christian Heiß and Angelina Cuomo are thanked for their help in experimental work.

4 Electrocatalytic hydrogenation of α,β -unsaturated aldehydes – Influence of external electric potential, electrolyte composition and catalyst structure on carbonyl-group activation

Abstract

Hydrogenation of α,β -unsaturated aldehydes on noble metal catalysts in water usually suffers from low selectivity for carbonyl group hydrogenation. On most common hydrogenation catalysts conversion of the double bond is thermodynamically favored over formation of alcohols.

The selectivity of electrocatalytic *trans*-2-penten-1-al hydrogenation in aqueous phase can be influenced *via* choice of noble metal, promoter species and variation of the externally applied electric potential. Additionally, electrolyte pH, catalyst support acidity as well as metal particle size play a minor role in tuning reaction selectivity. Best yields of (un)saturated alcohols were achieved with a Ru-based catalyst that was doped with Fe as electropositive promoter. The selectivity towards CO group hydrogenation raises at increasing cathodic overpotential. These findings are supported by adsorption isotherm measurements performed *via* standard volumetric method and cyclic voltammetry.

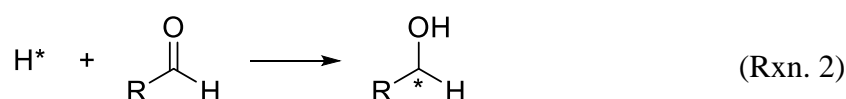
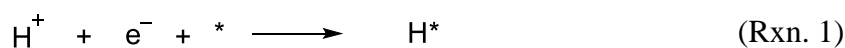
Decreasing the hydronium ion concentration in bulk solution and increasing the mean particle diameter of catalyst material also help to improve alcohol formation. The effect of altering the concentration of acid surface sites on carbon nanotube support is ambiguous.

Product formation rates on bimetallic Ru-Fe catalysts are enhanced by rising negative overpotential, increasing support acidity and larger metal particle size.

4.1 Introduction

Biomass is a green and sustainable alternative to fossil resources like crude oil for the production of a broad variety of base chemicals and fuel-range compounds.^[1] The production of chemicals and fuels *via* transformation of biomass-derived feedstock requires the hydrodeoxygenation of oxygenated intermediates, e.g., carboxylic acids, aldehydes or phenolic compounds.^[2] The amount of unsaturated carbon-carbon bonds as well as the oxygen-content needs to be reduced in order to make these molecules high-value chemicals that can be used in the transportation sector or the production of pharmaceuticals and fine chemicals.^[3] Usually, this step is done by thermal hydrogenation at elevated temperatures and high pressures, in which the reacting hydrogen is still supplied from reforming of non-sustainable fossil resources.^[4] These drawbacks make the hydrogenation of oxygen-containing intermediates the most energy- and capital-intensive step during biomass upgrading.^[5]

Electrocatalytic hydrogenation (ECH), in contrary, is a promising, sustainable technology for the ambient reduction of organic molecules. The required hydrogen is produced *in situ* from reduction of hydronium ions or water electrolysis that is driven by renewable resources.^[6] In a proton coupled electron transfer (PCET), H atoms adsorbed on metal electrode surface are formed according to *Volmer* reaction and consecutively transferred to an organic substrate (Reactions 1-2).^[7]



Electrocatalytic hydrogenation can be performed at low temperature and under atmospheric pressure.^[8] Together with an energy supply that is not based on fossil resources, ECH can help to reduce the anthropogenic carbon footprint and associated environmental harms, e.g., climate changes and global warming.^[1b, 6b, 9]

After decomposition and pyrolysis of biomass and lignocellulose a pool of unsaturated and oxygen-rich aldehydes, ketones, carboxylic acids and aromatics is generated.^[10] α,β -Unsaturated aldehydes like *trans*-2-penten-1-al can be used as model compounds for these group of molecules.^[11] The selective hydrogenation of α,β -unsaturated aldehydes towards their corresponding allylic alcohols is a significant reaction in academia and in industry due to their application in production of fine chemicals, fragrances and pharmaceuticals.^[12] However, the selective hydrogenation of α,β -unsaturated aldehydes towards their corresponding α,β -unsaturated alcohols has proven difficult in the past, even under thermo-chemical

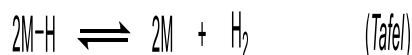
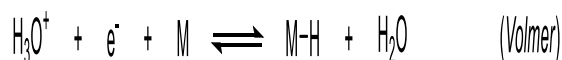
conditions.^[13] When using common hydrogenation catalysts that are based on noble metals, e.g., Pd, Rh, Ru hydrogenation of the double bond towards saturated aldehydes is thermodynamically favored over conversion of the carbonyl moiety.^[14]

Therefore, researchers have put lots of efforts in developing new catalysts that are capable of selectively converting α,β -unsaturated aldehydes towards allylic alcohols under thermal conditions. The addition of promoters specifically activating the CO bond, e.g., metal oxide species or oxophilic metals is one approach that has proven beneficial in tuning the reaction selectivity.^[15] Another approach towards selective hydrogenation of the carbonyl group is the repulsion of C=C bond from catalyst surface either electrostatically *via* changing the charge density on catalyst surface or sterically *via* particle size effects.^[16]

The present study investigates the electrocatalytic hydrogenation of *trans*-2-penten-1-al using transition metal catalysts supported on carbon nanotubes in aqueous phase (Scheme 1). The influence of different noble metals as well as promoter species on reaction selectivity is analyzed. Furthermore, the impact of external electric potential, particle size and solution pH on product distribution and reaction kinetics is evaluated. The effect of different metals, promoters as well as the presence of an external electric potential on the kinetic data shall be related to adsorption measurements of organic species on catalyst surface *via* cyclic voltammetry (CV) and volumetric method.

In a recent study, we have shown that adding phenol to an aqueous electrolyte gradually blocks sites for H adsorption and hence, diminishes H_{upd} peaks in CV of Pt.^[17] Now, we are seeking to perform similar measurements with molecules containing different functional groups, i.e., valeraldehyde, *trans*-2-penten-1-ol and correlate the findings to adsorption isotherms measured *via* volumetric method. This can help answering the question whether various moieties, e.g., double bond, carbonyl group, lead to changes in the adsorption and activation of different organic molecules on the electrode surface that explain the differences in reaction kinetics and product distribution. Furthermore, we want to shed light on the influence of an increasing negative charge density on electrostatic repulsion of electron-rich moieties, e.g., the C=C bond.

Depending on external electric potential, catalyst properties, i.e., noble metal, particle size, promoter species and electrolyte pH the yield towards formation of alcohols during electrocatalytic hydrogenation of *trans*-2-penten-1-al can be increased by almost two orders of magnitude compared to thermo-chemical hydrogenation without application of conditions promoting carbonyl group activation.



Scheme 1: Reaction network of electrocatalytic hydrogenation of *trans*-2-penten-1-al.

At open circuit potential (OCP), the standard heat of adsorption of an organic molecule, e.g., valeraldehyde or *trans*-2-penten-1-ol on Pd- and Ru-containing catalysts were derived from volumetric adsorption isotherm measurements using linearized *Langmuir* equation and *van't Hoff* correlation (Equations 1-2, Figure 1).

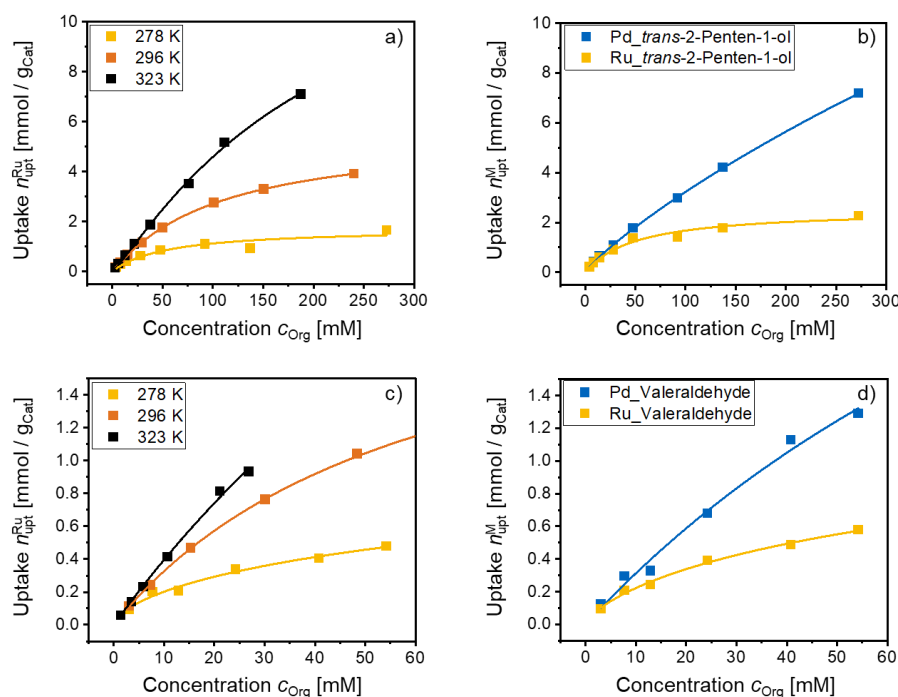


Figure 1: Adsorption isotherms of *trans*-2-penten-1-ol and valeraldehyde on 5 wt% Ru/CNT-COOH at different temperatures (a, c) and on various catalysts supported on CNT-COOH, at 278 K (b, d).

$$\frac{1}{n_{\text{upt}}^{\text{M}}} = \frac{1}{n_{\text{upt,ML}}^{\text{M}} \cdot K_{\text{ads}}^{\text{M}}} \cdot \frac{1}{c_0} + \frac{1}{n_{\text{upt,ML}}^{\text{M}}} \quad (1)$$

$$\ln(K_{\text{ads}}^{\text{M}}) = -\frac{\Delta H_{\text{ads}}^{\text{o,M}}}{R} \cdot \frac{1}{T} + \frac{\Delta S_{\text{ads}}^{\text{o,M}}}{R} \quad (2)$$

A detailed derivation is given in Section 2 of SI.

For Pd-containing catalysts, the uptake under external electric potential was determined from CV curves at different concentrations of adsorptive in electrolyte. The coverage of catalyst

surface and hence, the adsorbed amount of organics is determined from suppression of H_{upd} signals at increasing concentration of valeraldehyde or *trans*-2-penten-1-ol (Figure 2).

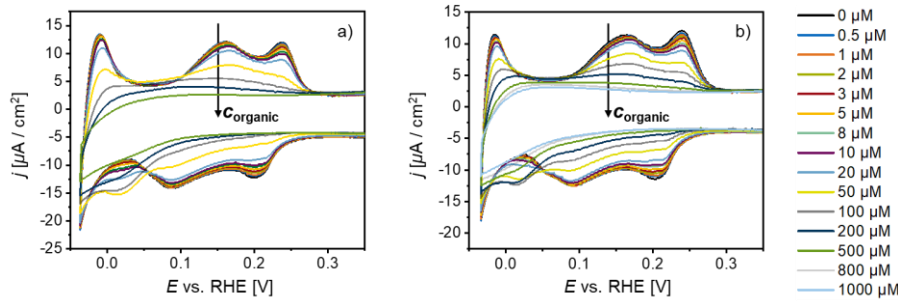


Figure 2: Cyclic voltammograms of 5 wt% Pd/CNT-COOH in pH 5 electrolyte with increasing concentration of **a)** *trans*-penten-1-ol and **b)** valeraldehyde.

The standard free energy of adsorptive uptake on Pd in water ($\Delta G_{\text{ads}}^{\circ} = \Delta G_{\text{ads}}^{c=0}$) is calculated based on the assumption of Reactions 3-4 being quasi-equilibrated, i.e., the change in *Gibbs* free energy of the reactions being zero ($\Delta G = 0$) and the chemical potentials of reactants and products being equal (Equations 3-4, Section 3 SI).



$$\mu_{H^{+}} + \mu_{e^{-}} = \mu_{H^{*}} \quad (3)$$

$$\mu_{H^{+}} + \mu_{e^{-}} + \mu_{\text{BzHO}} = \mu_{H^{*}} + \mu_{\text{BzHO}^{*}} \quad (4)$$

With the expression of $\mu_{H^{+}}$, and $\mu_{e^{-}}$ defined in Equations S22-S23 and the expressions of $\mu_{H^{*}}$, $\mu_{\text{Org}^{*}}$ and $\mu_{\text{Org}^{*}}$ in Equations S24-S26, Equation 4 can be reformulated to Equation 5.

$$\Delta G_{\text{Org}}^{\circ} = RT \ln c_{\text{Org}} - RT \left(\ln \frac{\theta_{H}}{1 - \theta_{H} - \theta_{\text{Org}}} + \frac{\theta_{\text{Org}}}{1 - \theta_{H} - \theta_{\text{Org}}} \right) - F\eta - (\Delta G_{\text{upd}}^{\circ} + \mu_{\text{excess}}) \quad (5)$$

Equation 5 includes the relation between SHE and RHE according to *Nernst* equation (Eq. S28) as well as the term of the standard free energy of pure H_{upd} adsorption (Eq. S32).

4.2 Results and discussion

4.2.1 Influence of noble metal and promoter species

When comparing Pd- and Ru-based catalysts in ECH of *trans*-2-penten-1-al, materials containing Pd show higher rates and *Faradaic* efficiencies (FE) of product formation than their Ru-containing analogues (Figure 3). At an overpotential of -1.2 V vs. RHE the turnover frequencies (TOF_{ECH}) and FE of formation of valeraldehyde, *trans*-2-penten-1-ol and pentan-1-ol on Pd are 2536, 59 and 67 1/h and 64.8, 1.5 and 3.4 %, respectively. The selectivity towards alcohol formation is below 5 %. In contrast, on Ru TOF_{ECH} and current efficiency are 925, 54 and 212 1/h and 16.4, 1.0 and 7.5 %. The selectivity for carbonyl group hydrogenation is increased to 20 %.

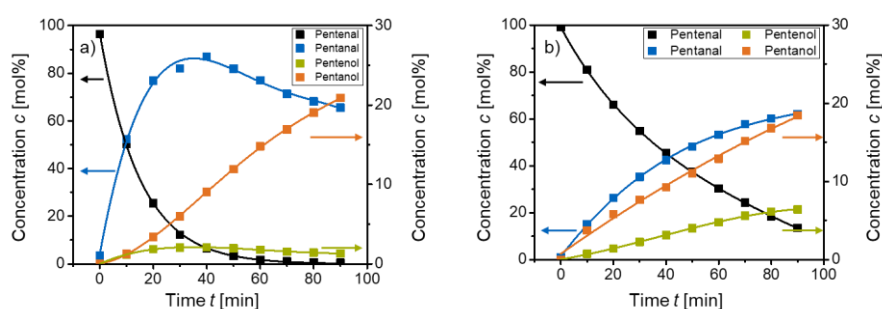


Figure 3: Conversion of *trans*-2-penten-1-al and product formation during ECH at $E_{\text{RHE}} = -1.2$ V on **a)** 5 wt% Pd/CNT-COOH and **b)** 5 wt% Ru/CNT-COOH.

Sokolskii and coworker found similar trends in thermo-chemical hydrogenation of crotonaldehyde on carbon-supported transition metals in water.^[16, 18] The selectivity towards alcohol formation was increased in the order Pd < Pt < Ru < Ir < Os. This is supported by *Giroir-Fendler* et al. who showed almost the same trend in transition metal activity for carbonyl group hydrogenation.^[19] These observations can be attributed to an increased d-band population of Ru as was theoretically calculated by *Delbecq* and *Soutet* as well as by *Hückel*.^[20] An increased electron density on transition metal surface leads to destabilization of the four-electron interaction between C-C double bond and metal surface while at the same time favoring the two-electron π -bonding between carbonyl group and metal species.^[21] This behavior is even more pronounced on metals with a large radial expansion of d-orbitals, which is the case for ruthenium; palladium, in contrast, shows rather small d-orbitals.^[22] Additionally, the activation energies (E_{A}^{M}) of hydrogenation of double bond and carbonyl group change depending on noble metal. On Pd-based catalysts, the activation barriers for CO and C=C hydrogenation are 40 and 17 kJ/mol, respectively (Figure 4a). In case of Ru-containing materials, these values lie much closer and are 29 and 22 kJ/mol rendering a simultaneous conversion of both functional groups more likely (Figure 4b).

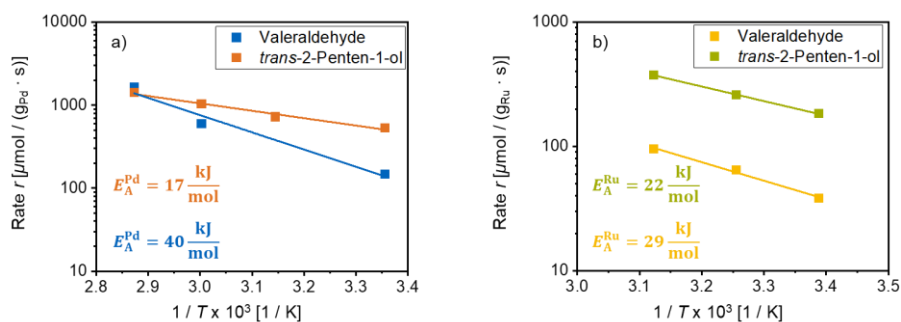


Figure 4: Arrhenius plots for determining activation energies of hydrogenation of CO and C=C group of *trans*-2-penten-1-al on **a)** Pd and **b)** Ru, at 1 bar H₂.

Increasing the concentration of *trans*-2-penten-1-al in ECH experiments leads to enhanced selectivity towards unsaturated alcohol, especially at high concentrations. This is hypothesized to be caused by a large steric hindrance inducing a pronounced repulsion of double bond from electrode surface. Consequently, *trans*-2-penten-1-ol is formed with a reaction order of 0.5 throughout the investigated concentration range on Pd and Ru (Figure 5). Valeraldehyde formation also shows a positive reaction order of 0.5 up to a concentration of unsaturated aldehyde of 30 mM, before dropping to zero. Pentan-1-ol is generated with a negative reaction order of -1.5 and -0.25 on Pd and Ru, respectively.

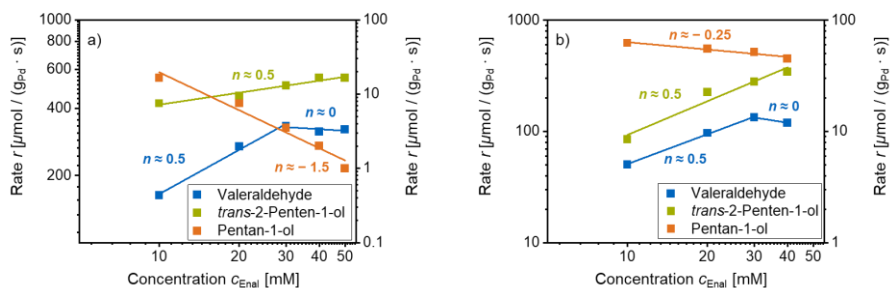


Figure 5: Reaction orders of formation of various products in electrocatalytic *trans*-2-penten-1-al hydrogenation on **a)** 5 wt% Pd/CNT-COOH and **b)** 5 wt% Ru/CNT-COOH.

The selectivity towards *trans*-2-penten-1-ol and pentan-1-ol is further increased by addition of iron (1 wt%) as electropositive promoter to Pd- and Ru-containing catalysts (Figure 6). On Pd, the effect is rather subtle. The TOF_{ECH} of formation of *trans*-2-penten-1-ol and pentan-1-ol only raise to 88 1/h, both. At the same time, the turnover frequency for valeraldehyde generation increases slightly to 2636 1/h. Consequently, the selectivity towards these molecules is 2.9, 3.0 and 94.2%, respectively. In contrast, on Ru/CNT-COOH the addition of 1 and 3 wt% Fe gives a more pronounced selectivity increase towards alcohol formation. The relative amount of *trans*-2-penten-1-ol climbs from 4.3 to 7.5 and 18.6% when going from 0 *via* 1 to 3 wt% Fe. The corresponding numbers for pentan-1-ol and valeraldehyde are 17.3, 19.5, 20.4% and 78.4, 73.0, 61.8%. The turnover frequencies for formation of valeraldehyde, *trans*-2-penten-1-ol and pentan-1-ol during ECH of *trans*-2-penten-1-al on different catalysts at $E_{RHE} = -1.2$ V are summarized in table 1. As can be seen, on bimetallic Ru-Fe materials the

formation rates of alcohol products increase with an increasing iron content whereas TOF_{ECH} of valeraldehyde decreases.

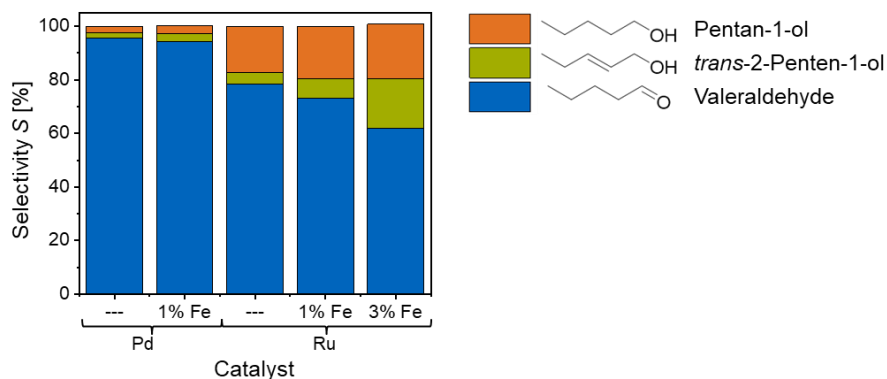


Figure 6: Development of product selectivity during ECH of *trans*-2-penten-1-al at $E_{\text{RHE}} = -1.2$ V on Pd- and Ru-based catalysts with increasing iron content.

Table 1: Turnover frequencies (TOF_{ECH}) for formation of various products in ECH of *trans*-2-penten-1-al on different catalysts.

	Turnover frequency TOF [h^{-1}]				
	5 wt% Pd	5-1 wt% Pd-Fe	5 wt% Ru	5-1 wt% Ru-Fe	5-3 wt% Ru-Fe
Valeraldehyde	2536	2636	925	967	768
trans-2-Penten-1-ol	59	88	54	79	228
Pentan-1-ol	67	88	212	230	228
H_2	1157	983	3611	3265	4896

These findings are in line with results from *Yang* and *Figueiredo* and coworker who investigated the selective hydrogenation of cinnamaldehyde. Adding iron to carbon nanotube-supported Pt catalysts enhanced the selectivity towards carbonyl group hydrogenation by almost 20%.^[23] *Ponec* as well as *Baciller-Baeza* et al. suggested that this change in selectivity is due to electronic effects arising from promoter species.^[24] In their view, the metallic promoter is partly oxidized under reaction conditions forming a *Lewis* acid site that is only activating CO bond but not the double bond. Additionally, iron can act as an electron-donor enhancing the electron-density on primary metal and hence, increasing the repulsive interaction between catalyst surface and C=C bond.

4.2.2 Impact of external electric potential

As bimetallic 5-3 wt% Ru-Fe/CNT-COOH showed the best results concerning selective hydrogenation of the carbonyl group further investigations were based on this material.

Increasing the externally applied negative overpotential from -0.35 to -1.20 V vs. RHE enhances the selectivity towards formation of *trans*-2-penten-1-ol from 10.0 to 18.6%. The relative amount of valeraldehyde and pentan-1-ol change from 81.2 to 61.8% and from 10.3 to 20.4%, respectively (Figure 7). As table 2 shows the turnover frequencies of valeraldehyde formation is only doubled, whereas TOF_{ECH} of formation of alcohols reveals a fivefold increase.

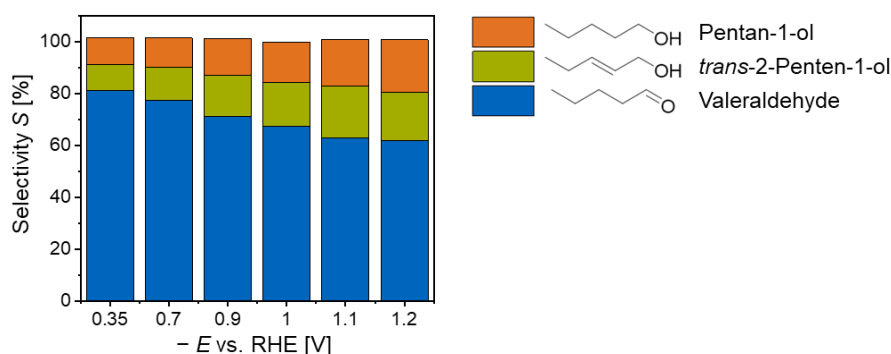


Figure 7: Product selectivity as function of external electric potential for electrocatalytic hydrogenation of *trans*-2-penten-1-al on 5-3 wt% Ru-Fe/CNT-COOH.

Table 2: Turnover frequencies (TOF_{ECH}) for formation of various products in ECH of *trans*-2-penten-1-al on 5-3 wt% Ru-Fe/CNT-COOH at increasing cathodic overpotential.

	Turnover frequency TOF [h ⁻¹] at $-E_{RHE}$ [V]					
	0.35	0.70	0.90	1.00	1.10	1.20
Valeraldehyde	391	580	612	788	729	768
<i>trans</i> -2-Penten-1-ol	46	91	117	182	221	228
Pentan-1-ol	52	91	137	176	195	228
H₂	610	1403	2283	3065	4036	4896

This behavior is hypothesized to be caused by an enhanced repulsion of organic molecules from electrode surface upon increasing the negative charge density on metal particles. A reduced binding strength of different functional groups on the catalyst surface renders a conversion of these moieties more likely. This is supported by adsorption isotherm measurements and calculation of the adsorption heat of functional groups in *trans*-2-penten-1-ol and valeraldehyde, i.e., double bond and carbonyl group on Pd and Ru surface (SI Sections 2-3).

At open circuit potential, the respective adsorption heat was determined *via* volumetric adsorption isotherm measurements. The isotherms recorded at different temperatures on different catalysts were analyzed using linearized *Langmuir* equation (Eq. 1). The monolayer uptake ($n_{\text{upt,ML}}^{\text{M}}$) and adsorption equilibrium constant ($K_{\text{ads}}^{\text{M}}$) were determined from the

y-intercept and the slope of $1/n_{\text{upt,ML}}^{\text{M}}$ vs. $1/c_0$ plots (Figure 8). Table S5 summarizes the determined values of $n_{\text{upt,ML}}^{\text{M}}$ and $K_{\text{ads}}^{\text{M}}$.

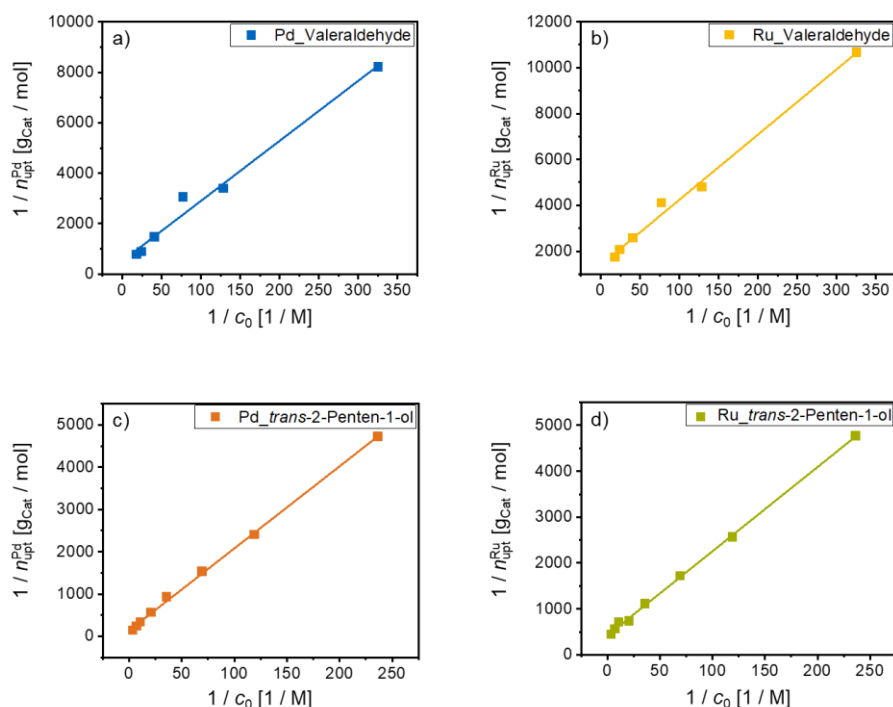


Figure 8: Plots of linearized *Langmuir* equation for adsorption isotherms of **a), b)** valeraldehyde and **c), d)** *trans*-2-penten-1-ol on Pd and Ru supported on CNT-COOH, at 278 K.

The adsorption heat of carbonyl group and double bond on different metals, i.e., Pd, Ru were received from *van't Hoff* plots ($\ln(K_{\text{ads}}^{\text{M}})$ vs. $1/T$) and evaluating the slope of the resulting straight line (Eq. 2). Figure 9 and Table 3 summarize the results. As can be seen, on Pd-based catalysts the carbonyl group is bound much stronger than the double bond, i.e., -104 kJ/mol vs. -31 kJ/mol, which might explain why hydrogenation of CO group and alcohol formation are suppressed almost completely. It is hypothesized that the interaction between carbonyl group and metal surface is too strong making a conversion essentially impossible. The double bond however, is readily hydrogenated towards the saturated molecule due to its moderate binding strength on Pd surface. In case of Ru-containing materials, the heat of adsorption of valeraldehyde and *trans*-2-penten-1-ol are moderately high, i.e., -45 kJ/mol vs. -70 kJ/mol. This might explain the increased selectivity towards hydrogenation of CO group and alcohol formation on Ru, in general. In addition, the binding strength of double bond is larger on Ru in comparison to Pd, which could also be a reason for the decreased activity for C=C bond hydrogenation on Ru.

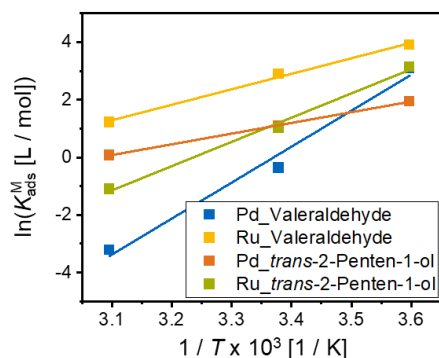


Figure 9: *van't Hoff* plot for determining the adsorption heat of valeraldehyde and *trans*-2-penten-1-ol on 5 wt% Pd/CNT-COOH and 5 wt% Ru/CNT-COOH, respectively.

Table 3: Adsorption heat of valeraldehyde and *trans*-2-penten-1-ol on Pd- and Ru-containing catalysts.

		Valeraldehyde		<i>trans</i> -2-Penten-1-ol	
		Pd	Ru	Pd	Ru
E_{RHE} [V]					
$\Delta H_{ads}^{O,M}$ [kJ/mol]	0.85	-104	-45	-31	-70
	0.50		0		-54
	0.20	-48		-12	
	0.15	-38		0	
	0.10	-23	47	8	-25
	0.05	-16		12	

The influence of external electric potential on the adsorption heat of different functional groups on Ru were investigated using the same approach like for measurements at OCP (Figure 11). However, the potential at the catalyst surface was set to more cathodic values, i.e., 0.50, 0.10 V vs. RHE. Figure S2 shows linearized *Langmuir* plots of adsorption isotherms of valeraldehyde and *trans*-2-penten-1-ol on Ru-containing materials at 295 K. Calculated adsorption equilibrium constants and monolayer uptakes are given in table S6. Figure S3 depicts the resulting *van't Hoff* plots of $\ln(K_{ads}^M)$ vs. $1/T$.

In case of Pd, adsorption heats at various electric potentials were derived from suppression of H_{upd} features in cyclic voltammetry at increasing concentration of organics (Figure 2). The (standard) free energies of adsorption of valeraldehyde and *trans*-2-penten-1-ol and of underpotential deposited hydrogen were calculated using Equation 5 and Equation S32. Extrapolating ΔG_{Org}^o vs. c_{Org} plots to zero concentration gives the standard free energy of adsorption of CO and of C=C bond at zero coverage. Corresponding standard adsorption enthalpies are derived from linearized *Gibbs-Helmholtz* equation and plotting $\Delta G_{Org}^o / T$ against $1/T$ (Figure 10, Figure S4).

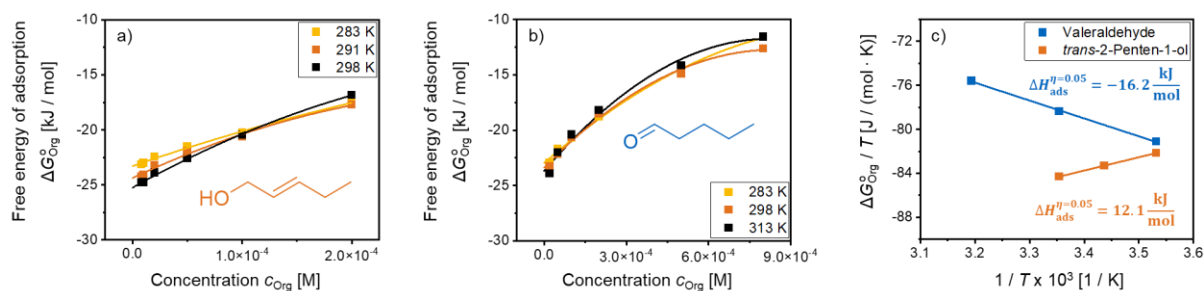


Figure 10: Development of free energy of adsorption of **a)** *trans*-2-penten-1-ol and **b)** valeraldehyde on Pd with organics concentration, at $E_{\text{RHE}} = 0.05$ V and **c)** corresponding plot of $\Delta G_{\text{Org}}^0 / T$ vs. $1/T$ for determining the corresponding heats of adsorption on Pd.

As can be seen in Figure 11, $\Delta H_{\text{ads}}^{\text{o,M}}$ of valeraldehyde and *trans*-2-penten-1-ol decrease with increasing cathodic overpotential. At 0.10 V vs. RHE the adsorption enthalpy of carbonyl group and of double bond on Pd and Ru are reduced to -23 and 47 kJ/mol and to 8 and -25 kJ/mol, respectively. These numbers are in line with results from Singh et al. who found adsorption enthalpies of phenol on Pt and Rh in aqueous phase between -12 and 38 kJ/mol within the potential range of 0.05-0.40 V vs. RHE.^[25] Campbell and coworker determined a liquid phase adsorption heat of benzaldehyde and phenol on Pt of around -40 kJ/mol.^[17] A reduced stabilization of functional groups on catalyst surface enhances their probability for being converted in electrocatalytic hydrogenation reactions. In case of valeraldehyde, the destabilization effect is more pronounced on Ru- and Pd-containing materials. Hence, the selectivity towards carbonyl group hydrogenation and alcohol formation is favored, especially on Ru-based catalysts at highly negative overpotentials. Currently, it cannot be excluded that this might also be observed on Pd at even more negative external electric potentials. Figure 8a suggests that $\Delta H_{\text{ads}}^{\text{o,M}}$ of valeraldehyde and of *trans*-2-penten-1-ol might cross at a certain point. From a certain threshold potential on the carbonyl group on Pd might also be more destabilized than the double bond.

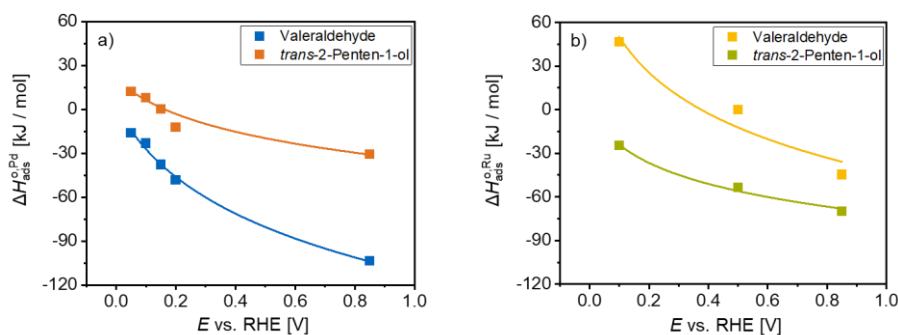


Figure 11: Adsorption heat of valeraldehyde and *trans*-2-penten-1-ol on **a)** Pd and **b)** Ru as function of external electric potential.

4.2.3 Influence of support and electrolyte acidity and of metal particle size

Increasing the concentration of H_3O^+ in bulk solution reduces the selectivity towards alcohol formation in ECH of *trans*-2-penten-1-al on 5-3 wt% Ru-Fe. At pH 5, the relative amounts of valeraldehyde, *trans*-2-penten-1-ol and pentan-1-ol are 66.5, 21.2 and 12.2% whereas at pH 2 the respective selectivity is 84.1, 5.5 and 10.4% (Figure 12a). This is hypothesized to be due to increased accumulation of hydronium ions at metal surface that counterbalances the negative charge on metal electrode. Consequently, the beneficial effect of displacing C=C bond is weakened, at low pH. In the pH range of 5-2, TOF_{ECH} of formation of unsaturated and saturated alcohol are halved, whereas the formation rate of saturated aldehyde is slightly increased (Table 4).

In contrast, increasing support acidity has only small impact on the overall reaction selectivity, at pH 5 (Figure 12b). The values received on carbon nanotubes with an acid site concentration of 1.25 wt% might be an outlier. Nevertheless, the overall rates of product formation are improved on more acidic supports (Table 4). The TOF_{ECH} of valeraldehyde and of pentan-1-ol doubled though, the value for *trans*-2-penten-1-ol decreased to only 20% of its original value, which might be an outlier. Consequently, the overall *Faradaic* efficiency of the reaction is almost doubled from 22.8 to 38.3% at an acid site concentration of 0.0-1.25 wt%.

These findings match results from *Singh* and *Song* and coworker who showed that TOF of aqueous phase (electrocatalytic) phenol hydrogenation on Pt is enhanced from 5 to 35 1/s and 15 to 29 1/s when the pH of solution is decreased from 10 to 1.^[8, 26] As *Yang* et al. revealed TOF of Pt/zeolite catalyzed phenol hydrogenation in water raises from 0.5 to 4.5 1/s when increasing the concentration of *Brønsted* acid sites (BAS) on zeolite support from 50 to 650 $\mu\text{mol}/\text{g}_{\text{zeolite}}$.^[27] In studies performed by *Chen* and coworker, the rate of aqueous phase phenol hydrogenation on Pt was improved by almost a factor of six, i.e., from 0.035 to 0.2 1/s when decreasing the pH from 5 to 2.^[28]

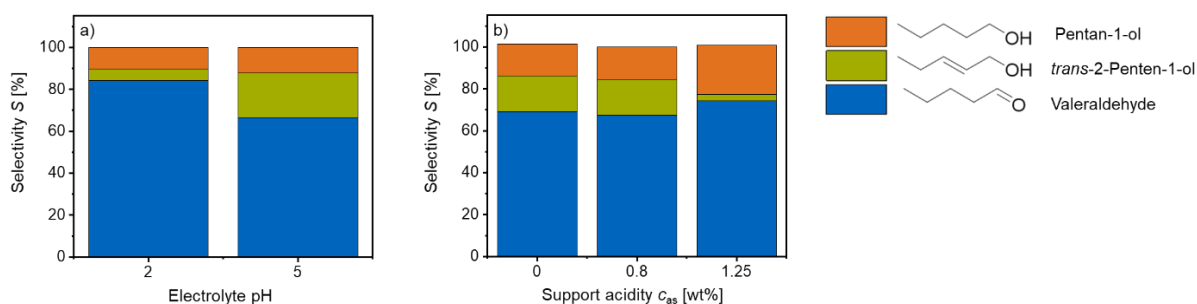





Figure 12: Dependence of product selectivity of 5-3 wt% Ru-Fe catalyzed electrocatalytic hydrogenation of *trans*-2-penten-1-al on **a)** electrolyte and **b)** support acidity.

Table 4: Turnover frequencies (TOF_{ECH}) for formation of various products in ECH of *trans*-2-penten-1-al on 5-3 wt% Ru-Fe at various electrolyte and support acidity.

Turnover frequency TOF [h ⁻¹] at $E_{RHE} = -1.0$ V					
	pH 2	pH 5	$c_{as} = 0$ wt%	$c_{as} = 0.80$ wt%	$c_{as} = 1.25$ wt%
	357	335	612	788	1166
	24	54	150	182	33
	60	115	156	176	332
H₂	1545	1329	3088	3021	2466

It has to be noted that experiments investigating the effect of solution pH have been performed with Ru-Fe materials with smallest particle size, whereas the remaining reactions discussed so far have been run with catalysts revealing the largest mean particle diameter. This is why the numbers at pH 5 do not match the ones shown above for the influence of external electric potential on ECH of *trans*-2-penten-1-al.

In general, rising the reduction temperature during synthesis increases the mean metal particle diameter of the catalyst. In *trans*-2-penten-1-al ECH on 5-3 wt% Ru-Fe/CNT-COOH, this enhances the reaction selectivity towards carbonyl group hydrogenation as well as the formation rates of different products (Figure 13). When the particle size is changed from 4.3 to 9.3 nm TOF_{ECH} of valeraldehyde formation increases from 335 to 788 1/h. Similar effects can be observed for turnover frequencies of *trans*-2-penten-1-ol and pentan-1-ol formation, which climb from 54 to 182 1/h and from 115 to 176 1/h (Table 5).

Similar results of an overall rate increase and an improved selectivity towards alcohol formation in hydrogenation of α,β -unsaturated aldehydes, e.g., crotonaldehyde, cinnamaldehyde have been found by several researchers in the past.^[23a, 29] *Giroir-Fendler* et al. attributed an increased selectivity towards carbonyl group hydrogenation on large and hence, less curved Pt and Rh particles to an enhanced steric constraint of cinnamaldehyde molecule adsorbed on flat surfaces.^[30] Consequently, due to deflection of the double bond from catalyst surface hydrogenation of the CO group is favored. Additionally, *Coloma* and coworker showed that a higher TOF of crotonaldehyde hydrogenation on Pt/AC is caused by a reduced activation energy on large metal particles.^[31] When the mean diameter was increased from 5 to 12 nm the activation barrier of reaction was decreased from 40 to 20 kJ/mol.

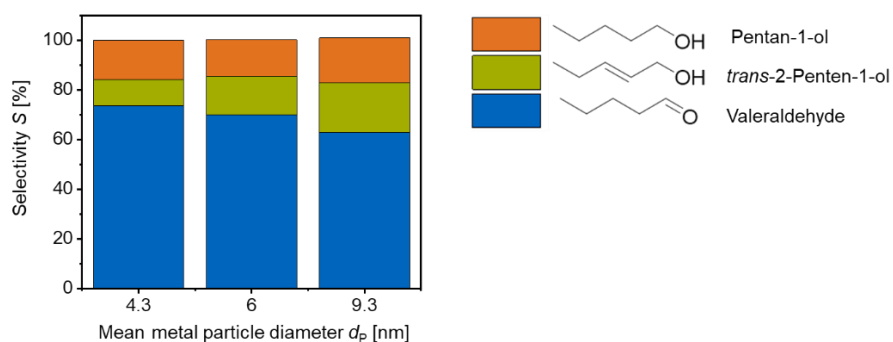





Figure 13: Selectivity of *trans*-2-penten-1-al ECH on 5-3 wt% Ru-Fe/CNT-COOH at $E_{RHE} = -1.1/1.2$ V towards valeraldehyde, *trans*-2-penten-1-ol and pentan-1-ol at different metal particle sizes.

Table 5: Turnover frequencies (TOF_{ECH}) for formation of various products in ECH of *trans*-2-penten-1-al on 5-3 wt% Ru-Fe/CNT-COOH with different metal particle size.

Turnover frequency TOF [h^{-1}] at $E_{RHE} = -1.1/1.2$ V			
	$d_p = 4.3$ nm	$d_p = 6.0$ nm	$d_p = 9.3$ nm
	360	528	729
	42	104	221
	85	104	195
H₂	1284	1980	3019

4.3 Conclusion

In summary, the selectivity towards alcohol formation in electrocatalytic hydrogenation of *trans*-2-penten-1-al can be increased up to almost 40%.

The largest impact arises from the transition metals that are used to catalyze the reaction. Especially, metals with large d orbitals, e.g., Pt, Ru improve the selectivity towards carbonyl group hydrogenation due to repulsion of the double bond. This effect is even more pronounced when an increasing concentration of oxophilic and electropositive promoter species, e.g., Co, Fe is added to catalyst surface. However, this comes along with decreased overall reaction rates.

Apart from transition metal species the externally applied electric potential also has a positive effect on selective formation of unsaturated and saturated alcohols and catalyst activity. Applying large negative overpotentials to catalyst surface enhances the selectivity towards CO group hydrogenation. Due to increased negative charge density various functional groups are destabilized on the electrode surface. Especially, the interaction between CO and metal surface is weakened leading to improved formation of alcohols.

Changing the electrolyte pH from 2 to 5 has a similar effect on reaction selectivity like increasing the negative overpotential from -0.35 to -1.20 V vs. RHE. However, the rate of product formation remains constant. If the concentration of acid sites on carbon nanotube support is increased from 0 to 1.25 wt% the turnover frequency is enhanced by 50%.

Finally, maximizing the metal particle size also slightly improves the relative amount of alcohols formed in ECH of *trans*-2-penten-1-al. Due to steric constraints at flat surfaces the interaction between C=C bond and catalyst surface is hindered on large metal clusters, which favors hydrogenation of the carbonyl moiety. Additionally, the overall reaction rate is doubled when the mean particle diameter is increased from 4.3 to 9.3 nm.

4.4 Supporting information

4.4.1 Experimental

Materials

Graphitized Multiwalled Carbon Nanotubes (GMWCNT, ≥ 99.9 wt%), COOH-functionalized graphitized multiwalled carbon nanotubes (GMWCNT-COOH, ≥ 99.9 wt%, $c_{\text{COOH}} = 0.8$ wt%) and COOH-functionalized multiwalled carbon nanotubes (MWCNT, ≥ 95.0 wt%, $c_{\text{COOH}} = 1.25$ wt%) with an outer diameter of 20-30 nm, an inner diameter of 5-10 nm and a length of 10-30 μm , in the following referred to as *CNT*, *CNT-COOH* and *MCNT-COOH*, respectively were purchased from *Cheap Tubes Inc.*

Palladium(II) chloride (PdCl_2 , 99.999%), Ruthenium(III) chloride hydrate ($\text{RuCl}_3 \cdot x\text{H}_2\text{O}$, 99.98%), Iron(II) chloride tetrahydrate ($\text{FeCl}_2 \cdot 4\text{H}_2\text{O}$, 99.99%) as well as ethanol ($\geq 99.8\%$) were supplied by *Sigma-Aldrich*. *trans*-2-Penten-1-al ($\geq 95\%$), valeraldehyde (97%) and *trans*-2-penten-1-ol for hydrogenation and adsorption experiments and *m*-cresol (for synthesis) for GC analysis were also from *Sigma-Aldrich*. Sodium phosphate monobasic (NaH_2PO_4 , $\geq 99.0\%$), sodium phosphate dibasic dihydrate ($\text{Na}_2\text{HPO}_4 \cdot 2\text{H}_2\text{O}$, $\geq 98.0\%$) and phosphoric acid (H_3PO_4 , $\geq 99.0\%$) were purchased from *Sigma-Aldrich*. Aqueous buffer solutions with different pH, were prepared by dissolving the required amounts of salts and phosphoric acid in 1 L ultrapure water with a resistivity of 18.2 $\text{M}\Omega$ from a *Purist* system supplied by *Rephile* (Table S1). All chemicals were used without further purification. Helium gas (He , 99.996 Vol%) for purging the electrolyte solution and hydrogen gas (H_2 , 99.999 Vol%) for electrode calibration were both supplied by *Westfalen*.

Table S1: Amount of $\text{Na}_2\text{HPO}_4 \cdot 2\text{H}_2\text{O}$, NaH_2PO_4 and H_3PO_4 dissolved in 1.0 L ultrapure H_2O for electrolyte preparation.

pH	$m(\text{Na}_2\text{HPO}_4 \cdot 2\text{H}_2\text{O})$ [g]	$m(\text{NaH}_2\text{PO}_4)$ [g]	$m(\text{H}_3\text{PO}_4)$ [g]
2.4	---	30.0	24.5
4.9	1.34	59.1	---

Catalyst synthesis

Various carbon nanotube-supported metal catalysts were prepared *via* impregnation followed by reduction in H_2 . Therefore, the desired amount of the respective precursor salts to reach a 5 or 3 wt% metal loading were dissolved in 200 mL ethanol (Table S2). After addition of 1.00 g of support the suspension was stirred and sonicated for 15 minutes, each. The suspension was alternatively stirred and sonicated three times. Afterwards, the solvent was evaporated and the solid was dried at 60 $^\circ\text{C}$ overnight. The final catalyst was received after reducing the precipitate at 473, 623 or 773 K (0.5 K min^{-1}) for 3 hours under flowing H_2 (100 mL min^{-1}).

Table S2: Amount of precursor salts for synthesis of respective metal catalysts supported on carbon nanotubes. The number in brackets determine the target metal loading in wt%.

	Pd/C (5)	Pd-Fe/C (5-1)	Ru/C (5)	Ru-Fe/C (5-1)	Ru-Fe/C (5-3)
PdCl ₂	87.7 mg	88.3 mg			
RuCl ₃ · xH ₂ O			136.2 mg	140.1 mg	140.1 mg
FeCl ₂ · 4H ₂ O		35.8 mg		35.8 mg	116.1 mg

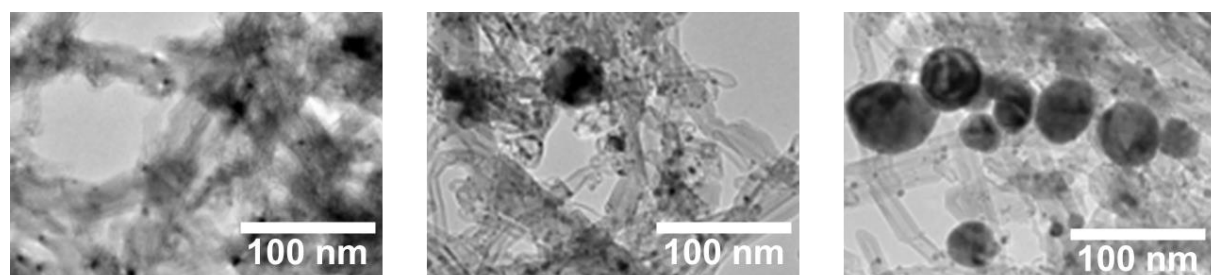
In order to determine the metal particle size, the metal dispersion and the external surface area the final catalysts were analyzed *via* H₂ chemisorption and N₂ physisorption measurements using a *Surfer* station from *Thermo Fischer Scientific* and by transmission electron microscopy (TEM) (Figure S1). The exact metal loading of the catalyst was determined by atomic absorption spectroscopy (AAS) using an *iCE 3000 SERIES AA Spectrometer* from *Thermo Fisher Scientific*. The results are summarized in Tables S3-S4.

Table S3: Metal loading and external surface area of synthesized catalysts and mean particle diameter and metal dispersion of Pd-containing catalysts.

	Pd/C (5)	Pd-Fe/C (5-1)	Ru/C (5)	Ru-Fe/C (5-1)	Ru-Fe/C (5-3)
C _{Metal} [wt%]	5.1	4.7-1.0	4.8	5.0-0.8	5.2-3.0
d _P (TEM) [nm]	5.0	5.0			
d _P (H ₂) [nm]	3.0	3.0			
D (TEM) [%]	22.1	22.1			
D (H ₂) [%]	37.0	37.0			
A _{BET} [m ² / gc]	120				

Table S4: Mean particle size and metal dispersion of Ru-containing catalysts after reduction at different temperatures determined from TEM images.

	473 K	623 K	773 K
d _P (TEM) [nm]	4.3	6.0	9.3
D (TEM) [%]	20.9	15.2	9.7

**Figure S1:** TEM images of 5-3 wt% Ru-Fe/CNT-COOH reduced at 200, 350 and 500 °C (left to right).

The catalyst dispersion according to TEM was calculated based on the determined mean particle diameter d_p using Equations S1-S2.^[32]

$$d_p = \frac{\sum_{i=1}^n d_i^3}{\sum_{i=1}^n d_i^2} \quad (\text{S1})$$

$$D = \frac{g \cdot V}{d_p \cdot S} \cdot 100 \quad (\text{S2})$$

The d_i are the particle diameters measured from TEM images. The g refers to the particle shape correction factor that is 6 for spherical particles. The V refers to the volume per Pd and Ru atom, respectively calculated with a mean atomic radius of 1.51 Å and 1.48 Å. The S is the Pd and Ru average transversal section, which has a value of 7.8 Å² and 9.0 Å².

It has to be noted that H₂ chemisorption of bimetallic catalysts is not reliable for determining their particle diameters and metal dispersion. As only the total amount of hydrogen adsorbed on all metal sites is recorded a relative distribution of different metals on catalyst surface cannot be achieved. Furthermore, the adsorption properties of H on various metals can be altered upon formation of bimetallic clusters of different size and composition. Hence, different bimetallic particles on the same material can lead to different results in H₂ chemisorption.^[33]

In case of Ru-containing catalysts, the formation of a RuO₂ layer on material surface hinders an accurate investigation *via* H₂ chemisorption and leads to underestimation. *Chetty* and coworker found that depending on the reduction temperature of Pt-Ru/*CNT* catalysts the relative amount of Ru⁰ within the sample only reaches up to 50%, with the rest being present in its oxidized form.^[34]

When measuring H₂ chemisorption of Pd-containing materials, in contrast, the resulting particle size and metal dispersion might be overestimated due to absorption of hydrogen into the lattice and palladium hydride formation.^[35]

Therefore, only values gathered from TEM analysis were considered when calculating rates, turnover frequencies and the active metal surface area of different catalysts.

Cyclic voltammetry

Cyclovoltammetry (CV) on Pd-containing catalysts was performed in a rotating disk electrode (RDE) setup using a *Modulated Speed Rotator* (MSR) and an RDE glass cell with water jacket both from *PINE research*. The electric potential was controlled with an *SP-300* potentiostat from *BioLogic*. In a three-electrode configuration, a glassy carbon RDE tip (5.0 mm OD) with catalyst coating (0.3 mg) was used as working electrode (WE). For catalyst coating, 2.0 mg of

Pd/CNT was suspended in 200 μL ethanol and sonicated for 30 min. 30 μL of suspension were transferred onto glassy carbon disk and dried before immersion into electrolyte. A platinum wire served as counter electrode (CE) and an Ag/AgCl electrode was used as reference electrode (RE). The RDE tip as well as CE and RE were purchased from *PINE research*. Before each experiment, the Ag/AgCl electrode was calibrated against a reversible hydrogen electrode (RHE). Therefore, its potential was measured against a platinum wire in a H_2 saturated electrolyte that was intended to be used in CV. The RDE glass cell was stored in a potassium permanganate solution prior to use to remove any organic contaminations. Before filling with electrolyte, it was flushed with a 3% H_2O_2 / 1 M H_2SO_4 solution followed by rinsing with ultrapure water. The WE, CE and RE were immersed in 100 mL phosphate buffer and the temperature (283-313 K) was adjusted with a *FC 600s* chiller from *Julabo*. The rotation speed of RDE tip was set to 400 rpm and the external electric potential was cycled between -0.05 and 1.45 V vs. RHE during CV. The scanning rate was 50 mV s^{-1} . Stable CV curves were reached after the tenth cycle. Excess H_2 and O_2 were removed from electrolyte solution *via* purging with He (20 mL min^{-1}) throughout the experiments.

For determination of valeraldehyde and *trans*-2-penten-1-ol adsorption heat on Pd, different concentrations (0-200 μM) of organics were added to the electrolyte during CV.

The current density measured during CV was calculated by normalizing the measured current to Pd surface area using catalyst metal dispersion (Equations S3-S4).

$$n_{\text{Pd-Surf.}} = \frac{m_{\text{Cat}} \cdot c_{\text{Pd}} \cdot D}{M_{\text{Pd}}} \quad (\text{S3})$$

$$A_{\text{Pd.Surf.}} = \frac{n_{\text{Pd-Surf.}}}{2 \cdot 10^{-9}} \quad (\text{S4})$$

The m_{Cat} refers to the mass of catalyst, c_{Pd} stands for the metal concentration of the catalyst, D is its metal dispersion and M_{Pd} is the molecular weight of Pd.

Electrocatalytic hydrogenation of trans-2-penten-1-al

Electrocatalytic hydrogenation (ECH) experiments were performed in a two-compartment batch cell. In a three-electrode setup, the working and reference electrode (WE, RE) were placed in the cathode compartment. The counter electrode (CE) was located in the anode half-cell and both compartments were separated by a *Nafion*TM N117 membrane from *Ion Power*. The membrane was activated by a treatment in 3% H_2O_2 (1 h), deionized water (2 h) and 1 M H_2SO_4 (1 h) at 90°C before storage in deionized water. The working electrode consisted of a carbon felt ($30 \times 15 \times 6.35 \text{ mm}$) that was coated with catalyst and attached to a

titanium rod (Gr. 2). For catalyst coating, 20 mg of material were suspended in 2 mL of an isopropyl alcohol/water (25/75 v/v) mixture. After sonication for 30 min the suspension was drop casted onto the felt and allowed to dry at room temperature. The reference electrode was a leakless miniature Ag/AgCl reference electrode from *eDAQ* that was calibrated against RHE prior to each experiment. A Pt-wire ($\varnothing 1.0$ mm, 99.997%) from *Alfa Aesar* served as counter electrode. The potential during ECH was controlled *via* a *SP-300* potentiostat from *BioLogic*.

Before each experiment, the anode and cathode half-cells were filled with 60 mL aqueous electrolyte, of which the catholyte was stirred at 650 rpm throughout the experiment. Furthermore, the electrolyte was continuously purged with He (20 mL min^{-1}) to avoid accumulation of H_2 and O_2 from HER and OER at cathode and anode, respectively. After an initial polarization step of WE (-40 mA , 30 min) to assure for complete reduction of metal particles supported on carbon nanotubes, the required amount of *trans*-2-penten-1-al to reach the desired concentration (10-50 mM) was added to catholyte. Electrocatalytic hydrogenation was performed at different *jR*-corrected potentials in the range of -0.35 to -1.2 V vs. RHE that were applied to WE. All experiments were performed at room temperature.

During ECH runs, 0.5 mL aliquots were regularly withdrawn from the catholyte and extracted in 1.0 mL EtOAc. *m*-Cresol (5 mM) was added as external standard and the organic phase was analyzed by gas chromatography (GC). A *GC-2010 Plus* gas chromatograph with an *AOC 20i* autosampler from *Shimadzu* and a *DB-WAX* column (30 m, 0.32 mm, $0.25 \mu\text{m}$) from *Agilent Technologies* was used for investigating reaction kinetics of *trans*-2-penten-1-al ECH.

Turnover Frequencies (TOF_{ECH}) and initial rates ($r_{\text{init,ECH}}$) of formation of different reaction products were calculated according to Equations S5-S6.

$$r_{\text{init,ECH}} = \frac{\partial n}{\partial t} \cdot \frac{1}{m_{\text{M-Surf.}}} \quad (\text{S5})$$

$$\text{TOF}_{\text{ECH}} = \frac{\partial n}{\partial t} \cdot \frac{1}{n_{\text{M-Surf.}}} \quad (\text{S6})$$

The $m_{\text{M-Surf.}}$ and $n_{\text{M-Surf.}}$ refer to the mass and mol of surface metal that were determined from metal dispersion of the catalyst (Equations S7, S3).

$$m_{\text{M-Surf.}} = m_{\text{Cat}} \cdot c_{\text{M}} \cdot D \quad (\text{S7})$$

The m_{Cat} refers to the mass of catalyst, c_{M} refers to the metal concentration of the catalyst and D is the metal dispersion.

The current efficiency, i.e., *Faradaic* efficiency (FE) of ECH of *trans*-2-penten-1-al was calculated with respect to the various reaction products as the ratio between the amount of

electric charge used for hydrogenation (Q_{ECH}), that equals the amount of product formed and the total charge passed through the cell (Q_{HER}), that is the amount of hydrogen, which is activated *via* reduction of protons from electrolyte solution (Equations S8-S10).

$$Q_{\text{ECH}} = n_{\text{Prod}} \cdot z \cdot N_{\text{A}} \cdot e \quad (\text{S8})$$

$$Q_{\text{HER}} = \int_0^t I \cdot dt \quad (\text{S9})$$

$$FE = \frac{Q_{\text{ECH}}}{Q_{\text{HER}}} \quad (\text{S10})$$

The n_{Prod} refers to the amount of product formed, the z is the number of electrons required for electrocatalytic hydrogenation of *trans*-2-penten-1-al, which is two or four depending on the investigated product. The N_{A} is *Avogadro* constant, e refers to the elemental charge and I is the current passed through the cell. The t stands for the reaction time.

Thermal hydrogenation of trans-2-penten-1-al

Activation energies of hydrogenation of different functional groups of *trans*-2-penten-1-al on Pd and Ru were determined *via* thermo-chemical hydrogenation of the respective molecule, i.e., valeraldehyde or *trans*-2-penten-1-ol at 1 bar hydrogen pressure. Therefore, the same setup and the same two-compartment batch cell as in ECH experiments were used but without *Nafion*TM N117 membrane. The catalyst (20 mg) was added directly to solution (120 mL, pH 5, 650 rpm) without coating onto the felt and the cell was heated to the desired temperature (295-348 K). Gas chromatography was performed in the same way as in electrocatalytic hydrogenation runs. Turnover Frequencies (TOF_{TCH}) and initial rates ($r_{\text{init,TCH}}$) of formation of different reaction products were calculated according to Equations S5-S6. Activation energies (E_{A}^{M}), with M standing for the respective metal, were determined *via Arrhenius* equation and plots of $\ln(\text{TOF}_{\text{TCH}})$ vs. $1/T$ (Equations S11-S13).

$$\text{TOF}_{\text{TCH}} = A_0 \cdot e^{-\frac{E_{\text{A}}^{\text{M}}}{RT}} \quad (\text{S11})$$

$$\ln(\text{TOF}_{\text{TCH}}) = \ln(A_0) - \frac{E_{\text{A}}^{\text{M}}}{R} \cdot \frac{1}{T} \quad (\text{S12})$$

$$E_{\text{A}}^{\text{M}} = -m \cdot R \quad (\text{S13})$$

The A_0 is the pre-exponential factor, the R is the universal gas constant and T stands for the temperature. The m is the slope of the resulting $\ln(\text{TOF}_{\text{TCH}})$ vs. $1/T$ plot.

Adsorption isotherm measurements

Adsorption isotherms of valeraldehyde and *trans*-2-penten-1-ol on Ru- and Pd-containing catalysts were measured with and without application of an external electric potential. For measurements at open circuit potential (OCP, $E_{\text{RHE}} = 0.85 \text{ V}$), 20 mg of catalyst were suspended in 1 mL solutions of different concentrations of adsorptive in phosphate buffered electrolyte (pH 5). The suspensions were stored at constant temperature (278-323 K) and periodically shaken for 48 h in order to allow for complete equilibration. Afterwards, the catalyst was filtrated off and the remaining solution was analyzed by gas chromatography according to the procedure introduced above. A detailed derivation for calculating thermodynamic properties from volumetric adsorption isotherm measurements is given in Section 2 of SI.

In case of adsorption isotherms recorded under an additional external electric potential, either a volumetric approach or cyclovoltammetry was applied.

When Ru-containing catalysts were used the same setup as in ECH experiments was used but without *Nafion*TM N117 membrane. Furthermore, the cell was only filled with 100 mL of electrolyte (pH 5) and the platinum wire was used as CE and RE. For catalyst coating, only 10 mg of material was suspended in 1 mL of an isopropyl alcohol/water (25/75 v/v) mixture. Different concentrations of adsorptive were added to solution and the potential at WE was set to 0.50 and 0.10 V vs. RHE, respectively. After 24 h of equilibration the solution was analyzed by GC. Due to adsorption on bare carbon felt, which could not be neglected, for each concentration of adsorptive a blank run on a felt without catalyst coating was performed and subsequently subtracted from the actual experiment. The resulting data were evaluated in the same way like the results received at OCP.

For Pd-containing catalysts, the uptake under external electric potential was determined from CV curves recorded in electrolytes containing different concentrations of adsorptive. The suppression of H_{upd} signals with increasing concentration of valeraldehyde or *trans*-2-penten-1-ol allowed for calculating the surface coverage with organics and hence, the adsorbed amount. A detailed derivation is given in Section 3 of SI.

4.4.2 Evaluation of volumetric adsorption isotherm measurements

The adsorbed amount of organic species, i.e., valeraldehyde or *trans*-2-penten-1-ol on catalyst surface ($c_{\text{ads}}^{\text{M}}$) was determined *via* subtracting the concentration in the filtrate (c_{filt}) from the initial concentration (c_0) according to Equation S14. The respective uptake ($n_{\text{upt}}^{\text{M}}$) was calculated by taking into account the solution volume (V_{sol}) and catalyst amount (m_{Cat}) as shown in Equation S15.

$$c_{\text{ads}}^{\text{M}} = c_0 - c_{\text{filt}} \quad (\text{S14})$$

$$n_{\text{upt}}^{\text{M}} = \frac{c_{\text{ads}}^{\text{M}}}{m_{\text{Cat}}} \cdot V_{\text{sol}} \quad (\text{S15})$$

Plotting of $n_{\text{upt}}^{\text{M}}$ against c_0 resulted in the adsorption isotherm of adsorptive on the respective catalyst material. Adsorption equilibrium constants ($K_{\text{ads}}^{\text{M}}$) were determined *via* linearizing *Langmuir* adsorption equation (Equation S16-S17) and plotting $\frac{1}{n_{\text{upt}}^{\text{M}}}$ vs. $\frac{1}{c_0}$. The resulting linear graphs showed a y-axis intercept of $\frac{1}{n_{\text{upt,ML}}^{\text{M}}}$ and a slope of $\frac{1}{n_{\text{upt,ML}}^{\text{M}} \cdot K_{\text{ads}}^{\text{M}}}$, from which the respective equilibrium constants were derived (Table S5-S6). The $n_{\text{upt,ML}}^{\text{M}}$ is the uptake of adsorptive on the metal catalyst that is necessary to reach full monolayer coverage.

$$n_{\text{upt}}^{\text{M}} = \frac{n_{\text{upt,ML}}^{\text{M}} \cdot K_{\text{ads}}^{\text{M}} \cdot c_0}{1 + K_{\text{ads}}^{\text{M}} \cdot c_0} \quad (\text{S16})$$

$$\frac{1}{n_{\text{upt}}^{\text{M}}} = \frac{1}{n_{\text{upt,ML}}^{\text{M}} \cdot K_{\text{ads}}^{\text{M}}} \cdot \frac{1}{c_0} + \frac{1}{n_{\text{upt,ML}}^{\text{M}}} \quad (\text{S17})$$

The standard adsorption enthalpy ($\Delta H_{\text{ads}}^{\text{o,M}}$) of a given adsorptive, i.e., valeraldehyde or *trans*-2-penten-1-ol on Ru- and Pd-containing catalysts was determined using *van't Hoff* equation (Equation S18) and plotting $\ln(K_{\text{ads}}^{\text{M}})$ against $1/T$. The $\Delta H_{\text{ads}}^{\text{o,M}}$ was determined from the slope of the resulting straight line according to Equation S19.

$$\ln(K_{\text{ads}}^{\text{M}}) = -\frac{\Delta H_{\text{ads}}^{\text{o,M}}}{R} \cdot \frac{1}{T} + \frac{\Delta S_{\text{ads}}^{\text{o,M}}}{R} \quad (\text{S18})$$

$$\Delta H_{\text{ads}}^{\text{o,M}} = -m \cdot R \quad (\text{S19})$$

Table S5: Adsorption equilibrium constants and monolayer uptakes for adsorption of valeraldehyde and *trans*-2-penten-1-ol on 5 wt% Pd/CNT-COOH and 5 wt% Ru/CNT-COOH at OCP.

		Valeraldehyde		<i>trans</i> -2-Penten-1-ol	
		Pd	Ru	Pd	Ru
278 K	$K_{\text{ads}}^{\text{M}}$ [L / mol]	22.0	49.3	6.9	23.0
	$n_{\text{upt}}^{\text{M}}$ [mmol / g _{cat}]	1.9	0.7	7.4	2.4
295 K	$K_{\text{ads}}^{\text{M}}$ [L / mol]	0.7	18.0	3.0	2.8
	$n_{\text{upt}}^{\text{M}}$ [mmol / g _{cat}]	57.8	2.3	17.0	18.1
323 K	$K_{\text{ads}}^{\text{M}}$ [L / mol]	0.04	3.4	1.1	0.3
	$n_{\text{upt}}^{\text{M}}$ [mmol / g _{cat}]	100.0	11.9	46.7	150.2

Figure S2 shows plots of $\frac{1}{n_{\text{upt}}^{\text{M}}}$ vs. $\frac{1}{c_0}$ of valeraldehyde and *trans*-2-penten-1-ol adsorption on

Ru at 295 K and a potential of 0.50 and 0.10 V vs. RHE, respectively.

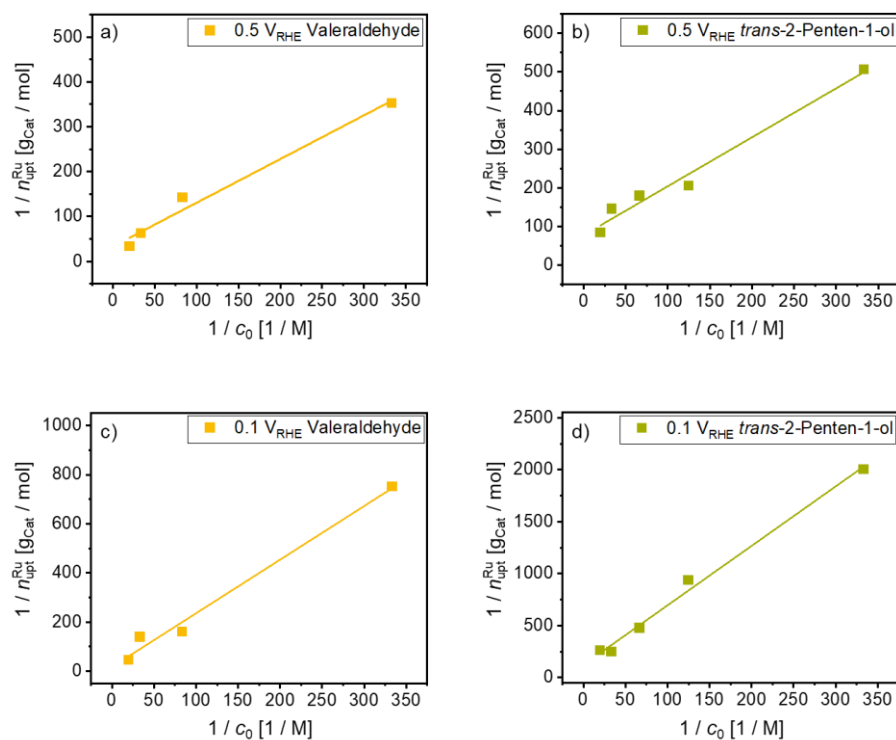
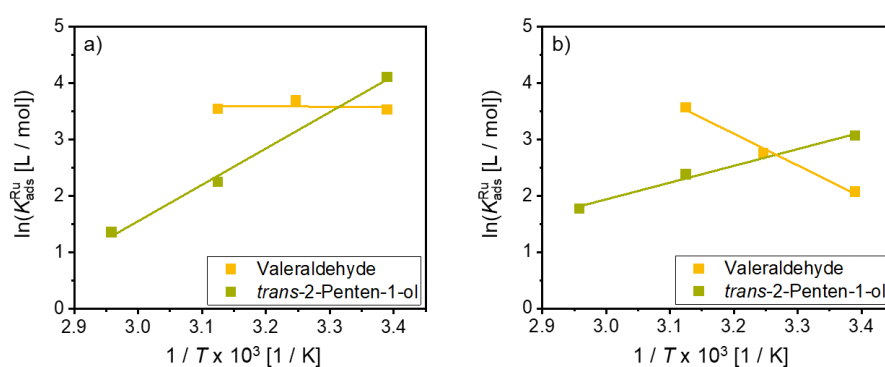
**Figure S2:** Plots of linearized *Langmuir* equation for adsorption isotherms of **a), c)** valeraldehyde and **b), d)** *trans*-2-penten-1-ol on Ru supported on CNT-COOH at 295 K and different E_{RHE} .

Figure S3 contains the resulting *van't Hoff* plots for determining the adsorption heat of valeraldehyde and *trans*-2-penten-1-ol on 5 wt% Ru/CNT-COOH at various external electric potentials.

Table S6: Adsorption equilibrium constants and monolayer uptakes for adsorption of valeraldehyde and *trans*-2-penten-1-ol on 5 wt% Ru/CNT-COOH at different external electric potentials.

		Valeraldehyde		<i>trans</i> -2-Penten-1-ol	
E_{RHE} [V]		0.50	0.10	0.50	0.10
295 K	K_{ads}^M [L / mol]	34.1	7.9	60.8	21.5
	n_{upt}^M [mmol / g _{Cat}]	30.1	57.9	13.0	8.1
308 K	K_{ads}^M [L / mol]	39.9	15.8	9.5	10.8
	n_{upt}^M [mmol / g _{Cat}]	78.0	82.7	52.9	75.6
320 K	K_{ads}^M [L / mol]	34.5	35.2	3.9	5.9
	n_{upt}^M [mmol / g _{Cat}]	94.6	29.2	426.5	131.8

**Figure S3:** *van't Hoff* plots for determining the adsorption heat of valeraldehyde and of *trans*-2-penten-1-ol on 5 wt% Ru/CNT-COOH at a) $E_{RHE} = 0.5$ V and b) $E_{RHE} = 0.1$ V.

4.4.3 Evaluation of thermodynamic adsorption properties on Pd

The standard free energy of adsorptive uptake on Pd in water ($\Delta G_{\text{ads}}^{\circ} = \Delta G_{\text{ads}}^{c=0}$) is calculated based on the assumption of Reactions 3-4 being quasi-equilibrated, i.e., the change in *Gibbs* free energy of the reactions being zero ($\Delta G = 0$) and the chemical potentials of reactants and products being equal (Equations S20-S21).

$$\mu_{\text{H}^+} + \mu_{\text{el}} = \mu_{\text{H}} \quad (\text{S20})$$

$$\mu_{\text{H}^+} + \mu_{\text{el}} + \mu_{\text{BzHO}} = \mu_{\text{H}} + \mu_{\text{BzHO}^*} \quad (\text{S21})$$

With the expression of μ_{H^+} , and μ_{el} defined in Equations S22-S23 and the expressions of μ_{H} , μ_{Org} and μ_{Org^*} in Equations S24-S26, Equation S21 can be reformulated to Equation S27.

$$\mu_{\text{el}} = -F\phi_{\text{Pd}} \quad (\text{S22})$$

$$\mu_{\text{H}^+} = \mu_{\text{H}^+}^{\circ} + RT \ln \frac{a_{\text{H}^+}}{a_{\text{H}^+}^{\circ}} + F\phi_{\text{aq}} \quad (\text{S23})$$

$$\mu_{\text{H}} = \mu_{\text{H}}^{\circ} + RT \ln \frac{\theta_{\text{H}}}{1 - \theta_{\text{H}} - \theta_{\text{Org}}} + \mu_{\text{excess}} \quad (\text{S24})$$

$$\mu_{\text{Org}} = \mu_{\text{Org}}^{\circ} + RT \ln c_{\text{Org}} \quad (\text{S25})$$

$$\mu_{\text{Org}^*} = \mu_{\text{Org}^*}^{\circ} + RT \ln \frac{\theta_{\text{Org}}}{1 - \theta_{\text{H}} - \theta_{\text{Org}}} \quad (\text{S26})$$

$$\begin{aligned} & \mu_{\text{H}}^{\circ} - \left(\mu_{\text{H}^+}^{\circ} + F\phi_{\text{aq,SHE}} \right) - \left(-F\phi_{\text{Pd,SHE}} \right) + \mu_{\text{excess}} + \mu_{\text{Org}^*}^{\circ} - \mu_{\text{Org}}^{\circ} = \\ & = RT \ln c_{\text{Org}} - RT \left(\ln \frac{\theta_{\text{H}}}{1 - \theta_{\text{H}} - \theta_{\text{Org}}} + \frac{\theta_{\text{Org}}}{1 - \theta_{\text{H}} - \theta_{\text{Org}}} \right) - F\eta \end{aligned} \quad (\text{S27})$$

The μ_{H^+} is the hydronium ion's chemical potential, and μ_{H} is the chemical potential of adsorbed H on Pd surface. The electron is treated as a reactant with a chemical potential (μ_{el}) that is its *Fermi* level according to *IUPAC* definition. The μ_{el} is determined by the electric potential on Pd, ϕ_{Pd} (Eq. S22). The μ_{H^+} comprises its standard chemical potential $\mu_{\text{H}^+}^{\circ}$, a thermodynamic activity (a_{H^+}) dependent term and an electrostatic potential energy term ($F\phi_{\text{aq}}$) that arises from the potential (ϕ_{aq}) in bulk electrolyte (Eq. S23). Here, F is *Faraday* constant. The μ_{H} comprises the standard chemical potential of H_{ads} (μ_{H}°), a term that is determined by the

coverage of Pd with H_{upd} and adsorbate (θ_{H} , θ_{Org}), respectively and an excess chemical potential μ_{excess} accounting for the effect from non-ideality (Eq. S24).

The μ_{Org} is the chemical potential of adsorptive in aqueous phase that is determined by its standard chemical potential (μ_{Org}°) and its concentration in water, c_{Org} (Eq. S25). The μ_{Org^*} is the chemical potential of adsorbate on Pd surface consisting of the standard chemical potential of adsorbed species ($\mu_{\text{Org}^*}^{\circ}$) and a term depending on θ_{H} and θ_{Org} (Eq. S26).

At open circuit potential, the system is essentially the reversible hydrogen electrode, i.e., electric potential on Pd and in bulk aqueous phase are $\phi_{\text{Pd,RHE}}$ and $\phi_{\text{aq,RHE}}$. When applying an overpotential (η), the electrode potential has the following relations:

$$\phi_{\text{Pd}} - \phi_{\text{aq}} = \eta + (\phi_{\text{Pd,RHE}} - \phi_{\text{aq,RHE}}) \quad (\text{S28a})$$

$$\phi_{\text{Pd,RHE}} - \phi_{\text{aq,RHE}} = \phi_{\text{Pd,SHE}} - \phi_{\text{aq,SHE}} + RT \ln \frac{a_{\text{H}^+}}{a_{\text{H}^+}^{\circ}} \quad (\text{S28b})$$

Equation S28b is the relation between RHE and SHE (Standard Hydrogen Electrode) based on *Nernst* equation and substitutes the $(\phi_{\text{Pd}} - \phi_{\text{aq}})$ term to give Equation S27.

Hence, the left side of Equation S27 comprises the standard free energy of H_{upd} adsorption on Pd on RHE scale (Equation S29), an excess chemical potential, i.e., an excess free energy of H_{upd} adsorption, at a given electrolyte composition and external electric potential, and the standard free energy of adsorption of organics on Pd in aqueous phase (Equations S30-S31).

$$\Delta G_{\text{upd}}^{\circ} = \mu_{\text{H}}^{\circ} - (\mu_{\text{H}^+}^{\circ} + F\phi_{\text{aq,SHE}}) - (-F\phi_{\text{Pd,SHE}}) \quad (\text{S29})$$

$$\Delta G_{\text{Org}}^{\circ} = \mu_{\text{Org}^*}^{\circ} - \mu_{\text{Org}}^{\circ} \quad (\text{S30})$$

$$\Delta G_{\text{Org}}^{\circ} = RT \ln c_{\text{Org}} - RT \left(\ln \frac{\theta_{\text{H}}}{1 - \theta_{\text{H}} - \theta_{\text{Org}}} + \frac{\theta_{\text{Org}}}{1 - \theta_{\text{H}} - \theta_{\text{Org}}} \right) - F\eta - (\Delta G_{\text{upd}}^{\circ} + \mu_{\text{excess}}) \quad (\text{S31})$$

It has to be noted that the last term of Equation S31, $(\Delta G_{\text{upd}}^{\circ} + \mu_{\text{excess}})$, is calculated for an adsorptive-free electrolyte according to Equation S32.

$$\Delta G_{\text{upd}}^{\circ} + \mu_{\text{excess}} = -RT \ln \frac{\theta_{\text{H}}}{1 - \theta_{\text{H}}} - F\eta \quad (\text{S32})$$

Extrapolating plots of $\Delta G_{\text{Org}}^{\circ}$ vs. c_{Org} at a given external electric potential to $c_{\text{Org}} = 0$ and inserting the resulting standard free energies of organics adsorption into a linearized

Gibbs-Helmholtz equation results in the standard adsorption heat of the respective molecule on Pd surface, that is the slope of $\Delta G_{\text{Org}}^{\circ} / T$ over $1/T$ plot (Figure S4).

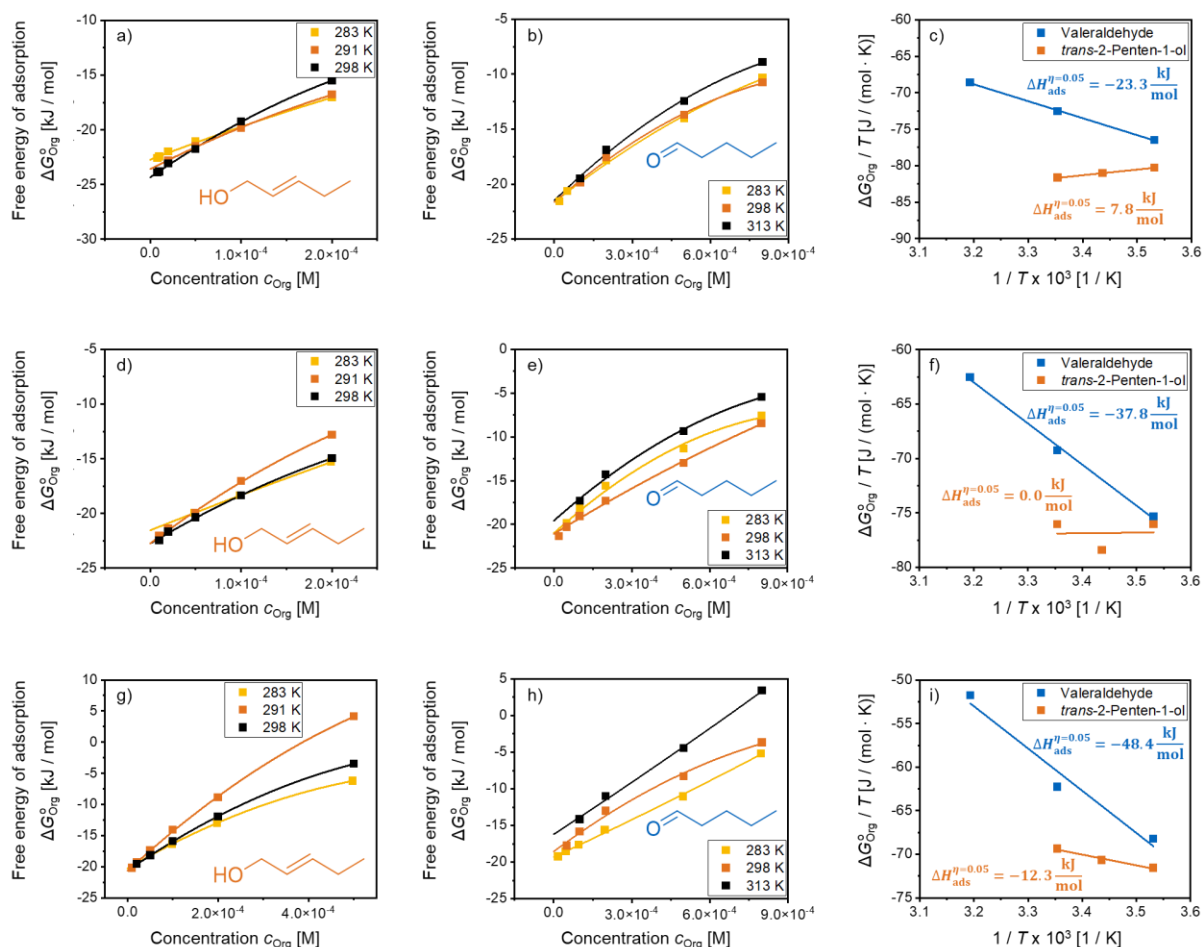


Figure S4: Development of free energy of adsorption of *trans*-2-penten-1-ol (a, d, g) and valeraldehyde (b, e, h) on Pd with organics concentration, at $E_{\text{RHE}} = 0.10, 0.15, 0.20$ V and corresponding plots of $\Delta G_{\text{Org}}^{\circ} / T$ vs. $1/T$ for deriving the organics heat of adsorption on Pd (c, f, i).

4.5 References

- [1] a) B. M. Upton, A. M. Kasko, *Chemical Reviews* **2016**, *116*, 2275-2306; b) F. Johnsson, J. Kjärstad, J. Rootzén, *Climate Policy* **2019**, *19*, 258-274.
- [2] a) G. W. Huber, S. Iborra, A. Corma, *Chemical Reviews* **2006**, *106*, 4044-4098; b) U. Sanyal, J. Lopez-Ruiz, A. B. Padmaperuma, J. Holladay, O. Y. Gutiérrez, *Organic Process Research & Development* **2018**, *22*, 1590-1598; c) E. Andrews, J. A. Lopez-Ruiz, J. D. Egbert, K. Koh, U. Sanyal, M. Song, D. Li, A. J. Karkamkar, M. A. Derewinski, J. Holladay, O. Y. Gutiérrez, J. D. Holladay, *ACS Sustainable Chemistry & Engineering* **2020**, *8*, 4407-4418.
- [3] C. H. Lam, S. Das, N. C. Erickson, C. D. Hyzer, M. Garedew, J. E. Anderson, T. J. Wallington, M. A. Tamor, J. E. Jackson, C. M. Saffron, *Sustainable Energy & Fuels* **2017**, *1*, 258-266.
- [4] a) E. J. Biddinger, O. Y. Gutierrez, J. Holladay, *Journal of Applied Electrochemistry* **2021**, *51*, 1-3; b) L. Zhang, T. U. Rao, J. Wang, D. Ren, S. Sirisommoonchai, C. Choi, H. Machida, Z. Huo, K. Norinaga, *Fuel Processing Technology* **2022**, *226*, 107097.
- [5] a) A. F. Ghoniem, *Progress in Energy and Combustion Science* **2011**, *37*, 15-51; b) N. Bauer, I. Mouratiadou, G. Luderer, L. Baumstark, R. J. Brecha, O. Edenhofer, E. Kriegler, *Climatic Change* **2016**, *136*, 69-82.
- [6] a) U. Sanyal, J. Lopez-Ruiz, A. B. Padmaperuma, J. D. Holladay, O. Y. Gutiérrez, *Organic Process Research & Development* **2018**, *22*, 1590-1598; b) C. H. Lam, W. Deng, L. Lang, X. Jin, X. Hu, Y. Wang, *Energy & Fuels* **2020**, *34*, 7915-7928; c) K. Li, Y. Sun, *Chemistry – A European Journal* **2018**, *24*, 18258-18270.
- [7] Y. Song, U. Sanyal, D. Pangotra, J. D. Holladay, D. M. Camaioni, O. Y. Gutiérrez, J. A. Lercher, *Journal of Catalysis* **2018**, *359*, 68-75.
- [8] Y. Song, O. Y. Gutiérrez, J. Herranz, J. A. Lercher, *Applied Catalysis B: Environmental* **2016**, *182*, 236-246.
- [9] a) S. A. Akhade, N. Singh, O. Y. Gutiérrez, J. Lopez-Ruiz, H. Wang, J. D. Holladay, Y. Liu, A. Karkamkar, R. S. Weber, A. B. Padmaperuma, M.-S. Lee, G. A. Whyatt, M. Elliott, J. E. Holladay, J. L. Male, J. A. Lercher, R. Rousseau, V.-A. Glezakou, *Chemical Reviews* **2020**, *120*, 11370-11419; b) N. Singh, U. Sanyal, G. Ruehl, K. A. Stoerzinger, O. Y. Gutiérrez, D. M. Camaioni, J. L. Fulton, J. A. Lercher, C. T. Campbell, *Journal of Catalysis* **2020**, *382*, 372-384.
- [10] a) T. Kan, V. Strezov, T. J. Evans, *Renewable and Sustainable Energy Reviews* **2016**, *57*, 1126-1140; b) D. K. Ratnasari, A. Bijl, W. Yang, P. G. Jönsson, *Catalysts* **2020**, *10*; c) A. V. Bridgwater, *Biomass and Bioenergy* **2012**, *38*, 68-94.
- [11] J. Iglesias, I. Martínez-Salazar, P. Maireles-Torres, D. Martin Alonso, R. Mariscal, M. López Granados, *Chemical Society Reviews* **2020**, *49*, 5704-5771.
- [12] P. Mäki-Arvela, J. Hájek, T. Salmi, D. Y. Murzin, *Applied Catalysis A: General* **2005**, *292*, 1-49.
- [13] a) P. Gallezot, D. Richard, *Catalysis Reviews* **1998**, *40*, 81-126; b) P. Claus, *Topics in Catalysis* **1998**, *5*, 51-62.
- [14] a) X. Lan, T. Wang, *ACS Catalysis* **2020**, *10*, 2764-2790; b) C. Louis, L. Delannoy, in *Advances in Catalysis, Vol. 64* (Ed.: C. Song), Academic Press, **2019**, pp. 1-88.
- [15] M. Tamura, K. Tokonami, Y. Nakagawa, K. Tomishige, *ACS Catalysis* **2016**, *6*, 3600-3609.
- [16] E. Bailón-García, F. J. Maldonado-Hódar, A. F. Pérez-Cadenas, F. Carrasco-Marín, *Catalysts* **2013**, *3*.
- [17] N. Singh, U. Sanyal, J. L. Fulton, O. Y. Gutiérrez, J. A. Lercher, C. T. Campbell, *ACS Catalysis* **2019**.
- [18] D. Sokolskii, A. Pak, M. Ginzburg, V. Vozdvizhenskii, *DOKLADY AKADEMII NAUK SSSR* **1978**, *239*, 897-900.
- [19] a) A. Giroir-Fendler, D. Richard, P. Gallezot, **1988**, *41*, 171-178; b) A. Giroir-Fendler, D. Richard, P. Gallezot, in *Studies in Surface Science and Catalysis, Vol. 41*, Elsevier Amsterdam, **1988**, p. 171.
- [20] a) F. Delbecq, P. Sautet, *Journal of Catalysis* **1995**, *152*, 217-236; b) F. Delbecq, P. Sautet, *Journal of Catalysis* **2002**, *211*, 398-406.
- [21] a) P. Claus, Y. Önal, *Handbook of Heterogeneous Catalysis: Online* **2008**, 3308-3329; b) P. Sautet, *Topics in Catalysis* **2000**, *13*, 213-219.
- [22] J. L. Davis, M. A. Barteau, *Journal of Molecular Catalysis* **1992**, *77*, 109-124.
- [23] a) Y. Dai, X. Gao, X. Chu, C. Jiang, Y. Yao, Z. Guo, C. Zhou, C. Wang, H. Wang, Y. Yang, *Journal of Catalysis* **2018**, *364*, 192-203; b) N. Mahata, F. Gonçalves, M. F. R. Pereira, J. L. Figueiredo, *Applied Catalysis A: General* **2008**, *339*, 159-168.
- [24] a) V. Ponc, *Applied Catalysis A: General* **1997**, *149*, 27-48; b) B. Bachiller-Baeza, A. Guerrero-Ruiz, P. Wang, I. Rodríguez-Ramos, *Journal of Catalysis* **2001**, *204*, 450-459.
- [25] J. Akinola, N. Singh, *Journal of Applied Electrochemistry* **2021**, *51*, 37-50.

- [26] N. Singh, M.-S. Lee, S. A. Akhade, G. Cheng, D. M. Camaioni, O. Y. Gutiérrez, V.-A. Glezakou, R. Rousseau, J. A. Lercher, C. T. Campbell, *ACS Catalysis* **2019**, *9*, 1120-1128.
- [27] G. Yang, V. Maliekkal, X. Chen, S. Eckstein, H. Shi, D. M. Camaioni, E. Baráth, G. L. Haller, Y. Liu, M. Neurock, J. A. Lercher, *Journal of Catalysis* **2021**, *404*, 579-593.
- [28] X. Chen, Y. Liu, J. A. Lercher, *ECS Meeting Abstracts* **2021**, *MA2021-02*, 792-792.
- [29] a) A. Solhy, B. F. Machado, J. Beausoleil, Y. Kihn, F. Gonçalves, M. F. R. Pereira, J. J. M. Órfão, J. L. Figueiredo, J. L. Faria, P. Serp, *Carbon* **2008**, *46*, 1194-1207; b) B. F. Machado, H. T. Gomes, P. Serp, P. Kalck, J. L. Figueiredo, J. L. Faria, *Catalysis Today* **2010**, *149*, 358-364.
- [30] A. Giroir-Fendler, D. Richard, P. Gallezot, *Catalysis Letters* **1990**, *5*, 175-181.
- [31] F. Coloma, A. Sepúlveda-Escribano, J. L. G. Fierro, F. Rodríguez-Reinoso, *Applied Catalysis A: General* **1997**, *150*, 165-183.
- [32] A. Borodziński, M. Bonarowska, *Langmuir* **1997**, *13*, 5613-5620.
- [33] a) A. Shastri, *Journal of Catalysis* **1985**, *95*, 271-283; b) J. Rodriguez, *Surface Science Reports* **1996**, *24*, 223-287.
- [34] R. Chetty, W. Xia, S. Kundu, M. Bron, T. Reinecke, W. Schuhmann, M. Muhler, *Langmuir* **2009**, *25*, 3853-3860.
- [35] a) K. Christmann, *Progress in Surface Science* **1995**, *48*, 15-26; b) P. Canton, G. Fagherazzi, M. Battagliarin, F. Menegazzo, F. Pinna, N. Pernicone, *Langmuir* **2002**, *18*, 6530-6535.

4.6 Associated content

Publication

This chapter is based on a manuscript planned for submission (Philipp Fischer, Yue Liu, Johannes A. Lercher)

Contributions

P.F. did main contributions in catalyst preparation, CV and kinetic analysis, adsorption measurements, data analysis and manuscript preparation. Y.L. contributed to data analysis and manuscript preparation. Y.L. and J.A.L. conceived the research. The manuscript was written through contributions of all authors.

Acknowledgements

The authors would like to thank German Research Foundation DFG, the Federal Ministry of Education and Research of Germany as well as the Bavarian Ministry of Science and Art and the cluster of e-conversion for their support. Xaver Hecht, Muhammad Iqbal and Andreas Marx are thanked for their technical support and measuring H₂ chemisorption as well as N₂ physisorption, Martin Neukamm for doing elemental analysis and Roland Weindl as well as Simon Krebs for measuring TEM. Angelina Cuomo, Daniel Rottmann and Fabio Fidelibus are thanked for their help in experimental work.

5 Summary and conclusion

Fundamental steps during electrocatalytic hydrogenation of oxygenated compounds on transition metal catalysts in water were investigated. The analysis of these elementary reactions provides insights into charge transfer processes within the electrochemical double-layer. These are influenced by external electric potential, electrolyte composition and catalyst properties.

The electrocatalytic activation and adsorption of hydrogen on metal electrode surface, e.g., Pt is controlled by variation of applied overpotential. An increasing negative electric bias raises electrode *Fermi* level and consequently, the filling of Pt-H antibonding state. The stabilization of hydrogen on Pt electrode surface is reduced and the corresponding adsorption heat is lowered. A decreased binding strength of H on metal surface at high cathodic overpotentials increases rates of hydrogen evolution reaction and electrocatalytic hydrogenation of benzaldehyde. However, due to an increased catalyst selectivity towards H₂ formation instead of ECH the *Faradaic* efficiency is reduced.

The thermodynamic properties of hydrogen on Pt electrode surface are altered upon variation of electrolyte composition. In highly acidic solutions, the adsorption heat and entropy of H on metal surface are reduced. This accelerates HER and ECH rates though, the current efficiency on Pt is decreased. The electrochemical double-layer is displaced from electrode surface upon hydrogen adsorption. The associated energetic contribution depends on the accumulation of hydronium ions within EDL. At low pH, the compensation of the heat that is released during H adsorption is large while the entropy loss upon immobilization of H₃O⁺ at OHP is diminished due to a reduced entropy in bulk solution. Hydrated alkali metal cations with a large radius, e.g., K⁺ show a high activity for hydrogenolysis and release of hydronium ions. The pH in close proximity to electrode surface is lowered and Pt-H bond is destabilized. The *Faradaic* efficiency of electrocatalytic benzaldehyde hydrogenation is slightly reduced in comparison to metal cations with small radii. An enhanced ionic strength of electrolyte seems to influence thermodynamic properties of adsorbed H and BzHO on Pt electrode surface. Due to a more rigid double-layer and a reduced concentration of H₃O⁺ close to metal surface the adsorption heat and entropy of H on Pt are increased and the current efficiency is improved. The compactness of EDL at high ionic strength also reduces the binding strength of organic molecules, e.g., benzaldehyde on electrode surface. This renders a conversion of benzaldehyde more likely and raises its rate of electrocatalytic hydrogenation on Pt.

The selectivity of electrocatalytic hydrogenation of *trans*-2-penten-1-al is influenced by catalyst properties and electrolyte pH. In general, a large negative charge density on metal electrode surface is beneficial for selective hydrogenation of CO group. This can be achieved

by application of a large negative overpotential to metals with large and highly populated d orbitals. The population of d orbitals can be further increased *via* addition of an oxophilic and electropositive promotor metal that also activates CO group. Due to steric constraints adsorption and activation of the double bond are decreasing with increasing particle size. A low concentration of hydronium ions in bulk solution favors the selective formation of (un)saturated alcohols. Consequently, on bimetallic Ru-Fe catalysts with large metal particles the selectivity towards alcohol formation in ECH of *trans*-2-penten-1-al in pH 5 electrolyte is increased to 40% whereas it is below 5% without application of promoting effects.